UNIVERSITÉ DE STRASBOURG

ÉCOLE DOCTORALE DE PHYSIQUE ET CHIMIE-PHYSIQUE

Institut Charles Sadron UPR 22

THÈSE présentée par :

Tetiana MUKHINA

soutenue le : 15 **novembre 2019**

pour obtenir le grade de : **Docteur de l'université de Strasbourg**

Discipline/ Spécialité : PHYSIQUE

Active Fluctuations and Electrostatic Interactions in Floating Lipid Membranes

THÈSE dirigée par :

M CHARITAT Thierry	Professeur, Université de Strasbourg
Mme FRAGNETO Giovanna	Directrice de Recherche, Institut Laue-Langevin

RAPPORTEURS :

Mme BASSEREAU Patricia	Directrice de Recherche, Institut Curie, CNRS
M SCHNECK Emanuel	Professeur, TU Darmstadt

AUTRES MEMBRES DU JURY :

M HAACKE Stefan	Professeur, Université de Strasbourg

INVITÉS :

M DAILLANT Jean	Directeur de Recherche, Synchrotron SOLEIL
M GERELLI Yuri	HDR, Institut Laue-Langevin

Contents

Foreword

Two different projects were carried out during this PhD thesis work, which was focused on the investigation of structure, function and physical properties of phospholipid membranes by combining a large number of experimental techniques.

The first project focused on the investigation of out-of-equilibrium membrane fluctuations caused by protein Bacteriorhodopsin pumping activity.

Within the second project the interaction between strongly confined highly negatively charged lipid bilayers in the presence of only monovalent counterions was investigated.

This manuscript consists of five parts. The introduction to the thesis is given in Part I. Sample description, sample preparation protocols and used experimental techniques are discussed in Part II. The results obtained within the two projects are discussed in Part III and Part IV, which can be read independently. Developments of sample environment and experimental setup that have been carried out within this thesis are presented in Chapter 2 of Part II.

In Part V the general conclusions of the thesis work is presented.

Acronyms

DSPC	1,2-distearoyl-sn-glycero-3-phosphocholine
POPC	1-palmitoyl-2-oleoyl-glycero-3-phosphocholine
DPPC	1,2-dipalmitoyl-sn-glycero-3-phosphocholine
d_{75}DPPC	1,2-dipalmitoyl-d62-sn-glycero-3-phosphocholine-1,1,2,2-d4-N,N,N-trimethyl-d9
DPPS	1,2-Dipalmitoyl-sn-glycero-3-phosphoserine
DMPC	1,2-dimyristoyl-sn-glycero-3-phosphocholine
DMPS	1,2-dimyristoyl-sn-glycero-3-phospho-L-serine
DOPS	1,2-dioleoyl-sn-glycero-3-phospho-L-serine
DOPC	1,2-dioleoyl-sn-glycero-3-phosphocholine
NBD-PE	1,2-dipalmitoyl-sn-glycero-3-phosphoethanolamine-N-(7-nitro-2-1,3-benzoxadiazol-4-yl) (ammonium salt)
PM	Plasma membrane
BR	Bacteriorhodopsin
Arch-3	Archaerhodopsin-3
DDM	N-Dodecyl-b-D-Maltopyranoside
LB	Langmuir-Blodgett
LS	Langmuir-Schaefer
NR	Neutron reflectometry
XRR	X-ray reflectometry
SR	Synchrotron radiation
QCM-D	Quartz crystal microbalance with dissipation monitoring
AFM	Atomic force microscopy
FRAPP	Fluorescence recovery after pattern photobleaching
SLB	Supported lipid bilayer
SLD	Scattering length density
ED	Electron density
SUV	Small unilamellar vesicles
MUV	Multi unilamellar vesicle
t.r.	Transfer ratio
SC	Strong-Coupling
WC	Weak-Coupling
PB	Poisson-Boltzmann
ILL	Institut Laue-Langevin
IBS	Institut de Biologie Structurale
ILM	Institut Lumiére Matiére

Symbols

Ξ	Coupling constant
ℓ_{B}	Bjerrum length [m]
ℓ_{GC}	Gouy-Chapman length [m]
σ_s	Surface charge density [e^-/nm^{-2}]
ℓ_{D}	Debye-Hückel length [m]
H	Hamaker constant [J]
qe	Ion charge
q	Ion valency
d	Distance between charged plates [m]
$d_{w,1}$	Water layer thickness between silicon substrate and first bilayer [m]
$d_{w,2}$	Water layer thickness between two bilayers [m]
ε_w	Water dielectric constant
T	Temperature [K]
T_m	Transition temperature [K]
k_{B}	Boltzmann constant [J/K]
P	Pressure [Pa]
$a_\perp$	Lateral distance between ions [m]
A	Area per molecule [m^2]
Q	Wave vector [m^{-1}]
θ_{in}	Incident angle [rad]
θ_{sc}	Scattered angle [rad]
θ_{cr}	Critical angle [rad]
$\hbar$	Planck constant [Js]
Z	Number of electrons
n	Refractive index
r_e^-	Classical radius of an electron [m]
$V(r)$	Fermi pseudopotential [J]
E	Kinetic energy [J]
U	Interaction potential [Jm^{-2}]
R	Reflectivity []
γ	Membrane tension [Nm^{-1}]
κ	Bending modulus [J]
ρ	Scattering length density [m^{-2}]
b	Scattering length [m]
V_m	Molecular volume [m^3]
σ	Roughness [m]

Part I

Introduction

CHAPTER 1

Membrane-protein systems

1.1 The cell membrane

Biological membranes are omnipresent in living organisms and perform a wide range of vitally important functions. They cover cell organelles (plasma membrane) and serve as separator and compartmentalizer, enclosing the subcellular structures and organelles in eukaryotic cells (intracellular membranes). The plasma membrane (PM) functions like a semi-permeable barrier, which surrounds biological cells and separates their internal and external mediums, selectively controlling the flux of ions and molecules and maintaining cell homeostasis.

A cell membrane is a very complex system composed of several different constituents. Lipids (phospholipids, glycolipids, and sterols), which self assemble into a lipid bilayer, carbohydrates (glycoproteins and glycolipids) and proteins (lipid anchored proteins, peripheral and integral (transmembrane) proteins), which can be attached to the lipid bilayer or inserted into it, are the main constituents of cell membranes. Despite the high complexity and great variety of components, cell membranes possess a very well-defined organization and structure, which is provided mainly by the self-assembly properties of the lipid bilayer.

The lipid bilayer constitutes the skeleton of membranes and serves as a viscous medium and support for all membrane proteins, mediating and promoting protein activity and a wide range of additional vital processes which are unceasingly running in the cell [1].

Different models have been proposed in order to describe the structure, composition and organization of biomembranes. The fluid mosaic model proposed by Singer and Nicolson in 1972 stays the most complete and realistic description of the

natural membrane [2]. This model describes the PM structure as a mosaic of its main components: lipids, cholesterol, proteins and carbohydrates (Fig. I.1.1). It was suggested that the peripheral and integral proteins are distributed asymmetrically and inhomogeneously across the bilayer and all other constituent molecules (sterols, proteins, carbohydrates) are floating in a medium composed of lipids. In turn, phospholipid molecules are asymmetrically distributed between the two leaflets of the bilayer: charged phosphatidylserines, phosphatidylethanolamines and a small number of phosphatidylcholines are mainly present in the internal leaflet and large amounts of phosphatidylcholines, sphingolipids and glycolipids compose the outer leaflet of the PM [3]. The important elements of the fluid mosaic model are membrane dynamics and fluidity, reponsible for the lateral diffusive properties of membrane components, lipid flip-flop, rotational and translational motions, chain motion, lipid protrusion and membrane shape fluctuations.

The fluid mosaic model implies that a biological membrane is dynamic, fluid and constantly evolving and that it is permeable for ions and small molecules [3].

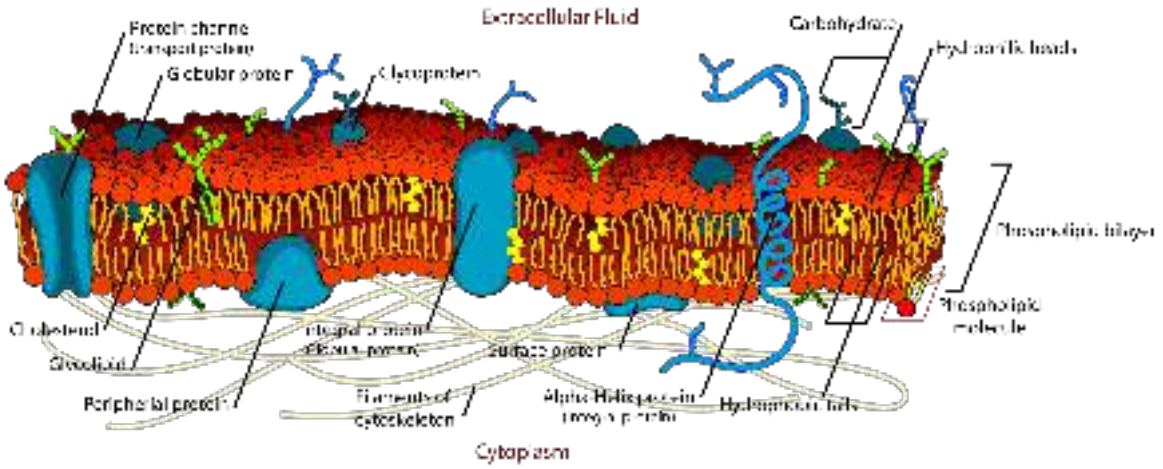

Figure I.1.1 – Fluid mosaic model of the cell membrane [4].

The fluid mosaic model of PM predicts free lateral diffusion of membrane components. However, labelling experiments indicate that sphingolipids, lipid-linked proteins and cholesterol may segregate into small size (10-200 nm) tightly packed liquid-ordered microdomains called rafts, which prevent lateral diffusion of some proteins in the membrane [5]. Rafts are dynamic structures with an ability to assemble and disassemble rapidly. It was shown that these nanodomains are resistant to solubilization by detergents [6] and therefore they were often called as detergent-

insoluble glycolipid-enriched complexes or detergent resistant membranes [7]. Rafts play significant biological roles in membrane signaling and trafficking [8].

The existence of these domains was predicted a long time ago [9] and it was remaining controversial for a long time. Due to their very small size (<200 nm), which is below the diffraction limit of a conventional optical microscope, and their instability, as they may form on time scales which are below the time scale of diffusion processes [3], it was a difficult task for scientists to observe and confirm their existence. But the development and application of several biochemical and biophysical tools, such as super-resolution optical microscopy techniques (photoactivated localization microscopy, stimulated emission depletion microscopy and nearfield scanning optical microscopy) and single-molecule based techniques (such as single-particle tracking, interferometric scattering microscopy and fluorescence correlation spectroscopy) help to shed light on this concept, allowing to visualize lipid-protein clustering and to perform dynamic measurements and to probe the diffusion of membrane molecules, attributing this property to the membrane heterogeneous organization [10–12]. However, these domains still lack direct in vivo visualization and numerous controversies concerning the organization and dynamics of these membrane domains are still remained unsolved. Therefore the further application and development of hight spacial and resolution techniques is required, which imposes that the field of lipid raft research will remain of great importance.

The great complexity of biological membranes, their heterogeneous composition and diverse functionality make them a very difficult, but very interesting system to investigate. In order to study the specific features and function of a particular constituent of the biomembrane, the implementation of specific approaches based on the use of simplified model systems is required and is usually implemented. Such an approach allows to characterize different constituents of the membranes, their intrinsic properties and performed functions independently. Structural characterization of membrane models and understanding of the relationship between their structure and function can provide an excellent platform for a better understanding of more complex natural biosystems.

1.2 Membrane fluctuations

As discussed above, real biological membranes are very complex systems comprising a big variety of active entities: transmembrane and peripheral proteins, channels and pumps, which unceasingly perform their vital functions. In living systems, the PM plays a crucial role in the transport of small molecules as it ensures the entry of nutrients, transfer of ions through the membrane, which are necessary to trigger activation of the molecular motors in muscle cells, signal propagation along axons or induction of acidification of some cell compartments, etc. These active processes involve specific membrane proteins, which use metabolic energy produced during ATP hydrolysis or photochemical reactions in the cell. The cytoskeleton network attached to the membrane has a big impact on the membrane dynamics, restricting membrane shape undulations and lipid and/or protein diffusion. Activity of macro-molecules, which periodically adhere to the membrane surface in order to fulfill their functions, has a huge influence on the membrane behavior as well. Therefore, a natural membrane is a very active system and it is continuously subject to the action of external forces, which have a great impact on the membrane shape fluctuations and physical properties.

Membranes are known to exhibit thermal fluctuations, but the presence of an active center, as it was discussed above, brings an active noise source to the system. The behavior of such a dynamic system does not satisfy the fluctuation-dissipation theorem anymore and leads to out-of-equilibrium membrane fluctuations [13]. Active fluctuations have been widely described theoretically [13–17], with the prediction of a new fluctuation spectrum in the presence of a non-equilibrium noise source.
The first experiments on Bacteriorhodopsin (BR) as a light-activated proton pump reconstituted in giant unilamellar vesicles (GUVs) were performed by J.-B. Manneville and co-workers [16, 18, 19] using micropipette aspiration [16, 19] and refined video-microscopy analysis [20]. These inspiring experiments on GUVs with reconstituted BR have demonstrated the influence of protein pumping activity on the membrane fluctuation spectrum for the first time. In fact, a larger excess area could be pulled out by micropipette when the protein was active, demonstrating that the light-driven BR proton pumping activity induces an amplification of the membrane shape fluctuations and a strong decrease in the effective bending modulus of the

membrane. This information was provided only at the micrometer scale and the membrane fluctuation spectrum was not measured. A complete understanding of the mechanisms at play in the active membrane fluctuations implies the need for a fine characterization of the fluctuation spectrum at sub-micronic length scales.

1.3 Protein reconstitution into membrane model systems

A comprehensive structural and functional study of PM is a non-trivial task, as all molecular components of the PM are involved in numerous processes running continuously in living cells. The interplay between the structure and functions of the PM constituents is a very complex and crucially important phenomenon mainly determined by the morphology and function of the integral and peripheral proteins attached or embedded into the membrane.

Membrane proteins perform a wide range of functions: they may be receptors for signal translocation across the cell, they perform an active or passive transport of molecules and ions across the membrane, they serve as attachment points for cytoskeleton and extracellular matrix, they can perform recognition functions and act as enzymes to catalyze reactions in the cell. In summary they play an essential role in the physiological functions of the living cells.

In turn, a very specific composition of the lipid bilayer is necessary to maintain protein and cell activity and vitality. Any slight variation in membrane lipid composition can lead to faulty modifications in the performance of the whole biosystem. As already mentioned, due to the incredible complexity of plasma membranes, to understand the specific functions and processes running in the cell by studying real biological samples is almost an impossible task. A simplified system composed only of a lipid bilayer with a reconstituted transmembrane protein can serve as a good model to mimic the cell membrane. Therefore the creation of a biologically relevant, simple and robust model system is the first step towards a better understanding of complex biological membranes and all their specific functions [21].

Reconstitution of membrane proteins into membrane-mimic systems (lipid bilayers) serves as a powerful tool to better understand the functional, structural and

physical properties of bio-membranes and to determine the specific role of transmembrane proteins [22]. Isolation of a specific integral membrane protein from biological membranes often involves the use of detergent, as detergent molecules can shield the hydrophobic area of transmembrane proteins from exposure to water, helping them to preserve their structural and functional integrity. To extract the specific protein from the PM, the cell has to be fully solubilized by the appropriate detergent and a target compound has to be extracted by purification from the formed biomass. At the end of a multi-step process a high purity protein-detergent solution can be obtained [23].

Numerous protocols involving use of detergent for the protein reconstruction in artificial membranes are extensively present in literature [21, 22, 24–30]. Such a large variety of employed approaches can be justified by the specificity of reconstituted transmembrane proteins, composition of lipid bilayers and type of membrane systems (vesicles, single, double or multibilayers, tethered systems, etc.).

In order to be reliable, the method for protein reconstitution has to provide a robust and reproducible outcome, fulfilling different criteria such as homogeneous insertion and distribution of protein in the membrane, controllable amount of proteins inserted, no denaturation or precipitation and no loss of protein functional activity during the reconstitution, unidirectional orientation in the membrane, ability to control and define the ionic strength and ionic composition of the medium and lipid composition and symmetry/asymmetry of the model membrane.

The choice of an appropriate lipid model system has to be made thoroughly as well. The protocols available in the literature deal, in most cases, with either small, large or giant unilamellar lipid vesicles. The choice of the model system depends on the aim of the study and available experimental techniques used to investigate the membrane-protein systems.

High-resolution surface-sensitive techniques are used to study the structure of planar membrane-protein systems and to probe their physical properties. Experiments devoted to the structural and functional investigation of reconstituted transmembrane proteins can also be performed, utilising the lipid bilayer as a natural medium for the protein. In this context, development of a reliable protocol for protein reconstitution into membrane-model systems opens the way for a wide

range of new experiments, allowing to investigate structure and dynamics of more complex membrane-model systems.

1.4 Main aim of project I

Main aim of this thesis work is the investigation of the out-of-equilibrium fluctuations of phospholipid membranes induced by active transmembrane proteins. In this context, Bacteriorhodopsin (BR) and Archaerhodopsin-3 (Arch-3) are used as light-driven proton pumps, which activity can be triggered by visible light. Model systems such as solid-supported single and floating phospholipid bilayers are used to study the structure and physical properties of lipid bilayers and their interactions with protein molecules. We aim to adapt the detergent-mediated protein incorporation method [31–33] for protein insertion into planar bilayers using the sugar-based detergent DDM. We aim to develop a robust protocol for protein reconstitution into membrame-mimic systems, while preserving the structural integrity and functional activity of the protein molecules and lipid bilayer. The method is optimized using available experimental lab techniques such as QCM-D, fluorescence microscopy, AFM and in-house X-ray reflectometry.

By means of large scale facility surface-sensitive techniques such as neutron (NR) and synchrotron radiation (SR) reflectometry experiments, we aim to characterize the structure of a pristine single and double lipid bilayer systems at Å resolution and to reveal all induced structural and compositional modifications caused by protein incorporation, as well as to quantify the amount of protein inserted in the membrane.

Off-specular SR reflectivity experiments were also performed and they will allow us to probe the lateral structural features of the solid-supported bilayers with and without embedded proteins and to directly access the physical properties of the system such as bending modulus, surface tension and interaction potential between adjacent membranes. Due to lack of time within this thesis project, the complete analysis of the synchrotron experiments could not be performed. Despite this fact, a preliminary analysis of a specular SR reflectivity experiment will be presented and the collected data during off-specular scattering experiment will be discussed.

CHAPTER 2

Interaction between charged lipid membranes

2.1 Introduction

Membranes are complex and heterogeneous assemblies, whose structural and physical properties such as membrane rigidity, structural stability and membrane undulations substantially depend on the interplay of various interactions which the system undergoes. Natural lipid bilayers are negatively charged due to the presence of a significant amount of negatively charged lipid species (such as cardiolipin, PS, PG lipids) in their composition. Due to the presence of a liquid environment surrounding lipid bilayers, counterions (and coions) are ubiquitously present in the solution making the overall system electroneutral. Electrostatic interactions play one of the dominant roles in determining the membrane behavior and they govern the cell-cell adhesion, cell fusion, protein binding kinetics, affinity and numerous other processes occurring in the cell [34].

Supported lipid bilayers offer a unique highly controlled configuration ideally suitable to study and finely characterize the extremely complex interplay between membranes and their environment. Lipid bilayers are often chosen as idealized and simplified models to study two-dimensional soft systems. Bilayer-bilayer interactions, interaction of proteins, peptides or nanoparticles with the membrane and fundamental physical properties of the system [35] can be investigated using these simplified model systems. In turn, the system behavior is moderated by coions and counterions present in the solution, which form an ionic double layer in the proximity of the membrane surface. Ion distribution is defined by the interplay between Coulombic forces and ion entropy and it modulates the overall properties and behavior of the system.

Electrostatic interaction is the major player in defining and understanding interaction between charged membranes in electrolyte solutions [34]. Therefore, understanding the behavior of charged systems starts with the understanding of counterion distribution around charged surfaces [36]. The first developed approach to treat the counterion-mediated interaction between charged systems is the Poisson-Boltzmann (PB) theory within the mean-field approximation, which predicts the counterion distribution around charged surfaces. The PB theory correctly predicts the interaction pressure in case of weakly coupled systems with low surface charge, low counterion valency and high temperature conditions in the weak coupling regime (WC). However, when multivalent ions are present in the solution and the surface charge is high, the PB theory reaches its limit and fails to describe the interaction between charged bodies correctly. At this limit the ion-ion correlation and ion pair formation start to be essential and should be taken into account, which goes beyond the mean field approach of the PB theory.

It is known that highly charged planar surfaces can attract each other in the presence of multivalent counterions (colloidal particles coagulation or flocculation [37], polyelectrolite aggregation [38], DNA packing [39]), but from the theoretical point of view this observation is counterintuitive and challenging to describe. The main approach used to explain the observed like-charge attraction going beyond PB theory is the Strong-Coupling (SC) theory. The SC approach takes into account ion-ion correlations and ion binding, which are essential in the SC limit of multivalent counterions, highly charged surfaces and low temperature. SC theory was pioneered by Rouzina and Bloomfield [40] and developed further by Netz and Moreira [36, 41–44] and Samaj and Trizac [45–48]. WC and SC approaches allow to treat the ion-mediated interaction between charged systems at the two opposite limits of weakly and strongly charged surfaces, depending on ion valency and distance between surfaces.

It was shown that in a strongly confined geometry the molecular structure of bulk water and water close to interfaces is substantially different, as the presence of the surface induces water molecules arrangement into a layered structure, which causes a decrease of the dielectric constant of the interlayer water [49]. Due to the differences in the correlation which bulk water molecules and interfacial water molecules composing the hydration shell of ions experience, they possess different

electrostatic properties, which influence the interaction between two charged surfaces and can lead to the conversion of repulsion into attraction at sufficiently low separations. Therefore the effect of a strong confinement on the system's behavior should be considered as well.

2.2 Main aim of project II

Within this thesis project we aim to study the interaction between two negatively charged lipid bilayers composed of DPPS phospholipids in the presence of monovalent ions only, without added salt (coions). We aim to perform XRR and NR experiments in order to study the structural arrangement of DPPS double and triple bilayer systems with Å resolution. The interaction between highly charged bilayers in the strongly confined geometry (interlayer water thickness < 2 nm) is investigated considering the equilibrium distance between like-charged bilayers (water layer thickness). The modulation of the water layer thickness between silicon support and bilayer and between two bilayers induced by variation of the concentration of added salt and temperature is studied as well.

We aim to obtain a realistic theoretical explanation for our experimental observations of a like-charge attraction phenomenon between highly negatively charged planar lipid bilayers, by implementing the existing WC and SC theoretical approaches. We can note that the PB theory in the mean-field approximation predicts only repulsion between charged object, neglecting the ion correlation effect. The surface of DPPS lipid bilayers possesses a moderate surface charge density ($\sigma \approx 0.77\ e^{-}/\mathrm{nm}^2$, coupling constant (defined below) $\Xi \approx 3$) meaning that the system description does not fall into the attractive region of the SC theory. We aim to show an agreement with the existing SC theory, which naturally predicts a like-charge attraction, taking into account a decrease of the water dielectric constant (which in turn leads to an increase of the coupling constant) induced by the rearrangement of water molecules near the charged surface in the strong confinement. Considering these observations, a description of the interactions between DPPS double lipid bilayers systems within the attractive region of the SC limit will be provided [50].

Part II

Materials and Methods

CHAPTER 1

Samples and sample preparation

1.1 Lipids

A huge variety of membrane proteins (inserted, peripheral or lipid-linked), their activity and interaction with the surrounding environment and external molecules, a tremendous diversity of lipid species and carbohydrates, all together make a cell membrane incredibly complex.

Lipids are the main components of biological membranes. 50% of the membrane weight is occupied by phospholipids, which are the main type of lipids present in the cell membrane. Phospholipid molecules are composed of hydrophobic (lipid tails) and hydrophilic (lipid head) parts, thus lipid molecules possess an amphiphilic nature (Fig. II.1.1). Hydrophobic lipid tails consist of two fatty acid chains linked to carbons 1 and 2 of a glycerol molecule through an ester oxygen. A phosphate group is linked to carbon 3 of the glycerol via ester bond and this assembly forms the backbone of a phospholipid molecule. A polar headgroup of chemically different types is grafted onto the phosphate and varies between lipid species.

Thanks to their amphiphilic nature, lipids in a liquid environment can self-assemble into a large variety of molecular nano-structures (bilayers, micelles, bicelles, nanodiscs, bicontinuous cubic phases, etc.).

Abbreviations composed of four capital letters are often used to indicate phospholipids: the first two letters refer to the lipid chains and the last two letters to the lipid headgroup. The most common headgroups for phospholipids are: phosphatidylcholine (PC), phosphatidylserine (PS), phosphatidylethanolamine (PE), phosphatidylglycerol (PG), and phosphatidylinositol (PI). The most abundant head groups that can be found in biomembranes are the zwitterionic PC and PE. PS, PI, PG head-

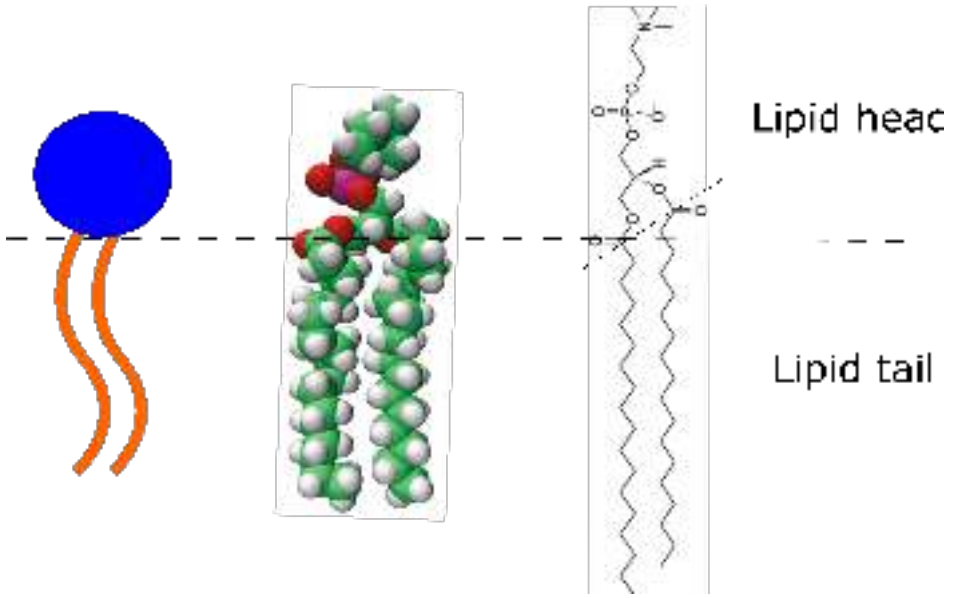

Figure II.1.1 – Schematic representation of the phospholipid structure. Hydrophilic head and two hydrophobic tails regions are shown.

groups are negatively charged and they essentially contribute to the overall negative charge of the biomembrane. Phospholipid chain length and number of unsaturations are indicated in the following nomenclature: "n:m headgroup" , where "n" corresponds to the number of carbons in the chain and "m" to the number of unsaturated bonds; "headgroup" denotes the two-letter abbreviation of the headgroup type of the lipid. A list of the phospholipids used within this work together with their properties are listed in Tab. 1.1.

In Fig. II.1.2 the chemical structure of the used phospholipid molecules with two hydrocarbon chains and phosphatidylcholine (PC) or phosphatidylserine (PS) head groups are shown. The hydrophobic and hydrophilic regions are highlighted by the dotted line.

As mentioned above, an important aspect of the physical properties of natural membranes is their fluidity. The way membrane fluidity (and lipid mobility) changes with temperature is defined by the lipid phase behaviour. The temperature at which lipids undergo a transition from gel to fluid phase is called the main transition temperature. The value of this temperature depends on the lipid structure, the alkane chain length and the number of unsaturations presented in the lipid tails. The transition temperatures for the used phospholipids are given in Tab. 1.1. The values of the transition temperatures were taken from the Avanti webpage [52].

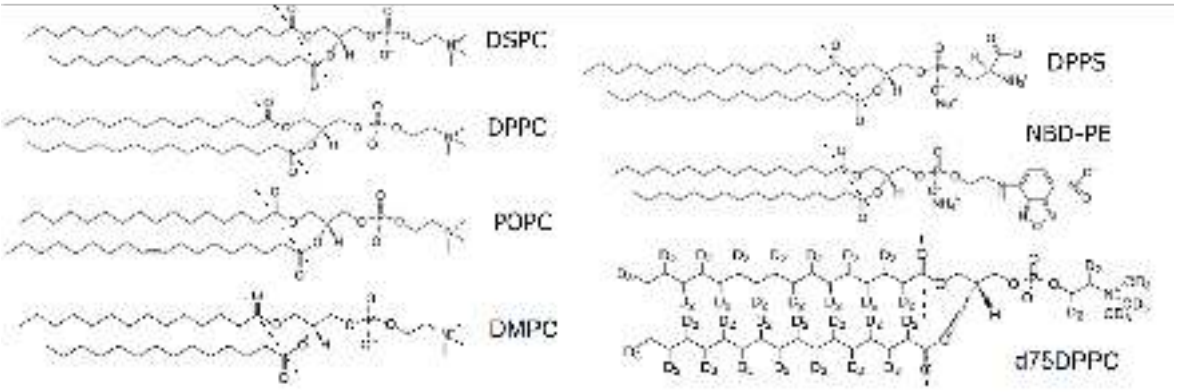

Figure II.1.2 – Chemical structure of phospholipids used in this thesis. The hydrophobic and hydrophilic regions are defined by the dotted lines [51].

Table 1.1 – Characteristics of the phospholipid molecules used within this thesis [52].

Name	Abbreviations		Type	T_m
1,2-distearoyl-sn-glycero-3-phosphocholine	DSPC	18:0 PC	zwitterionic	55 °C
1,2-dipalmitoyl-sn-glycero-3-phosphocholine	DPPC	16:0 PC	zwitterionic	41 °C
1,2-dipalmitoyl-d62-sn-glycero-3-phosphocholine-1,1,2,2-d4-N,N,N-trimethyl-d9	d_{75}DPPC	16:0PC-d75	zwitterionic	41 °C
1,2-dimyristoyl-sn-glycero-3-phosphocholine	DMPC	14:0 PC	zwitterionic	24 °C
1-palmitoyl-2-oleoyl-glycero-3-phosphocholine	POPC	16:0-18:1PC	zwitterionic	-2 °C
1,2-dipalmitoyl-sn-glycero-3-phospho-L-serine (sodium salt)	DPPS	16:0 PS	negatively charged	54°C

We should note that the phase transitions in solid supported lipid bilayers (SLBs), vesicles in solution and multibilayers occur at different temperatures. Gerelli [53] has shown that the temperature range at which lipids undergo transition is broader for SLBs than for freestanding bilayers in solution. It was shown as well that deuteration has an effect on the lipids phase behaviour. Bryant *et al.* [54] have shown that the gel-fluid phase transition temperature is 4.3±0.1°C lower for phospholipids (DSPC, DPPC and DMPC) with deuterated chains.

1.2 Solid supported lipid bilayers (SLBs)

Model lipid bilayer systems serve as a good platform to study the physical properties and structure of cell membranes, functional activity of membrane components and a range of processes, such as membrane-protein interactions, cell fusion and fission. The most common models for natural cell membranes are lipid vesicles of different size and lamellarity and supported lipid bilayers (SLBs) either on solid support, tethered to a surface or cushioned. Each of the membrane model systems has its advantages and disadvantages, which should to be thoroughly considered before their use. The appropriate choice of model system is case-dependent and it is based on the target experiment, available techniques for the investigation and the final aim of the study [55].

SLBs are among the most widely used model systems. A SLB is a self-assembled lipid bilayer composed of one type or a mixture of lipid species (natural or synthetic) at a solid/liquid interface. A small hydration layer (3-20 Å) separates the SLB from the substrate.

SLBs can be deposited on solid substrates of different kinds. Chemical composition, roughness, hydrophilicity and surface charge are important properties which have to be taken into account when choosing the appropriate support for the experiment. The most widely used substrates are atomically flat and chemically inert mica, gold, titanium, glass, quartz and silicon oxide surfaces.

Experimental studies have shown that the proximity of the substrate has an impact on the lipid bilayer properties: restricted lateral mobility of lipids or integrated proteins [56], membrane fluidity and fluctuations [13], decoupled phase transitions [53] and an asymmetric lipid distribution in the upper and lower leaflet of the lipid bilayer [57]. Substrate close proximity can hamper the process of protein incorporation or can provoke protein denaturation and aggregation [58].

On the other hand, SLBs are stable, with a well-defined structure and chemical composition, fixed near the substrate bilayers. The closeness to the solid support provides a planar membrane orientation suitable for investigation with a wide range of surface sensitive techniques. SLBs can be formed in a liquid environment of variable pH and ionic strength, which is crucially important and very advantageous for the investigation of membrane protein, nanoparticle, peptide or other macro-

molecules' interaction with SLBs as they require a specific liquid medium to keep their structural integrity and functional activity [59].

1.2.1 Model systems

Lipid bilayers composed of one type of synthetic phospholipids can be considered as the simplest model of biomembrane and can serve as a good biologically relevant model for a range of tasks. For our research projects focused on protein reconstitution studies and out-of-equilibrium fluctuations of membrane-protein systems (Project I) and investigation of the interaction between two highly charged lipid bilayers (Project II), we have chosen planar membrane model systems such as solid-supported single and double lipid bilayers composed of zwitterionic and negatively charged synthetic phospholipids. A sketch of the membrane-mimic model systems used within this work is shown in Fig. II.1.3.

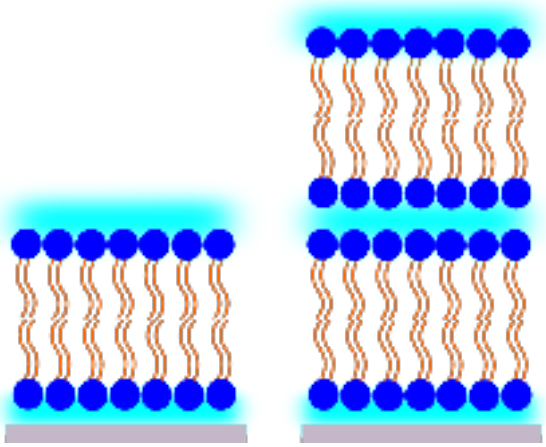

Figure II.1.3 – Sketch of the model systems used within this thesis: single and double lipid bilayers.

1.3 Sample preparation

Lipid bilayers can be formed on solid supports using different techniques including the Langmuir-Blodgett (LB) and Langmuir-Schaefer (LS) deposition techniques, spin coating, vesicle fusion, the fast solvent-exchange method, deposition using lipid - surfactant micelles and performing tethering of a lipid bilayer by a

polymer brush [28]. Many experimental protocols reporting detailed procedures for lipid bilayer preparation of different lipid composition and on different types of substrate are available [28, 55, 60–69], however, producing SLBs of a certain lipid composition remains challenging.

Langmuir-Blodgett/Langmuir-Schaefer (LB/LS) deposition and vesicle fusion are the most commonly used techniques for SLBs preparation. A detailed description of these methods will be presented below.

1.3.1 Vesicle fusion

Vesicle fusion is a simple and widely used technique to form symmetric single lipid bilayers on solid supports. Protocols for good SLB deposition should be optimized case by case, taking into account parameters such as lipid phase and electrostatic balance. Other parameters defining vesicle - substrate interactions also have a significant effect on the successful SLB formation: chemical composition, roughness, hydrophylicity of the surface, composition and size of lipid vesicles, pH, temperature and ionic strength of the solution [28]. To promote the formation of SLBs, it is important to i) facilitate vesicle-substrate adhesion and ii) stimulate vesicle rupture via applied stress, if spontaneous rupture does not occur. We have to note that there is no universal recipe for SLB formation by vesicle fusion. A successful protocol suitable for a specific type of lipid-substrate combination and environmental condition has to be developed experimentally [28].

Several scenarios to explain spontaneous transformation of lipid vesicles into planar lipid bilayers, which occurs upon interaction of lipid vesicles with a solid support were reported [58]. In Fig. II.1.4 three different pathways for SLB formation are shown: a) upon adsorption on the solid support vesicles do not fuse or break immediately, but when a critical vesicle concentration is reached, the vesicles fuse and transform into a SLB; b) as soon as vesicles reach the substrate they rupture, forming an SLB; c) vesicles do not fuse or rupture, forming an adhesive vesicle layer. The outcome of these pathways can be manipulated by tuning the environmental conditions in order to promote complete SLB formation. It was shown that the specific kinetics of vesicle fusion or rupture and SLB formation do not have an influence on the final quality of the bilayer [55].

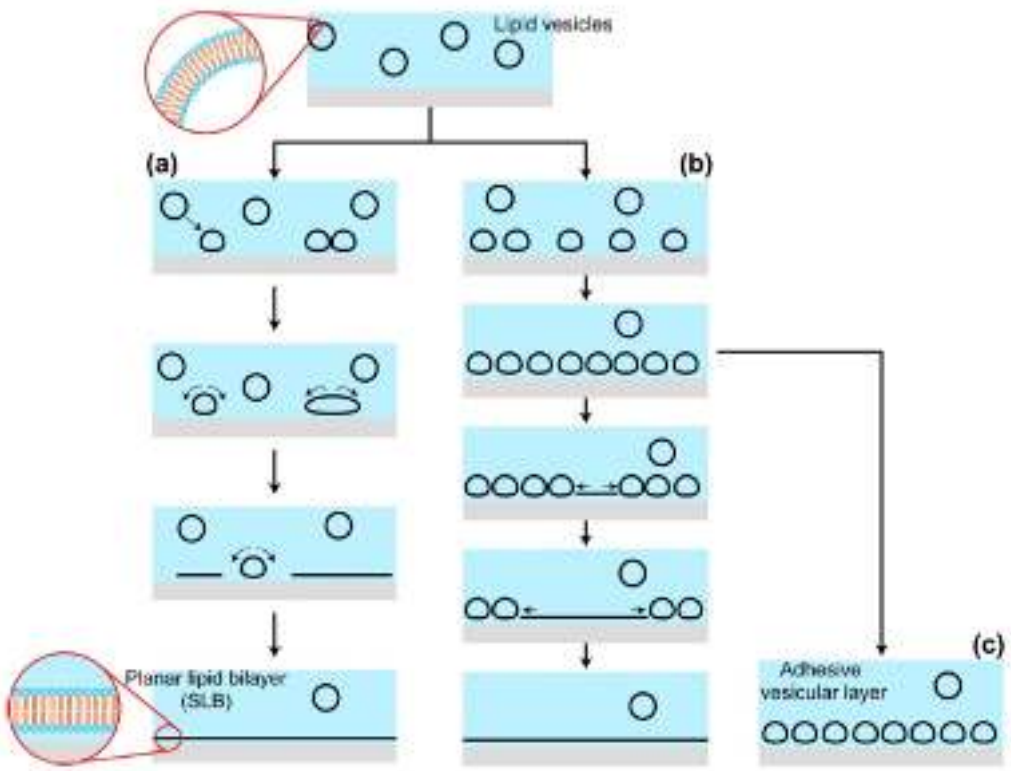

Figure II.1.4 – Possible outcomes of lipid vesicle fusion process at the solid/liquid interface [58].

1.3.2 Lipid vesicle preparation and fusion protocols

During this thesis single SLBs composed of POPC and DPPC:POPC (1:1 mol:mol) lipids were studied extensively. Lipid vesicle fusion protocols to form SLB on SiOx and mica substrates were optimized by QCM-D and AFM experiments. In all the cases, SLBs were formed starting from a small unilamellar vesicle (SUV) solutions.

SUV preparation

In order to obtain solutions of SUVs composed of POPC lipids or mixtures of DPPC:POPC (1:1 mol:mol) lipids, the appropriate amount of lipid powder were solubilized in chloroform. The volatile solvent was evaporated using a nitrogen flow while the vial containing the solutions was continuously rotated to form a uniform dry lipid film on its walls. The film was re-hydrated with water (D_2O, H_2O or D_2O, H_2O PBS buffer, depending on the experiment) to reach a concentration of 0.5 mg/ml for QCM-D experiments and 1 mg/ml for AFM and NR experiments. To obtain monodisperse SUVs the lipid suspension was extruded through a polycarbonate

filter with 50 nm pore size.

An alternative method consisting in tip sonication (for 15-20 minutes with repeated pulses (5 s on, 5 s off) at 50% amplitude power) was used as well. This method does not ensure SUV monodispersity and absence of MUVs. However, due to the simplicity, ease in use and availability, tip sonication was routinely used to produce SUVs suitable for the vesicle fusion procedure.

1.3.3 Vesicle fusion for NR experiments

Single SLBs composed of POPC lipids were used as a model system to study protein reconstitution with NR experiments performed on the MARIA reflectometer. POPC SLBs were formed on the 5x8 cm^2 surface of silicon crystal cut and highly polished along the (111) plane (roughness $\approx$ 5 Å). The thoroughly cleaned silicon block (see section A in the Appendix for the implemented cleaning procedure) was tightly sealed inside the solid/liquid cell (section 2.7). To produce single lipid bilayers, 3 ml of 1 mg/ml of POPC SUV solution in MilliQ water was injected into the solid/liquid cell prefilled with MilliQ. The system was incubated for 20 minutes in order to induce vesicle adhesion on the silicon surface. The cell was then rinsed with 3 ml of 500 mM NaCl solution to subject the vesicles to osmotic shock. Due to the difference in ion concentration in the internal and external medium of vesicles, there are subjected to an osmotic pressure, which promotes and facilitates vesicles rupture and fusion in presence of a surface. Afterwards the cell was rinsed with D_2O or H_2O PBS buffer to remove all unbound lipids vesicle from the cell. A single POPC lipid bilayer deposited on the silicon block was obtained. The developed protocol provides robust and reproducible results giving high quality samples (full coverage) as confirmed by NR measurements (see section 3.2.3).

1.3.4 Vesicle fusion for AFM experiments

Single SLBs composed of POPC and mixtures of DPPC:POPC (1:1 mol:mol) lipids were used as a model system to study BR reconstitution by AFM experiments (IBS, Grenoble, France). POPC and DPPC:POPC single lipid bilayers were formed on mica sheets of 7 mm diameter by vesicle fusion.

To prepare SLB composed of POPC lipids, 100 μl of SUV solution was drop-cast on the wetted mica surface and the sample was left to incubate for 15 minutes at room temperature, after which the sample was carefully rinsed with 200 μl of 500 mM NaCl solution to promote vesicles rupture and SLB formation. The sample was further rinsed with PBS buffer and as a final system a single POPC bilayer on mica was formed.

In order to form single lipid bilayers composed of POPC and DPPC lipids that form separated gel and fluid domains at room temperature [70], the SUV solution and the wetted mica surface were both heated up to 60°C. This step was done in order to perform vesicle fusion at a temperature higher than the main transition temperature of the used lipids (Tab. 1.1). This condition facilitates the vesicle fusion process by promoting fast vesicle rupture. Subsequently, 100 μl of the heated DPPC:POPC (1:1 mol:mol) SUV solution was drop-cast on the wetted and heated sample support. The sample and a wetted wipe were kept together covered and sealed in the petri dish to prevent sample evaporation and were placed into an oven at 60°C for at least 30 minutes. After removing the sample from the oven, it was carefully rinsed with 200 μl of heated up to 60°C 500 mM NaCl solution and left to incubate for 15 minutes at 60°C. At the end of the incubation period, the sample was rinsed thoroughly with heated PBS buffer and left to cool down slowly and stabilize at room temperature. This procedure led to the formation of DPPC:POPC SLBs on a mica surface.

1.3.5 Vesicle fusion for QCM-D experiments

Planar POPC bilayers were used as a model system to investigate BR reconstitution with QCM-D experiments. POPC SLBs were formed on a silicon crystal chip (section 2.1) using the following protocol: 1 ml of 0.5 mg/ml POPC vesicle solution in PBS buffer was injected at a flow rate of 150 μl/min into the solid/liquid chambers of the QCM-D setup. These cells were filled with PBS buffer and stabilized at 25°C beforehand. The flow was stopped and the samples were incubated for 15 minutes to allow the vesicles to fuse on the silicon chips and to form SLBs. The sample cells were rinsed with MilliQ water (or 500 mM NaCl solution) to subject vesicles to an osmotic shock and to promote their fusion. In order to remove residuals of lipid vesicles, the cells were rinsed again with PBS buffer by restarting the flow at 150

μl/min until stable frequency and dissipation signals were obtained. Stabilization of frequency and dissipation denotes the completion of the POPC lipid bilayer formation. A dissipation signal of around 0.2 x 10^{-6} and a frequency shift of around -24 Hz indicate a high quality (full coverage) lipid bilayer formation.

Several QCM-D experiments were performed in order to study BR reconstitution into DMPC and DPPC:POPC (1:1 by mol) lipid bilayer systems. The protocol for the DMPC lipid bilayer formation by vesicle fusion is identical to the reported above for the POPC SLB formation. DPPC:POPC lipid bilayer formation and BR reconstitution was performed at 45°C, therefore the QCM-D solid/liquid chambers, SUVs solution, PBS buffer and 500 mM NaCl solution were heated up to 45°C beforehand. Otherwise, the protocol for POPC:DPPC SLB formation is identical to the one reported above.

1.3.6 Langmuir-Blodgett (LB) and Langmuir-Schaefer (LS) deposition techniques

Lipid bilayers with a well-defined composition and structure can be formed on solid supports by LB/LS techniques. A key feature of these techniques, which makes them extremely advantageous over vesicle fusion, is the possibility to perform the deposition of multibilayer systems. More than one lipid bilayer (double and multi bilayers, depending on the nature of the used lipids) can be formed on solid supports of different types. In fact, the deposition of each layer by LB/LS techniques is performed independently and therefore the composition of each monolayer of the bilayer system can be varied and can be chosen separately. This is in contrast to the vesicle fusion technique, which only allows to form a single bilayer without control of the lipid bilayer's compositional arrangement. The LB technique allows to precisely control the quality of the deposited layer and, in addition, to measure the physical properties of a monolayer at the liquid-air interface before its transfer to a solid substrate. Therefore, the LB/LS deposition techniques provide symmetric or asymmetric lipid bilayers on solid supports with a well-controlled structure and composition.

In order to prepare lipid bilayer samples deposited on solid supports a Langmuir trough of the appropriate size has to be available. The used instrument will

be described in the next section. As solid supports for LB/LS deposition, highly polished (roughness ≈ 5 Å) and thoroughly cleaned silicon and quartz substrates were used. The minimum size of the blocks, which were used to form lipid bilayers, was 2.5x2.5x1 cm^3.

1.3.7 Langmuir-Blodgett troughs

To form single, double and triple lipid bilayers samples composed of DSPC, DPPC and DPPS lipids in order to study BR insertion and membrane-protein system fluctuations (project I) and interaction between highly charged lipid bilayers (project II), the LB/LS deposition techniques were used.

NIMA 611 and NIMA 1212D Langmuir troughs available at the ILL, Grenoble, France and NIMA 312LL and KSV-NIMA Langmuir troughs available at the ICS, Strasbourg, France were used to prepare the samples.

A Langmuir trough consists of a Langmuir-Blodgett trough top (reservoir), a set of barriers, a surface pressure sensor (Wilhelmy plate), a dipping mechanism for the vertical (LB) deposition and a manual setup for the horizontal (LS) deposition.

The used troughs were equipped with a deep well, which allows to completely immerse the solid substrate into the liquid subphase and to dip it in and out through the monolayer at the liquid-air interface in a highly controlled manner. The dipping mechanism holds the solid substrate and the deposition cycle(s) are controlled via a computer. Computer-controlled barrier(s) can move at a user-defined speed to compress the lipid molecules at the water/air interface in order to perform isotherm measurements and to form lipid monolayers in different lipid phases.

Trough and barrier setup were made from PTFE, which is a very hydrophobic material. This prevents the lipid molecules' adhesion to the surface of the trough and barriers. Another advantage that makes PTFE a very suitable material is the possibility to clean the trough top and barriers with volatile solvents such as choloroform or ethanol in order to remove easily the contamination from the surface.

Thanks to a water circuit in the trough bottom the temperature of the subphase can be controlled by a thermal bath which allows fast cooling or heating of the subphase.

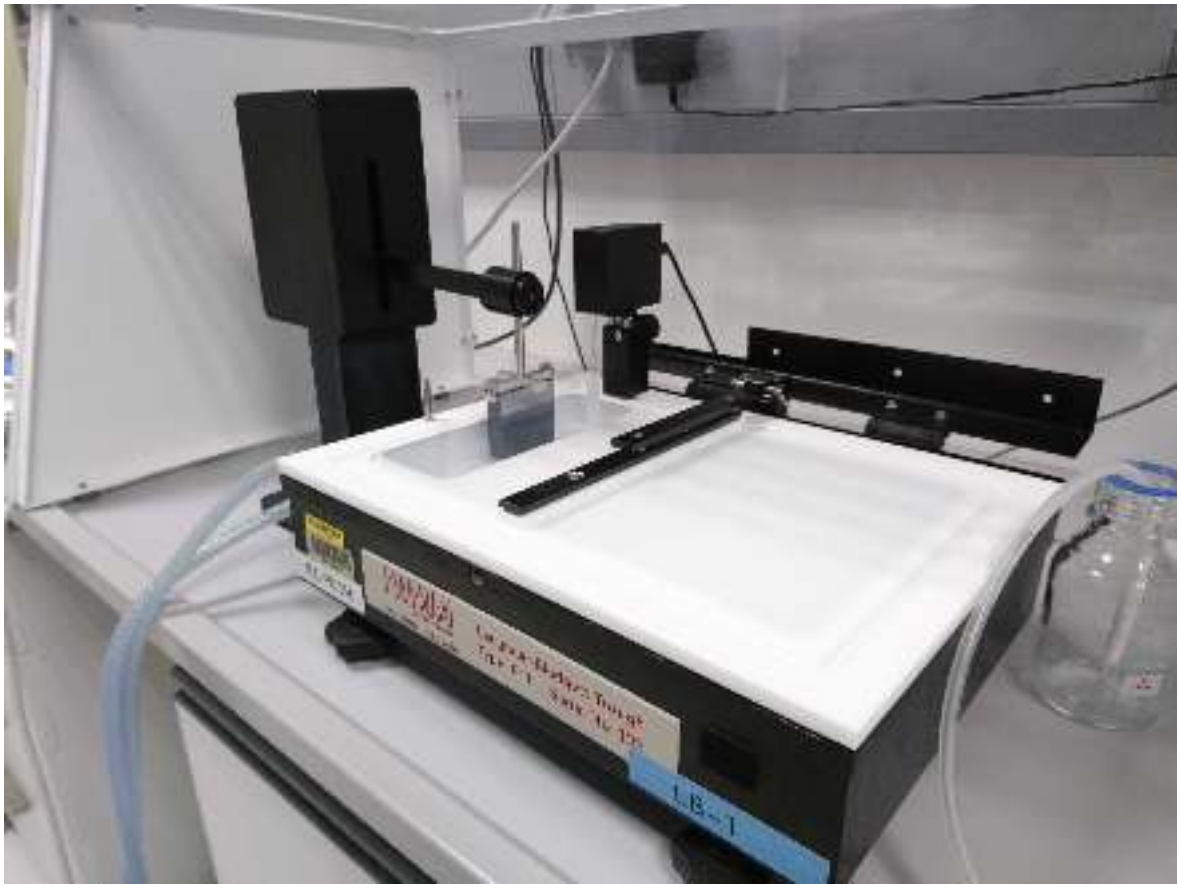

Figure II.1.5 – Langmuir Trough NIMA 611.

1.3.8 Pressure measurements

To measure the surface pressure of the Langmuir lipid monolayers, the Wilhelmy plate method is implemented. It is a very simple and elegant method to measure and follow changes in the surface pressure of an air/liquid interface. In our case the Wilhelmy plate sensor consisted of a thin paper plate with a well defined mass and dimensions (density 80 g/m^2, perimeter 20.6 mm) [71]. The plate is attached to a piezoelectric sensor on one side while the other side is immersed into the liquid subphase. Changes in the force acting vertically on the plate sensor are converted into changes in the surface pressure. The measured surface pressure is defined as the decrease in surface tension when the amphiphilic molecules are added to the surface:

$$\Pi = \gamma_0 - \gamma \tag{1.1}$$

where γ is the surface tension of subphase with monolayer, γ_0 is the surface tension of pure subphase. Amphiphilic molecules lower the surface tension of water, thus

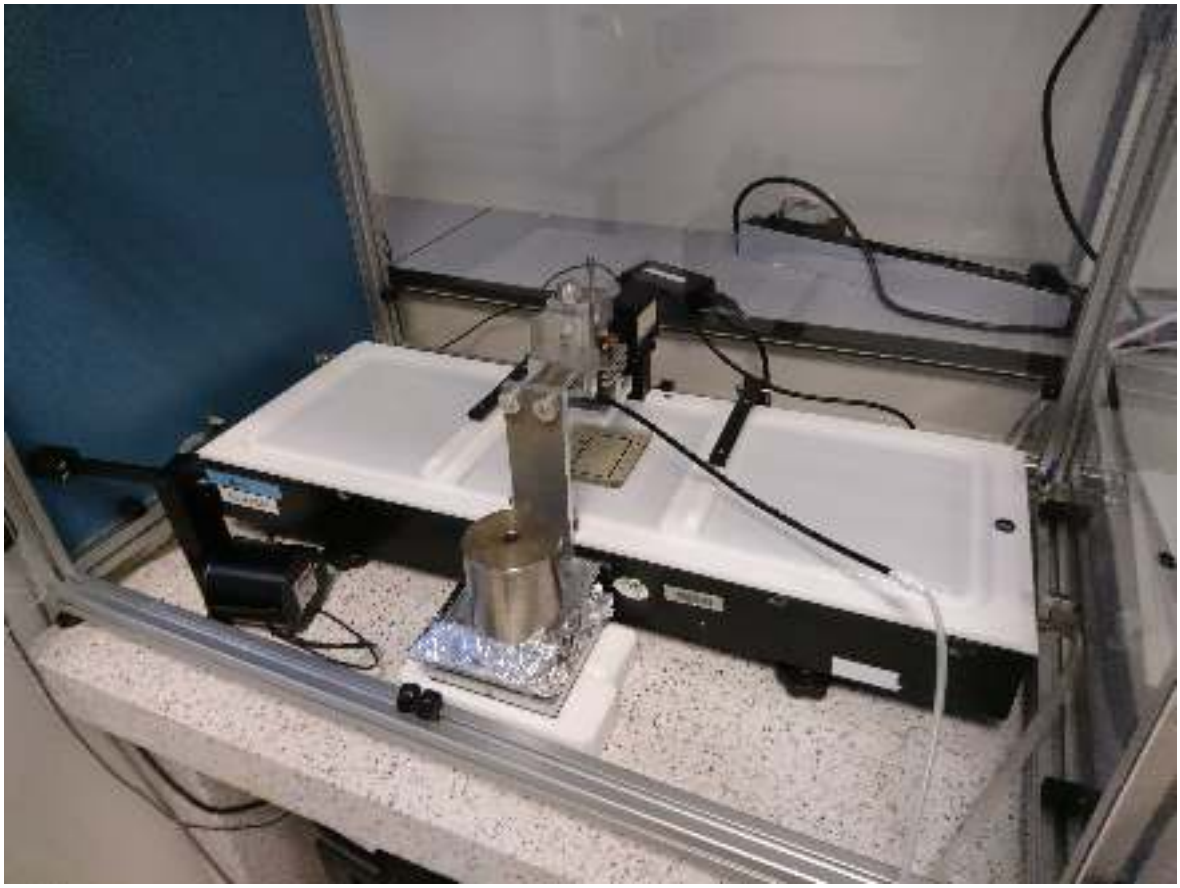

Figure II.1.6 – Langmuir Trough NIMA 1212D.

the value of the measured pressure is always positive.

1.3.9 Isotherm measurements

The Wilhelmy plate method allows to monitor changes of surface pressure induced by the lipid monolayer compression or decompression using movable barrier(s) or adding other surface active molecules to the already formed monolayer at the interface. The area per molecule in the monolayer can be controlled by reducing or increasing the available surface area at the interface by moving the barrier(s). The collected pressure-area curve (Langmuir isotherm) provides information on the organization of the lipid molecules at the interface at a defined temperature [72, 73].

As an example, the pressure-area isotherm for a DPPC monolayer deposited on a ultrapure water subphase (MilliQ, resistance > 18 MΩ) at room temperature (T = 21 ± 1°C) and compressed at 10 cm^2/min is shown in Fig. II.1.7. The isotherm demonstrates the modifications of the area of the lipid monolayer at the air-water interface versus the induced pressure in the monolayer. The main phases of the lipid

monolayer are indicated in the figure.

Compression of the DPPC molecules on the interface generates a phase transitions of the monolayer through different phases. The lipid monolayer is in a gaseous phase in the region where the area per lipid molecule is high (more than 60 Å^2/molecule) (region LG) and the interfacial pressure is low. Then DPPC monolayer undersdoes a transition into the liquid-expanded phase (region LE), which is followed by the coexistence region of liquid-expanded and liquid-condensed phases (region LE-LC), which ends below 10 mN/m. Upon the further reduction of the pressure, the monolayer undergoes a transition into the liquid-condensed (region LC), followed by solid phase (region S) at a surface pressure of around 35 mN/m [74]. The collapse pressure at which the lipid monolayer starts to be unstable and lose of materials into the subphase or the formation of multilayer structures start to occur is around 5 mN/m for DPPC lipids [75].

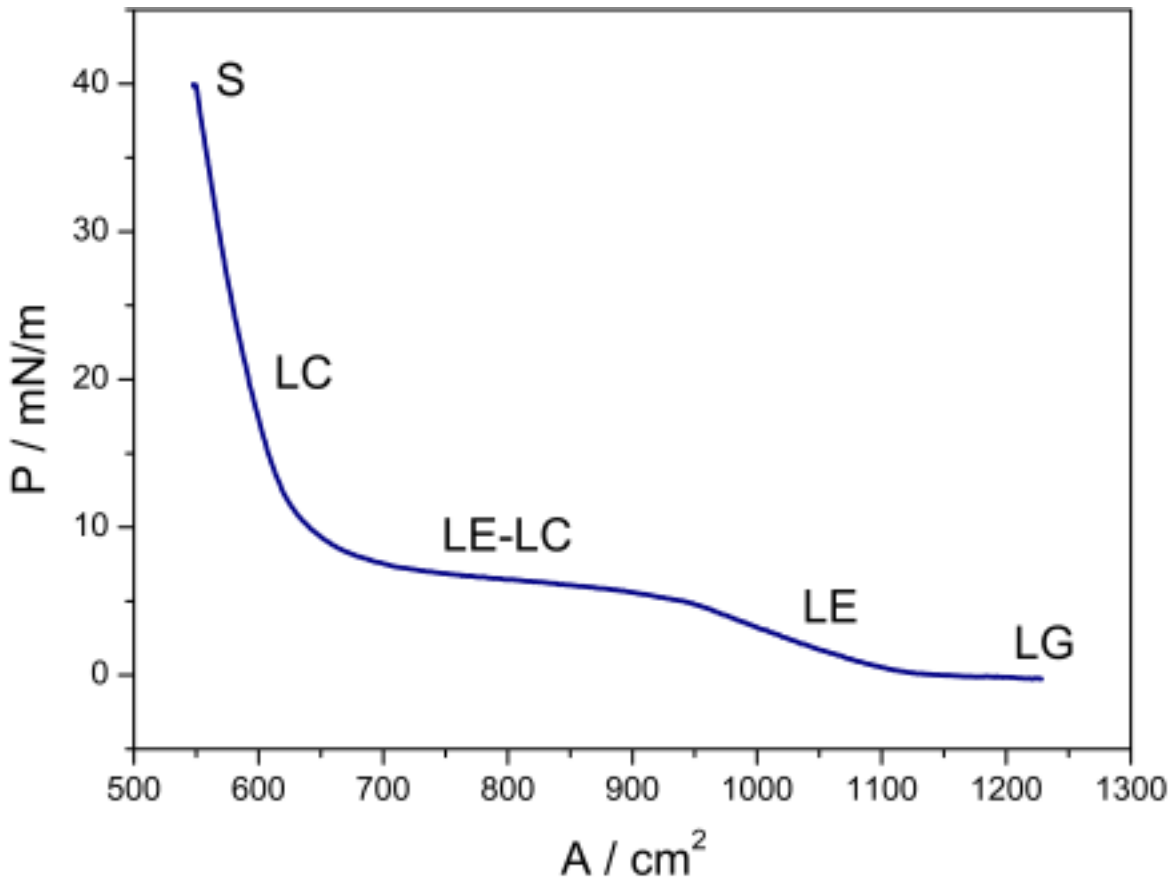

Figure II.1.7 – DPPC monolayer isotherm at room temperature. Lipid phases are indicated in the figure.

This behaviour of the lipid monolayer was routinely used in the sample prepa-

ration by LB/LS techniques: lipid bilayer deposition was always performed at a pressure of 40 nN/m with the lipid monolayer in the solid phase.

1.3.10 Sample preparation by LB/LS techniques

LB/LS deposition techniques were routinely used for the solid-supported single and double lipid bilayer preparation. Substrates of different type and size (see Tab. 1.2) were used for sample preparation depending on the target experiment.

The Langmuir-Blodgett trough was thoroughly cleaned and filled with ultra pure MilliQ water. The cleaned solid substrate with a hydrophilic surface (see section A in the Appendix) was immersed into the water sub-phase with the large face oriented vertically. Phospholipids were dissolved in chloroform or a chloroform/methanol/water mixture (65:25:4 $CHCl_3$:MeOH:H_2O) at a concentration of 1 mg/ml. The lipid solution was spread on the liquid/air interface of the trough using a glass Hamilton syringe. After total evaporation of the solvent ($\approx$ 30 minutes) the lipid molecules formed an insoluble monolayer at the air/liquid interface with the lipid head groups immersed into the sub-phase and the hydrophobic tails facing towards air. The monolayer formed at the air/water interface was further compressed by moving the computer controlled barrier(s) until the target pressure value was reached. A compression speed of 15 cm^2/min was generally used and the target pressure was chosen to be fixed at 40 mN/m, at which the lipid monolayer is in the gel phase.

LB deposition was performed by subsequently moving up and down the substrate at a constant speed of 4 mm/min through the lipid monolayer at the interface, while simultaneously keeping the surface pressure constant at the target pressure value. By slowly raising the substrate from the water sub-phase the first monolayer was deposited on the solid support. The second monolayer was deposited on top of the first monolayer by lowering down the sample at constant speed (the tails of each monolayers are facing each other) and a lipid bilayer was formed. The third monolayer was deposited on top of the formed bilayer by raising the solid support again (Fig. II.1.8). For the case of fully negatively charged DPPS lipids, the deposition of the fourth and fifth (up to seventh) subsequent monolayers were performed by LB deposition technique as well.

The last monolayer of the bilayers systems was prepared by LS deposition. Usually the NIMA 1212D or KSV-NIMA troughs were used for the final step of sample preparation as these troughs were equipped with a deep and wide well at the trough center, which allows to place the solid/liquid cell inside in order to seal the sample chamber.

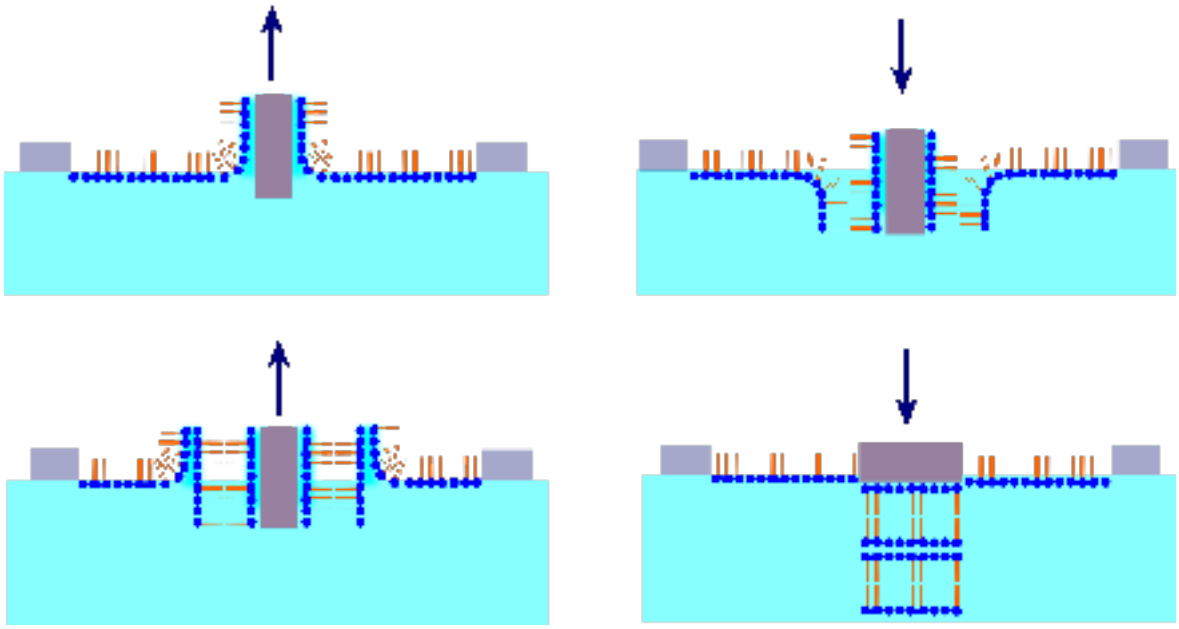

Figure II.1.8 – Schematic illustration of Langmuir-Blodgett, Langmuir - Schaefer (LB/LS) deposition techniques.

Therefore in order to complete the lipid bilayer formation by the LS deposition step, a part of the solid/liquid cell was placed inside Langmuir trough filled with MilliQ water. The lipid monolayer was formed and compressed at the interface following the same procedure as for the LB deposition step. The solid substrate with the deposited monolayer (or trilayer, or pentalayer) was turned by 90° and fixed to the manual dipping setup by a vacuum suction pump. The silicon surface had to be aligned perfectly parallel to the air/liquid interface and moved very slowly and gently towards the lipid monolayer at the air/liquid interface using the manual dipping mechanism. The bilayer is formed when the silicon block with the deposited monolayer/trilayer/pentalayer system moves into close contact with the lipid monolayer spread on the water surface. The substrate had to be pushed through the water interface and positioned on the part of the solid/liquid cell placed in water beforehand. The solid/liquid cell was sealed tightly by placing the second part of the cell over the solid substrate and screwing the two parts together. This way the

sample was tightly sandwiched between the cell parts to avoid water leakage.

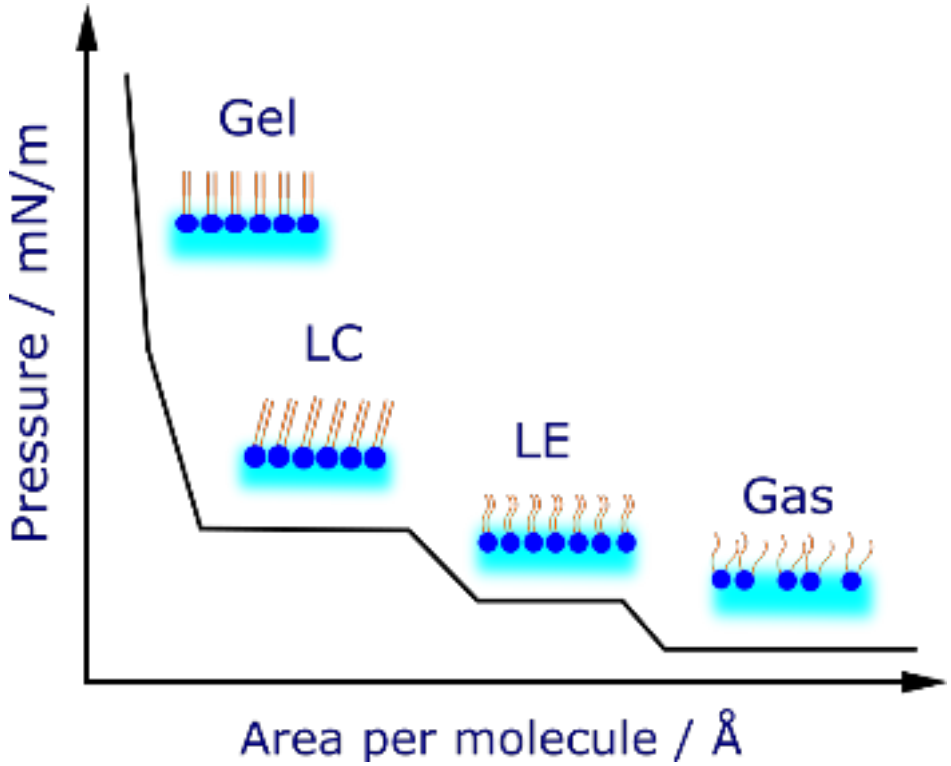

Figure II.1.9 – Schematic illustration of the gas to gel lipid transition.

As mentioned above, the great advantage of the LB technique is the possibility to instantly estimate the quality of the deposited monolayers. This estimation can be performed by calculating the transfer ratio (t.r.) defined as the ratio between the decrease in monolayer area during a LB deposition step and the total surface area of the substrate onto which the transfer is performed. A t.r. value around 1 indicates full coverage of a substrate and a high quality of the formed monolayer. By evaluating the t.r. it is possible to discard poorly prepared samples in the early stage of the experiment. A further discussion on the t.r. estimations can be found in section C of the Appendix.

Samples prepared by Langmuir-Blodgett and Langmuir - Schaefer depositions

In Tab. 1.2 the samples prepared using LB/LS deposition are listed. The sample composition, substrate type, amount of lipid solution used for the monolayer formation in the LB and LS transfers and the trough type are specified. All the listed sample were prepared using the procedure reported above.

We would like to note that:

1. Fluorescence microscopy experiments were performed at the ICS, Strasbourg, thus we have used the NIMA Technology 312LL and KSV-NIMA troughs for the sample preparation by LB/LS techniques.

2. For the case of asymmetric lipid bilayer depositions, the lipid monolayer was removed from the air/water interface, while keeping the solid support with the deposited monolayer or bilayer hanging in air or immersed in water. A new lipid solution was spread on the cleaned air/water interface and afterwards the LB/LS deposition routine was continued.

3. The SLB samples for AFM experiments performed at the ILM and at the ILL were prepared by LB and LS deposition and the formed samples were hosted in a special solid/liquid cell (section 2.2.4). In order to study the SLB by AFM, a solid/liquid cell had to be opened, while keeping the bilayer on the silicon substrate hydrated. To achieve this the cell was turned upside down. The cell was then slowly unscrewed while holding the two parts of the cell together and parallel to the ground to avoid water leakage. The cell was placed steadily on the table and the upper lid of the cell was removed. These manipulations had to be done very carefully to avoid leakage and keep the water on the silicon block to ensure the hydration of the deposited bilayer. After this last step the sample was ready to be examined with AFM.

Table 1.2 – Samples prepared by Langmuir-Blodgett and Langmuir - Schaefer depositions

Experiment	Sample	Substrate type	Substrate dimention	Lipid solution for LB deposition	Lipid solution for LS deposition
AFM	DSPC double bilayer DSPC single bilayer	Silicon block	2.5x2.5x1 cm^3	100 μl of DSPC 70 μl of DSPC	70μl of DSPC
Fluorescence microscopy	DSPC single bilayer DSPC double bilayer DSPC-DPPC double bilayer	Glass slide	700x0.15 mm^3	35 μl of DSPC 50 μl of DSPC 35 μl of DSPC, 35 μl of DPPC	70 μl of DSPC + 1% NBD-PE 70 μl of DSPC + 1% NBD-PE 70 μl of DPPC + 1% NBD-PE
in-house XRR	DSPC-DPPC double bilayer DSPC single bilayer DSPC double bilayer	Silicon block	2.5x2.5x1 cm^3	70 μl of DSPC, 60 μl of DSPC 70 μl of DSPC 70 μl of DSPC	60 μl of DPPC 60 μl of DSPC 60 μl of DSPC
NR	DSPC-DPPC double bilayer DPPS double bilayer DPPS triple bilayer DPPC/DPPS-DPPS/DPPC double bilayer d_{75}DPPC/DPPS-DPPS/d_{75}DPPC double bilayer	Silicon block	5x8x1.5 cm^3	100μl of DSPC, 70μl of DPPC 100μl of DPPS 120μl of DPPS 100μl of DPPS, 90μl of DPPC 100μl of DPPS, 90μl of d_{75}DPPC	100 μl of DPPC 100 μl of DPPS 100 μl of DPPS 110 μl of DPPC 110 μl of d_{75}DPPC
XRR SOLEIL	DSPC double bilayer	Silicon block	5x5x1.5 cm^3	130 μl of DSPC	100 μl of DSPC
XRR ESRF	DPPS double bilayer	Silicon block	5x5x1.5 cm^3	100 μl of DPPS	120 μl of DPPS

1.4 Bacteriorhodopsin (BR) and Archaerhodopsin-3 (Arch-3) transmembrane proteins

1.4.1 The choice of transmembrane protein

The transmembrane protein Bacteriorhodopsin (BR) was selected for the reconstruction and active fluctuations studies performed within this thesis project for several reasons: BR is one of the most widely studied membrane proteins with a crystal structure resolved at 1.3 Å resolution [76]; BR is a transmembrane protein with the size matching the height of DSPC and DPPC lipid bilayers used within this thesis project, thus, no hydrophobic mismatch can occur; the atomic composition, protein function and kinetic of protein pumping activity have been extensively studied and are well known [77–86].

The functional activity of BR as a light activated proton pump is perfectly suitable for the main aim of the project: to study the active membrane fluctuation. In such a way, BR can serve as a switchable active noise source giving the possibility to probe thermal and active fluctuations of the membrane-protein system.

BR is a very structurally and functionally stable protein, as it is capable to keep its structural integrity and activity over a wide range of experimental conditions (pH, temperature, ionic strength, presence of cations, etc.), which makes it one of the most stable proteins known [87]. It was shown that upon heating from 20 to 100°C, BR exhibits two thermal phase transitions: a pre-melting transition at ≈ 80°C (reversible upon cooling back to 60°C) and irreversible transition at ≈ 97°C that causes protein denaturation (melting) [87]. The thermal stability of BR is important for the protein reconstitution into fluid lipid bilayers, which sometimes requires the sample heating up to 60°C.

1.4.2 Bacteriorhodopsin

Bacteriorhodopsin (BR) is a very well understood ion transport protein that has become a paradigm for membrane proteins and transporters. It is a relatively small and highly hydrophobic protein, with a size of 27 kDa, and it is composed of 248 amino residues, 70 % of which are hydrophobic [88, 89]. BR is folded into seven

alpha helices labeled from A to G that fully span the membrane. A retinal molecule is covalently bound via a protonated Schiff base to the lysine residue Lys216 of the protein (Fig. II.1.10) [81, 90]. BR has a form of a cylinder with the radius 1.8 nm and height 5.5 nm (Protein Data Bank).

BR functions like a light-driven proton pump: upon absorption of a photon of green light ($\lambda_{max} \approx 568$ nm) by the retinal molecule, BR undergoes conformational changes and pumps protons out of the cell [84, 88, 91]. In nature BR can be

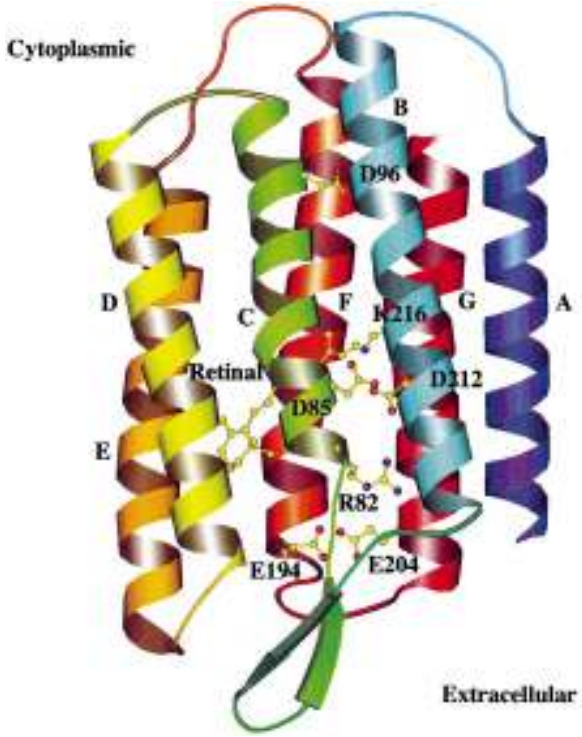

Figure II.1.10 – Structure of BR: seven TM helices, retinal and residues involved in proton relocation are shown [83].

found in the specific light-sensitive region of plasma membranes of the salt-loving bacterium Halobacterium salinarum, called purple membrane. In the purple membrane, BR molecules organise into two-dimensional protein-lipid crystalline patches in the form of trimers. In the Fig. II.1.11 and II.1.12 the AFM topographs of purple membrane adsorbed to mica and electron density maps are shown respectively, demonstrating the trimer and crystalline organization of BR molecules in nature. BR is the only protein which can be found in purple membrane where it is present in a very high density: 75% of the dry weight of purple membrane is made of BR molecules, while the remaining 25% is made of specific lipids. It was shown that in the membrane 30 lipid molecules are bound to a BR trimer: 24 lipids surround

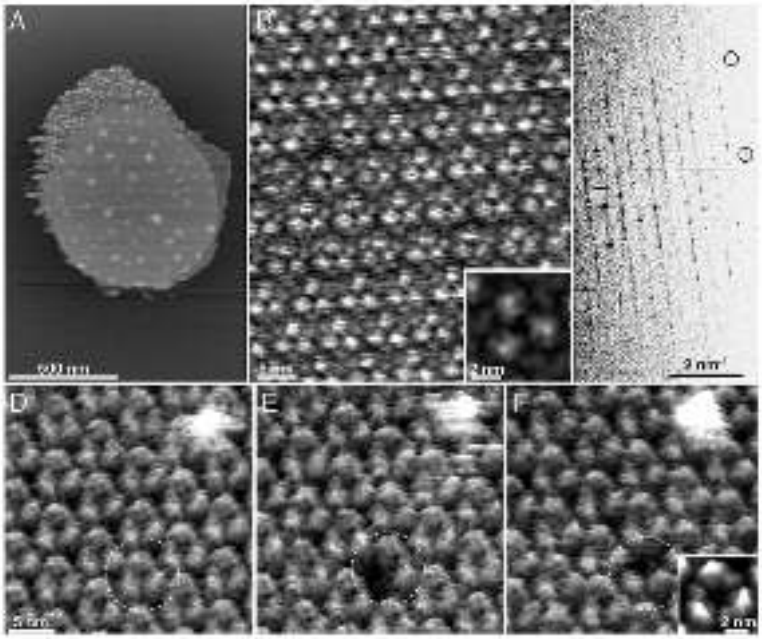

Figure II.1.11 – AFM topographs of purple membrane adsorbed on mica. [92].

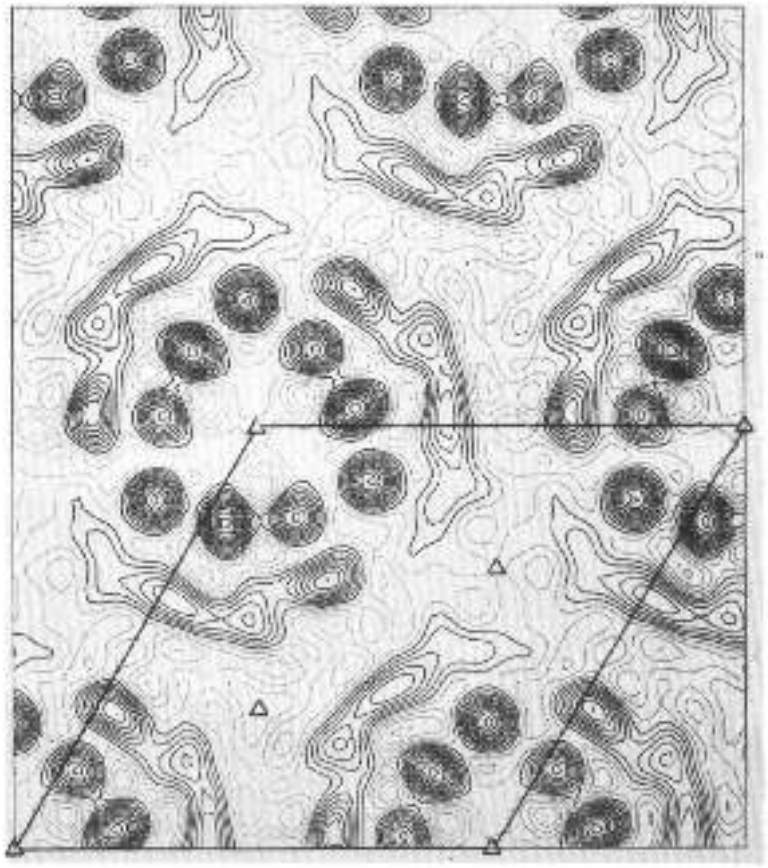

Figure II.1.12 – Electron density profile of the 2D crystalline purple membrane. The unit cell dimension is 62 Å x 62 Å. [93].

the assembly and six lipid molecules are positioned inside the trimer structure. This corresponds to 10 specific halobacterial lipids per monomer tightly bound to the BR molecule. Neutron diffraction data revealed the presence of 7-12 water molecules bound to BR and it was reported that these water molecules are crucial for a correct protein pumping activity [77, 80, 81, 94].

As mentioned above, BR functions as a light-driven proton pump. The release of a proton into the extracellular side and the uptake of a new proton from the cytoplasmic medium are simultaneously occurring events. This sequence of events is called Bacteriorhodopsin photocycle. BR undergoes significant conformation

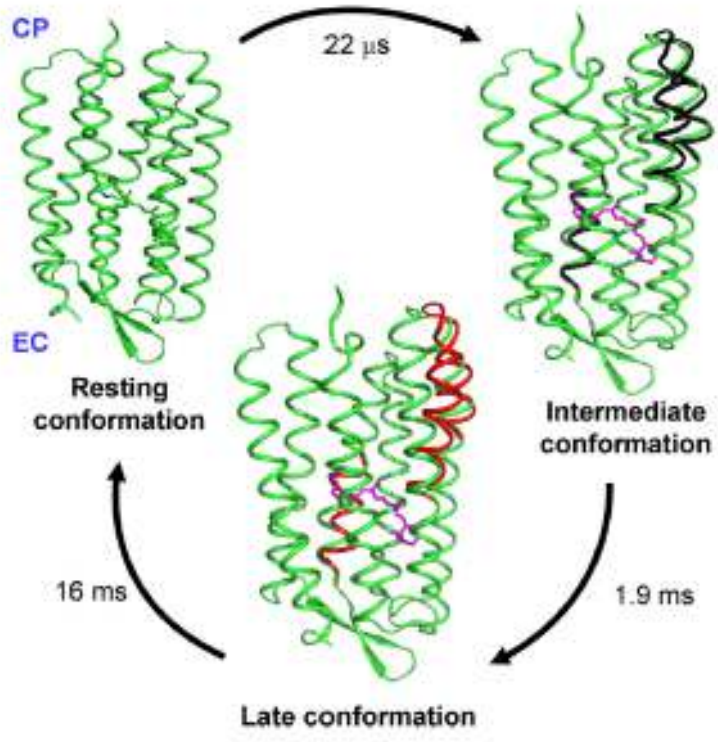

Figure II.1.13 – Conformational changes of Bacteriorhodopsin during its pumping activity. Significant movements of F, G, and C alpha helixes during the photocycle once the retinal is converted from all-trans (green) to 13-cis (magenta) are highlighted: resting conformation (green) of BR is superposed with intermediate (black) and late (red) conformations [78].

changes during the photocycle activity [78, 82, 83]. Intermediate conformational states of BR during the protein pumping cycle, changes in retinal and residues conformations, changes of protonation states and hydrogen-bonding of residues have been studied extensively [78, 95]. In Fig. II.1.13 spacious movements of the

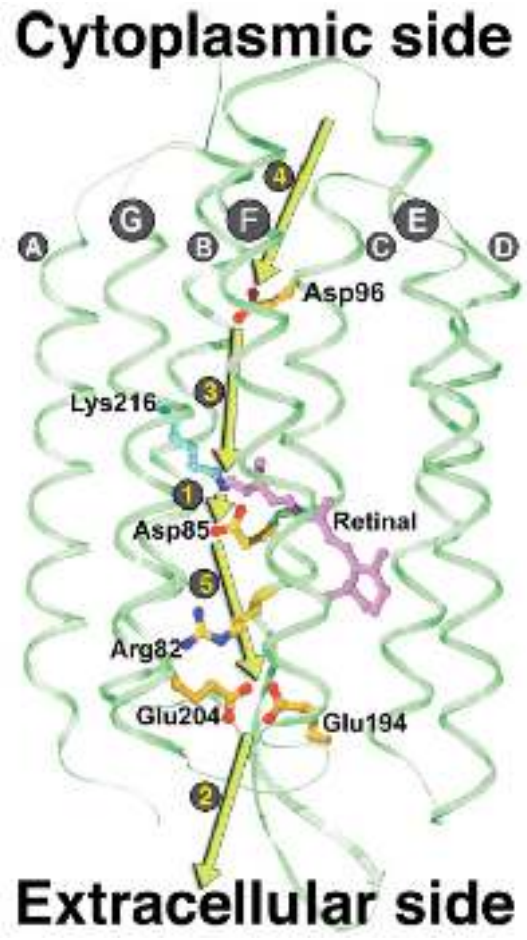

Figure II.1.14 – Schematic representation of the proton transfer steps (indicated by arrows and numbers from 1 to 5) in the BR photocycle. Labels A-G indicate 7 BR alpha helixes. Step 1 is release of a proton from the Schiff base to Asp85. In step 2 a proton is released to the extracellular medium (via Glu204 or Glu194). In step 3 the Schiff base is reprotonated by Asp96. Step 4 is the reprotonation of Asp96 from the cytoplasmic medium. Step 5 is the final proton transfer step from Asp85 to the either Glu204 or Glu194, which are involved in proton release at the extracellular side [84].

helices when the retinal is converted from all-trans (green) to 13-cis (magenta) upon the proton translocation are shown. The proton path during the cycle, a ribbon diagram of BR structure and important residues for the proton translocation across the protein are shown in Fig. II.1.13 and II.1.14.

1.4.3 Protein BR solution characterization

UV-Vis absorption spectra of BR can be used to define the purity, state (light-adapted, dark-adapted) and concentration of BR molecules in solution. A typical absorption spectrum of BR is shown in Fig. II.1.15. Protein concentration in the solution can be estimated using the Beer-Lambert law:

$$A = \log_{10} \frac{I_0}{I} = lc\epsilon \tag{1.2}$$

where A is the absorbance, I_0 is incident laser intensity and I is the transmitted intensity, ϵ is the molar absorption coefficient or molar extinction coefficient, $\mathrm{lmol^{-1}cm^{-1}}$; l is the length of the light path in cm; c is the solution concentration, $\mathrm{moll^{-1}}$. The typical values for molar extinction coefficients of BR are ϵ_{554} = 47 $\mathrm{mM^{-1}cm^{-1}}$ and ϵ_{280} = 81 $\mathrm{mM^{-1}cm^{-1}}$ [89, 96].

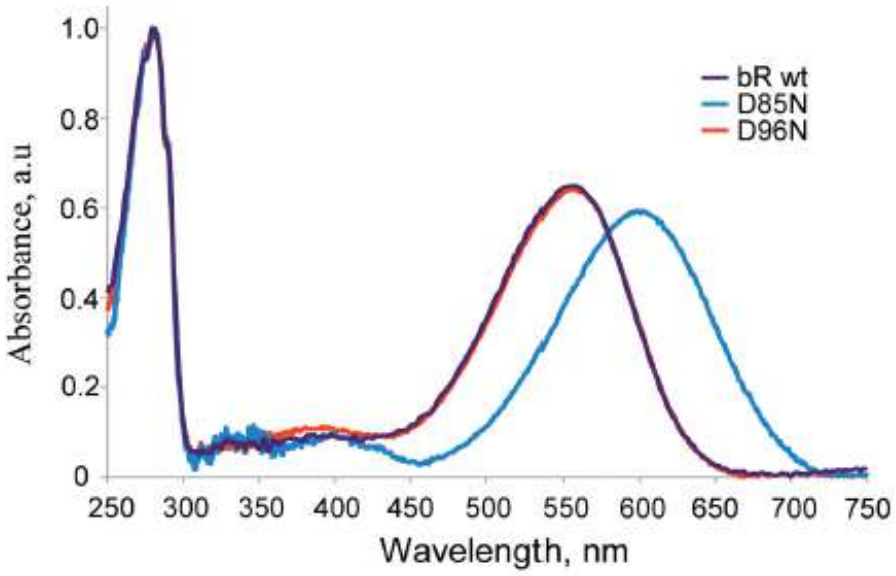

Figure II.1.15 – UV-Vis absorption spectra of the samples of the wild type BR and D85N and D96N mutants normalized by absorbance at 280 nm [79].

BR absorption spectrum exhibits two distinctive peaks: the retinal absorption peak at 558 nm and a peak at 280 nm caused by absorption of protein amino acids (mainly by Tryptophan (280 nm), Tyrosine (275 nm) and Phenylalanine (255 nm)). The position of the retinal absorption peak indicates the light-adapted (568 nm) or dark-adapted (558 nm) state of the protein [97]. The BR purity can be evaluated by measuring the absorbance at 280 nm and 568 nm using a UV-vis spectrometer and

calculating the peak to peak ratio A_{280}/A_{568}. A value of A_{280}/A_{568} between $\approx$ 1.4-1.8 is a good indication that the solution contains no denaturated proteins [98].

1.4.4 Protein expression and purification

Expression of BR from the purple membrane provides a very high yield of BR molecules. The process of protein purification is straightforward and a lot of protocols for protein extraction and purification are available and usually involve use of detergent. Solutions of BR in DDM detergent of defined concentration were obtained thanks to the collaboration with the group of Valentin Gordeliy at the IBS, Greboble, France.

The protocol used by the group to purify BR was adapted from reference [79] and consists of several steps. Shortly, purple membranes were extracted from Halobacterium salinarum following the protocol of Oesterhelt and Stoeckenius [99]. Purple membranes were solubilized in DDM as described by Gordeliy et al. [100] and Borshchevskiy et al. [101], except that 50 mM NaH_2PO_4 pH 6.0, 100 mM NaCl buffer was used. BR was purified from the membrane suspension by performing a series of centrifugation steps. BR was collected as a supernatant and concentrated with the use of a microconcentrator. The concentration of BR was determined by UV-vis spectroscopy. The obtained protein-detergent solutions of defined concentrations in 50 mM NaH_2PO_4 pH 6.0, 100 mM NaCl buffer were stored at -80 °C.

1.4.5 BR labelling

In order to perform fluorescence microscopy experiments on solid supported lipid bilayers and visualise BR, we have labelled BR with Cy3 Mono NHS Ester dye (G.E. Healthcare) via amine group. The labelling procedure was adapted from [102] and is summarized below.

1. 200 μl of dimethylformamide (DMF, Sigma) solvent was mixed with 1 mg of Cy3-mono NHS ester dye solution to achieve 5mg/ml solution concentration.

2. A solution of 25 mM Na/K phosphate buffer at pH 7.1 and pH 5.5 with 0.1% w/v DDM detergent was prepared.

3. 25 μg of Cy3-mono NHS ester in DMF and 500 μg of BR were mixed with 25 mM Na/K phosphate pH 7.1, 0.1% w/v DDM buffer solution to obtain final volume of in 500 μl.

4. The solution prepared in step 3 was incubated in the dark and at 4 °C for 4 hours.

5. Size-exclusion column was equilibrated with 25 mM Na/K phosphate buffer, 0.1% w/v DDM at pH 5.5 and was used to separate labeled protein from free dyes.

6. The collected fractions containing proteins were concentrated using Amicon Ultra-15 Centrifugal Filter device with a 30 kDa molecular weight cutoff.

7. UV-vis absorption spectra were recorded to estimate the protein concentration in the solution and check solution purity.

1.4.6 Archaerhodopsin-3

Archaerhodopsin-3 (Arch-3) is another type of transmembrane protein, which was used for the reconstitution studies during this project. Arch-3 is a light-driven proton pump from Halorubrum sodomense archaebacteria. The protein activity can be triggered by yellow-green light illumination, similar as to BR. It was shown that Arch-3 spontaneously recovers from light-dependent inactivation [103]. Arch-3 is closely related to BR and shares with BR 75% similar sequence homology. Significantly, all key residues involved in proton pumping in BR are conserved in Arch-3, but the full crystal structure of Arch-3 is not yet available (Fig. II.1.16)) [104]. It was reported that Arch-3 and BR molecules have showed small differences in kinetics of the photocycles and in their absorbance maxima [105].

Motivation to study the reconstitution of Arch-3 and its pumping activity was driven from the recent studies reporting that unlike the more extensively studied BR from Halobacterium salinarum, Arch-3 readily incorporates into the PM of both E. coli and mammalian cells [104]. It was shown that Arch-3 can serve as a high-performance genetically-targetable optical neural silencer and as a voltage-dependent fluorescence sensor of transmembrane potential [106]. Therefore Arch-3

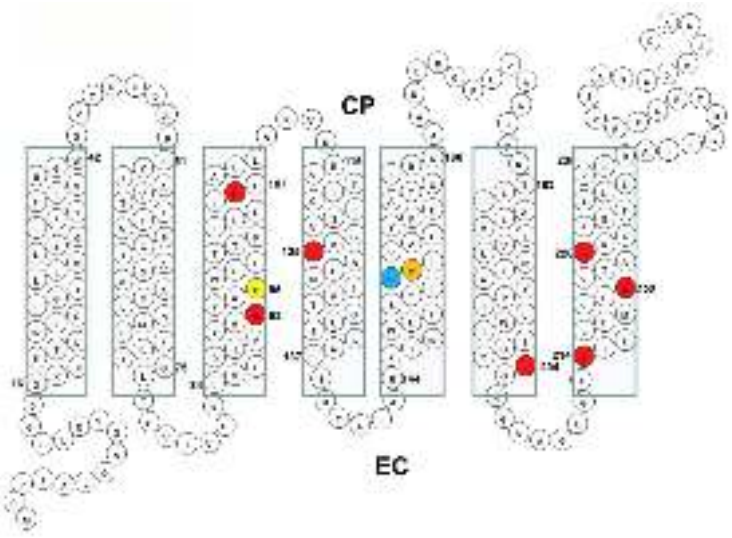

Figure II.1.16 – Sequence of Arch-3 and predicted folding pattern in membrane based on earlier models of archaerhodopsins and other microbial rhodopsins. Red highlighted residues are involved in the BR proton transport mechanism [104].

is one of the most widely used tools in optogenetics, which allows to activate or inhibit neuronal electrical activity using light of specific wavelength [107]. These protein features make Arch-3 one of the most studied protein nowadays. Within this thesis project we aimed to investigate Arch-3 reconstitution into the model membrane systems and to resolve the differences between BR and Arch-3 in protein-lipid bilayer interactions.

1.5 Detergent - mediated incorporation method

1.5.1 Protein reconstitution into the planar lipid bilayer systems

SLBs are widely used to mimic cell membranes. In fact, lipid bilayer can be formed on the solid support using different techniques such as vesicle fusion, LB/LS deposition, solvent exchange, as discussed in section 1.3. The possibility to form lipid bilayers samples in a wide range of experimental environmental conditions, varying and controlling the bilayer composition makes lipid bilayers on solid support potentially great candidates for the studies aimed to investigate the fundamental physical properties of biological membranes, their structure and composition. SLBs are excellent model systems to monitor the interaction of proteins, nanoparticles or macro-molecules with lipid bilayers.

However, planar membrane systems were not used so extensively unlike the free-standing lipid vesicles for the protein reconstitution studies, as it is assumed that the proximity of the substrate can hamper or forbid the protein insertion and drastically alter the protein functional activity. Although these effects can be present for a certain number of proteins, SLBs can provide a native-like lipid environment for the wide range of proteins maintaining their structural integrity and functional activity. In this framework, a lot of different approaches have been reported for protein incorporation into planar bilayers systems [63, 108, 109]. Most of the protocols were adapted from those already available for the proteoliposomes formation [21–23, 29, 33, 110–117], while only a few of them were specifically developed for the preparation of complex planar membrane systems [31, 32, 63].

A commonly used method to incorporate integral proteins into the SLBs system is detergent-mediated incorporation method. This protocol for the reconstitution of transmembrane proteins by direct incorporation into supported lipid bilayers destabilized by detergent had been introduced for the first time by the team of Rigaud, Levy and Milhiet in Institute Curie, Paris, France [29, 31, 33, 110, 113, 118, 119].

The developed protocol reported by Milhiet [31] was focused on the reconstitution of transmembrane proteins by direct incorporation into a preformed planar lipid bilayer, destabilized by DOTM or DDM detergents either in gel or fluid phases.

Unidirectional incorporation of LH2, LH1 and LH1-RC proteins at high density into the lipid bilayer was confirmed by high-resolution AFM measurements. Lately Berquand *et al.* [32] have studied the influence of calcium on the reconstitution of transmembrane proteins (LH1, LH1-RC) by direct incorporation into supported lipid bilayers (SLBs) composed of a mixture of DPPC:DOPC lipids. It was shown that calcium strongly stabilizes the SLBs, decreasing the insertion of low *cmc* detergents (DDM, DOTM and Fos-Choline-16) and prevent the insertion of proteins. The amount of the protein inserted can be regained by increasing the detergent concentration in the solution.

These works inspire and motivate us to adapt and develop the existing protocols further, eliminating the drawbacks of the proposed approaches and taking into account the requirements imposed by the implemented experimental techniques.

Therefore, based on the results published by Milhiet [31], we have optimized the detergent - mediated reconstitution protocol to incorporate transmembrane proteins BR and Arch-3 into solid-supported single and floating phospholipid bilayers systems in the gel or fluid phases. Detergent concentration, protein concentration and incubation time with the detergent-protein solution were optimized using QCM-D, AFM, fluorescence microscopy, neutron and X-ray reflectometry techniques in order to obtain a good quality defect-free membrane-protein system.

The concentration of the detergent solution had to be optimised in order to ensure that detergent molecules did not have a strong effect on the lipid bilayer structure as a full coverage and homogeneous lipid bilayer has to remain at the end of all manipulations. It is essential to have a good quality defect-free sample for NR and XRR experiments, as the result of the measurements is extremely sensitive to the average structure of the samples in the lateral direction. It has to be noted that it is particularly hard to produce high quality (full surface coverage) lipid bilayers samples of such big dimensions (up to 40 cm^2) needed for reflectometry experiments. The amount of BR in the solution has to be adjusted as well and scaled up/down according to the sample size required for the target experiment.

It is crucially important as well that the transmembrane protein retains it structural integrity and functional activity upon the reconstitution step. To keep transmembrane proteins stable in solution, their hydrophobic area has to be sur-

rounded/protected by amphiphilic molecules such as lipid or detergent micelles. The reconstitution protocol that we have developed employed the widely used sugar-based detergent n-Dodecyl-β-D-maltoside (DDM). DDM was chosen since it can shelter BR molecule from exposure to water environment and it had already been used for the protein solubilisation from purple membrane. The main step consisted in optimizing the appropriate detergent concentration allowing to preserve the structural integrity of the lipid bilayer system and protein molecules while ensuring incorporation of transmembrane proteins in the lipid bilayer systems.

1.5.2 Detergent-mediated protein incorporation method

The detergent-mediated protein incorporation protocol consisted of several steps:

1) Single or double lipid bilayer systems were formed on the solid support using one of the techniques for the SLBs preparation.

2) Transmembrane proteins BR (or Arch-3) was solubilized in detergent solution at a well defined concentration. The concentration of the detergent solution was experimentally optimized and it was shown that 0.05 mM DDM solution does not induce bilayer structural modification (see section 3.2) and therefore this solution was used for the incorporation procedure. Protein BR concentration ranged from 0.5 to 60 μg/ml and was adjusted depending on the performed experiment.

3) The obtained BR-DDM solution was injected into the closed sample cell and left to incubate for $\backsim$ 10-15 minutes, which allowed detergent molecules to penetrate and destabilize lipid bilayers sample promoting protein insertion into it (Fig. II.1.17, b).

4) As the last step, the sample cell was extensively rinsed with ultrapure water or buffer in order to remove all unbound proteins and detergent molecules from the bulk and supposedly from the lipid bilayer (Fig. II.1.17, d).

The preincubation step (Fig. II.1.17, a), when the detergent solution is added

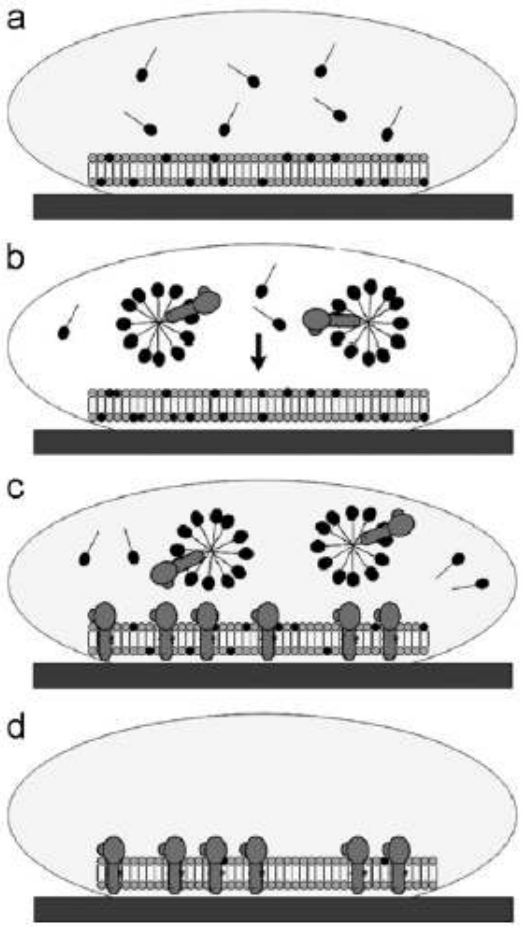

Figure II.1.17 – Schematic illustration of the detergent-mediated incorporation method [32].

to the lipid bilayer system, helps to destabilize the lipid bilayer and facilitates the protein insertion. This step is especially important when the target bilayer is in gel phase or when Ca^{2+} ions are present in solution as it is known that Ca^{2+} ions have a rigidifying effect on a lipid membrane causing its stabilization and decreasing the insertion ability of protein and detergent molecules [32].

To preserve the structure and integrity of the membrane, this step was omitted when working with the fluid single and floating lipid bilayer system (in both gel and fluid phases), as these model systems are very fragile and their structural integrity can be compromised if a pre-incubation step is performed.

CHAPTER 2

Experimental techniques

2.1 Quartz crystal microbalance with dissipation monitoring

Quartz crystal microbalance with dissipation monitoring (QCM-D) is a nanogram sensitive technique widely used to study adsorption/desorption processes on solid surfaces. Thanks to the dissipation measurements, QCM-D enables to monitor the tiniest changes in mass of the adsorbed material and at the same time to follow the modification of its viscoelastic properties as a function of time [120].

The QCM-D technique is a sensitive tool to study absorption and interaction of polymers [121], proteins [120], peptides [122, 123], nanoparticles [124], cells [125] to a solid-liquid interface or a solid-supported membrane [126]. Vesicle adsorption and membrane formation on different types of substrates (silicon, titanium oxide, gold, ..) [127, 128] can be also monitored in the liquid environment as well. Information about the properties of the sample on the sensor surface such as total adsorbed mass, thickness, density and viscosity can be obtained simultaneously.

The QCM-D sensor is a small thin quartz crystal disk sandwiched between two metallic electrodes on both sides and it is the main component of the QCM-D instrument (Fig. II.2.1). Quartz is a piezoelectric material and this inherent quartz property is laying at the base of the QCM-D working principle: application of an electric alternating potential induces a mechanical deformation of the quartz crystal (and vice versa). The alternating potential causes the crystal to oscillate at its characteristic resonance frequency f. This generates a mechanical shear wave that propagates in the perpendicular direction to the quartz surface and penetrates through the sample deposited on the chip and through the facing media (air or

liquid). For the sensors used (diameter of D = 14 mm, thickness of $h \approx 0.2$ mm) the QCM resonance frequencies are in the order of MHz, therefore the penetration depth of the generated wave is around 300 nm in a water environment. When the wavelength of the generated wave is an odd integer of thickness of the quartz sensor, the resonance condition is satisfied. Thus, the QCM-D instrument works only at the odd number of overtones [125]. When the thickness of the quartz sensor changes proportionally to the deposited mass on the sensor surface, shifts in resonant frequencies are induced and can be followed with time.

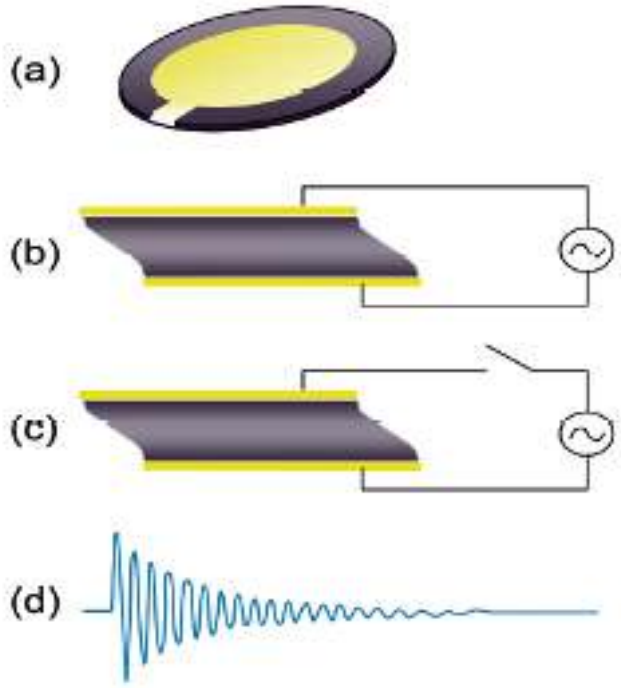

Figure II.2.1 – (a) QCM-D sensor with Au electrodes; (b) QCM-D sensor with the applied AC potential; (c) QCM-D sensor when the AC potential is turned off; (d) decay of oscillation (dissipation). Image is taken from [125].

In the case of rigid films, the amount of mass deposited on the surface can be determined through the Sauerbrey relation [129]:

$$\Delta m = -C\frac{\Delta f_n}{n}, \tag{2.1}$$

where n = 1, 3, 5, 7 is the overtone number, Δf_n is the frequency shift for a given overtone and C is the Sauerbrey constant, which depends on the material of the quartz sensor and is defined as:

$$C = \frac{t_q \cdot \rho_q}{f}, \tag{2.2}$$

where t_q = 330 μm and ρ_q = 2.648 g/cm^3 are the thickness and density of the quartz sensor respectively. For the resonance frequency f = 5 MHz, the Sauerbrey constant is C = 17.7 Hz·ng·cm^{-2} [120].

It is worth noting that the possibility of recording several harmonics for the frequency and dissipation signals increases the sensitivity of the measurement. Propagation of the generated wave into the sample decreases with increasing overtone number, meaning that high overtone can be more sensitive to the deposited layer and in some cases also to its internal features. The signal from the first overtone is usually omitted in the data analysis as it is sensitive to the environment [128].

The thickness d of the adsorbed layer can be estimated as:

$$d = \frac{\Delta m}{\rho}, \tag{2.3}$$

where ρ is the density of the adsorbed layer.

The relation 2.1 holds for rigidly adsorbed and homogeneously distributed thin films with a thickness up to 300 nm for a quartz crystal of f = 5 MHz. For measurements in liquid environment and studies of soft and viscoelastic materials, which do not rigidly adsorb on the crystal surface, these underlying assumptions might not be satisfied.

To take into account additional viscoelastic properties of the adsorbed material, QCM-D provides the possibility to simultaneouly monitor changes in the resonant frequency (Δf) and energy dissipation (ΔD) in the system. Thus, QCM-D gives information about two independent properties of the system: Δf quantifies the changes of the adsorbed mass and ΔD provides the information on viscoelastic properties of the adsorbed layer [130].

ΔD is obtained by monitoring the decay of the sensor oscillations amplitude $A(t)$ once the applied alternating potential to the crystal is turned off :

$$A(t)_n = A_{0n} \exp^{-t/\tau_n} \sin(2\pi f_n t + \phi_n). \tag{2.4}$$

From Eq. 2.4 the overtone frequency f_n and characteristic decay time τ_n can be

obtained. In the case of liquid media, the wet adsorbed mass is estimated, as the value of the frequency f_n takes into account all the water stored in the sample.

For each overtone, the dissipation factor, D_n, can be derived as :

$$D_n = \frac{1}{\pi f_n \tau_n}. \tag{2.5}$$

It is important to perform all the QCM-D measurements under the same buffer conditions, as QCM-D measurements are extremely sensitive to properties of the bulk solution like presence of ions, viscosity and temperature. Any slight change in the environmental conditions will lead to changes in Δf and ΔD signals. These changes can be indistinguishable from those originated from the sample itself.

If Eq. 2.1 does not hold, two models (Voigt model and Maxwell model) can be used to qualitatively analyses the QCM-D data [121]. Within this work, only qualitative analysis of the collected data were performed and the adsorbed mass was estimated using the Sauerbrey relation (Eq. 2.1).

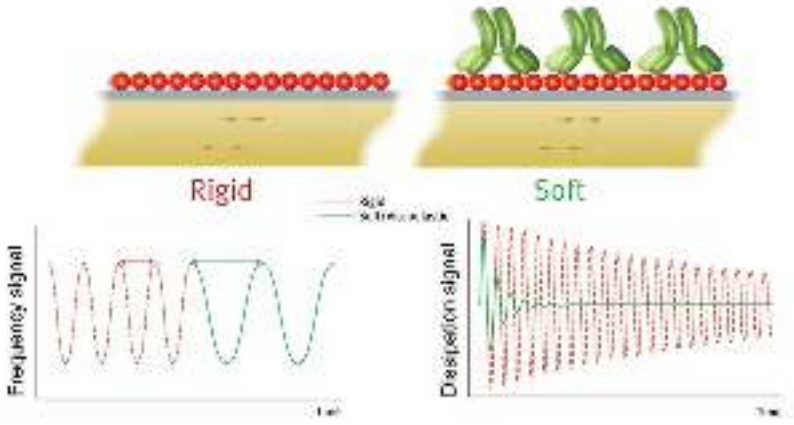

Figure II.2.2 – Frequency and dissipation QCM-D signals for a soft (green) and rigid (red) films on the sensor surface. The dissipation is recorded when the applied AC potential is turned off [131].

2.1.1 The QCM-D instrument

The QCM-D measurements were performed using a Q-Sense series E4 instrument (Q-Sense, Sweden). This instrument is equipped with 4 solid/liquid sample chambers, a pump flow control system and a precise temperature control system.

Figure II.2.3 – QCM-D Q-Sense series E4 instrument used in this thesis.

2.2 Atomic force microscopy

Atomic force microscopy (AFM) is a well-established technique, which allows to obtain bi-dimensional surface maps with nm resolution. The surface roughness, sample thickness, height of sample features and lateral size of domains can be imaged and quantified by means of AFM experiments [132, 133].

The working principle of AFM is based on the ability to probe interaction forces between the AFM probe and the surface. AFM allows to perform topography and force spectroscopy measurements by measuring the sample-tip interaction forces with high spatial (lateral down to ≈ 5 Å and vertical down to ≈ 1 Å) and force (≈ 10 pN) resolution [134]. Such high sensitivity is a great advantage, which offers the possibility to study not only hard condensed matter systems, but also soft matter and biological materials in a non-destructive manner [135].

A typical AFM instrument consists of a cantilever with a μm-size tip at the free end, a laser, a position sensitive photodiode detector (PSPD), a piezo-scanner and a

sample stage.

The cantilever and tip assembly is called AFM probe, which is usually made of silicon or silicon nitride (Si_3N_4). The tip height can range from 3 - 15 μm and the radius is below than 10 nm and the length of the cantilever can vary from 100 - 500 μm depending on the desired probe stiffness and type of experiment [136].

To obtain an AFM image the tip is brought in very close to the surface of the sample. Depending on the chosen operational mode the probe can be in close contact with the sample (contact) or it can hover over the sample surface (non-contact mode). AFM surface topography images are created by scanning the probe over the sample in a raster pattern (line by line motions of the tip in the x-y plane).

AFM instruments consist of a magnetic sample stage allowing to position and fix the sample. The AFM probe is magnetically mounted on a piezoelectric stage which allows a very fine probe-to-sample surface approach. In fact, the piezo-scanner can move in the x, y and z directions with high accuracy providing a precise control of the probe position over the sample. The position and deflection of the cantilever is monitored by recording the signal of the reflected laser that is bouncing off onto the PSPD detector. The PSPD detects any cantilever deflection during the sample scan and provides feedback (of the values of force, amplitude, frequencies, depending on the chosen AFM mode) to maintain the accurate response and a constant setpoint. This feedback loop allows to move the piezo-stage, adjusts the cantilever position and minimizes the error signal. These accurate movements of z-piezo in the x, y, z directions yield information on surface topography. The feedback parameter (setpoint value) is a user-input parameter, which depends on the AFM working mode: in contact mode the feedback parameter is a cantilever deflection, whereas in tapping mode the oscillation amplitude of the cantilever is kept constant during the scans [137].

The resulting error signal, which is the difference between the setpoint and the actual measured value of force, amplitude or frequency, is minimized by the feedback control loop. High resolution and a low noise-to-signal ratio allow to obtain detailed information on the structural features of the sample.

Due to the attractive or repulsive interactions (van der Waals, electrostatic, capillary, magnetic, etc.) occuring between the tip and the sample, a negative or

positive bending of the cantilever occurs. The spring-like cantilever deflection is characterized by Hooke's Law:

$$F = -kx, \tag{2.6}$$

where k is the spring constant, x is the cantilever deflection. The magnitude of the cantilever deflection depends on the value of the generated force between tip and sample and the spring constant (stiffness) of the cantilever.

2.2.1 Operational modes

The AFM instrument can be operated in a number of different imaging modes, providing the possibility to study a wide range of samples ranging from biological and soft matter specimens to magnetic and ceramics specimens. Lipid bilayers, proteins, nucleic acids, biological cells, etc. can be investigated in the natural medium thanks to the ability of AFM to work in liquid environment. AFM imaging modes are classified depending on the cantilever behavior. Contact, non-contact and tapping modes are the most widely used operational modes of AFM. The difference and main features of the selected operational modes of AFM will be shortly discussed below.

Contact mode

In contact mode, the tip is in physical contact with the surface and moves above the surface in a raster pattern. A topography image of the surface can be recorded in two ways, either by maintaining the force between the tip and the sample constant using the feedback loop (constant-force mode) or by fixing the position of the probe at a defined height above the sample and monitoring the cantilever deflection while dragging the tip over the sample surface (constant-height mode).

The feedback loop has to be regulated according to the size of the surface features: the z-piezo has to respond relatively fast to changes in sample height to map all the surface features, but not too fast to avoid noisy oscillations of the cantilever. The applied force to the sample should be chosen attentively as well, as too large applied force can cause sample damage, tip pollution and appearance of

imaging artifacts.

Tapping mode

In tapping mode the cantilever oscillates at, or close to, its resonance frequency (usually 100-400 kHz) with a defined amplitude (usually 10-200 nm) in the close proximity to the sample surface. The oscillation amplitude of the cantilever is the feedback parameter and it is maintained constant during the imaging process.

The movement of the piezoelectric scanner in the z direction, caused by the changes in the tip-sample separation during imaging, and thus changes in the oscilation amplitude, defines the sample topography.

In tapping mode the oscillating probe interacts gently with the sample surface, only touching the sample at the minimum of its oscillating motion. Thanks to the short contact time, the probability of the tip damage and pollution is reduced.

Compared to contact mode, the drawback of tapping mode is the lower spatial resolution due to the intermediate contact with the sample, but the gentle interaction with the surface makes it the right choice to study soft, elastic and fragile samples.

Non-contact mode

In non-contact mode, the cantilever never touches the surface and hovers above the sample while oscillating with a low amplitude (< 10 nm) at a frequency slightly higher than its resonance frequency. Due to the forces acting between the tip and the sample, the oscillation amplitude or frequency of the cantilever changes. The feedback loop reacts to these variations keeping the setpoint value constant and a topography of the sample is generated.

As the oscillating cantilever never touches the surface, no force is exerted on the sample. This is a great advantage when fragile and soft samples are examined, as no damage can occur. The drawback of this mode is a very low temporal resolution, thus the specimen has to be stable in time.

PeakForce Tapping

PeakForce Tapping Mode is a recently developed mode by Bruker, which allows to record topography and force spectroscopy data with very high resolution in air

and liquids [138].

PeakForce Tapping operates similarly to tapping mode. The cantilever oscillates with a frequency well below its resonance frequency and periodically touches the sample surface, performing a very fast force curve at each pixel in the image [138]. The interaction force at each touch is measured instantaneously and the peak force of every force curve is used by the feedback loop to control and minimize the applied force on the sample. This mode of operation allows to work at very low imaging forces (< 200 pN), which is about 5 times lower than those used in tapping mode (≈ 1nN). Thanks to the direct and instantaneous force control, the integrity of the AFM probe and sample is preserved [138].

ScanAsyst is an image optimization technique developed for the PeakForce Tapping imaging mode [138]. The implemented algorithm continuously monitors the image quality and adjusts the appropriate parameters during the scan. The ScanAsyst automatically optimizes peak force setpoint, imaging gains, scan rate, tip-sample separation to obtain the best quality image.

2.2.2 AFM instrument and measurements

A Multimode 8, Nanoscope V (Bruker) AFM instrument was used to perform AFM measurements at the IBS, Grenoble, France in order to investigate SLBs with or without reconstituted BR. The instrument setup is shown in Fig. II.2.4. The ScanAsyst image optimization technique, which is integrated in the AFM software, was used to perform the automatic image optimization. The AFM was operated in Peak Force Tapping mode with the force set point value of ≈ 300 pN at a scan frequency of a 1-2 Hz. An AFM XE-70 Park system (Fig. II.2.5) was used for AFM experiments at the IML, Lyon, France and at the ILL, Grenoble, France in order to study the lateral structure of single and floating bilayer systems. The AFM was operated in contact mode, applying forces below 1 nN at a scan frequency of 1 Hz.

2.2.3 Cantilever choice

The AFM probe defines the resolution and quality of the obtained topography images and force measurements. Therefore a proper and deliberate choice has to be

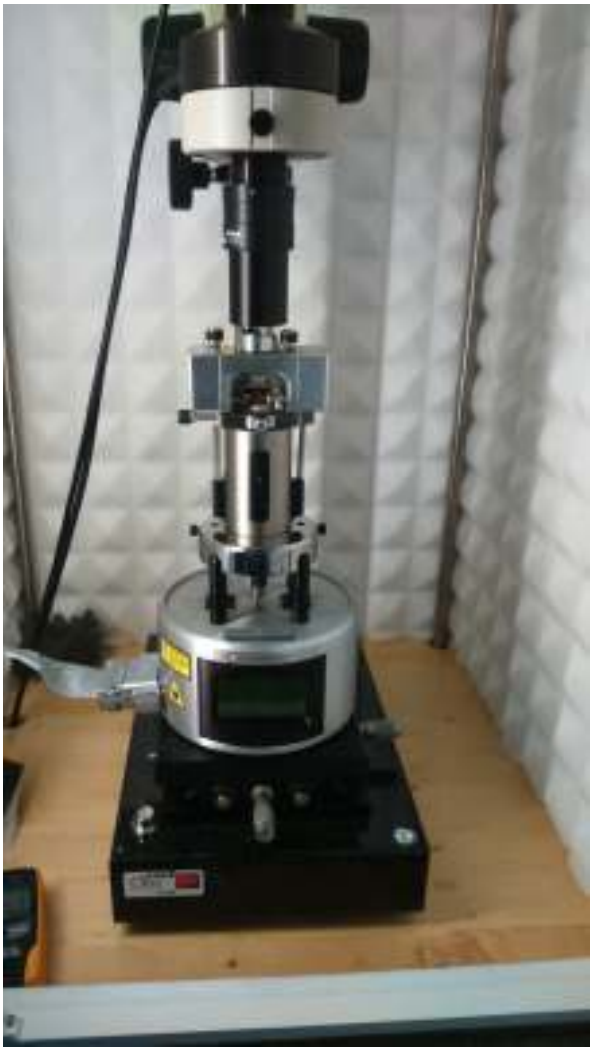

Figure II.2.4 – The Multimode 8, Nanoscope V AFM instrument from Bruker [139].

done when choosing the probe for the experiments. The critical parameters to take into account are the stiffness, geometry and physical dimensions (length, width, and thickness) of a cantilever, as the force resolution, the thermal noise and the spring constant of a cantilever are related and have crucial influence on the measured data quality.

The specifications of the used cantilevers within this thesis project are listed in Tab. 2.1. For the AFM experiments performed at the IBS, Grenoble, France, a ScanAsyst-fluid probe from Bruker [140] was chosen, as it has a dull tip, which is ideal for imaging extremely delicate samples such as lipid bilayers in fluids and it is suitable for the PeakForce Tapping mode.

A silicon nitride AFM probe called SiNi from BudgetSensors [141] was used for the AFM imaging at the IML, Lyon, France and at the ILL, Grenoble, France. The

Figure II.2.5 – The XE-70 Park AFM instrument. A teflon sample cell is mounted on the instrument.

SiNi probe has two different cantilevers of different spring constant and dimension (see Tab. 2.1). The long cantilever of the SiNi tip was used to obtain the AFM images presented in this thesis. The choice of the probe was based on cantilever stiffness, dimensions and availability.

Table 2.1 – Cantilevers used for the AFM experiments

Specifications	SiNi short	SiNi long	ScanAsyst-fluid
Shape	Triangle	Triangle	Triangle
Resonance frequency (kHz)	30	10	150 ± 50
Spring constant (N/m)	0.27	0.06	0.70 ± 0.35
Length (μm)	100 ± 10	200+/-10	70 ± 5
Width (μm)	16 ± 5	30 ± 5	10 ± 5

2.2.4 AFM solid/liquid cell

To investigate planar lipid bilayer systems prepared by LB and LS deposition techniques, a solid/liquid cell made of PTFE was used (Fig. II.2.6). The cell consists of two parts: a lower part including a water reservoir and O-ring and an upper cover part machined to host a solid substrate. The two parts are tightly sealed together with four screws. The cell holds a 2.5x2.5x1 cm^3 silicon crystal block on which the sample deposition is performed. The cell can be thoroughly cleaned using strong solvents in the ultrasound sonication bath, thus it can be placed inside a Langmuir trough for sample transfer.

Figure II.2.6 – Solid/liquid cell used for AFM experiments on double lipid bilayers prepared by LB and LS depositions.

Improvements of the cell were done in collaboration with Wayne Clancy, LSS instrument technician, to solve problems of weak sealing and water leakage from the cell interior. An O-ring and brass threads were placed into the body of the cell. The PTFE cover part was modified (by Simon Wood, LSS instrument technician) in order to allow accommodation of larger liquid volumes in the cell interior.

2.3 Fluorescence Microscopy

Fluorescence microscopy is a widely used technique in modern cell biology and medicine to study living cells and tissues, to trace stained proteins, to examine cancer cells and to reveal organization of the DNA or to examine fluorescence-stained neurons in brain slices as well as to trace marked synaptic vesicles [142].

Implementation of the fluorescence microscopy technique is not limited to biology. Membrane model systems such as LUV, GUV and proteoliposomes with incorporated fluorescently labelled proteins or planar lipid bilayers systems have been studied with this technique as well, allowing to probe the vesicles-to-sponge phase transition [143], lipid oxidation [144], protein reconstitution [33], lipid phase transitions [145], vesicle fusion and fission events [146, 147].

Fluorescence microscopy allows to visualise and obtain images of samples which possess intrinsic fluorescent properties or which are stained with a fluorophore molecule. This technique offers the possibility to study the localization of fluorescent areas in the specimen, to quantify the intensity of the emitted light and to follow the decay of the intensity due to the photobleaching, allowing to probe the diffusion properties of the molecules.

2.3.1 Fluorescence principle

During fluorescence microscopy experiments, the sample being illuminated (excited) with light of a defined wavelength will absorb photons of a specific wavelength. Upon light energy absorption, electrons of the fluorescent molecules are excited form the ground state to the excited state of higher energy level. Relaxation of the electrons from the excited state to the lower energy level can occur in several ways including vibrational relaxation (energy dissipation from the molecule to the surroundings, nonradiative process), internal conversion (nonradiative transition), intersystem crossing (can lead to phosphorescence or delayed fluorescence) or fluorescence. The electronic state of the molecule and the mentioned transition between them can be illustrated using Jablonski diagrams.

In this way, upon electron relaxation from the high energy level to the more energy favorable ground state, photon emission can occur and this phenomenon is

called fluorescence. Between absorption and emission processes, some energy can be lost (due to vibrational relaxation or internal conversion) and the emitted photon will possess a lower energy than the absorbed one. The emitted light will therefore have a longer wavelength than that the light used for the sample excitation. This shift in wavelength of emitted and absorbed light is called the Stokes shift.

Due to the Stokes shift, excitation and emission wavelengths can be separated. A set of coloured filters are implemented in the microscopes to separate bright excitation light from the emitted fade signal from the sample caused by the fluorescence phenomenon. This filter absorbs the short-wavelength light and transmits the long-wavelength fluorescent light, thus a high contrast is established and fluorescent light is visible as a bright light against a dark background. In practice this set of filters is implemented in the microscope as a filter cube (discussed below) or automated filter changer [148]. Thus, the light collected by the microscope camera corresponds to the light emitted only by the fluorescent molecules. This is a great advantage of the techniques as even a small amount of the fluorescent dyes or molecules hosted in the sample can be detected.

2.3.2 Microscope resolution

The resolution of the microscope is limited by the diffraction limit, therefore only objects at the micron resolution (higher than 1 μm) can be visualized using optical microscopy. Despite different constituents of the biomembrane cannot be resolved below the micron scale, the image resolution is high enough to observe and study the behavior of complex biological cells, large or giant lipid vesicles, as well as planar lipid bilayers on solid supports at micron scale.

The lateral resolution of a microscope is defined as the minimal distance between the two points on the sample which can be distinguished by the camera. The maximal lateral resolution r_{max} of a microscope is determined by the λ wavelength of the light used for the sample observation and the numerical aperture NA of the microscope [149]:

$$r_{max} = \frac{\lambda}{2NA}. \tag{2.7}$$

The lateral resolution can be enhanced using light for the illumination with shorter

wavelength λ or increase the NA of the microscope.

The longitudinal resolution of a microscope, its depth of field, is defined as a distance from the closest object and the farthest object simultaneously located in focus. The longitudinal resolution of a microscope can be estimated using the formula:

$$d = \frac{\lambda n}{2NA^2} + \frac{n}{2MNA}e, \tag{2.8}$$

where NA is the numerical aperture of the objective, M is the magnification of the objective, λ is the wavelength of the light used for illumination, n is the refractive index of the medium between the coverslip and the objective (n = 1.000 for air, n = 1.33 for water and n = 1.515 for the immersion oil), e is the smallest distance that can be resolved by a detector located in the image plane of the objective. The value of e is given by the size of pixels of the camera (including binning) [150].

2.3.3 Microscope

To perform fluorescence microscopy experiments, we have used used a Nikon TE-2000 inverted microscope (Nikon, Japan) equipped with a mercury light source (Nikon Instruments Inc., Japan) in epifluorescence mode. An oil-immersion objective LEICA with x100 magnification and with a numerical aperture NA 1.3 was used. The temperature of the sample was precisely controlled with an heating chamber.

The inverted microscope is equipped with a filter cube, which is composed of two filters (an excitation filter and a emission filter) and a dichroic mirror at 45°. The filter cube is used to direct the filtered light of a specific wavelength from the mercury lamp to the sample and from the sample to the camera. The dichroic mirror has significantly different reflection and transmission properties at two different wavelengths. In the epiillumination experiments the dichroic mirror separates the illumination and emission light, reflecting the short wavelength excitation light towards the sample and transmitting the long wavelength emitted light from the sample towards the camera [148]. The blocking filters in the fluorescence cube are used to select the suitable excitation and emission wavelengths, transmitting only the required range of wavelengths.

In this work the first cube was used to visualize fluorescently labelled lipid

Figure II.2.7 – Nikon TE-2000 inverted microscope (Nikon, Japan).

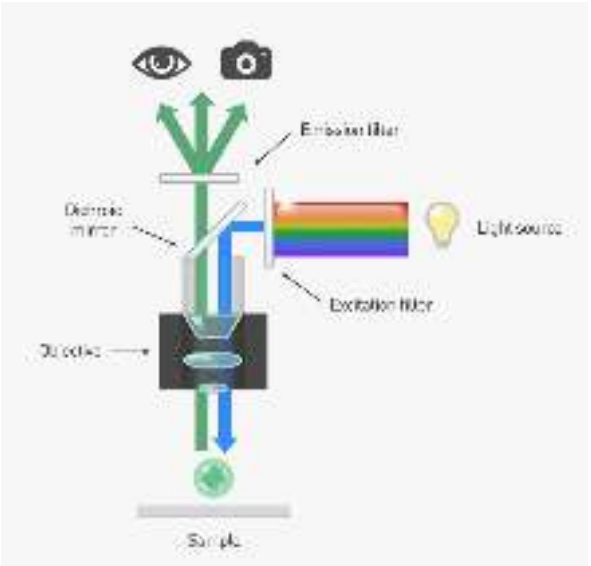

Figure II.2.8 – Sketch of epifluorescence microscope. The dichroic mirror, exitation and emission filters are shown [151].

bilayers and the second cube to observe BR stained with a fluorescent marker. The lipid solutions were labelled adding 1% (by weight) of NBD-PE fluorescent lipids (Avanti Polar Lipids) (460 nm absorbance maximum and 535 nm emission maximum) to the lipid solution in chloroform, used further for the lipid bilayers preparation. BR was labelled with Cy3 Mono NHS Ester dye (G.E. Healthcare) (an excitation

maximum at 550 nm and emission maximum at 570 nm) [152]. The protocol of BR labelling is reported in section 1.4.5.

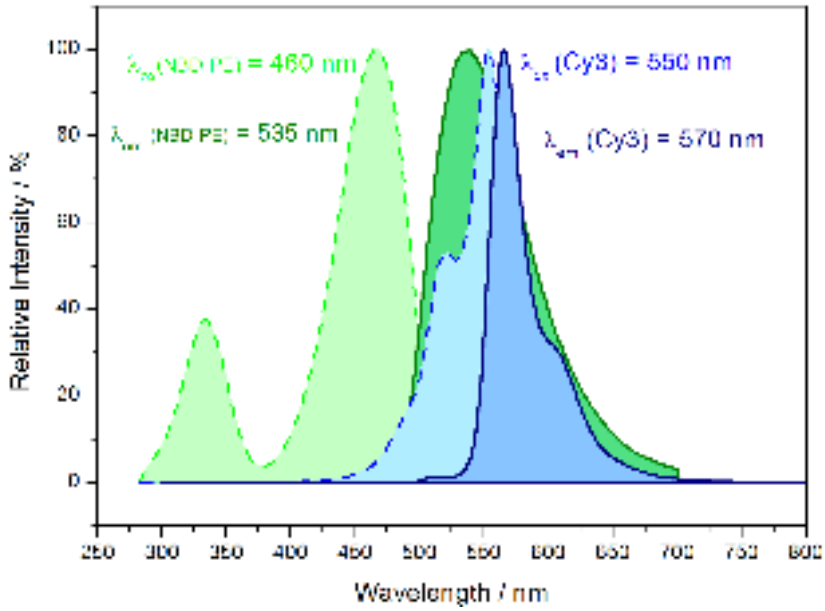

Figure II.2.9 – Excitation (dotted line) and emission (filled line) spectra for NBD-PE lipids (green) and Cy3 Mono NHS Ester dye (yellow) molecules [152].

Two filter cubes with 482 nm/506 nm/536 nm and 543 nm/562 nm/593 nm fluorescent filters (band pass center for excitation filter/ dichroic mirror/ emission filter) were used for the lipids' and proteins' observation respectively.

Images were recorded with a digital camera Insight 18000 from Diagnostic Instrument. All images were recorded using a piece of software developed by André Schröder (ICS, Strasbourg) and further all images were analysed and processed using the free software ImageJ [153].

The lateral and axial resolution of the microscope can be estimated using the listed above Eq. 2.7 and 2.8. For the lipid visualization experiments, using the values listed above and the value e = 146.8 nm per pixel (binning 2) for the used microscope, the lateral and longitudinal resolution (depth of field) were estimated to be equal r_{max} = 185 nm and d = 433 nm, accordingly. For the protein visualization experiments the lateral and longitudinal resolution were estimated to be equal r_{max} = 209 nm and d = 488 nm, respectively. The estimated longitudinal resolution of the microscope is around 450 nm and the average thickness of lipid bilayer is 5 nm, thus it is well below the maximal resolution of the used microscope.

2.4 Development of sample environment

In order to perform experiments using different experimental techniques, we have developed several sample environment cells.

As known, lipid bilayers samples are stable only in a water environment. To avoid bilayer collapse and disruption of its structure, any contact with air or any turbulent water movement around the supported samples have to be avoided. To keep the sample in water and protected from turbulent flows in the surrounding liquid environment, tightly sealed solid/liquid cells were used for the sample preparation and manipulations.

A lot of specific requirements to the cell design are imposed by the sample preparation techniques and the target experiment: solid/liquid cells have to be resistant to cleaning with strong solvents such as chloroform, acetone and ethanol, and they have to be compatible with LB/LS and vesicle fusion techniques of lipid bilayer preparation; substrates of different types and sizes depending on the target experiment should be accommodated in the cell; the possibility to position the sample cell vertically or horizontally and to vary the interface (solid/liquid or liquid/solid) should be allowed, the ability to perform contrast variation or solution injection has to be allowed as well, etc.

The two main sample preparation methods for the lipid bilayer formation used within this project were vesicle fusion and LB/LS deposition techniques. LB/LS techniques require very clean working environment conditions (clean room like) and the substrates and solid/liquid cells have to be thoroughly cleaned to avoid any external impurities, as these parts have to be placed inside the Langmuir troughs in order to perform bilayer deposition. Any external pollution of water sub-phase and trough are strictly undesirable, as it can hamper the bilayer transfer and sample formation. Therefore solid/liquid cells have to be resistant to cleaning in strong solvents such as chloroform, acetone and ethanol to remove any possible contaminations and impurities. The vesicle fusion technique requires as well the perfectly clean solid/liquid cells and also the possibility to perform injection of SUVs solution into the cell in order to form bilayer. Therefore, the used cells have to be equipped with an inlet and and outlet to perform solution injections, change of the solvent contrasts during NR experiments or perform proteins reconstitution step.

Highly polished silicon crystals, quartz blocks or thin glass slides were used for the QCM-D, NR, synchrotron radiation XRR and in-house XRR measurements, AFM and fluorescence microscopy experiments.

Two different sample environments are required for the NR and XRR experiments due to the different penetration properties of the beams and measurement geometry. The neutron beam goes though the silicon block and hits the interface, whereas X-ray beam has to go though the bulk water to reach the sample surface. Different size of substrates were used for NR and XRR (synchrotron and in-house) experiments due to the difference in beam intensity. In turn, fluorescence microscopy experiments require a very compact sample cell, which allows to host very thin transparent substrates.

In order to perform sample illumination with light to activate reconstituted proteins, the designed sample cells have to allow the light to reach the sample either via an integrated transparent window or through a transparent sample substrate. The setup to hold and direct the light source has to be available as well.

Due to the immense list of specific experimental conditions and particular requirements to the sample size, substrate type, sample positioning at the instrument, it is not possible to create a multipurpose sample cell taking into the account all imposed requirements. Therefore, no universal sample cell can be fabricated and a specific sample environment for each experimental technique must be available.

Heating chambers with the possibility to heat or cool the solid/liquid cell to perform precise temperature control of the sample and to tune the lipid bilayer phase should be developed as well.

A solid/liquid cell for NR experiments with in-situ illumination

To perform sample illumination during NR measurements in order to activate the reconstituted proteins in the membrane we have developed an illumination setup for the existing solid/liquid cells. To be able to tune the wavelengths of the light used for the illumination, the possibility to install filters with different cut-on wavelength was implemented as well. This development was performed in collaboration with Grant Wallace, an instrument technician at the ILL (Grenoble, France). The developed setup is compatible with the configuration of the D17

reflectometer at the ILL.

The developed setup consists of a solid/liquid cell itself, an optical collimator, an optical fiber which connects optical collimator to the mercury lamp, a sample holder, as well as a filters holder, which allows to perform manual and fast replacement of the filters (Fig. II.2.10).

The solid/liquid sample cell used for the NR experiments is composed of a lower PEEK part (water reservoir), a solid substrate on which the sample is deposited and an upper cover part made of aluminium and PTFE. The illumination window was cut through the second aluminium part of the cell to allow sample illumination though the solid substrate. Instead of designing a window for the sample illumination through the PEEK part of the cell, we chose to use a transparent substrate (quartz or sapphire) to allow in-situ sample illumination. The end-stage collimation of the optical setup was directly mounted on the sample changer, which allows to place up to three solid/liquid cells at once on the D17 reflectometer (Fig. II.2.10 and II.2.11).

Figure II.2.10 – Setup for in-situ sample illumination during NR experiment.

A solid/liquid cell for fluorescence microscopy experiments

In collaboration with technician Patrick Allagayer and scientist André Schroder at the ICS (Strasbourg, France), we have developed a solid/liquid cell to accommodate lipid bilayers samples during fluorescence microscopy experiments. This solid/liquid cell can be used with the inverted microscopes available at the ICS and it is compatible with the LB/LS deposition techniques.

The fluorescence microscopy solid/liquid cell is made of PEEK, which allows its fast and easy cleaning before the sample preparation. A very thin round microscopy glass slide can be hosted as a solid support for the lipid bilayer samples. The diameter

Figure II.2.11 – Sample changer stage and an illumination setup on the D17 reflectometer.

of the appropriate glass substrate is 30 mm and its thickness is around 0.13-0.17 mm. PEEK module is equipped with connections for the inlet and outlet tubes, which allow to perform solution injections and cell rinsing either manually or by means of a pump. An O-ring is placed between the PEEK module and glass substrate to ensure the tight cell sealing in order to avoid sample leakage, as to perform fluorescence microscopy experiments, the cell should be mounted on the instrument with the glass substrate down. The developed cell is shown in Fig. II.2.12.

Figure II.2.12 – Solid/liquid cell for fluorescence microscopy experiments.

A solid/liquid cell for in-house X-ray reflectometry and synchrotron experiments

In collaboration with Kalvin Buckley, instrument technician at the ILL (Grenoble, France), we have developed solid/liquid sample cells adapted for SR reflectometry experiments and in-house XRR measurements using a lab X-ray source.

The main body of the cell is made of PEEK. Cell windows are fabricated from PTFE by polishing the material down to a thickness of 3 mm. This idea of windows fabrication was inspired by from the developments performed in the Emanuel Schneck group at the Max Planck Institute in Potsdam, Germany. The PTFE material was chosen due to its high hydrophobicity and a very thin film allow a reasonable transmission of X-ray. The cell was designed to accommodate substrates of size 5x5x1 cm^3. Typically, a cut along (111) plane and highly polished silicon crystal block was used as sample support. The developed X-ray cells were equipped with a round quartz window (diameter 3.7 cm). The window was cut through the bottom part of the PEEK cell, which allows to illuminate the sample through the bulk water.

The cell was equipped with inlet and outlet tubes to allow solution injections and/or cell rinsing. In total, one solid/liquid cell without and four solid/liquid cells with quartz illumination windows were fabricated.

Figure II.2.13 – Solid/liquid cell for X-ray reflectometry experiments at the synchrotron.

To be able to precisely control the temperature of the sample during the measurements, we have developed a heating chamber made of copper and brass 2.4. The chamber was connected to a water circulation thermal bath allowing the fast and efficient sample cooling and heating. Unfortunately, the temperature of the sample (solid substrate) could not be measured directly. After sufficiently long equilibra-

tion time (≈ 15 min), we assumed that temperature of the sample was equal to the temperature of the heating chamber. The cut-through window was fabricated on the bottom of the chamber to enable sample illumination. This chamber was also equipped with the holder for the optical collimator and for the light filters to have a possibility to tune the wavelength of the illumination light. A smaller version of

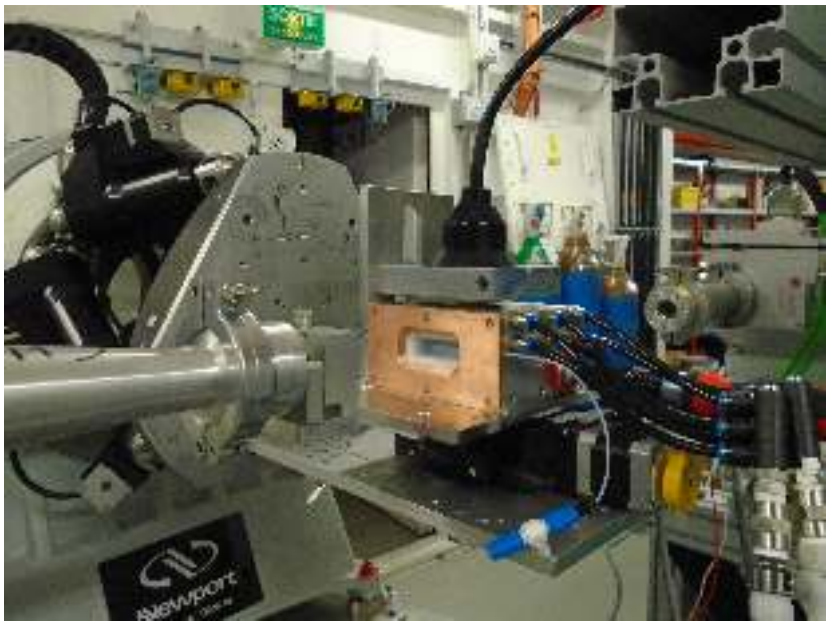

Figure II.2.14 – A heating chamber and illumination set up for the X-Ray reflectometry experiment mounted on the SixS beamline at the SOLEIL synchrotron.

this sample cell was developed for the in-house XRR bench experiments. A smaller cell was required to reduce the path for photons in the bulk water and was therefore designed to host a 2.5x2.5x1 cm^3 block (vs 5x5x1 cm^3 for the "synchrotron" version). In total three cells were manufactured, two of them are equipped with small quartz windows (diameter ≈ 2 cm) and thus the effect of the in-situ illumination on the sample can be tested in-house as well. Typically, a silicon crystal cut and highly polished along (111) plane was used as a solid substrate for this cell. No heating chamber for this sample cell was developed due to the lack of time within this thesis project.

Importance of the sample environment developments

The ability to study SLBs samples using different experimental techniques was often limited by availability of the appropriate sample environment. Easily available sample environment provides the possibility to perform new lab and large scale

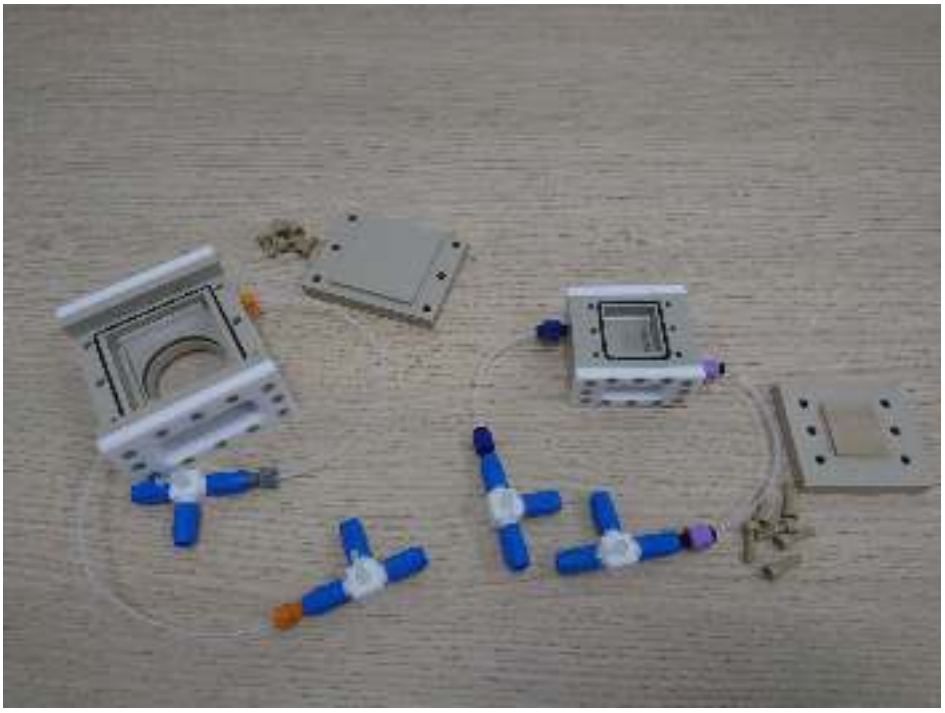

Figure II.2.15 – Developed solid/liquid cells suitable for XRR experiments in-house (smaller cell) and synchrotron (bigger cell) experiments.

structure experiments, which were not possible to carry out before. Developed solid/liquid cells are now available within the SMSS and LSS groups at the ILL, Grenoble, France.

The performance of successful and on time developments of the sample environment were crucial for the success of this work, as no lab and NR and XRR experiments could be performed without the suitable sample cells. Performed lab experiments have provided the complementary and necessary information on the studied systems; they helped to develop and optimise the protocol for the sample preparation and protein reconstitution and gave new insight on sample behaviour. Lab experiments were very helpful and valuable for the preparation and success of large scale facility experiments.

2.5 Neutron and X-ray reflectometry

Reflectometry, of neutrons (NR) and of X-rays (XRR), is a powerful tool which allows to determine the structure and the composition of thin films at interfaces with sub-nanometer resolution, thanks to the short wavelengths of the probe [154].

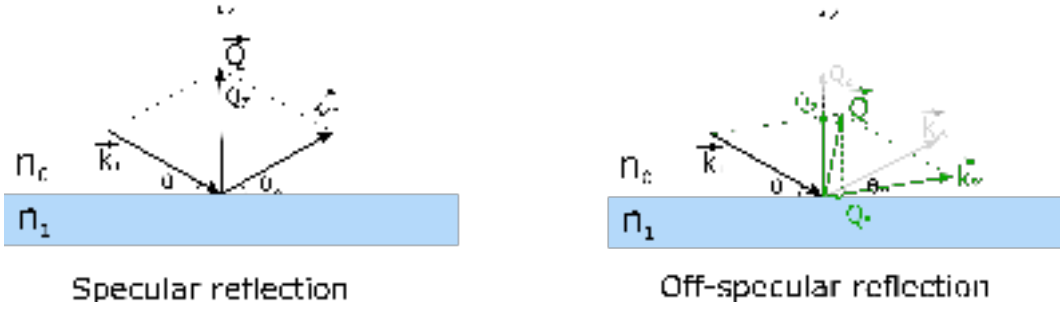

Figure II.2.16 – Schematic representation of specular and off-specular reflection from an ideal interface.

In a reflectometry experiment, a beam of neutrons or X-rays hits the sample at an incident angle θ_{in}. Upon the interaction with the surface of interest, different scattering events might occur: the probe can be scattered (elastically or inelastically) or it can be transmitted (refracted) or even absorbed. The discussion that will follow will consider only elastic scattering events resulting in the reflection of the probes in the plane of incidence and at the same angle as the incident one (specular reflection) or at a different angles (off-specular reflection). The case of refracted beams is of importance for the calculation of the total reflectivity from stratified media. Any other scattering event will be neglected in the discussion.

The momentum transfer vector Q, defined as $Q = k_f - k_i$, describes the change in the wavevector of a probe upon the interaction with the surface. In specular reflectometry the scattering wave vector Q will possess only a z-component in the direction normal to the surface and $Q_z \simeq 2k_i$ (see Fig. II.2.16) and it is defined in the plane of incidence ($Q_y = 0$). In the case of off-specular scattering, the resulting Q-vector is not perpendicular to the sample surface anymore and it has a non null Q_x component. However, it is still defined in the plane of incidence, i.e. the Q_y component is always null. Because of these considerations, from specular reflectometry, the sample structure in the direction perpendicular to the interface of interest can be obtained while, from off-specular measurements also lateral structural features of the sample, such as surface homogeneities, interfacial roughness and fluctuation spectrum, can

be deduced.

2.5.1 Reflection of neutrons and X-ray photons from interfaces

A range of different features makes neutron and X-rays unique and complementary probes for surface sensitive studies. Neutrons interact with atomic nuclei via the strong short-range nuclear forces, while X-rays interact with the electron cloud of atoms. Neutrons can penetrate deeply into the matter and travel large distances through many materials without being massively scattered or absorbed, as they have no charge and their dipole moment is zero [155], therefore they are optimal probes to study buried interfaces. Cold neutrons have wavelengths on the order of interatomic distances, thus the structure of samples at molecular resolution can be resolved, and they are also nondestructive probes, which make them suitable for the study of soft and biological matter.
X-rays are an electromagnetic radiation with wavelengths ranging from ~0.01 to ~1 nm. They are essential probes for the investigation of sample with atomic resolution. Since they interact with the electron clouds, X-ray are strongly scattered and adsorbed by many materials, containing atoms with large atomic number. For this reason the use of high energy X-rays photons is necessary for the study of buried interface. The drawback of this necessity is the so-called "radiation damage", i.e. irreversible changes in the sample induced by the energy brought to the sample by photons.

Thanks to the difference in the sample-probe interaction between neutrons and X-rays, neutron and X-ray reflectometry can be used as complementary techniques, having a different sensitivity for the same atomic species. While neutron beam is available only at large scale facilities, X-rays produced by laboratory sources can be used in addition to synchrotron radiation. The main advantage of the use of synchrotron radiation with respect to the laboratory sources resides in the high photon flux, small beam size and divergence of beams generated at synchrotron facilities.

2.5.2 Reflectivity from an ideal interface: theory

The reflection of neutrons and photons is governed by different physical laws but the mathematical description of the two cases gives similar results. For this reason, in this section, only the treatment of neutron reflection will be given. The description of X-ray reflectivity will be derived in analogy to the neutron case.

In a reflectivity experiment an incident wave of energy E_i and wavelength λ hits the sample and a wave of energy E_f is scattered into a solid angle Ω. In the following section we will describe the reflection events considering only elastic scattering events, thus we assume that no energy transfer between the scattered particles and the sample can occur. In order to derive the reflectivity, scattering events will be described first within the Born approximation. The Born approximation implies that the perturbation of the incident beam due to the scattering from atoms is small (weak interaction of the incident beam and sample) and thus the multiple scattering events can be neglected.

Due to the wave-particle duality neutrons can be described as a wave with the wavelength λ. The Schroedinger equation, which describes the interaction of neutron's wave function $\psi(r)$ with the surface of potential $V(r)$ can be written:

$$\left[-\frac{\hbar^2}{2m}\nabla^2 + V(r)\right]\psi(r) = E\psi(r) \tag{2.9}$$

where $V(r)$ is the probe-sample interaction potential, E is the probe energy and m is the mass of the neutron. The short range interaction is described by the Fermi pseudopotential $V(r)$, which has a form :

$$V(r) = \frac{2\pi\hbar^2}{m} b\delta(r), \tag{2.10}$$

where b is the coherent scattering length. b has a characteristic value for the each atom and, depending on the nuclear spin state, it varies for isotopes of the same atomic species. As it will be described in section 2.9, the spatial resolution achievable in specular reflectometry does not allow to resolve individual atomic positions. In this framework, the discrete probe-sample interaction can be extended to the continuum

as :

$$V(r) = \frac{2\pi\hbar^2}{m}\rho\delta(r) \tag{2.11}$$

where ρ is the nuclear Scattering Length Density (SLD) that can be defined as :

$$\rho = \frac{\sum_j^{N=1} b_j}{V_m} \tag{2.12}$$

where b_j is the coherent scattering length of the $j-th$ nucleus, N is the number of nuclei present in the volume V_m. The expression 2.12 is commonly used to calculate SLD values for molecules and macromolecules since it allows the use of molecular volume information.

For X-ray reflectivity the quantity analogous to the SLD is the elecron density (ED) that can be obtained by simply substituting the number of electron Z_j to the scattering length b_j, leading to:

$$ED = \frac{\sum_j^{N=1} Z_j}{V_m}, \tag{2.13}$$

ED is related to the electron scattering length density (eSLD) via the relation :

$$eSLD = r_{e^-} \times ED, \tag{2.14}$$

where $r_{e^-} = 2.81 \cdot 10^{-15}$ m is a classical radius of an electron.

Contrast variation method

Scattering lengths vary differently for X-rays and neutrons across elements in the periodic table (see Fig. II.2.17). The X-rays scattering length increases linearly with the number of electrons of an atom, while for neutrons it varies "randomly". Moreover, the coherent scattering length for neutrons can have different values for isotopes of the same element [156]. Because of these differences, NR and XRR can be used to obtain complementary information about the sample. In case of neutron reflectometry, isotopic substitution can be exploited to highlight or hide the signal originated from certain regions of the sample, while keeping unaltered its structure [157]. This is a key feature of many neutron scattering techniques and it is known as

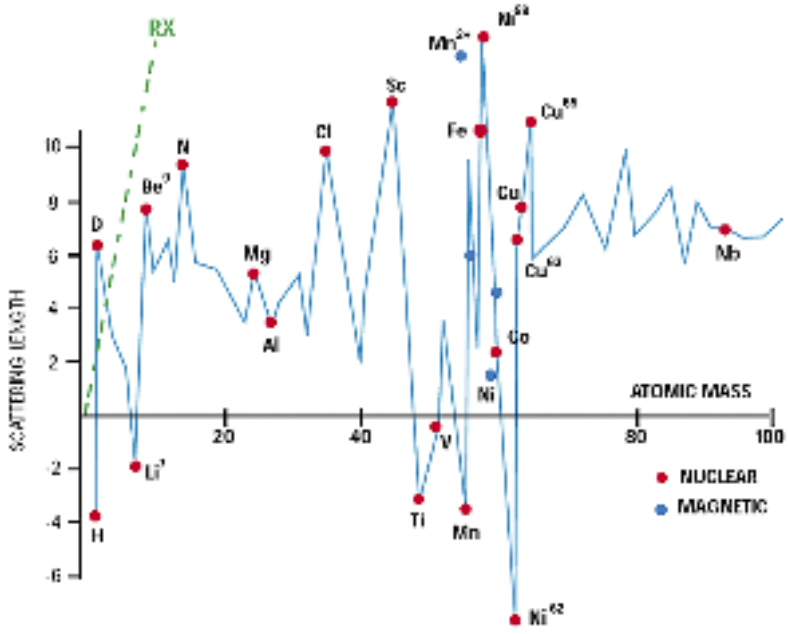

Figure II.2.17 – Nuclear neutron scattering length as a function of isotope (red points). The green dotted line RX is the scattering length for X-rays. Picture is a courtesy of Laboratoire Léon Brillouin [156].

contrast variation. In case of biological samples, one of the most common isotopic substitution involves the replacement of hydrogen atoms by deuterium ones. In practice, ^{1}H (or H) and ^{2}H (or D) have a different scattering power (and oppositely signed scattering lengths): H has a negative scattering length = -0.374 x10^{-15} m and D has a positive scattering length = 0.667 x 10^{-15} m.

Thus, by varying the H and D content in the sample we can tune the strength of neutron-sample interaction. More importantly, by adjusting the H-D ratio in a given region of the sample, compositions that highlight or nullify the signal from given regions can be obtained. The same approach can be used to tune the SLD value of water solutions: by mixing D_2O and H_2O, it is possible to adjust the SLD of the solvent in such a way that it will contrast match either the solid substrate (silicon/quartz/saphire blocks) or a selected part of the sample. The use of contrast variation, together with the co-refinement of XRR and NR data, allows to overcome the problem of the phase loss, typically affecting scattering techniques in reciprocal space.

Refractive index n

Reflectometry is a technique, which is sensitive to spatial changes in the scattering profiles of thin films. Its theoretical description is analogous to that of reflection of visible light. For this reason, a refractive index, n, can be defined for both X-rays and neutrons.

Assuming that a neutron of energy E_1 is approaching an ideal interface located between the media 1 and 2 and it is coming from the medium 1. The probe will experience a potential V_1 defined according to Eq. 2.11, while the medium 2 is characterized by a potential V_2. By definition the potential experienced by a neutron in vacuum is 0. If $V_1 = 0$ and by considering only elastic events at the interface, the conservation of energy implies that:

$$E_1 = E_2 + V_2, \tag{2.15}$$

where $E_1 = (\hbar k_1)^2/2m$ is the kinetic energy of the incoming neutron in the incoming medium 1 and $E_2 = (\hbar k_2)^2/2m$ is the kinetic energy of the neutron in the medium 2. Thus,

$$\frac{(\hbar k_1)^2}{2m} = \frac{(\hbar k_2)^2}{2m} + \frac{2\pi\hbar^2}{m}\rho_2 \tag{2.16}$$

$$\frac{(\hbar k_2)^2}{2m} = \frac{(\hbar k_1)^2}{2m} - \frac{2\pi\hbar^2}{m}\rho_2 \tag{2.17}$$

$$k_2^2 = k_1^2 - 4\pi\rho_2. \tag{2.18}$$

Following the definition used for visible light, the reflective index of the medium 2, can be written as :

$$n^2 \equiv \frac{k_2^2}{k_1^2}, \tag{2.19}$$

$$n^2 = 1 - \frac{4\pi\rho_2}{k_1^2} = 1 - \frac{\rho_2\lambda^2}{\pi}. \tag{2.20}$$

The use of Taylor expansion, since $\rho_2\lambda^2 << 1$, leads to :

$$n \approx 1 - \frac{\rho\lambda^2}{2\pi}. \tag{2.21}$$

Eq. 2.21 is defined for an incoming beam in vacuum. In general, when the medium 1 is a material, Eq. 2.21 can be rewritten as :

$$n \approx 1 - \frac{\Delta\rho\lambda^2}{2\pi}. \tag{2.22}$$

where $\Delta\rho = \rho_2 - \rho_1$ is a quantity called contrast. The derivation of refracting index was done specifically for neutrons. Only the final results (Eq. 2.21 and 2.22) are valid for both neutrons and X-ray, if the value of electron density multiplied by radius of electron r_{e^-} is used instead of SLD value. From Eq. 2.21 it is possible to show that, if coming from vacuum, the probe can be **externally** reflected from most surfaces, since $n < 1$ for the majority of the cases. If $n > 1$ a part of the beam can cross the interface as a refracted beam [158]. Expression 2.21 can be further generalised by taking into the account absorption; in this case the refractive index n becomes :

$$n \approx 1 - \delta - i\beta \tag{2.23}$$

where $\delta = (\lambda^2\Delta\rho) / (2\pi)$ and β is the adsorption coefficient. For organic molecules β is very small for both X-rays and neutrons and it is therefore often neglected.

Snell's law and critical angle θ_c of external reflection

As stated in the previous section, reflection and refraction events for X-ray photons and neutrons can be described classically in analogy with the formalism developed for visible light. Snell's law for an ideal interface between vacuum (n_{vacuum} = 1) and a medium with refractive index n can be written as:

$$\frac{\cos(\theta_{\text{inc}})}{\cos(\theta_{\text{tr}})} = n \tag{2.24}$$

where θ_{tr} is the angle of the transmitted (refracted) wave. The condition for the total external reflection ($\theta_{\text{tr}} = 0$) is satisfied when $\theta_{\text{inc}} \leq \theta_{\text{cr}}$, where θ_{cr} is a critical angle of the total reflection:

$$\cos(\theta_{\text{cr}}) = n \tag{2.25}$$

n is defined by Eq. 2.21 and using the expression :

$$\cos(\theta_{cr})^2 = 1 - \sin(\theta_{cr})^2, \tag{2.26}$$

we can derive

$$\sin(\theta_{cr}) \approx \theta_{cr} = \sqrt{\frac{\rho}{\pi}}\lambda \tag{2.27}$$

$$\Rightarrow \quad Q_{cr} = \frac{4\pi}{\lambda}\sin(\theta_{cr}) = 4\sqrt{\pi\Delta\rho}. \tag{2.28}$$

Thus, total external reflection occurs for incident angles satisfying the condition $\theta_{inc} \leq \theta_{cr}$ for a given wavelength λ (monochromatic beam). In time-of-flight measurements, when a polychromatic beam characterized by a wavelength spread $\delta\lambda$ is used, total reflection can occur when $\frac{4\pi}{\Delta\lambda}\sin(\theta_{cr}) \leq 4\sqrt{\pi\Delta\rho}$. Experimentally, by performing measurements of the position of θ_{cr} (corresponding to a critical wave vector Q_{cr}), the value of $\Delta\rho$ can be calculated [159].

Reflection from a perfectly smooth surface. Fresnel's Law

Based on Eq. 2.19, the reflectance r and transmittance t (amplitudes of the reflected and transmitted waves) can be expressed as :

$$r = \frac{k_{iz} - k_{tz}}{k_{iz} + k_{tz}} \tag{2.29}$$

and

$$t = \frac{2k_{iz}}{k_{iz} + k_{tz}}. \tag{2.30}$$

Reflectivity is defined as $R = rr^*$, and the transmissivity is defined as $T = tt^*$.

$$R = |r|^2 = \left(\frac{Q - (Q^2 - Q_{cr}^2)^{1/2}}{Q + (Q^2 - Q_{cr}^2)^{1/2}}\right)^2 \tag{2.31}$$

$$T = |t|^2 = \left(\frac{2Q}{Q + (Q^2 - Q_{cr}^2)^{1/2}}\right)^2 \tag{2.32}$$

Thus, Eq. 2.31 and 2.32 are the Fresnel equations for the reflectivity and transmittivity at an ideal interface, where Q is a wave vector and Q_{cr} is a wave vector

below which the total reflection occurs.

Since reflectivity is defined as the modulus of complex quantity, the phase information of the reflected wave is lost. Thus, an approach has to be developed to recover this information during the data analysis (see section 2.9).

For the $Q \gg Q_{cr}$ under the kinematic Born approximation (the probe-sample interaction is weak, multiple scattering events are ignored and incident neutrons wave is treated as a plane wave), the expression 2.31 can be simplified as :

$$R_F(Q) \approx \frac{16\pi^2}{Q^4}\rho^2 \tag{2.33}$$

and $R_F(Q)$ is the Fresnel reflectivity for the ideal interface. An important implication for the experiments from expression 2.33 is that $Q \gg Q_c$, the reflectivity decreases as Q^4.

Reflection from one layer (two interfaces)

To add further complexity to the system described above, we can consider the case of a thin layer of the thickness t. This system is characterised by two interfaces, thus multiple events of reflection and transmission have to be taken into account in the calculation of the total reflectivity.

The Fresnel's reflection coefficient can be written as :

$$r = \frac{r_{01} + r_{12}e^{2ik_{1z}t}}{1 + r_{01}r_{12}e^{2ik_{1z}t}} \tag{2.34}$$

where $r_{j,j+1}$ is the Fresnel reflection coefficient for the $j-th$ interface. Thus, according to the definition, reflectivity from a single layer is given by:

$$R = r^2 = \frac{r_{01}^2 + r_{12}^2 + 2r_{01}r_{12}cos2k_{1z}t}{1 + r_{01}^2r_{12}^2 + 2r_{01}r_{12}cos2k_{1z}t} \tag{2.35}$$

This description can extended to the case of a series of layers. The $r_{j,j+1}$ and $t_{j,j+1}$ coefficients can be derived from the boundary conditions for the wavefunction at any interface, being the reflection coefficient $r_{j,j+1}$ for an interface between two adjacent layers

$$r_{j,j+1} = \frac{r_{01} + r_{12}e^{2ik_{1z}t}}{1 + r_{01}r_{12}e^{2ik_{1z}t}} \tag{2.36}$$

For N layers, the number of interfaces is N+1; 2(N+2) is the total number of $r_{j,j+1}$ and $t_{j,j+1}$ coefficients to be calculated and 2(N+1) the number of equations to be solved [158]. For such a system, an approximation of the total reflectivity, under the Born approximation, is given by

$$R(Q) = \frac{16\pi^2}{Q^4}\left|\int \frac{\delta\rho(z)}{\delta z} e^{iQz} \mathrm{d}z\right|^2 \tag{2.37}$$

where a central role is played by the changes in SLD (or eSLD) along the vertical direction with respect to the sample surface. However, this approximation holds only for $Q \gg Q_{cr}$.

The exact calculation of the reflectivity from a multilayer system can be performed iteratively as described by Parratt [160] or as described by Abéles [161]. The second method consists in the use of a characteristic matrix M_j, which contains the reflection and the transmission coefficients for each j_{th} layer:

$$M_j = \begin{bmatrix} \cos(k_j t_j) & (-i/k_j)\sin(k_j t_j) \\ (-ik_j)\sin(k_j t_j) & \cos(k_j t_j) \end{bmatrix} \tag{2.38}$$

where k_j is the wave vector in the j_{th} layer in the perpendicular direction to the substrate.

For the sample consisting of N layers the total amplitude of the reflected wave can be written as a product of N matrices:

$$M = [M_1][M_2][M_3]...[M_N] = \prod_{j=1}^{N} M_j = \begin{bmatrix} M_{11} & M_{12} \\ M_{21} & M_{22} \end{bmatrix} \tag{2.39}$$

and the reflectivity can be defined as :

$$R = \left[\frac{(M_{11} + M_{12}k_{N+1})k_0 - (M_{21} + M_{22})k_{N+1}}{(M_{11} + M_{12}k_{N+1})k_0 + (M_{21} + M_{22})k_{N+1}}\right]^2. \tag{2.40}$$

Roughness and inter-diffusion effects

Up to now we have considered ideal (perfectly flat) interfaces. In a real sample interfaces can be rough or characterized by inter-diffusion (smooth transition between two neighbor layers). Roughness and inter-diffusion phenomena cannot be distinguished during the specular reflectivity measurement, as they produce the same features in the measured reflectivity. These effects are in fact taken into account by multiplying $R(Q)$ by a gaussian function characterised by a width σ :

$$R(Q) = R_F(Q)e^{-Q^2\sigma^2}. \tag{2.41}$$

In the direct space, Eq. 2.41 implies that changes in level of SLD at one interface are described by an error function $erf(\frac{z}{\sqrt{(\sigma)}})$ and not by a step function as in the ideal case.

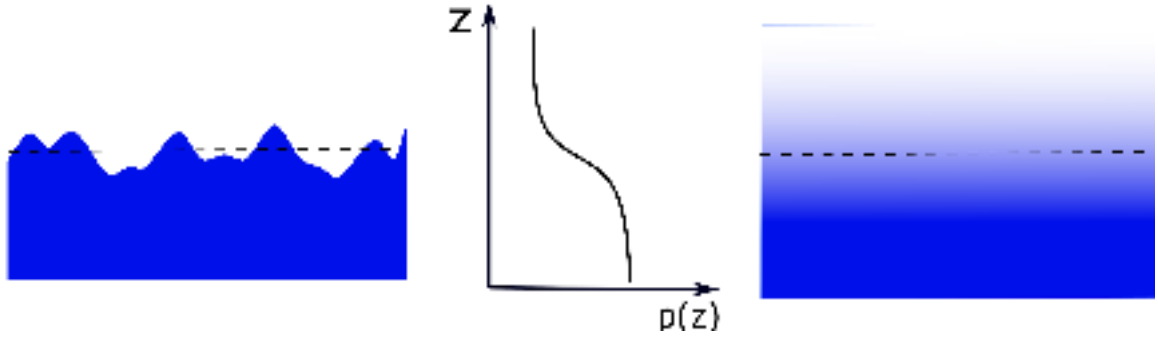

Figure II.2.18 – Schematic representation of roughness and inter-diffusion. The SLD profile obtained form the fit of the specular reflectivity data is the same for the two cases.

2.5.3 Off-specular synchrotron radiation X-ray reflectivity

So far, only the scattering events resulting in a beam reflected in the plane of incidence and at the same angle as the incident one (specular case) have been described. Off-specular reflectivity describes scattering events resulting in reflections in the plane of incidence, but at different angles than the incident one.

In the Born approximation the differential cross section is defined as the scattered intensity E_f per unit solid angle Ω in the direction of the scattered beam k_f divided by the incident intensity E_i in the k_i direction per unit surface area $r^2 d\Omega$ and it can be written in a form:

$$\frac{d\sigma}{d\Omega} = r_e^2 \left| \int \mathrm{d}\mathbf{r} e^{i\mathbf{Q}\cdot\mathbf{r}} \rho(\mathbf{r}) \right|^2 . \tag{2.42}$$

Intensity $I(q)$, measured at a distance $\mathbf{r}$ within an elementary surface area $r^2 \mathrm{d}\Omega$, is proportional to the differential cross section $\frac{\mathrm{d}\sigma}{\mathrm{d}\Omega}$ and it is defined as :

$$I = \int_\Omega \mathrm{d}\Omega \left(\frac{\mathrm{d}\sigma}{\mathrm{d}\Omega}(Q) \right). \tag{2.43}$$

The description of specular reflectivity was given within the framework of the Born approximation ($Q \geq Q_{cr}$). In the $Q \simeq Q_{cr}$, Born approximation is not longer valid, because multiple scattering events cannot be neglected [162]. Thus, another more precise approach called Distorted Wave Born Approximation (DWBA) should be used to describe the system. DWBA is a perturbative approach: reflected and

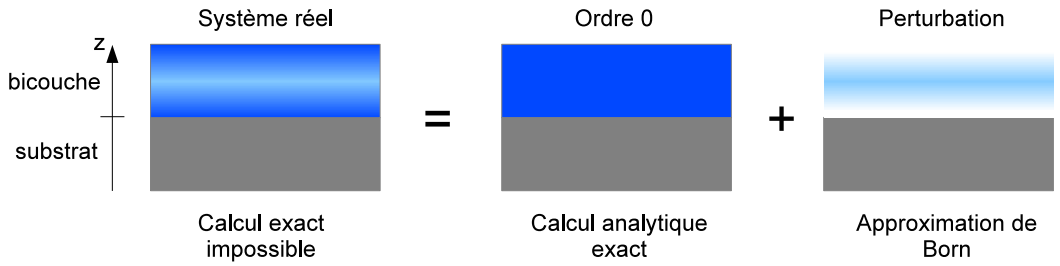

Figure II.2.19 – Schematic representation of the DWBA approximation [35]

transmitted intensities are calculated exactly for an ideal non-perturbed system. Variations between the real and ideal systems are treated as a perturbation. Thus, in

the DWBA approximation, reflectivity can be written as [163] :

$$R(Q) = R_F(Q)\left|1 + iQ\int \frac{\delta\rho(z)}{\delta\rho_{Si}} e^{iQz} dz\right|^2 . \tag{2.44}$$

Similarly, the differential cross-section can be decomposed into two parts [164] :

$$\begin{aligned}\frac{d\sigma}{d\Omega} &= \left(\frac{d\sigma}{d\Omega}\right)_{\text{ref}} + \left(\frac{d\sigma}{d\Omega}\right)_{\text{pert}} \\ &= \left(\frac{d\sigma}{d\Omega}\right)_{\text{ref}} + r_e^2 |t^{in}|^2 |t^{sc}|^2 (\mathbf{e}_{in}\cdot\mathbf{e}_{sc})^2 \left\langle \left| \int d\mathbf{r} e^{i\mathbf{Q}\cdot\mathbf{r}} \delta\rho(\mathbf{r}) \right|^2 \right\rangle ,\end{aligned} \tag{2.45}$$

where $(\mathbf{e}_{in}\cdot\mathbf{e}_{sc})^2 \sim 1$ defines the change in polarization between the incident and scattered wave. $|t^{in}|^2$ and $|t^{sc}|^2$ are the transmission coefficients for the interface (t^{in} is a good approximation of the incident wave scattered by the interface and t^{sc} describes how the wave propagates to the detector).

The differential cross section $(d\sigma/d\Omega)_{\text{ref}}$ is specular reflectivity from a perfectly flat (ideal) interface. The perturbed part $(d\sigma/d\Omega)_{\text{pert}}$ describes the contribution to the measured signal due to the presence of a thin film and interfacial roughness.

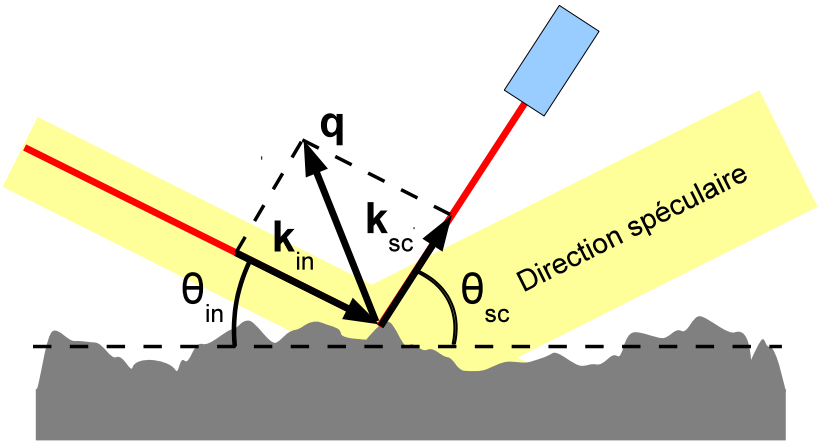

Figure II.2.20 – Illustration of the off-specular scattering due to the roughness of the substrate, k_{in} and k_{sc} are incident and diffuse wavevectors, q is the wave vector transfered [35].

In the case of single or double solid-supported lipid bilayers, main samples described in this work, the scattering cross section can be calculated as a perturbation

of the electron density of the ideal water silicon interface due to substrate roughness and presence of membranes (see Fig. II.2.19). The total electron density can be decomposed in three terms: $\delta\rho_{\text{sub}}$, $\delta\rho_{\text{M}_1}$ and $\delta\rho_{\text{M}_2}$ ($\delta\rho_{\text{M}_2} = 0$ for the case of a single lipid bilayer). Thus the perturbation term can be written as:

$$\delta\rho(z) = \delta\rho_{\text{sub}}(z - z_s) + \delta\rho_{\text{M}_1}(z - z_{1,th} - z_{1,st}) + \delta\rho_{\text{M}_2}(z - z_{2,th} - z_{2,st}). \tag{2.46}$$

Thus we can obtain the expression of the perturbation part of the differential cross section [165–167] :

$$\left(\frac{d\sigma}{d\Omega}\right)_{\text{pert}} = \mathcal{A} r_e^2 |t^{in}|^2 |t^{sc}|^2 (\mathbf{e}_{in} \cdot \mathbf{e}_{sc})^2 \left[g(Q)(2\pi)^2 \delta\left(\mathbf{Q}_{\parallel}\right) + \int d\mathbf{r}_{\parallel} e^{i\mathbf{Q}_{\parallel}\mathbf{r}_{\parallel}} f(\mathbf{r}_{\parallel}, Q) \right], \tag{2.47}$$

where $\mathcal{A}$ is the area of the sample illuminated by the beam (of the order of μm^2). The function $g(Q)$ describes the specular part of the perturbation. Eq. 2.44 returns directly the total reflectivity and not only to its perturbed part, which allows faster calculations during the data analysis. The functions $f(\mathbf{r}_{\parallel}, Q)$ have a form:

$$\begin{aligned}
f(\mathbf{r}_{\parallel}, Q) =& \left|\tilde{\delta\rho}_{\text{sub}}(Q)\right|^2 e^{-Q^2\sigma_s^2} \left(e^{Q^2\langle z_s(\mathbf{r}_{\parallel}) z_s(0)\rangle} - 1\right) \\
&+ \left|\tilde{\delta\rho}_{\text{M1}}(Q)\right|^2 e^{-Q^2\left(\sigma_{1,th}^2 + \sigma_{1,st}^2\right)} \left(e^{Q^2\langle z_{1,th}(\mathbf{r}_{\parallel}) z_{1,th}(0)\rangle} e^{Q^2\langle z_{1,st}(\mathbf{r}_{\parallel}) z_{1,st}(0)\rangle} - 1\right) \\
&+ \left|\tilde{\delta\rho}_{\text{M2}}(Q)\right|^2 e^{-Q^2\left(\sigma_{2,th}^2 + \sigma_{2,st}^2\right)} \left(e^{Q^2\langle z_{2,th}(\mathbf{r}_{\parallel}) z_{2,th}(0)\rangle} e^{Q^2\langle z_{2,st}(\mathbf{r}_{\parallel}) z_{2,st}(0)\rangle} - 1\right) \\
&+ \left(\tilde{\delta\rho}_{\text{M1}}^*(Q)\, \tilde{\delta\rho}_{\text{M2}}(Q) + \tilde{\delta\rho}_{\text{M1}}(Q)\, \tilde{\delta\rho}_{\text{M2}}^*(Q)\right) e^{-\frac{1}{2}Q^2\left(\sigma_{1,th}^2 + \sigma_{1,st}^2 + \sigma_{2,th}^2 + \sigma_{2,st}^2\right)} \\
&\times \left(e^{Q^2\langle z_{1,th}(\mathbf{r}_{\parallel}) z_{2,th}(0)\rangle} e^{Q^2\langle z_{1,st}(\mathbf{r}_{\parallel}) z_{2,st}(0)\rangle} - 1\right) \\
&+ \left(\tilde{\delta\rho}_{\text{M1}}^*(Q)\, \tilde{\delta\rho}_{\text{sub}}(Q) + \tilde{\delta\rho}_{\text{M1}}(Q)\, \tilde{\delta\rho}_{\text{sub}}^*(Q)\right) e^{-\frac{1}{2}Q^2\left(\sigma_{1,th}^2 + \sigma_{1,st}^2 + \sigma_s^2\right)} \left(e^{Q^2\langle z_{1,st}(\mathbf{r}_{\parallel}) z_s(0)\rangle} - 1\right) \\
&+ \left(\tilde{\delta\rho}_{\text{M2}}^*(Q)\, \tilde{\delta\rho}_{\text{sub}}(Q) + \tilde{\delta\rho}_{\text{M2}}(Q)\, \tilde{\delta\rho}_{\text{sub}}^*(Q)\right) e^{-\frac{1}{2}Q^2\left(\sigma_{2,th}^2 + \sigma_{2,st}^2 + \sigma_s^2\right)} \left(e^{Q^2\langle z_{2,st}(\mathbf{r}_{\parallel}) z_s(0)\rangle} - 1\right).
\end{aligned} \tag{2.48}$$

F is the Fourier transform, which takes as arguments electron density, interface roughness and height correlation functions $\left\langle z_i(\mathbf{r}_{\parallel}) z_j(0)\right\rangle$. In Eq. 2.48 i and j denote the first membrane, the second or the substrate. The details of the calculations can be found in [35, 165, 166].

Detector resolution and measured intensity

In contrast to the case of the specular reflectivity, the measured off-specular intensity is proportional to the resolution of the detector, thus one should take into account the dimensions of the beam and its divergence. To calculate the intensity measured by detector at the angle θ_{sc} , the differential cross section has to be integrated over all incident and scattered angles:

$$I = \frac{I_0}{h_i w_i} \int \left[\left(\frac{\mathrm{d}\sigma}{\mathrm{d}\Omega} \right)_{\mathrm{ref}} + \left(\frac{\mathrm{d}\sigma}{\mathrm{d}\Omega} \right)_{\mathrm{spec}} + \left(\frac{\mathrm{d}\sigma}{\mathrm{d}\Omega} \right)_{\mathrm{off-spec}} \right] \mathcal{R}es\,(\Omega)\,\mathrm{d}\Omega, \tag{2.49}$$

where h_i and w_i are width and height of the slits placed after the sample, $I_0/h_i w_i$ is an incident flux. $\mathcal{R}es\,(\Omega) \equiv \mathcal{R}es\,(\theta_{sc}, \psi)$ is the resolution of the detector as a function of

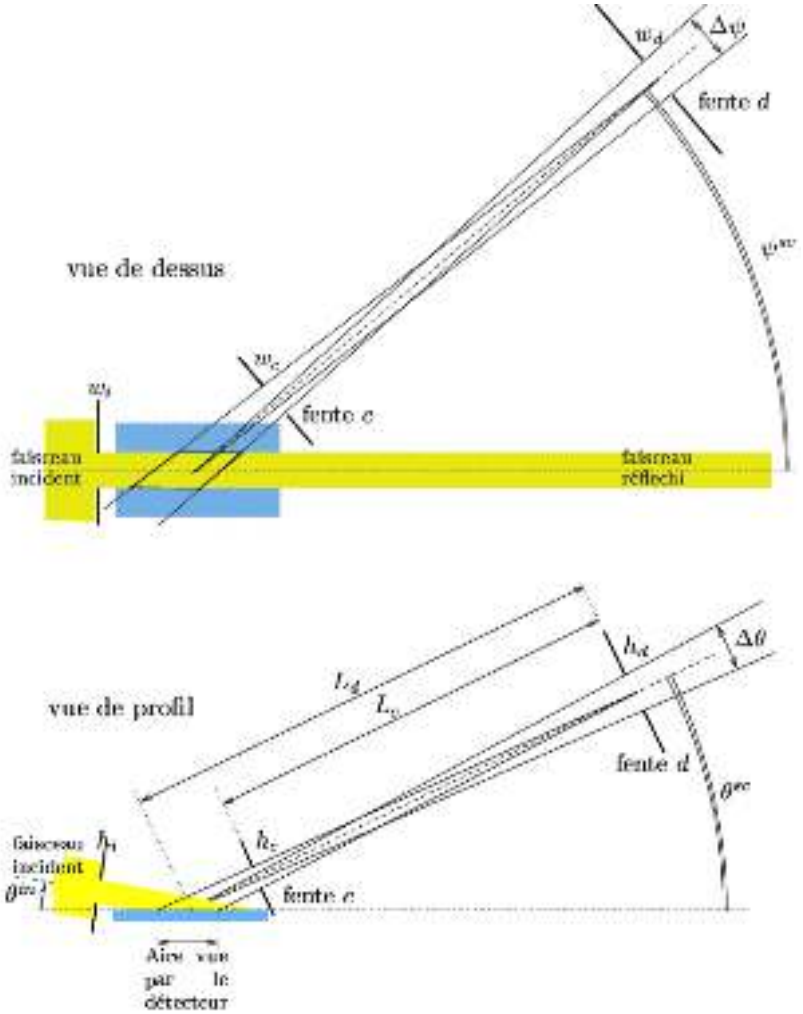

Figure II.2.21 – Experimental setup of the BM32 beamline and definition of parameters used to calculate the resulting intensity [167].

the slit width $\Delta\theta$ in the plane of incidence and $\Delta\psi$ in the transverse plane. If (θ_{sc}, ψ) lays in the direction to the detector, then $\mathcal{R}es\,(\theta_{sc}, \psi) = 1$, if not, $\mathcal{R}es\,(\theta_{sc}, \psi) = 0$. $\Delta\theta$ and $\Delta\psi$ are the dimensions of the slit d (Fig. II.2.21), which is placed before the detector in such way that the beam divergence is equal to $\delta\theta$:

$$\begin{cases} \Delta\theta = h_d/L_d + \delta\theta \\ \Delta\psi = w_d/L_d. \end{cases} \tag{2.50}$$

For off-specular experiments, the slits are widely opened, the resolution of the measurements does not depend on the Q_y : $\tilde{\mathcal{R}es}\left(\mathbf{Q}_{\|}\right) = \tilde{\mathcal{R}es}\,(Q_x)$.

For the case of the diffuse scattering measurements, when $\theta_{sc} \neq \theta_{in}$, Eq. 2.49 can be rewritten in such a way:

$$I_{\text{off-spec}}\left(\mathbf{Q}_{\|}\right) = \frac{I_0}{h_i w_i k_0^2 \sin\theta_{sc}} \int \left(\frac{\mathrm{d}\sigma}{\mathrm{d}\Omega}\right)_{\text{off-spec}} \tilde{\mathcal{R}es}\,(Q_x)\,\mathrm{d}Q_x \mathrm{d}Q_y. \tag{2.51}$$

2.6 Membrane Fluctuations

The main aim of this thesis was to study out-of-equilibrium fluctuations caused by protein activity in floating phospholipid bilayers by performing X-ray specular and off-specular scattering experiments. In fact, they can provide direct information about the membranes fluctuation spectrum in a wide, sub-micron, length scale and therefore they are optimal techniques to characterize membrane properties, such as bending rigidity, membrane tension and interaction potential. The combination of these two techniques can provide a unique opportunity to directly compare experimental data to theoretical predictions and to achieve a better understanding of active fluctuations mechanism at play.

Free standing lipid bilayers near a substrate passively fluctuate around their mean equilibrium shape due to Brownian motion and constantly exist in thermodynamic equilibrium. The only noise source in such passively fluctuating systems is thermal noise, which is uncorrelated in time and space and satisfies the fluctuation-dissipation theorem [18, 19]. Thermally driven membrane fluctuation behaviour has been studied extensively theoretically [13–15, 168] and experimentally [16, 18–

20, 169, 170], originating from the pioneering work of Helfrich on the elasticity theory of lipid bilayers [171]. In this framework, membrane fluctuations can be described by the Helfrich Hamiltonian, the membrane is modeled using a Monge representation as a geometrical plane surface, thus all molecular details of the membrane structure are neglected. The elastic energy of the membrane can be described within

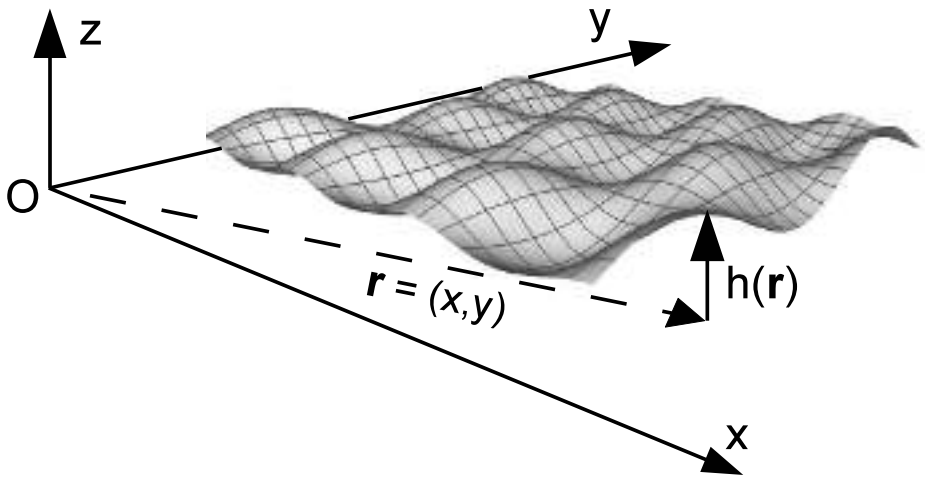

Figure II.2.22 – Monge representation of the membrane [35].

the classic harmonic approximation [171] and depends on the surface tension and the bending modulus of fluid membranes and on its interaction potential with the surrounding environment. Thus, the Helfrich Hamiltonian can be written as:

$$H[z(r)] = \int \mathrm{d}^2 r[\frac{1}{2}\kappa(\Delta z)^2 + \gamma(\nabla z)^2 + U''(z)] \tag{2.52}$$

Applying the equipartition theorem, the thermal fluctuation spectrum can be written as:

$$\langle z(Q_{\|})^2 \rangle = \frac{\kappa_B T}{U''(z) + \gamma Q_{\|}^2 + \kappa Q_{\|}^4} \tag{2.53}$$

where U''(z) is the second derivative of the interaction potential, γ is the surface tension, and κ is the bending modulus of a lipid bilayer.

The Fourier transform of Eq. 2.53, the height-height correlation function in real space, which defines the thermal fluctuation spectrum, can be obtained. The exact calculation of height-height correlation functions (auto correlation functions of each membrane and cross correlation functions of membrane/substrate, between

two bilayers, between first bilayer and substrate, floating bilayer and substrate) for the case of a double bilayer system can be found in [35, 165, 166].

The parameters γ, κ and U describe the main contribution to the lipid bilayer elastic behavior and thus define the membrane fluctuation spectrum at different length-scales. Different regimes can be defined depending on the values of the discriminant $\delta = \gamma^2 - 4U''\kappa$ [164]:

- for $\delta > 0$ and for the wavelength range corresponding to $Q < \sqrt{U''}/\gamma$, the membrane fluctuations are dominated by the interaction potential with the near surface or neighboring membrane.
- At the intermediate length scale $Q > (\gamma/\kappa)^{1/4}$, the membrane fluctuations are dominated by the membrane tension.
- For $\delta < 0$ the membrane fluctuations are stabilized by the bending rigidity κ.

The cross-over between these three regimes occurs at sub-micron length scales, thus it is not accessible through optical microscopy measurements, which can provide information on the fluctuation spectrum only at the micrometer scale. It was shown by Daillant *et al.* [164] that the developed X-ray off-specular surface scattering technique [166] can allow to study the fluctuations of a floating bilayer near a substrate [172], as well as membrane-membrane interactions [173–175].

2.7 Reflectivity Measurements and Instrumentation

During reflectometry experiments, a very well collimated neutron or X-ray beam of defined wavelength λ and intensity I_0 strikes the surface at an incident angle θ_{in}. Upon the interaction with the sample, the beam is reflected at an angle θ_{sc}. The intensity of the reflected beam I is measured as a function of the scattering angle. Reflectivity is defined as the ratio of the intensity of the reflected beam over the intensity of the incoming beam. When $\theta_{in} = \theta_{sc}$, the reflectivity is named specular, while when $\theta_{in} \neq \theta_{sc}$ reflectivity is called off-specular. In particular, specular reflectivity $R(Q_z)$ is measured as a function of wave vector Q_z, which is perpendicular to the sample surface:

$$Q_z = \frac{4\pi}{\lambda} \sin(\theta_{in}). \tag{2.54}$$

Being the wavevector defined as reciprocal distance, to obtain information at different length scales, measurements should be performed on the largest Q_z-range possible. This range can be covered by either changing the incident angle of the beam, while keeping the wavelength constant (monochromatic measurements, typically for X-rays and synchrotron radiation) or by using a distribution of wavelengths (Time-of-flight (TOF) measurements, often used on neutron instruments). In TOF mode, the incident angle can be varied as well, leading to a wider Q_z-range covered. If the neutron flux from the source is low, monochromatic beam can be obtained by means of a mechanical velocity selector that allows for a larger tolerance on the definition of the wavelength. By allowing the passage of more than one wavelength (although the pulse remains very limited in terms of wavelength spread), the incident flux can be improved, while the resolution is worsened.

In reflection geometry, incident and reflected beams crosses the part of the sample that is defined as "incident medium". This has to be as much transparent as possible for the chosen probe. The systems investigated in this thesis were deposited, in most of the cases, at the silicon/liquid interface. Additionally, quartz and sapphire substrates were used for NR experiments. In NR experiments the beam strikes the sample passing through the solid substrate, since the transmittance of several centimeters of water (either D_2O or H_2O) is rather low. On the contrary these

types of substrates have a very high transmission for cold and thermal neutrons. In the case of measurements performed using synchrotron radiation and in-house X-ray instruments, the beam was hitting the sample passing through the liquid environment (Fig. II.2.23) , which is more transparent for X-rays than the substrates used.

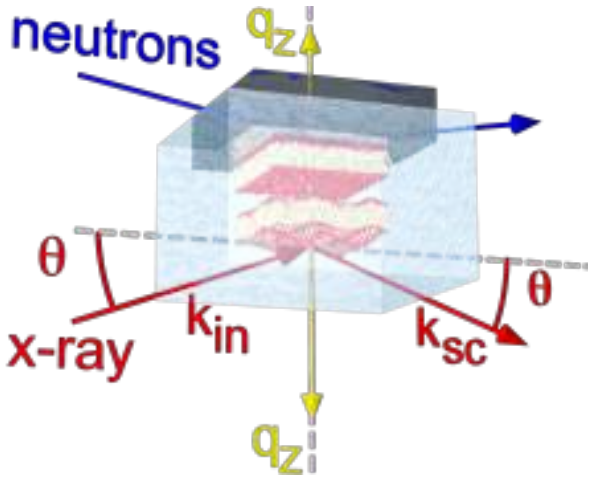

Figure II.2.23 – Schematic representation of X-ray and neutron beam approaching the sample.

Because of these constraints, samples for NR and XRR were enclosed in solid/liquid cells developed ad-hoc for different techniques (see section 2.4 for the development carried out during this PhD project). In addition, standard solid/liquid cells available at the ILL were routinely used for NR experiments (also for those performed at other neutron sources). This cell (see Fig. II.2.24) consisted of two parts: a water reservoir made of PEEK and a counter plate made of PTFE and aluminum. Highly polished silicon (or quartz, or sapphire) blocks of size of 5×8×1.5 cm^3 were sandwiched and tightly sealed between the two parts of the cell. The water reservoir was equipped with inlet and outlet connections, which allow to perform solutions injections and/or solvent exchange. The cell was thermalized by means of water circulation and could be mounted on the different instruments either in horizontal or vertical geometry.

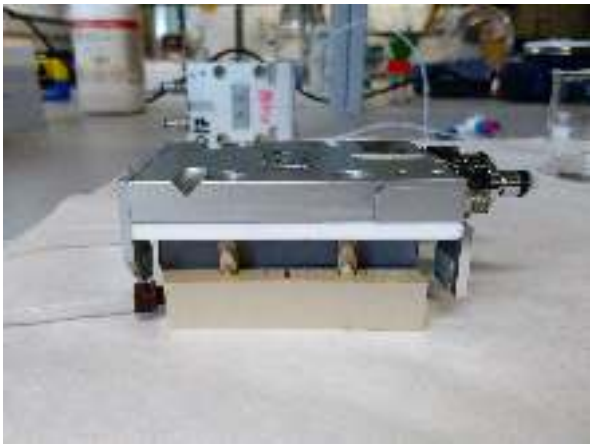

Figure II.2.24 – Solid/liquid cell used for the neutron reflectivity measurements.

2.7.1 Neutron reflectometers used within this project

NR experiments were performed on the FIGARO [176] and D17 [177] reflectometers at the ILL (Grenoble, France) and MARIA reflectometer at the MLZ (Garching, Germany) [178].

Figaro (Fluid Interfaces Grazing Angles ReflectOmeter) (Fig. II.2.25) is a neutron reflectometer with vertical scattering geometry, where reflection up or reflection down geometries are possible. Reflectivity measurements on Figaro were performed in TOF mode, using a wavelength spread from 2 to 20 Å. Such a polychromatic beam was defined by a set of choppers, which are synchronized in time. For the same wavelength spread, two different angular configurations were used (0.8° and 3.2°), allowing to cover the Q_z-range from 0.005 to 0.3 $Å^{-1}$ (see Eq. 2.54).

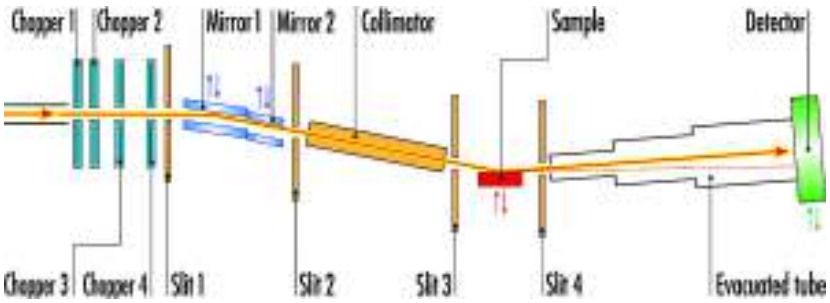

Figure II.2.25 – Layout of the FIGARO reflectometer at the ILL, Grenoble, France [179].

D17 (Fig. II.2.26) is a neutron reflectometer with horizontal scattering geometry. As for FIGARO, reflectivity measurements on D17 were performed in TOF mode, using wavelengths range from 2 to 30 Å. Two different angular configurations were

used (0.8° and 3.2°), allowing to cover the Q_z-range from 0.005 to 0.3 $Å^{-1}$ (see Eq. 2.54).

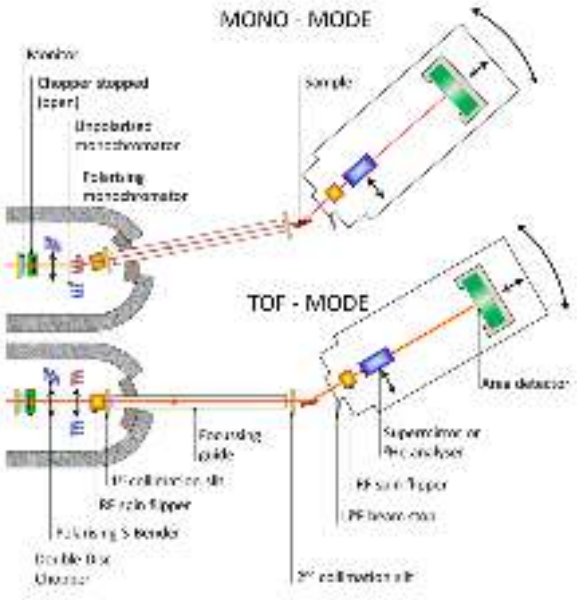

Figure II.2.26 – D17 reflectometer layout at monochromatic and time-of-flight modes at the ILL, Grenoble, France [179].

For both FIGARO and D17, the incoming neutron beam was configured to have low divergence (almost parallel beam) by using a pair of slits positioned before the sample. Slit openings were adjusted for each angular configuration used, in such a way approximately the 70 % of the sample surface was illuminated by the neutron beam.

MARIA (Magnetic reflectometer with high incident angle) (Fig. II.2.27) is a neutron reflectometer with horizontal scattering geometry. MARIA was used in monochromatic mode and the wavelength of the incoming beam was defined by means of a velocity selector and the reflectivity curve was collected point by point, while varying the incident and detector angles in a $\theta - 2\theta$ configuration from 0.4° to 4.5°. To optimise the measurements, two wavelengths, namely 5 Å and 10 Å, were used. This allowed to cover a Q_z range from 0.009 to 0.2 $Å^{-1}$.

Since the sample angle was changed continuously, the slits opening was adjusted for every angle in order to have a beam footprint illuminating a constant surface of the sample.

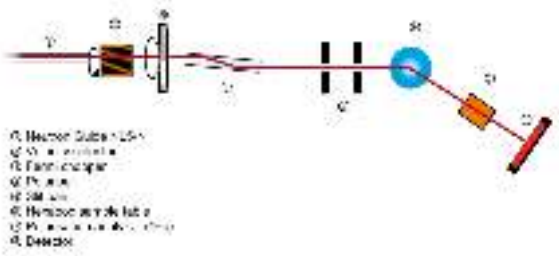

Figure II.2.27 – MARIA reflectometer layout, MLZ, Garching, Germany [180].

Instrumental resolution

In NR experiments, the resolution is defined by the 1) optical divergence of the beam, which takes into account detector resolution in θ and divergence of the incoming beam; 2) precision of the instrument alignment, which is usually highly precise and has therefore no effect on resolution; 3) the wavelength spread of the beam.

For the monochromatic measurements, the resolution is defined by the angular $\delta(\theta)$ and wavelength $\delta(\lambda)$ divergences of the beam [154]. Therefore Q-resolution is defined by the relation:

$$\left(\frac{\delta Q}{Q}\right)^2 = \left(\frac{\delta\theta}{\theta}\right)^2 + \left(\frac{\delta\lambda}{\lambda}\right)^2. \tag{2.55}$$

For highly monochromatic beams (obtained by using a crystal monochromator), the resolution is dominated by the $\delta(\theta)$ term. For monochromatic beams obtained by using a velocity selector, the resolution is lower and dominated by the $\delta(\lambda)$ term.

For the TOF measurements the resolution is defined by the angular divergence $\delta\theta$ of the beam and the pulse width δt :

$$\left(\frac{\delta Q}{Q}\right)^2 = \left(\frac{\delta\theta}{\theta}\right)^2 + \left(\frac{\delta t}{t}\right)^2 \tag{2.56}$$

where t is the time-of-flight of neutrons. The instruments used during this project were operated at the following resolution (expressed in $\delta\lambda/\lambda$): 7% on FIGARO, 3-11%[1] on D17 and 10% on MARIA.

[1]The instrumental resolution on D17, for the configurations used in this project, increases from ~ 3% to ~ 11% going from low- to high-Q values.

2.7.2 Data reduction procedures

In order to convert raw detector images in reflectivity curves, a series of well established procedures have to be applied. Treatment of the data collected at the ILL (in TOF mode) was performed using the program COSMOS from the software LAMP (Large Array Manipulation Program) [181]. The data collected on the MARIA reflectometer was treated with the in-house-developed software.

TOF data were collected using a bi-dimensional position sensitive detector. The specular peak was integrated along constant λ cuts in order to obtain the total reflected intensity $I_{meas}(\lambda, \theta)$, for a given wavelength, in the specular direction. For each of these cuts, the background (originated from the environment and sample itself) to be subtracted was calculated by evaluating the average number of counts from detector pixel close to the specular line. The integrated and background subtracted intensity was then normalised by the intensity of the incident beam measured through the solid substrate. This allowed not only to define the reflectivity as $R(\lambda, \theta) = \frac{I_{meas}(\lambda,\theta)-bkg}{I_{DB}(\lambda,\theta)}$ but also to take into account the beam attenuation due to the passage through the sample support and environment. A direct beam measurement ($I_{DB}(\lambda, \theta)$) was collected for every angular configuration. If the use of an attenuator was necessary, the direct beam intensity was multiplied by the attenuator factor. As last step, $R(\lambda, \theta)$ was converted to $R(Q_z)$ by using the Eq. 2.54.

For monochromatic measurements, the data reduction procedure is the same with the only difference that a detector image contains information only about a given $I_{meas}(\lambda, \theta)$ and not about the entire spectrum of wavelengths used.

2.7.3 Synchrotron beamlines and the X-ray reflectometer

While X-ray specular reflectometry measurements can be performed by using laboratory equipments (provided that they are equipped with high-energy X-ray sources), the use of synchrotron radiation is crucial for off-specular measurements. In fact, the off-specular scattering signal is very low, especially at high Q_x where only one photon over 10^{12} incident ones was detected, a high photon flux is needed.

For this reason, only the sample pre-characterization was performed using the in-house equipments, while off-specular and most of the specular measurements were performed at synchrotron facilities.

The SixS beamline

Specular and off-specular synchrotron radiation reflectometry experiments were performed on the Surfaces interfaces X-ray Scattering (SixS) beamline at the SOLEIL Synchrotron (Saint-Aubin, France). The layout of the SixS beamline is shown in Fig. II.2.28. The sample stage was placed on a goniometer, which allowed to control precisely the orientation of the sample with respect to the incoming X-ray beam. The X-ray beam energy was fixed at 18.4 keV ($\lambda = 0.467$Å) by means of a monochromator. The divergence of the beam was ≈ 10 μrad.

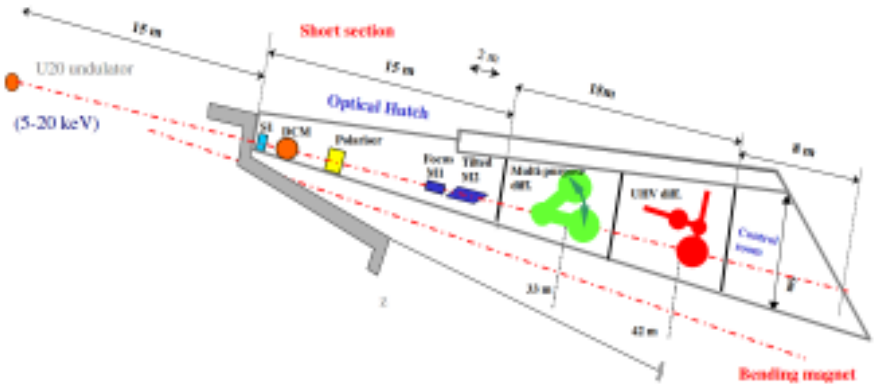

Figure II.2.28 – Schematic layout of the optical elements of the SixS beamline at the Synchrotron SOLEIL, Saint-Aubin, France [182].

Beam shape and size of the illumination area were controlled using the set of slits with the dimensions wxh (see Tab. 2.2, where w_c and h_c are width and height of the collimation slit and w_d and h_d are those of the detector slit). The slits size was selected according to the type of the experiment performed (specular or off-specular). For specular reflectivity experiments slits dimension was chosen taking into account the facts that slits should be open wide enough to ensure the detection of good reflected signal, but the slits opening should remain fine to limit the diffuse scatting contribution in the specular signal. For off-specular experiments, the slits were opened more then for specular experiments to guarantee the detection of the weak diffuse signal. As too large slits opening affects the experimental resolution,

a trade-off had to be found to balance the signal strength and the resolution of the measurements.

Table 2.2 – The dimension of the slits for source and detector at the SixS beamline at the Synchrotron SOLEIL, Saint-Aubin, France.

Dimensions	Specular	Off-specular
h_c	200 μm	200 μm
w_c	20 mm	20 mm
h_d	20 μm	20 μm
w_d	20 mm	20 mm

Specular reflectivity was measured by varying the incident angle θ from 0° to 3° (Q_z = 0 Å^{-1} coincides with the direct beam), which allowed to cover the Q_z-range from 0 Å^{-1} to 1 Å^{-1}. The background scattering signal was measured performing an "offset scan": signal was measured in a region of interest close (but outside) of the area containing the specular signal.

A great care was taken to avoid sample degradation due to the exposure to the X-ray beam (radiation damage). After each reflectivity measurement the sample was moved for 3 mm along the lateral direction and the next measurement was performed on a new area of the sample. Sample re-alignment was done before each new measurement. The high flux of the X-ray beam (10^{12} photons per second) allows to obtain measurements with a very good statistic and relatively fast. Specular and off-specular reflectivity curves were collected within one hour, taking into the account time needed for the sample alignment.

The off-specular signal was measured by fixing the incident angle at the value θ = 0.6°, which is slightly lower the critical reflection angle for the beam of energy 18.4 keV at the silicon/water interface (θ_{cr} = 0.06912°) and scanning the detector angle in the range form 0 to 3.5° , corresponding to a Q_x range from 1 x 10^{-6} to 3.4 x 10^{-2}. The background signal for the off-specular experiments was measured by moving the silicon substrate away from the X-ray beam scanning the detector angle from 0 to 3.5°.

The CRG-IF (BM-32) beamline

XRR experiments to study the structure of charged lipid bilayers samples were performed at the CRG-IF (B32) beamline of the European Synchrotron Radiation

Facility (ESRF, Grenoble, France), which is dedicated to study the surfaces and interfaces, using a 27 keV x-ray beam (wavelength λ = 0.0459 nm). BM32 beamline was equipped with a goniometer to control precisely the position and the orientation of the sample with respect to the incident beam. The schematic layout of the beamline is shown in Fig. II.2.29. The divergence of the beam was measured case by case, and was comprised between 10 and 70 μrad. The photon flux was 10^{11} photons/s, which allowed to measure the specular reflectivity curve within an hour.

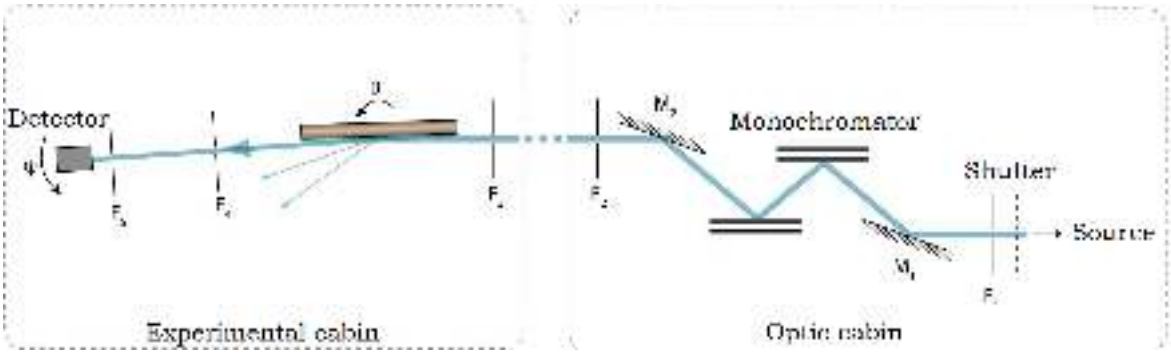

Figure II.2.29 – Schematic layout of BM32 beamline at the ESRF [183].

The size of the illumination area and the beam shape were controlled using a set of slits for the incident beam. The dimensions of the used slits are reported in Tab. 2.3, where w_c and h_c are width and height of the collimation slit and w_d and h_d are those of the detector slit. For the specular X-ray reflectivity the slits opening does not affect the resolution of the measurements. For the off-specular measurements, the dimension of the slits placed after the sample should be chosen very carefully as the slits opening defines the resolution of the measurement. A compromise had to be found to keep the detected scattered intensity (count rate) sufficiently large and the resolution sufficiently high.

Table 2.3 – The dimension of the slits for source and detector at the CRG-IF beamline at the ESRF, Grenoble, France.

Dimensions	Specular	Off-specular
h_c	200 μm	200 μm
w_c	2 mm	20 mm
h_d	200 μm	200 μm
w_d	2 mm	20 mm

The specular reflectivity measurements were performed in a θ - 2θ geometry (Fig. II.2.29), varying the incident angle θ in the range from 0 to 3°C, which resulted

in the Q-range from 0 to 1 $Å^{-1}$. Background scattering was measured by shifting the detector by $\delta\theta$ = 0.08 and by repeating the θ - 2θ scan.

Figure II.2.30 – Schematic geometry of a specular X-ray reflectivity measurement [35].

To measure off-specular scattering, the incident angle of the X-ray beam was fixed at the values θ = 0.04°, which is slightly less than the critical angle for a silicon/H_2O interface for a 27 keV X-ray beam (θ_{cr} = 0.048° for 27 keV) and the off-specular signal was measured by scanning the detector angle from 0 to 4° (Fig. II.2.31). At high Q_x the intensity of the diffuse signal is very low and it is mostly dominated by the background noise due to the large amount of water presented in the cell, which X-ray beam has to cross before reaching the sample on the surface. Thus, to extract the weak diffuse intensity coming only from the sample, the background noise signal has to be separately measured and subtracted from the off-specular intensity. The background scattering was measured by moving the substrate from the X-ray beam path scanning the detector from 0 to 4°.

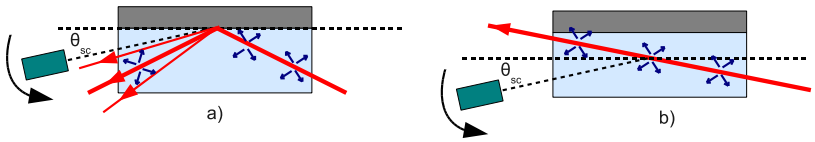

Figure II.2.31 – a) Schematic geometry of an off-specular reflectometry measurement. b) Schematic geometry of a background measurement [165].

2.8 In-house X-ray reflectometry

In-house specular X-ray reflectivity measurements were performed on the Empyrean X-ray bench from PANalytical [184] using an Ag source, which generates a beam of energy 22.4 keV and wavelength 0.56 Å. The instrument was equipped with a line detector, which has a high efficiency for Ag radiation, and a sample stage,

which allowed to move the sample in x, y and z directions (but that did not allow to adjust sample and tilt angles). The X-ray bench available at the ILL is shown in Fig. II.2.32. A set of slits for the incident and reflected beam was used to define

Figure II.2.32 – In-house Empyrean X-ray bench available at the ILL.

the beam size and to reduce the diffuse scattering in the specular direction. The dimensions of the slits used for the incident and reflected beam optics are reported in Tab. 2.4

Table 2.4 – Slits configuration for incident and diffracted beam optics on the ILL X-ray bench.

	Source		Detector
Anti-scatter slit	1/32° (0.05 mm)	Receiving slit	1/8° (0.19 mm)
Mask	20 x 10 mm	Mask	-
Soller slit	0.04 Rad	Soller slit	0.04 Rad
Divergent slit	1/16° (0.1 mm)	Anti-scatter slit	1/8° (0.19 mm)

Specular XRR measurements were performed varying the incident beam from 0° to 4°, which allowed us to cover a Q_z range from 0 $Å^{-1}$ to 0.8 $Å^{-1}$. Because of the low photon flux (if compared to synchrotron radiation beamlines) no sample degradation due to the long exposure to the X-ray beam was detected (up to 7 reflectivity curves could be measured on the same sample). One reflectivity curve could be measured in approximately 1.5 hours for bilayers at a solid/liquid interface (Fig. II.2.14).

Because of the use of fixed slits, the beam footprint at the sample surface was larger than the sample size at low incident angles. This situation goes under the

name of over-illumination and it causes a decrease in the detected intensity since part of the incident beam is not hitting the sample. An over-illumination factor B was calculated by taking into account the slits size and the dimension of the sample surface.

Indeed, the footprint D of the beam on the sample surface can be estimated as :

$$D = \frac{d}{\sin(\theta)} \tag{2.57}$$

where d is a beam width and θ is the incident angle. When D is larger than the size of the sample L, the reflectivity is reduced by the factor B:

$$B = \begin{cases} \frac{\sin(\theta)}{\sin(\theta_{\text{oi}})} & \text{for } \theta_{\text{oi}} > \theta, \\ 1, & \text{for } \theta_{\text{oi}} \leq \theta. \end{cases} \tag{2.58}$$

This correction had to be performed for incident angles defined based on the relation

$$\theta \leq \arcsin(\frac{d}{L}). \tag{2.59}$$

As a result, all reflectivity data points collected for $\theta \leq \arcsin(\frac{d}{L})$ had to be multiplied by the factor B.

2.9 Data modeling and analysis

2.9.1 NR and XRR

Solid-supported lipid bilayers are self-assembled structures composed by two leaflets of lipid molecules and deposited on the solid supports of a different kind. Being formed on substrates, SLBs are planar structures that can be described in terms of a layered model. Because of their chemical composition, each leaflet can be divided into a head-group region (hydrophilic) and a tail region (hydrophobic) that are characterized by different SLD and eSLD values and are therefore distinguishable during NR and XRR experiments. Being composed by two leaflets, a bilayer can be modeled by at least 4 individual layers. In addition, a central methyl groups layer might be necessary to model high-resolution XRR curves. Therefore, single lipid

bilayer and double lipid bilayer samples on solid supports were modeled according to N = 5 (if the tails of bilayer leaflets are combined) or N = 6 (if the tails of bilayer leaflets are separated) and N = 10 (if the tails of bilayers leaflets are combined) or N = 12 (if the tails of bilayers leaflets are separated) layers as shown in Fig. II.2.33. Any oxide layer present on the surface of the substrates and a water layer between the substrate and the lower bilayer as well as between the two bilayers (for double bilayer systems) were systematically included in the model.

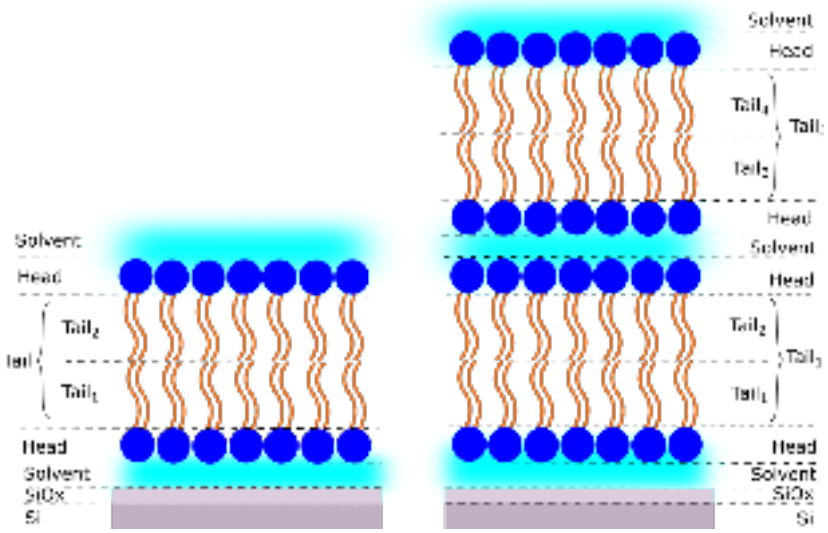

Figure II.2.33 – Schematic representation of the slab model used to fit NR and in-house XRR data.

In the model the j-th slab was characterised by four parameters: thickness d_j, the SLD or ED ρ_j^{dry}, water fraction ϕ_j^s and the surface roughness $\sigma_{j,j+1}$. The total SLD (or ED) of the j-th slab was be calculated as :

$$\rho_j = \phi_j^{\text{dry}} \rho_j^{\text{dry}} + \phi_j^s \rho^s \tag{2.60}$$

$$\phi_j^{\text{dry}} + \phi_j^s = 1 \tag{2.61}$$

where ρ_j^{dry} and ϕ_j^{dry} are the SLD and the dry fraction of the sample in the layer j and ρ^s and ϕ_j^s are the SLD of the solvent and solvent fraction in the layer j. Eq. 2.60 has a fundamental importance for experiments at the solid/liquid interface, because it allows the co-refinement of data sets collected according to the contrast variation method. In fact, during NR experiments the data was collected upon the use of aqueous phases containing different percentage of D_2O and H_2O. In this way the

value of the solvent SLD (ρ^s) could be changed continuously between 6.35 and -0.56 (in 10^{-6} Å^{-2} units). As a result, different reflectivity curves, originated from the same "dry" structure were consequently measured and simultaneously analysed. During the co-refinement, a unique set of structural parameters describing simultaneously all the different reflectivity curves was optimized [185]. The only parameter changing (in a controlled way) among different data sets was indeed ρ^s. Reference SLD values used in the analysis are given in section 2.10.

The structural parameters describing each slab in the model were optimised during the fitting procedure in order to obtain the best fit of the measured reflectivity data. Thus, for a sample modeled by N slabs, the maximum number of free parameters was 4N + 1. This number can be considerably reduced by constraining some of the parameters, according to the molecular information available. The goodness of the fit was evaluated in terms of the minimum of the χ^2 function (see Eq. 2.62), a quantity which describes the distance between the measured and estimated curves during the fitting process. The fitting procedure continued until a minimum of the χ^2 was reached.

$$\chi^2 = \frac{1}{PF} \frac{\sum_k^p (R_{M,k} - R_{C,k})^2}{(\sigma_k)^2} \tag{2.62}$$

where the $R_{M,k}$ and $R_{C,k}$ are the k-th point of the measured and calculated reflectivity curves, σ_k is the k-th standard error of the measured reflectivity, P is the number of data points and F is the number of free parameters (reduced by the number of constrains).

Thus, by applying physical and chemical constraints on the system and fitting simultaneously the reflectivity data sets collected in different isotopic contrasts, we could obtain the SLD profile of the system, which describes the unique structure of the sample at the interface [154].

In fact, the result of the analysis of $R(Q)$ data is a SLD or ED profile. In practice, NR and in-house XRR data were analyzed using the AuroreNR [185] and Motofit software packages [186], where the specular reflectivity is calculated by the Parratt's recursive formalism [160] (AuroreNR) and by Abeles' matrices (Motofit) [187]. A genetic algorithm for χ^2 minimization was implemented in Motofit, while MINUIT

algorithm was used in AuroreNR. Motofit software was used to fit the NR and XRR data, when the number of the layers implemented in the sample modeling exceeds 10 (the maximum number of layers allowed by AuroreNR software), otherwise, AuroreNR software was used due to its very fast fitting routine and user-friendly and intuitive GUI.

2.9.2 Synchrotron radiation reflectometry

Specular reflectivity data collected at synchrotron beamline were analyses with a different approach than the one described in the previous section. This was motivated by the necessity of using a model for the combined analysis of specular and off-specular measurements. In this combined approach, electron densities profiles were describes in terms of a 1G-hybrid gaussian continuous profile [164, 166] for which $\rho(z)$ was modelled by a sum of continuous functions describing the head ρ_{head}, tail ρ_{tail} and methyl ρ_{CH_3} regions of a bilayer structure.

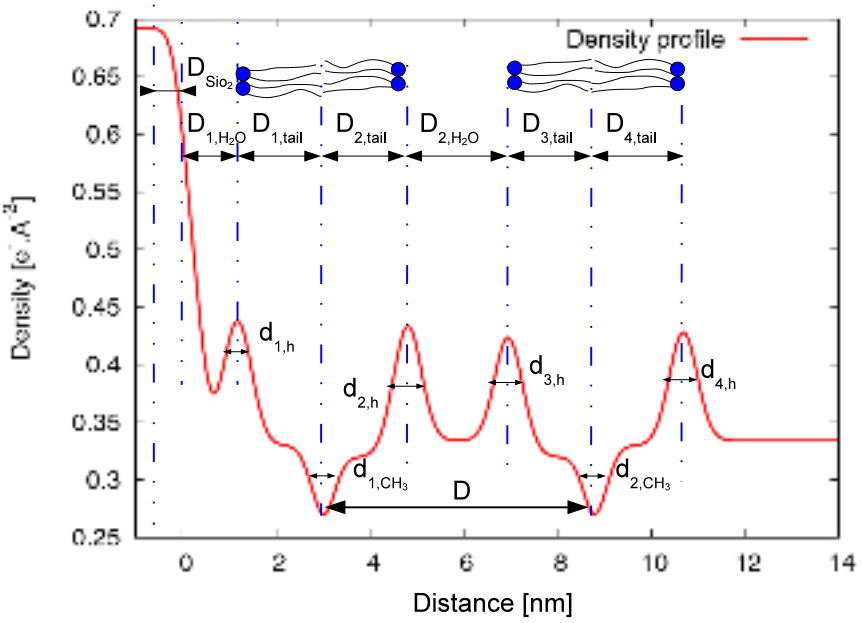

Figure II.2.34 – ED profile of a solid supported double lipid bilayer [35].

In particular, the ED for the head region ρ_{head} was described by a gaussian function :

$$\delta\rho_{head}(z) = (\rho_{head} - \rho_{H_2O}) \exp\left(-\frac{(z - z_{head})^2}{2d_{head}^2}\right). \tag{2.63}$$

The ED for the methyl group region ρ_{CH_3} was defined as :

$$\delta\rho_{CH_3}(z) = (\rho_{CH_3} - \rho_{H_2O}) \exp\left(-\frac{(z - z_{CH_3})^2}{2d_{CH_3}^2}\right), \tag{2.64}$$

while the ED of the chains region ρ_{tail} was modeled as :

$$\delta\rho_{tail}(z) = \frac{1}{2}(\rho_{tail} - \rho_{H_2O})\left[erf\left(\frac{z - z_{head} - d_{head}}{\varepsilon}\right) - erf\left(\frac{z - z_{CH_3} + d_{head}}{\varepsilon}\right)\right]. \quad (2.65)$$

In Eq. 2.65 the value of ε was chosen as small as possible ($\varepsilon = e^{-100}$). Finally, the chain region of each leaflet was connected to the head region and to the methyl group by sinusoidal functions. In such a way, the lipid bilayer was modelled by a continuous and smooth functions [35].

The data collected at synchrotron reflectometers were analysed using a home-made software developed by Charitat and Daillant [35, 164, 166] for the combined analysis of specular and off-specular synchrotron reflectivity originated from double lipid bilayer samples. The 1G-hybrid model described above consisted of 27 structural parameters for the specular part and of 25 structural and 7 elastic parameters for the combined specular and off-specular data analysis. The elastic parameters described the bilayer surface tension and bending modulus, as well as the membrane-substrate and the membrane-membrane interaction potentials.

A simulated annealing algorithm for the χ^2 minimization was implemented in order to obtain the best fit of the measured data [188]. This algorithm is particularly suitable for continuous multi-variable functions and it allows to escape the possibility to be "trapped" in a local minimum of the χ^2.

2.10 SLD and eSLD values used in the modeling

To perform fitting of neutron and X-ray reflectometry data, we have estimated the SLD and ED values of the lipids and proteins molecules used within this project. A lipid molecule was divided into tail and head regions for NR and head, methyl and tail regions for XRR as shown in Fig. IV.2.5. Temperature dependence of the volumes of the head and tail groups (and their atomic compositions) are know from the extensive studies of the structure of lipid species [189–192] and are listed in Tab. 2.5 and 2.6. Using the definitions reported in Eq. 2.12 and Eq. 2.13, SLD and/or ED values for the lipid tail, methyl and head regions were estimated and the corresponding values are summarized in Tab. 2.5 and 2.6. SLDs values of the silicon

and quartz substrates and solvent contrasted solutions, which were used within this work, are reported in Tab. 2.7.

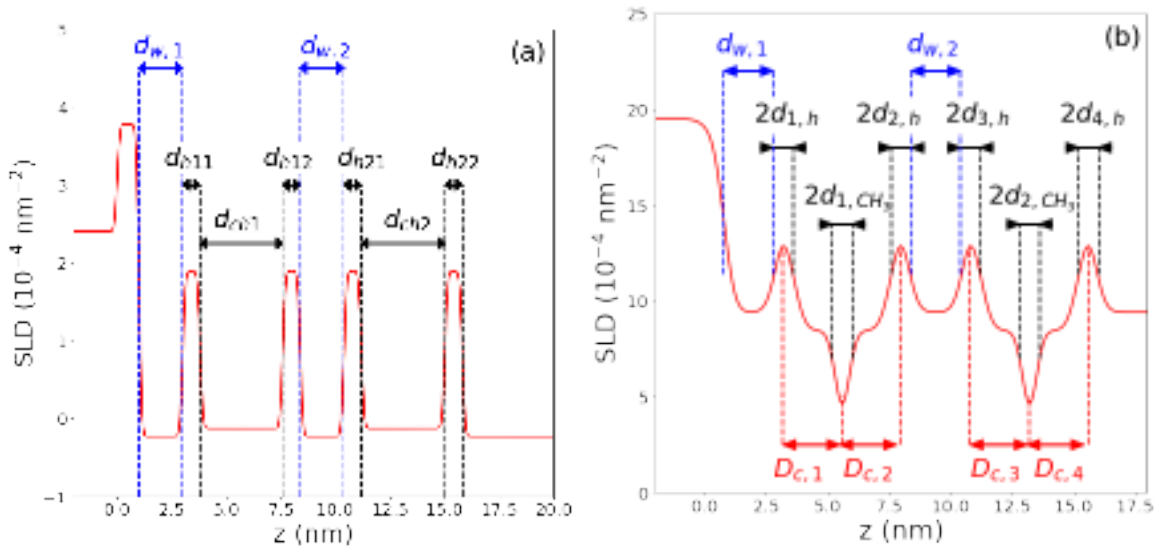

Figure II.2.35 – (a) Definition of parameters used for SLD profile in case of NR. For sake of clarity we used articial values for $\sigma_{i,j}$, $d_{w,1}$ and $d_{w,2}$ ($\sigma_{i,j}$ = 0.1 nm, $d_{w,1}$ = 2 nm, $d_{w,2}$ = 2 nm). (b). Definition of parameters used for SLD profile in case of XRR (1G-hybrid model). For sake of clarity we used articial values for $d_{w,1}$ and $d_{w,2}$ ($\sigma_{i,j}$ = 0.1 nm, $d_{w,1}$ = 2 nm, $d_{w,2}$ = 2 nm)

Table 2.5 – Neutron scattering length density (SLD) of the lipid molecules

Name		Structure	b_n	V (Å^3)	SLD (x10^{-6}Å^{-2})
DSPC	head	$C_{10}H_{18}O_8PN$	60.054	319	1.88
	tails (T = 20 °C)	$C_{34}H_{70}$	-35.836	917	-0.39
	tails (T = 55 °C)	$C_{34}H_{70}$	-35.836	1027.46	-0.35
DPPC	head	$C_{10}H_{18}O_8$ PN	60.054	319	1.88
	tails (T = 20 °C)	$C_{30}H_{62}$	-32.5	825	-0.39
	tails (T = 55 °C)	$C_{30}H_{62}$	-32.5	913	-0.36
POPC	head	$C_{10}H_{18}O_8PN$	60.054	319	1.88
	tails (T = 20 °C)	$C_{32}H_{64}$	-26.88	936	-0.28
DPPS	head	$C_8H_{11}O_{10}PNa$	81.55	310	2.63
	tails (T = 20 °C)	$C_{30}H_{62}$	-32.5	795	-0.41
	tails (T = 55 °C)	$C_{30}H_{62}$	-32.5	913	-0.36

In addition to SLD and ED for phospholipid molecules, these quantities were calculated also for proteins BR and Arch-3. Molecular volume of BR is 33844.7 Å^3 and a BR is composed of 1260 Carbon atoms, 291 Nitrogen atoms, 309 Oxygen, 9 Sulfur and 1921 Hydrogen atoms. The ED value of BR was estimated to be equal to

Table 2.6 – Electron density and eSLD of the lipid molecules

Name		Structure	Z_{el} (10^{-4}Å)	V (Å^3)	ED (e^-/Å^3)	eSLD (10^{-6}Å^{-2})
DSPC	head	$C_{10}H_{18}O_8PN$	164	319	0.52	14.45
	tails (T = 20°C)	$C_{34}H_{70}$	274	917	0.29	8.4
	tails (T = 55°C)	$C_{34}H_{70}$	274	1028	0.27	7.49
DPPC	head	$C_{10}H_{18}O_8PN$	164	319	0.52	14.45
	tails (T = 20°C)	$C_{34}H_{70}$	274	917	0.29	8.4
	tails (T = 55°C)	$C_{34}H_{70}$	274	1028	0.27	7.49
DPPS	head	Structure	172	310	0.56	15.5
	tails (T = 20°C)	$C_{34}H_{70}$	242	825	0.29	8.4
	tails (T = 55°C)	$C_{34}H_{70}$	242	913	0.27	7.49
POPC	head	$C_{10}H_{18}O_8PN$	164	331	0.49	13.92
	tails (T = 20°C)	$C_{32}H_{64}$	256	924	0.28	7.79
CH_3		CH_3	9	38	0.24	6.65

Table 2.7 – Neutron SLD, ED and eSLD of subphases and used substrates

	H_2O	D_2O	SiMW	4MW	Si	SiOx	Quartz
SLD (x10^{-6}Å^{-2})	-0.56	6.36	2.07	4	2.07	3.41	4.2
ED (e^-/Å^3)	0.334	-	-	-	0.65	0.692	-
eSLD (x10^{-6}Å^{-2})	9.41	-	-	4	18.5	19.5	-

0.4157 e/Å^3 and the SLD value of BR is 1.72 x 10^{-6} Å^2. The atomic composition of Arch-3 is not resolved yet, but it is known that Arch-3 structure and composition is very similar to BR (see section 1.4.6), therefore the same SLD and ED values were used for Arch-3.

During NR experiments, BR was immersed in different H_2O/D_2O mixtures. To take into account for the exchange of labile hydrogens between protein and solution, we used the biomolecular SLD calculator [193], where the amino acid sequence of the protein, taken from the PDB, can be loaded and molecular weight, molecular volume, scattering length and scattering length density of molecule are estimated. Assuming that 15% of hydrogens are labile, the SLD of BR was estimated to be equal to 1.84x 10^{-6} Å^2 in pure D_2O solution. The obtained value is close to the SLD value of BR in pure H_2O, therefore in the performed analysis of NR data the SLD value of BR was taken as an average value between the two 1.79x 10^{-6} Å^2.

Part III

Insertion of BR in floating lipid bilayers: active fluctuations

CHAPTER 1

Introduction

As already mentioned, the main objective of the project is to first reconstitute the transmembrane protein BR into a floating lipid bilayer system, keeping structural integrity of the lipid bilayer and functional activity of the protein, and to then trigger BR activity with light illumination of a specific wavelength in order to study the induced effect of protein pumping activity on the membrane structure and dynamics.

In order to develop a robust protocol for the protein insertion into floating lipid bilayers systems, we have performed series of experiments using available surface-sensitive techniques. We should note that a floating lipid bilayer is a very fragile and uncommon model system and only few experimental techniques suitable for this sample type investigation are available. A range of extensively used techniques to probe single SLBs cannot be employed to study double lipid bilayer systems, thus it becomes much more challenging. For example, QCM-D experiments cannot be performed on floating bilayers, as it is not possible to form double bilayer in QCM-D chamber and to our knowledge, no AFM experiments on the floating bilayer models formed by LB/LS technique were performed up to now and only few fluorescence microscopy studies were conducted.

Therefore it was necessary to optimise first the protocol for BR reconstitution into single lipid bilayer systems using QCM-D (section 2.1), AFM (section 2.2) and fluorescence microscopy (section 2.3). As a further step, we aimed to optimise the developed protocol for the case of floating lipid bilayers, performing AFM experiments on double lipid bilayer samples for the first time (section 2.2.5) and characterizing the structure of the obtained bilayers with embedded proteins by means of XRR and NR experiments (sections 3.1 and 3.2, respectively). Finally, we have performed SR reflectivity experiments to study the influence of BR pumping activity on the

structure and fluctuation of the floating lipid bilayer by triggering protein activity by illumination the membrane-protein system with visible light (section 4).

CHAPTER 2

Optimization of the insertion protocol on supported bilayers

2.1 QCM-D

Qualitative QCM-D measurements provide a great tool for the quick check and evaluation of protein interactions with planar systems in terms of changes in the absorbed mass and viscoelastic properties of the sample. QCM-D allows to monitor the influence of a wide range of parameters (temperature, pH, ionic strength, concentration, etc.) on sample formation and system properties. It permits fast verification of the developed protocol, its quick modification and adaptation. In general, values of frequency and dissipation shifts indicating formation of a good quality lipid bilayer are $\Delta F \approx -26\ Hz$ and $\Delta D \approx 0.2 \times 10^{-6}$ [28]. Thus, by performing QCM-D experiments we can quickly verify the quality of a formed bilayer and an effect of BR or detergent molecules on the bilayer properties through changes in the dissipation and frequency signals.

To monitor SLBs formation via vesicle fusion and protein reconstitution into fluid SLB, we have performed QCM-D experiments using a Q-Sense series E4 instrument (Q-Sense, Sweden). The instrument description can be found in section 2.1.1. The main aim of the performed experiments was to optimize the protocol for BR insertion into a single planar lipid bilayer by adjusting protein and detergent concentrations and incubation time of the BR-DDM solution with the lipid bilayer. Protein interaction with the bare substrate was studied as well. We have tested the influence of D_2O PBS buffer on the lipid bilayer formation and on protein reconstitution efficiency, which is important for NR experiments, where the method of solvent contrast variation is routinely used. QCM-D measurements do not provide a detailed infor-

mation on the bilayer morphology and its internal structure/organization, therefore QCM-D experiments were performed in combination with other surface-sensitive techniques, such as NR, XRR and AFM in order to obtain precise quantitative information on the sample structure and composition.

2.1.1 Optimization of detergent concentration

To prevent a drastic modification of the lipid bilayer or its full or partial solubilization caused by the interaction with detergent molecules, the concentration of the detergent solution used for the protein reconstitution should be properly optimized. To do so, we have performed QCM-D experiments to follow the lipid bilayer formation and to study the modifications (in terms of adsorbed mass) and changes of the viscoelastic properties of the sample caused by bilayer incubation with detergent solution. The optimization of the concentration of detergent solution helped to demonstrate that the structure of the fluid single SLB does not change significantly upon interaction with the selected detergent solution.

To perform this experiment, a POPC lipid bilayer was formed on a silicon chip by the vesicle fusion technique following the protocol reported in section 1.3.1. Upon the completed lipid bilayer formation, a solution of 0.05 mM DDM detergent in H_2O PBS buffer was injected into the solid/liquid cell with the POPC bilayer. After 15 minutes of incubation, the system was rinsed extensively in order to remove all detergent molecules from the cell. The concentration of 0.05 mM DDM solution was chosen based on results of previously performed fluorescence microscopy experiments and from values reported in literature for similar protocols [31, 32]. The main aim was to keep the detergent concentration as low as possible (lower than the critical micelle concentration for DDM detergent (*cmc*(DDM) = 0.17 mM in H_2O and *cmc*(DDM) = 0.12 mM in 0.2 M NaCl [194]) such that the lipid bilayer was unperturbed, while BR remained stable.

QCM-D frequency and dissipation signals collected for this experiment are shown in Fig. III.2.1. Different colors in the figure corresponds to the different oscilation harmonics (overtone numbers) of the QCM-D chip. The main steps carried out during this measurement are noted in the figure. Based on the measured frequency shifts, we can conclude that 0.05 mM DDM solution does not induce the

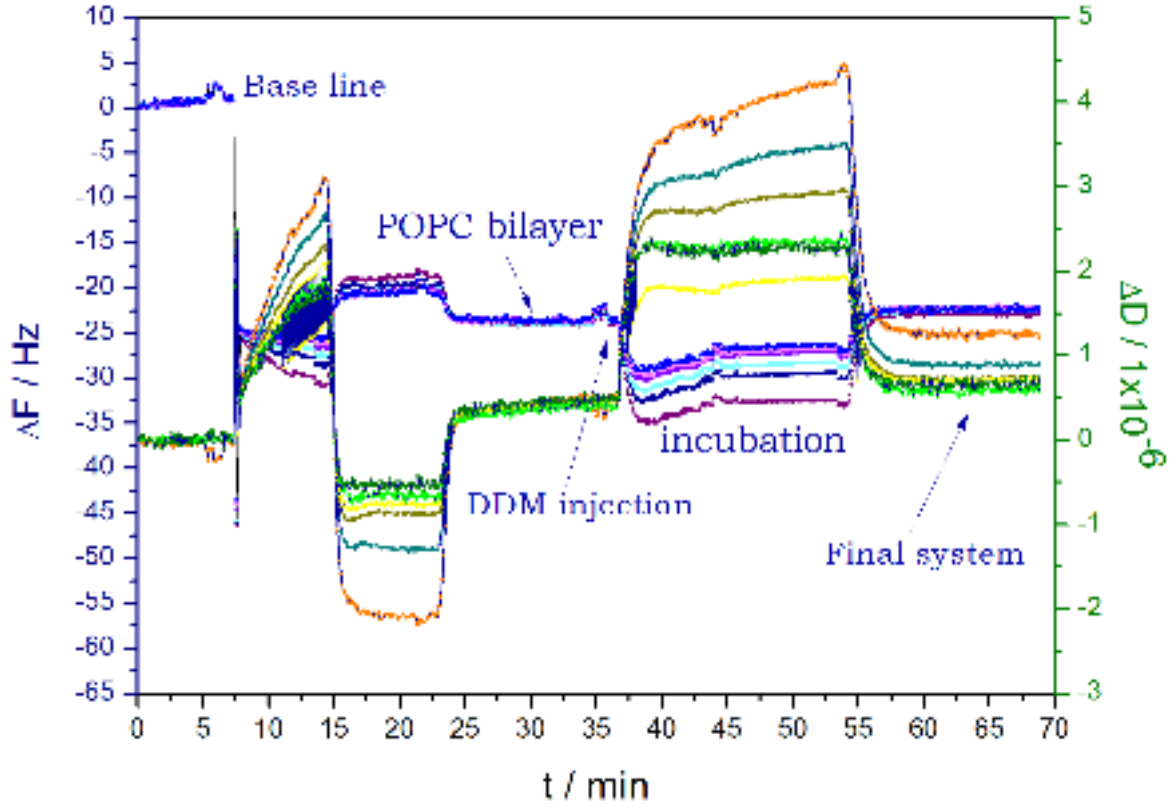

Figure III.2.1 – QCM-D data: frequency shifts (blue) and dissipation factors (green and orange) as a function of time for a POPC phospholipid bilayer formed by vesicles fusion, followed by 0.05 mM DDM injection. The system remained stable during all the steps.

lipid bilayer's removal from the silicon surface, despite strong interaction of the DDM solution with the POPC bilayer. Upon the performed injection of 0.05 mM DDM in PBS buffer solution into the cell the viscoelastic properties of a bilayer were substantially changed causing the lipid bilayer softening as can be seen from the changes of the dissipation signal (green and orange curves in Fig. III.2.1). The lipid bilayer regained its rigidity after removing the detergent molecules by rinsing the cell with buffer and no material loss from the substrate was detected. The fact that after sample rinsing with detergent-free buffer, the lipid bilayer rigidity increased back to the initial values, can serve as an indication that detergent molecules were removed not only from the bulk but from the lipid bilayer as well. We can conclude that 0.05 mM DDM solution does not induce lipid bilayer solubilization and drastic changes of the bilayer properties, therefore we have chosen this concentration of 0.05 mM DDM for the future reconstitution experiments.

As a reminder, we were also able to show using UV-vis spectrophotometry that

BR keeps its structural integrity in the 0.05 mM DDM solution (see section 1.4.3).

2.1.2 BR interaction with the lipid bilayer

Another set of QCM-D experiments were performed in order to study protein BR interaction with POPC lipid bilayers. Lipid bilayer formation by vesicle fusion (see section 1.3.1 for the sample preparation protocol) was monitored following the QCM-D frequency and dissipation signals. To study lipid bilayer modifications induced by proteins and detergent molecules, a 10 μg/ml BR in 0.05 mM DDM H_2O PBS buffer solution was injected into the cell. After 10 minutes of incubation, the system was rinsed with PBS buffer to remove all unbound proteins and detergent molecules. Collected frequency and dissipation shifts as a function of time are shown in Fig. III.2.2.

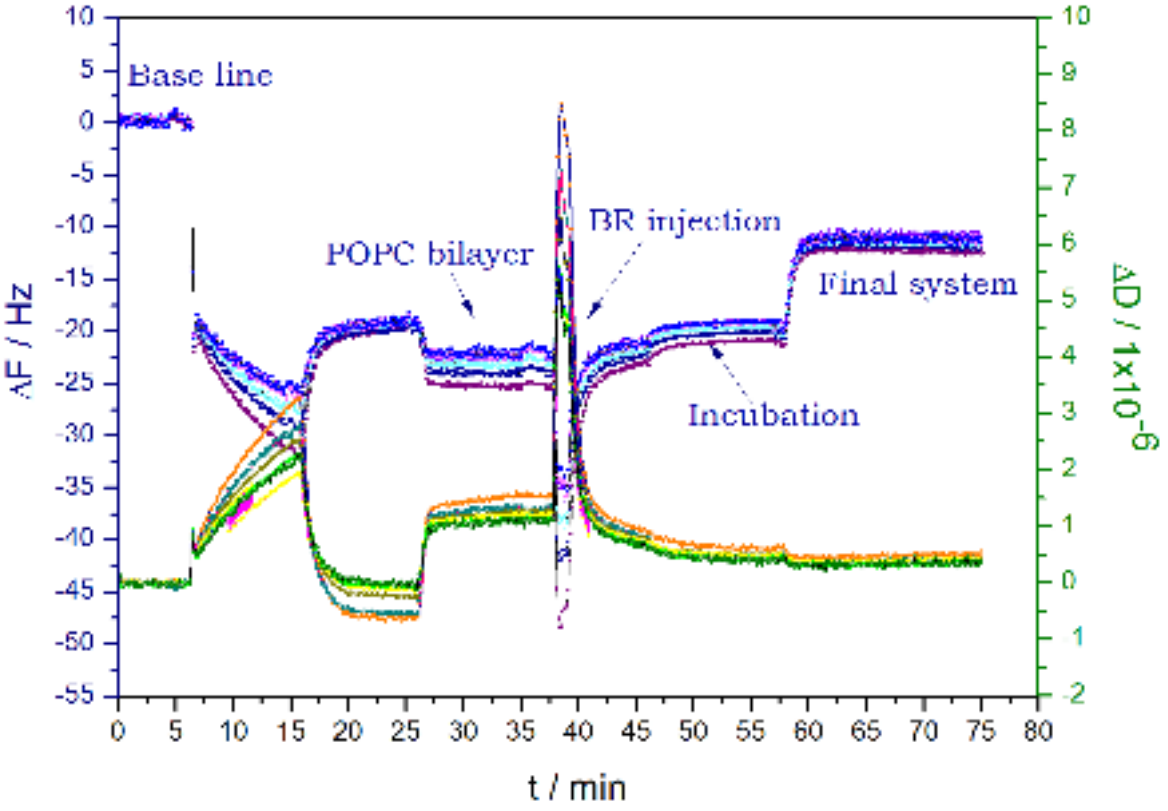

Figure III.2.2 – QCM-D data: frequency shifts (blue) and dissipation factors (green and orange) as a function of time for a POPC phospholipid bilayer formed by vesicle fusion, followed by BR reconstitution. A **10** μg/ml BR solution was used for the insertion step. The system remained stable during all steps.

Following the changes of the frequency signal (blue curve in Fig. III.2.2) which were caused by the bilayer formation and further by BR inclusion, we can conclude

that the protein reconstitution resulted in a change of the frequency signal from -24 to -11 Hz, which indicates the loss of material from the sensor surface. We have to note that in order to incorporate one BR molecule into a lipid bilayer, some lipid molecules should be removed from the surface. To estimate the amount of lipids which corresponds to one protein molecule (by volume), using simple geometrical considerations, we can assume that the volume of one BR molecule is equal to approximately 80 nm^3 (assuming that BR has a cylindiral shape with the diameter 4.5 nm and height 5 nm) and the volume of one POPC lipid molecule is equal to 1.255 nm^3 [195]. The ratio between these two values can be calculated to give the number R_v of lipid molecules displaced by one BR molecule :

$$R_v = \frac{V(BR)}{V(POPC)} = \frac{80}{1.255} = 64. \tag{2.1}$$

Thus, the total volume of 64 POPC lipids corresponds to the volume of one BR molecule. And if we divide the weight of BR by the total weight of displaced lipid molecules we obtain :

$$R_w = \frac{w(BR)}{64 * w(POPC)} = \frac{26500}{760 \cdot 64} = 0.54 \tag{2.2}$$

where $w(BR)$ = 26.5 kDa is the weight of one BR molecule and $w(POPC)$ = 760 g/mol is the weight of one POPC lipid.

This means that the weight of one BR molecule is approximately equal to half of the weight of 64 POPC lipids. Therefore, by determining the loss of material from the sensor surface after the BR reconstitution step, we cannot distinguish between the following conclusions: 1) partial removal of the lipid bilayer from the surface and no protein incorporation; 2) incorporation of BR into the bilayer and 3) a combination of the two.

By following the dissipation curve (green and orange curves in Fig. III.2.2), which gives us information about the viscoelastic properties of the sample on the surface, we can conclude that the final system is more rigid than the pristine POPC bilayer as no spreading of the dissipation signal is observed. The obtained final value of the dissipation $\Delta D \approx 0.4 \times 10^{-6}$ is consistent with a full coverage rigid sample adsorbed on the chip. Thus, by taking into account the outcome from the

dissipation signal, we suggest that BR incorporation into the POPC bilayer occurs.

2.1.3 Effect of the incubation time on protein reconstitution efficiency

To optimize BR reconstitution in order to maximise the amount of protein inserted without losing integrity of the bilayer, we have investigated the influence of the duration of the incubation period of BR-DDM solutions with the lipid bilayer. A solution of 10 μg/ml BR in 0.05 mM DDM H_2O PBS buffer was used for the reconstitution step and incubation times of 0, 10, 15, 20, 40 and 60 minutes were tested. In Fig. III.2.3 a QCM-D experiment on BR reconstitution into a POPC bilayer, with 0 incubation time with the DDM-BR solution is shown. Thus, immediately after protein-detergent solution injection, the cell was rinsed with buffer and no waiting time was allowed. Following the dissipation and frequency signals, we can conclude that upon BR-DDM solution injection, immediate interaction of BR with the POPC bilayer was observed. Subsequent cell rinsing with buffer induced material loss from the substrate, as observed also for the experiment reported in Fig. III.2.2 when 10 minutes of incubation time was allowed.

The outcome of all the experiments with different incubation periods were identical. In all cases, after BR-DDM solution injection, signals (frequency and dissipation) stabilization was observed and no changes appeared during the incubation period. An immediate and strong interaction of the DDM and BR molecules with the lipid bilayer was observed as well. The frequency and dissipation signal modifications occurred again upon cell rinsing with detergent-free buffer as was observed in Fig. III.2.2, denoting material loss from the surface and increased rigidity of the sample at the same time. As it was discussed above, taking into account both ΔF and ΔD shifts, the result is consistent with BR reconstitution into the POPC lipid bilayer. Based on the performed QCM-D experiments, we can conclude that the interaction of BR-DDM solution and BR reconstitution into a lipid bilayer are immediate processes and the duration of incubation period should not play an important role. Therefore, for the following experiments 10-15 minutes of incubation time were chosen to allow system stabilization.

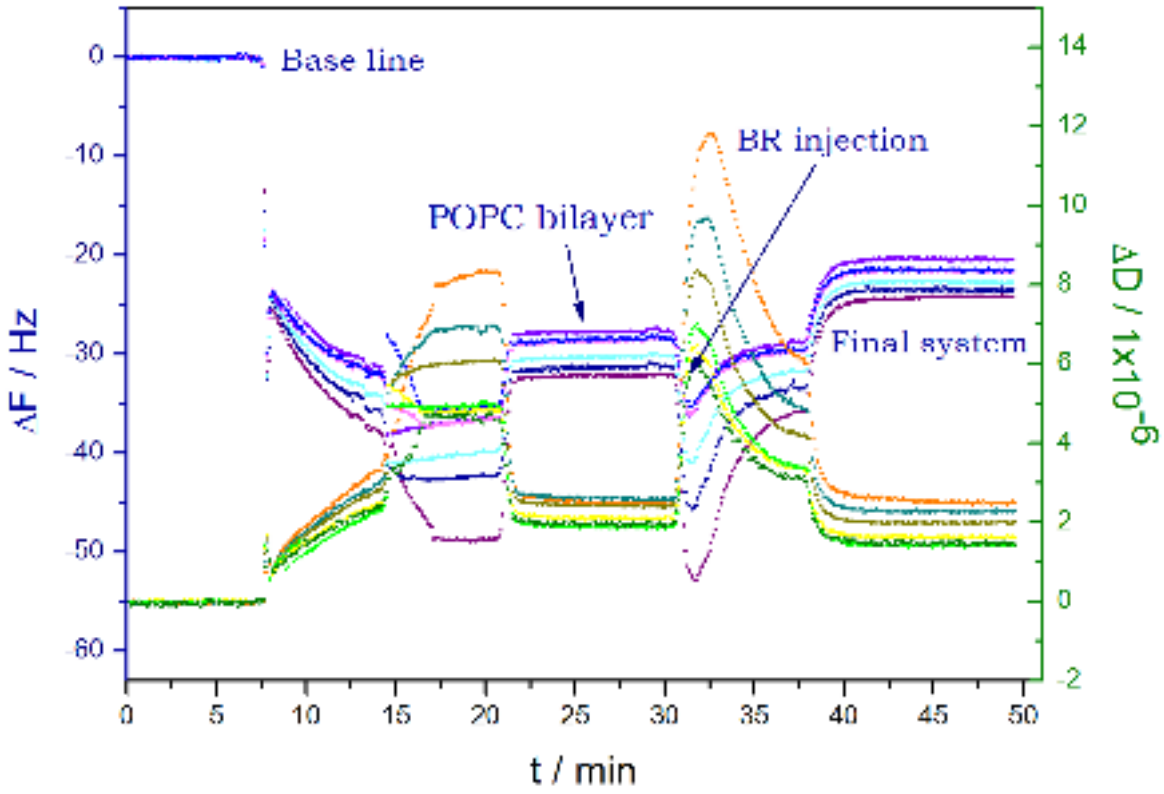

Figure III.2.3 – QCM-D data: frequency shifts (blue) and dissipation factors (green and orange) as a function of time for a POPC phospholipid bilayer formed by vesicle fusion, followed by BR reconstitution. A **10** μg/ml BR solution was used for the insertion step. No incubation time was allowed and after BR injection the cell was rinsed immediately. The system remained stable during all the steps.

2.1.4 Effect of H_2O and D_2O buffer substitution

We have performed QCM-D experiments to test the influence of D_2O PBS buffer on lipid bilayer formation and protein reconstitution efficiency. We aimed to obtain confirmation that there is no variation in the outcome of BR insertion due to D_2O - H_2O substitution. This effect is very important for NR experiments, where the solvent contrast variation method (see section 2.5.2) is routinely used and is essential.

We have performed QCM-D experiments identical to those reported above (POPC bilayer formation followed by BR reconstitution and POPC bilayer formation followed by DDM solution injection), replacing H_2O PBS buffer with D_2O PBS buffer.

The collected frequency and dissipation signals as a function of time for the experiment devoted to the investigation of influence of the DDM solution on the lipid bilayer are shown in Fig. III.2.4. As for the case of hydrogenated buffer, a strong and instant interaction of the detergent molecules with the lipid bilayer was observed. The viscoelastic properties of the lipid bilayer (green and orange curves)

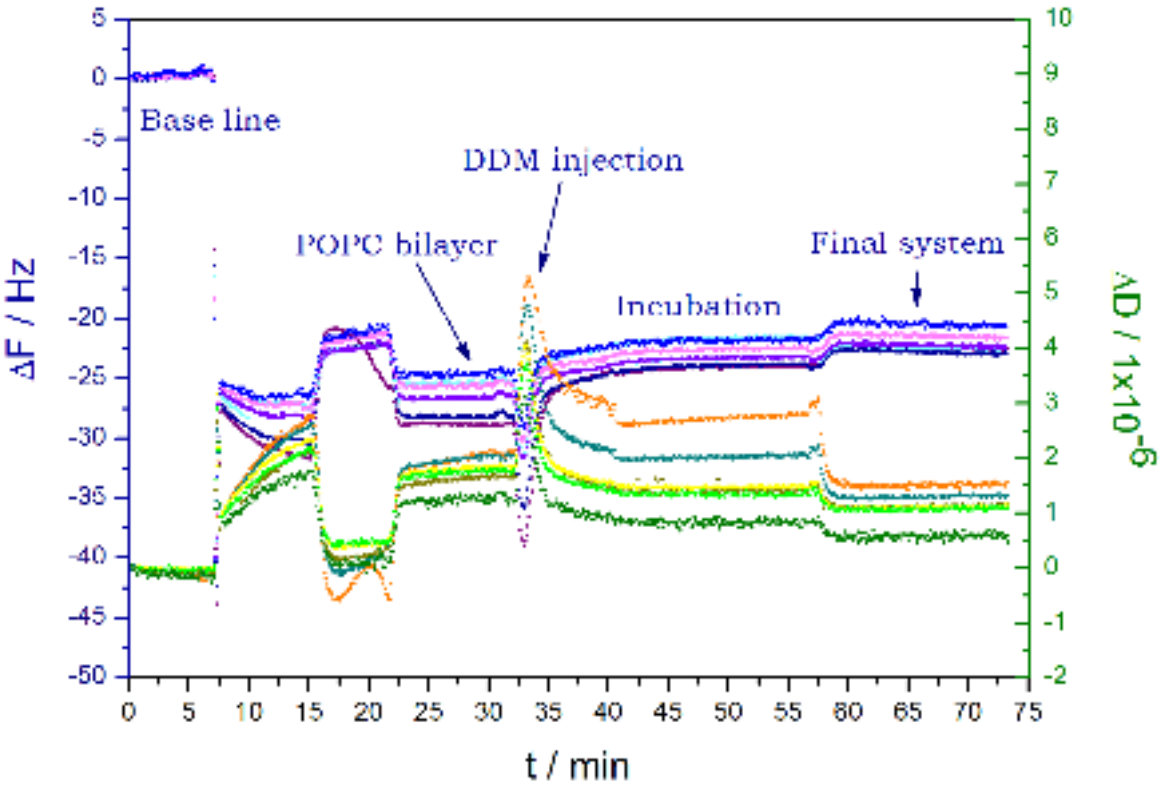

Figure III.2.4 – QCM-D data: frequency shifts (blue) and dissipation factors (green and orange) as a function of time for a POPC phospholipid bilayer formed by vesicles fusion, followed by 0.05 mM DMM solution injection. D_2O PBS buffer was used instead of H_2O PBS buffer. The system remained stable during all steps.

were changed upon DDM solution injection and incubation, indicating bilayer softening. The bilayer regained its rigidity upon cell rinsing and almost no material loss ($\Delta(\Delta F) \approx 2$ Hz) was detected upon sample rinsing (as for the case of H_2O buffer). There are no noticeable differences in the qualitative result compared to the case of H_2O buffer. A similar outcome was obtained from an experiment on BR insertion into a POPC bilayer in D_2O PBS buffer solution as when H_2O PBS buffer was used. Therefore, we can conclude that there is no influence of D_2O-H_2O PBS buffer substitution on the lipid bilayer formation and on protein reconstitution efficiency.

2.1.5 Influence of lipid bilayer composition

In order to investigate the influence of the lipid bilayer composition on the protein insertion, we have performed QCM-D experiments on bilayer systems of different lipid composition. Single lipid bilayers composed of a mixture of POPC:DPPC (1:1 by mol) at 45°C (both lipids are in the fluid phase) and DMPC lipids at 25°C

(gel-fluid phase coexistence, T_m = 24°C) were studied in order to monitor BR reconstitution into the bilayer. A solution of 10 μg/ml BR in 0.05 mM DDM H_2O PBS buffer was used for the detergent-mediated incorporation method. The influence of the incubation period duration on the protein reconstitution outcome was studied by varying the incubation time (10, 20, 40 and 90 minutes) of detergent-protein solutions with lipid bilayers of different composition.

In Fig. III.2.5 a QCM-D experiment on a DMPC lipid bilayer is shown. The lipid bilayer was formed by vesicle fusion technique (see section 1.3.1 for the sample preparation details) and BR reconstitution was performed by injecting a solution of 10 μg/ml BR in 0.05 mM DDM H_2O PBS buffer into the cell with the formed bilayer. A very long incubation period of 1.5 hours was allowed in order to follow the sample behavior. The cell was subsequently extensively rinsed with buffer to remove BR and DDM molecules. As for the experiment on BR reconstitution into a POPC lipid bilayer with 10 minutes incubation period (Fig. III.2.2), instantaneous interaction of BR with the DMPC lipid bilayer, frequency and dissipation signal stabilization during the incubation period, material loss and increase of bilayer rigidity upon removal of the BR-DDM solution from the cell were observed.

The outcome of the reconstitution experiment into the DMPC lipid bilayer with long incubation time is identical to the experiments on the POPC bilayer reported above. Similar results were obtained for the POPC:DPPC (1:1 by mol) lipid bilayer samples as well. Therefore, based on the reported observations, we can conclude that lipid bilayer composition did not play the main role for the BR insertion, as no distinct discrepancies in the sample behavior were noticed. No influence of incubation period duration was observed in agreement with results from the experiments on POPC bilayer samples.

2.1.6 BR adsorption on the bare substrate

To study the interaction of BR with the bare silicon substrate, we have monitored BR adsorption on the surface by injecting a 10 μg/ml BR in 0.05 mM DDM H_2O PBS buffer solution into the QCM-D chamber pre-filled with H_2O PBS buffer. The system was left to incubate for 10 minutes and rinsed with H_2O PBS buffer afterwards. The performed measurements are shown in Fig. III.2.6. Frequency shift of $\Delta F \approx$ - 20 Hz

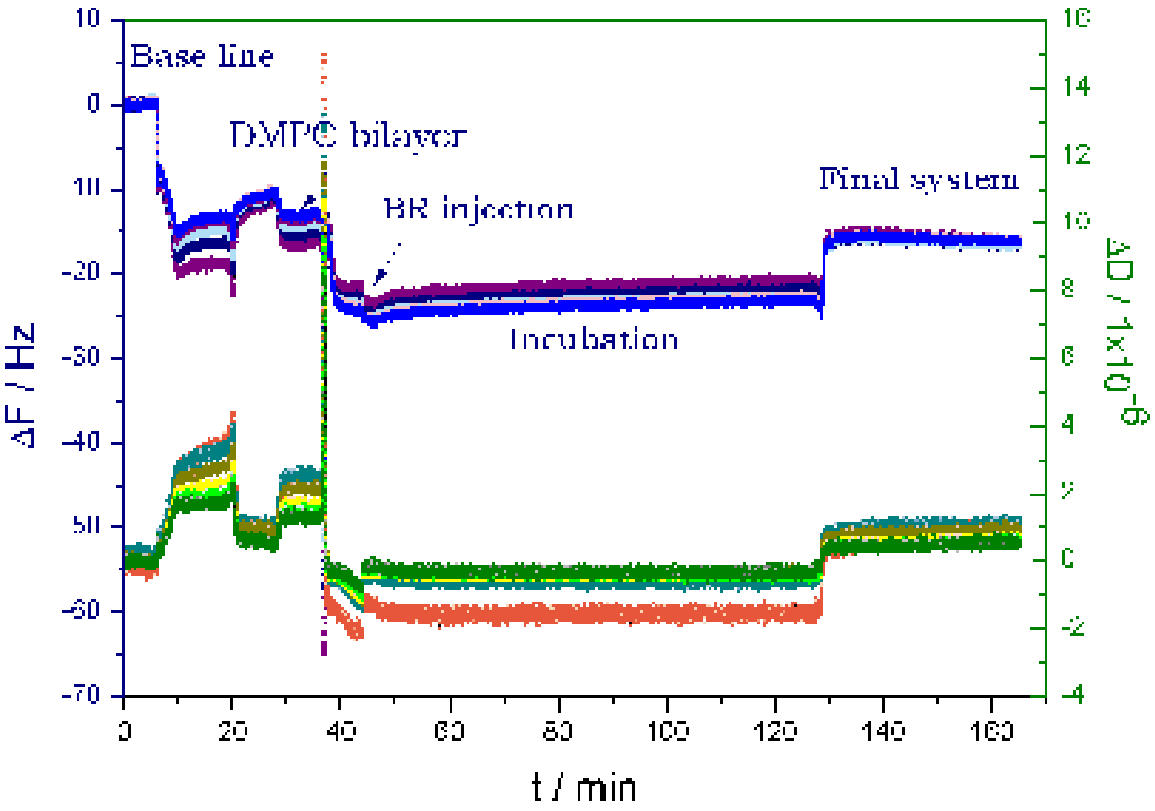

Figure III.2.5 – QCM-D data: frequency shifts (blue) and dissipation factors (green and orange) as a function of time for a DMPC phospholipid bilayer formed by vesicle fusion, followed by BR reconstitution. A **10** μg/ml BR solution was used for the insertion step. The system remained stable during all the steps.

and dissipation shift of $\Delta D \approx 1.5 \times 10^{-6}$ were observed upon BR injection and rinsing, which shows that a protein layer was formed on the bare surface. Comparing the obtained values to the values obtained for POPC lipid bilayers with and without BR we notice that the formed layer of BR (10 μg/ml) has induced similar dissipation and frequency shifts as the pristine POPC bilayer and the POPC bilayer with inserted proteins. The protein layer appears to be a softer system than the pure lipid bilayer, which is not surprising and can be probably explained by the large amount of water bound to the formed BR layer.

In addition, QCM-D experiment allowed to confirm the strong interaction of BR with the silicon substrate and protein adsorption to the bare surface (Fig. III.2.6), leading to a robust protein layer. The influence of D_2O PBS buffer on the protein adsorption efficiency was monitored as well. No effect of D_2O-H_2O buffer substitution was noticed.

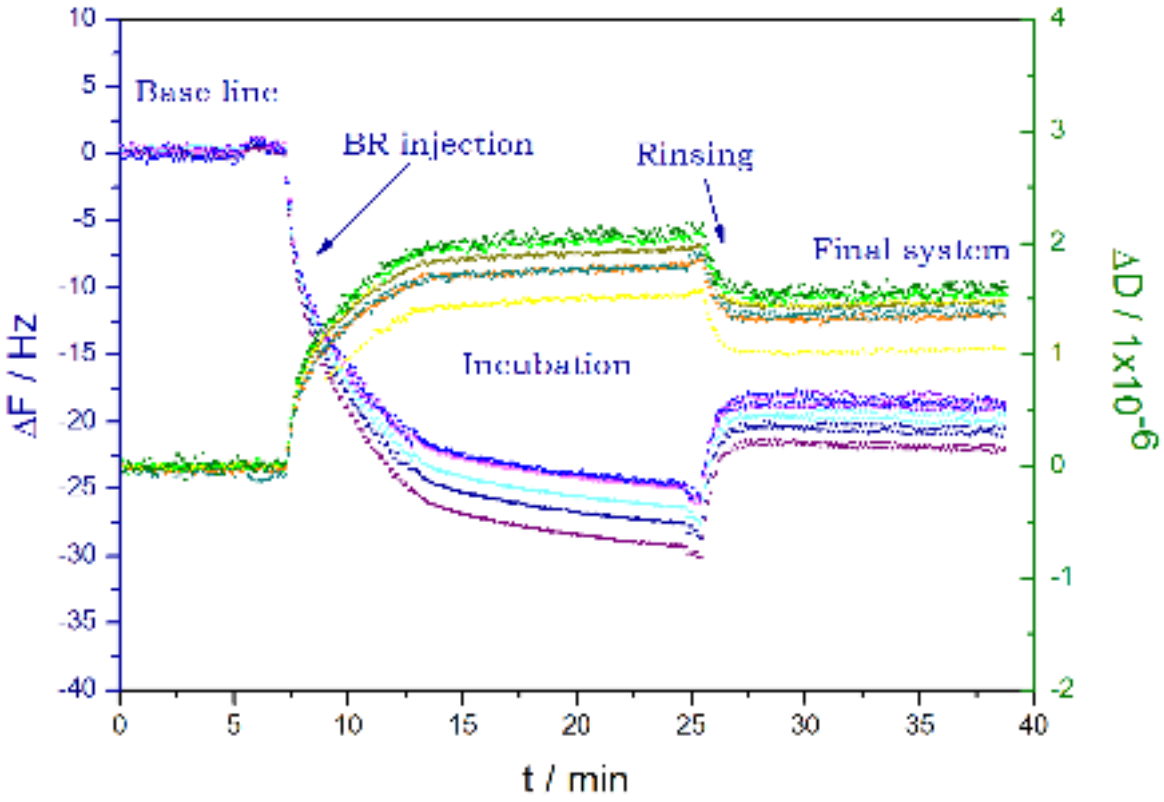

Figure III.2.6 – QCM-D data: frequency shifts (blue) and dissipation factors (green and orange) as a function of time for BR adsorption (10 μg/ml) on the bare substrate.

2.1.7 Arch-3 interaction with the lipid bilayer

The motivation to study Arch-3 reconstitution into fluid lipid bilayers was driven by the fact that Arch-3 is closely related to BR in terms of its structure and function (section 1.4.6), but as it was reported in [104], unlike BR, Arch-3 can be reconstituted easily into membranes of mammalian and bacterial cells. Therefore, we aimed to develop an easy and robust protocol for Arch-3 reconstitution and to investigate the differences in the protein-bilayer interactions for the two proteins. To start with, we have carried out QCM-D experiments in order to monitor the interaction of transmembrane protein Arch-3 with the membrane model system. The experimental scheme of the QCM-D measurements was identical to the one reported above for the case of BR reconstitution. As a model system a POPC lipid bilayer formed by vesicle fusion (sample preparation protocol reported in section 1.3.1) was chosen. In order to perform Arch-3 reconstitution, a solution of Arch-3 in 0.05 mM DDM H_2O PBS buffer was introduced into the cell, incubated for 10 minutes and rinsed with the H_2O PBS buffer.

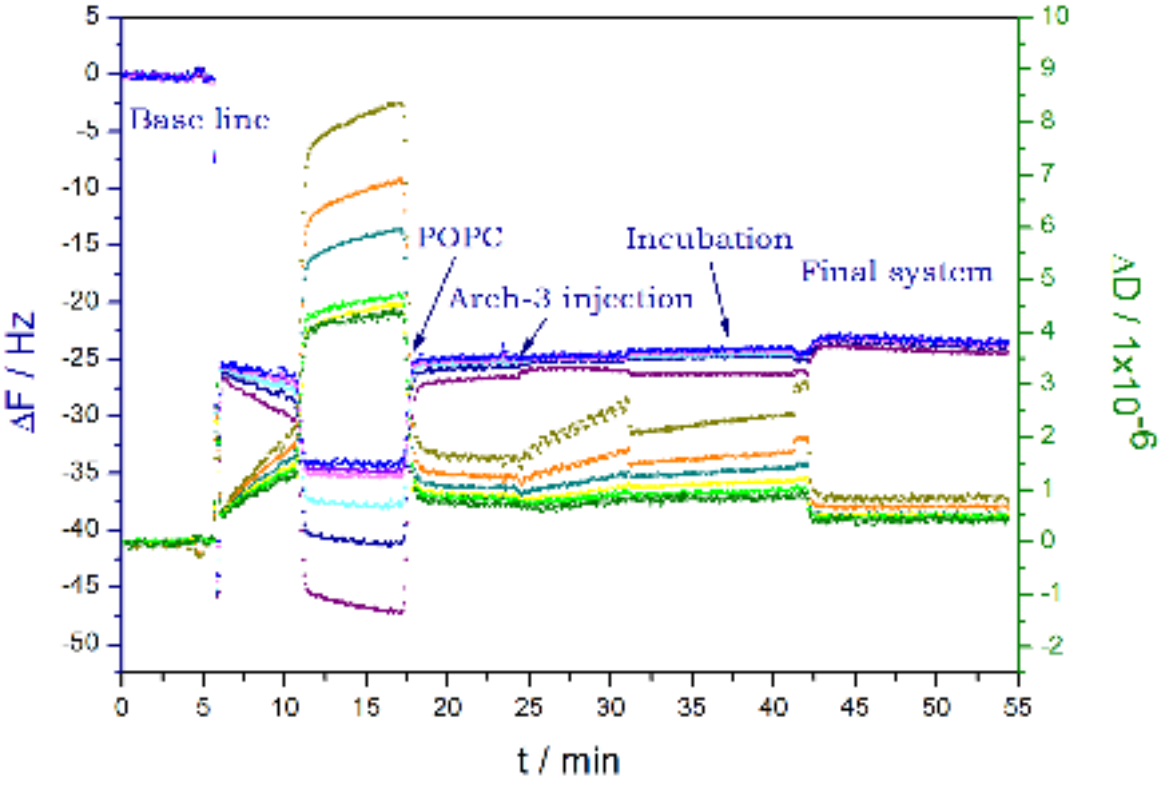

Figure III.2.7 – QCM-D data: frequency shifts (blue) and dissipation factors (green and orange) as a function of time for a POPC phospholipid bilayer formed by vesicle fusion and followed by Arch-3 reconstitution. A **1 μg/ml** of Arch-3 solution was used for the protein reconstitution. The system remained stable during all steps.

To maximise the amount of Arch-3 inserted without severe lipid bilayer modifications, different protein concentrations were tested for the reconstitution step. The results of the performed QCM-D experiments for the cases when 1 μg/ml and 10 μg/ml Arch-3 solutions were used (Fig. III.2.7 and III.2.8) are presented below.

Following the modifications of frequency and dissipation signals upon protein reconstitution, a very small shift in frequency (from -24 to -22 Hz, when a 10 μg/ml Arch-3 solution was used and from -25 to -24 Hz when 1 μg/ml Arch-3 solution was used (Fig. III.2.7 and III.2.8)) can be noticed, denoting that a very small modification of the weight of the lipid bilayer adsorbed on the QCM-D chip was induced by Arch-3-DDM molecules. This observation is in contrast to what was observed for the BR case, where BR-DDM solutions of the same concentration have triggered a more drastic effect, causing more noticeable frequency shifts (Fig. III.2.2). Large changes of the dissipation signal upon Arch-3-DDM solution injection and incubation periods are also observed.

As for the case of BR reconstitution, it is hard to confirm Arch-3 insertion

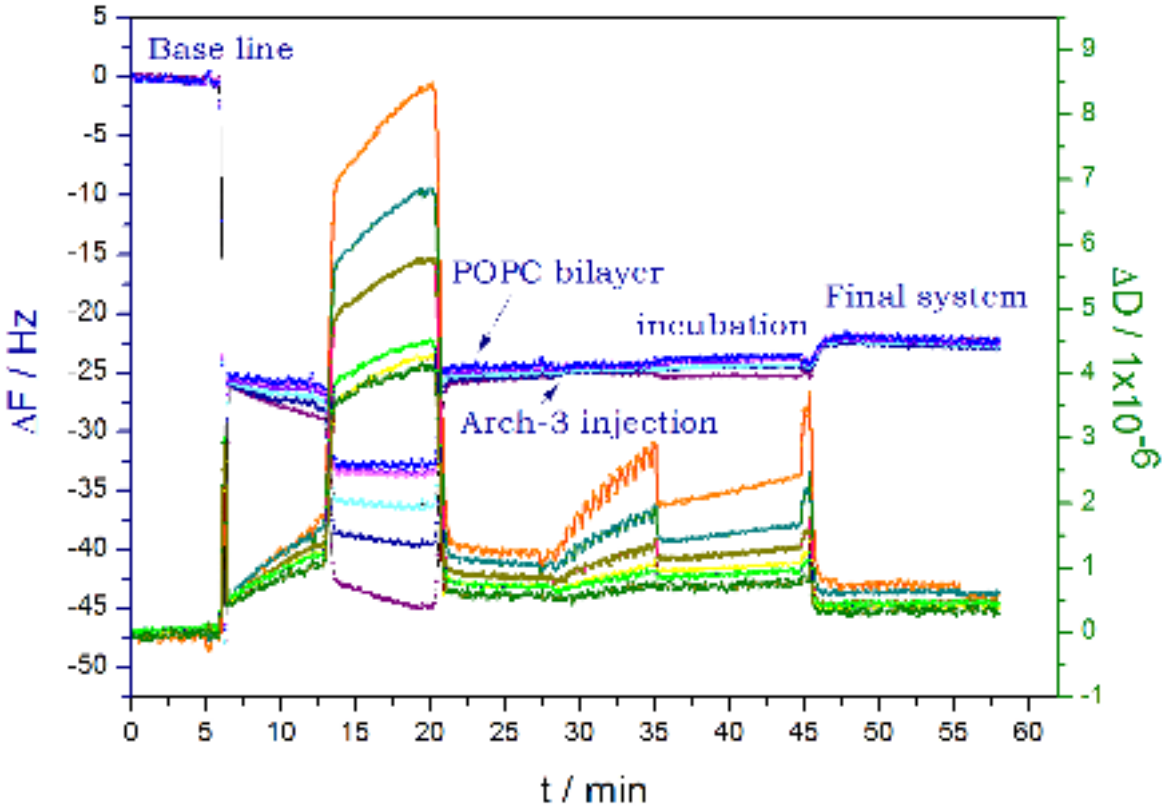

Figure III.2.8 – QCM-D data: frequency shifts (blue) and dissipation factors (green and orange) as a function of time for a POPC phospholipid bilayer formed by vesicle fusion, followed by Arch-3 reconstitution. A **10** μ**g/ml** of Arch-3 solution was used for the protein reconstitution. The system remained stable during all steps.

into the lipid bilayer based only on the observed changes of the frequency and dissipation shifts, which indicate mass removal and increase of sample rigidity upon the completion of the protein reconstitution procedure.

Arch-3 protein possesses very similar structural and functional features to BR as discussed in section 1.4.6. Therefore, the calculations done in section 2.1.2 in order to interpret QCM-D experiments on BR reconstitution should be valid for Arch-3 as well. We have estimated that the weight of one protein molecule corresponds to half of the weight of all lipid molecules that have to be removed from the surface in order to place one protein molecule. No conclusion can be made as the occurred frequency shift upon protein reconstitution (which demonstrates material loss from the surface) can be an indication of either lipid bilayer solubilization or protein reconstitution and it is not possible to distinguish definitely between these two cases based only on the frequency signal measurements. But as for the case of BR, the viscoelastic properties of the sample before and after Arch-3 insertion are different (dissipation

curves (green and orange) in Fig. *III*.2.7 and *III*.2.8) and the final system upon Arch-3 insertion appears to be more rigid. Taking into account both outputs from ΔF and ΔD signals, the obtained measurements can serve as an indirect evidence of Arch-3 reconstitution into the planar lipid bilayer.

We would like to highlight the noticeable difference in the way Arch-3 and BR interact with the POPC lipid bilayer. Upon injection of Arch-3 solution no modification of the frequency shift appears and only the dissipation signal starts to spread, which is in contrast to the BR case (compare Fig. III.2.2 and Fig. III.2.8), where large and immediate changes in both frequency and dissipation signals appear after BR solution injection. This is a very interesting observation, as BR and Arch-3 are very similar transmembrane proteins which share 75 % similar sequence homology and posses similar structure and identical functions, but as QCM-D shows these two proteins have a very different affinity to POPC lipid bilayers.

We have tested solutions at different concentrations (1, 5, 10, 20 μg/ml) of Arch-3 in order to study the differences in the protein-bilayer interaction through the discrepancies in the measured QCM-D signals. Injection of varying Arch-3 concentration did not have a strong effect on the final outcome of the experiments and almost no differences in the measured signals were spotted when either solutions of low or high concentration were used. This effect for the cases of 1 and 10 μg/ml Arch-3 solutions is clearly demonstrated in Fig.*III*.2.7 and *III*.2.8.

2.1.8 Arch-3 adsorption on the bare surface

As we did not observe the strong Arch-3 interaction with lipid bilayers samples, we have studied the interaction/adsorption of Arch-3 on a bare silicon crystal by monitoring the changes in QCM-D signals after Arch-3-DDM solution injection in the QCM-D chamber. After 15 minutes of incubation period, to allow proteins to be adsorbed to the surface, the cell was rinsed with H_2O PBS buffer. A wide range of Arch-3 protein concentrations (1, 2.5, 5, 7.5, 10, 20, 50 and 100 μg/ml) in 0.05 mM DDM H_2O PBS buffer was tested. QCM-D experiments on 10 and 50 μg/ml Arch-3 solution in 0.05 mM DDM H_2O PBS buffer are shown in Fig. *III*.2.9 and *III*.2.10. The performed experiments resulted in Arch-3 adsorption on the bare support and formation of the protein layer on the substrate.

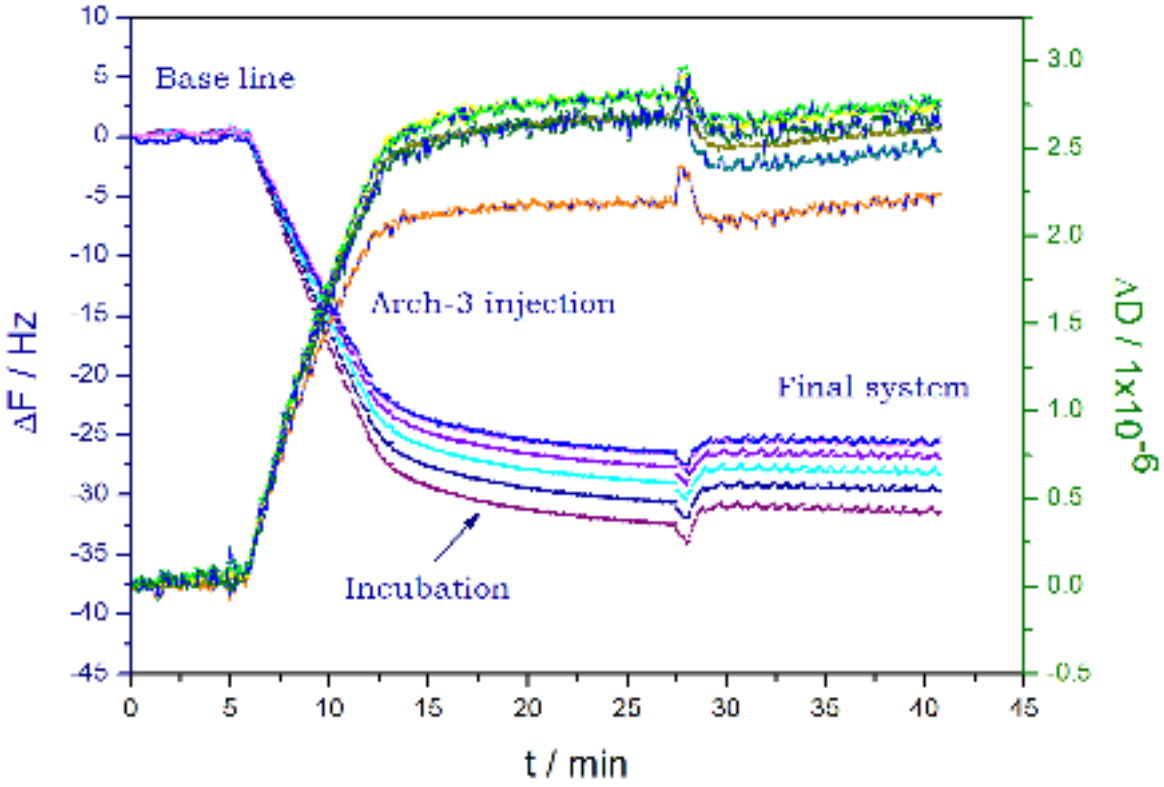

Figure III.2.9 – QCM-D data: frequency shifts (blue) and dissipation factors (green and orange) as a function of time for Arch-3 (10 μg/ml) adsorption on the bare substrate.

Table 2.1 – Summary of the experiments investigating Arch-3 adsorption on the bare substrate. The amount of proteins absorbed to the surface from the initially injected solution is estimated.

C, μg/ml	V_{inj}, ml	t_{incub}, min	ΔF, Hz	ΔD, x10^6	δm, ng/cm^2	m_{inj}, μg	m_{exp}, μg	% of m_{ads}
100	1	15	-47	1.4	831.9	105	0.6	0.6
100	3.3	15	-50	1.5	885	330	0.6	0.2
50	1	15	-56	1.4	991.2	52.5	0.7	1.4
50	3.3	15	-58	1.6	1026.6	165	0.7	0.5
20	1	15	-45	4	796.5	21	0.6	2.8
10	1	15	-27	2.5	477.9	10.5	0.35	3.4
7.5	1	15	-24	2.4	424.8	7.875	0.3	4.0
5	1	15	-8	1.2	141.6	5.25	0.1	4.0
2.5	1	15	-8	1.4	141.6	2.625	0.1	4.0
1	1	15	-7	1	123.9	1.05	0.09	8.9

We have observed that by increasing the concentration of injected protein solution, the amount of material adsorbed on the bare surface gradually increases (Tab. 2.1). We have also estimated the percentage of protein adsorbed on the surface of the total amount injected into the cell. By knowing the weight of the proteins in

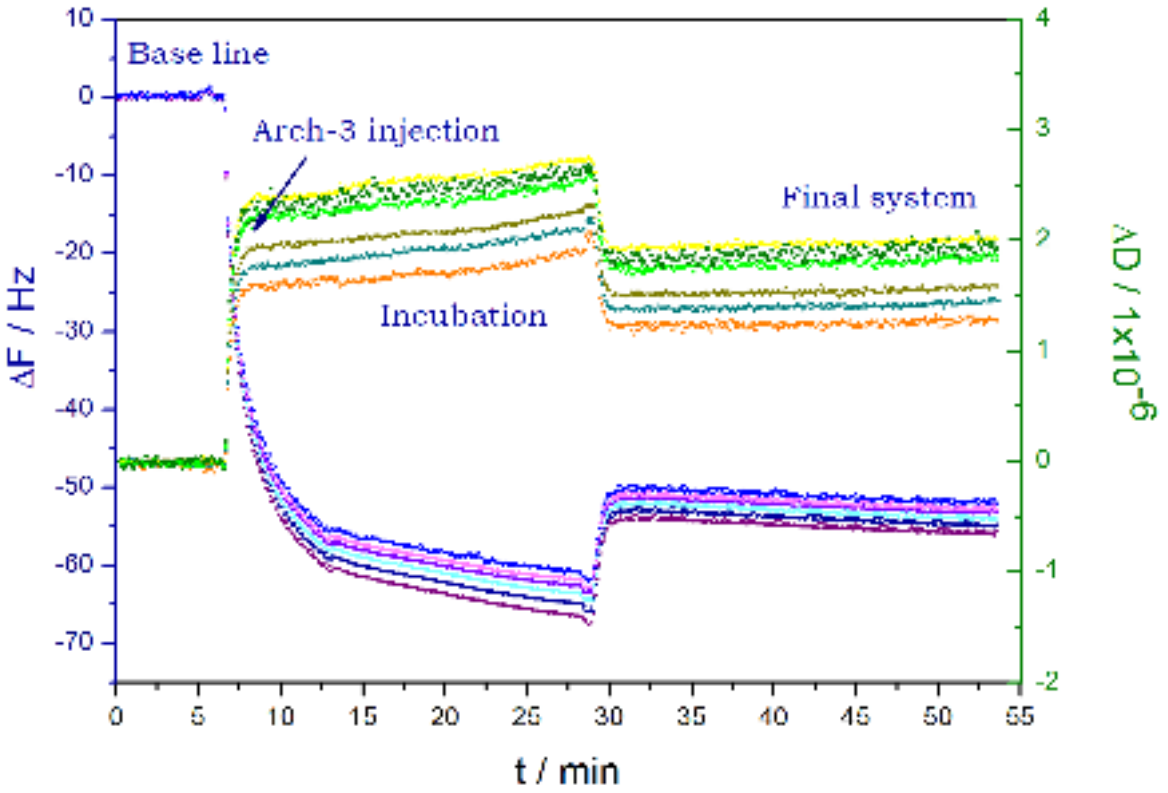

Figure III.2.10 – QCM-D data: frequency shifts (blue) and dissipation factors (green and orange) as a function of time for Arch-3 (50 μg/ml) adsorption on the bare substrate.

the initial solution (m_{inj}) and estimating the weight of the adsorbed protein layer (δm) though the Sauerbrey relation [129], we have calculated the amount of proteins which adsorbs to the surface (m_{exp}) . It is a very rough estimation, but we can conclude that only 8% by weight of the 1 μg/ml protein solution and 0.1 % by weight of the 100 μg/ml protein solution were adsorbed to the surface. The obtained results from these experiments are summarised in Tab. 2.1. Thanks to these experiments we were able to confirm that Arch-3 protein strongly interacts with the bare substrate, forming a firmly adsorbed protein layer.

2.1.9 Conclusions

Based on the experiments focused on BR reconstitution into POPC lipid bilayers and taking into account both frequency and dissipation QCM-D shifts, we have obtained an evidence of BR insertion into planar lipid bilayer systems. Different lipid bilayer compositions were probed for the reconstitution studies and similar outcomes were obtained for all performed experiments. We were able to show that BR-DMM solution interacts strongly and instantly with the lipid bilayer and the incubation time of BR-DDM solution with the lipid bilayer does not play the main role in the reconstitution experiments. We have demonstrated that 0.05 mM DDM solution does not cause lipid bilayer solubilization and material loss from the substrate, but DDM solution induces lipid bilayer softening. It was shown as well that sample rinsing with buffer promotes the removal of DDM molecules from both lipid bilayer and from the bulk solvent, based on the fact that the lipid bilayer regains its rigidity after the rinsing step.

We have shown that Arch-3 protein has a different affinity to planar POPC lipid bilayers and no strong protein-lipid bilayer interaction was observed (based on the frequency signal shifts). As for the case of BR, Arch-3-DDM solution causes changes of the viscoelastic properties of the sample, promoting bilayer softening. However, the lipid bilayer regained its rigidity after sample rinsing. From the observed material loss from the QCM-D chip, the increased rigidity of the final system and the strong protein interaction with the bare support, suggest that Arch-3 reconstitution was achieved.

Finally, we were able to confirm that both Arch-3 and BR proteins strongly interact with the bare support and form a robustly absorbed protein layer. QCM-D measurements do not provide information on the sample structure and composition, therefore other complementary techniques should be used to confirm the obtained evidences of BR and Arch-3 reconstitution into lipid bilayers and to resolve the structure and composition of membrane-protein systems.

2.2 AFM

To investigate the lateral structure and morphology of planar lipid bilayers and to follow the structural changes caused by membrane-protein-detergent interactions and by protein reconstitution, we have performed AFM experiments on single supported bilayers at the Institut de Biologie Structurale (IBS), Grenoble, France in collaboration with Jean-Marie Teulon and Jean-Luc Pellequer and on single and double lipid bilayer systems at the Institut Lumière Matière, Lyon, France in collaboration with Jean-Paul Rieu.

2.2.1 BR incorporation into POPC single bilayers

AFM experiments on single POPC lipid bilayers were performed at the IBS using a Multimode 8, Nanoscope V AFM instrument from Bruker in the scanfluid mode using scanasyst-fluid AFM tips. A description of the experimental procedure can be found in section 2.2. As a model system, mica-supported phospholipid bilayers composed of POPC lipids were chosen. POPC bilayers were prepared by vesicle fusion following the protocol described in section 1.3.1.

In Fig. III.2.11(a) the recorded AFM topography image of a POPC lipid bilayer on a mica surface is shown. Homogeneous POPC bilayers with high coverage and small amount of defects were usually formed. In Fig. III.2.11(b) the height profile corresponding to the marked region in Fig. III.2.11(a) is shown. The size of defects in the POPC bilayer ($h \simeq 3.3$ nm) is consistent with the height of POPC bilayer.

AFM experiments were performed at room temperature, thus the POPC bilayer was in the fluid phase (T_m = - 2°C). The lateral structure of the POPC bilayer appears to be homogeneous at μm-scale, therefore it was difficult to distinguish between the lipid bilayer sample and the bare support and thus to confirm the presence of the POPC bilayer on the surface. As the system was very soft and viscous, it was hard to perform AFM imaging avoiding artefacts caused by tip pollution and induced sample damage. Existence of small defects in the sample was helpful to prove the bilayer formation, different ways of tip-bilayer and tip-bare mica interactions have served as an indication of the presence of a bilayer sample on mica.

To perform protein incorporation, 10 μl of 10 μg/ml BR in 0.05 mM DDM

PBS buffer solution were pipetted onto lipid bilayer. The system was left for 15 minutes of incubation and then was rinsed with PBS buffer. In Fig. III.2.12 the POPC bilayer system after BR incorporation is shown. In Fig. III.2.12 the height profiles corresponding to the marked regions in Fig. III.2.11(a) are shown. As we can see, it is not possible to clearly distinguish the regions of the sample which correspond to the pure lipid bilayer. The height of the bright round spots in the image is $\approx$ 6 nm and the lateral size is $\approx$ 30 nm, which can be consistent with the dimension of BR trimers. We can assume that a dense protein layer was formed after BR solution injection, probably due to the highly concentrated BR-DDM solution. This measurement demonstrated that the protein concentration had to be adjusted properly as BR strongly interacts with the POPC lipid bilayer. Any topographic images of a smaller size than 2 μm were not obtained, because the final system was very soft and viscous, so it was not possible to perform sample imaging without major artifacts.

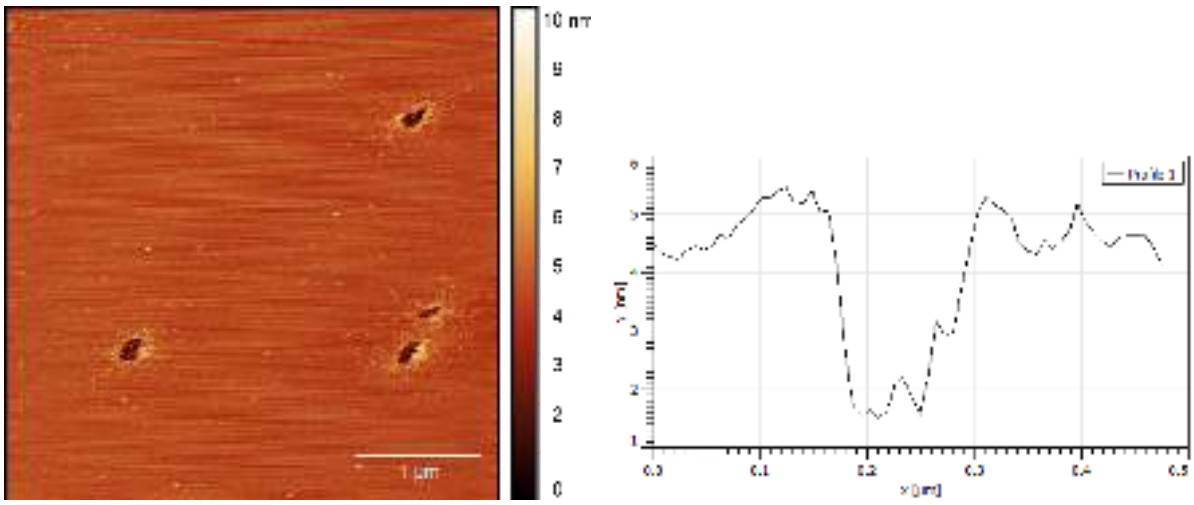

(a) (b)

Figure III.2.11 – (a) AFM topography images of a POPC single bilayer on mica. Image size: 4 μm; (b) Height profile corresponding to the marked region in Fig. III.2.11(a).

Since it was not trivial to work with pure POPC lipid bilayers, we have decided to use domain forming lipid bilayers from a mixture of POPC and DPPC lipids, which are more easily visible with AFM.

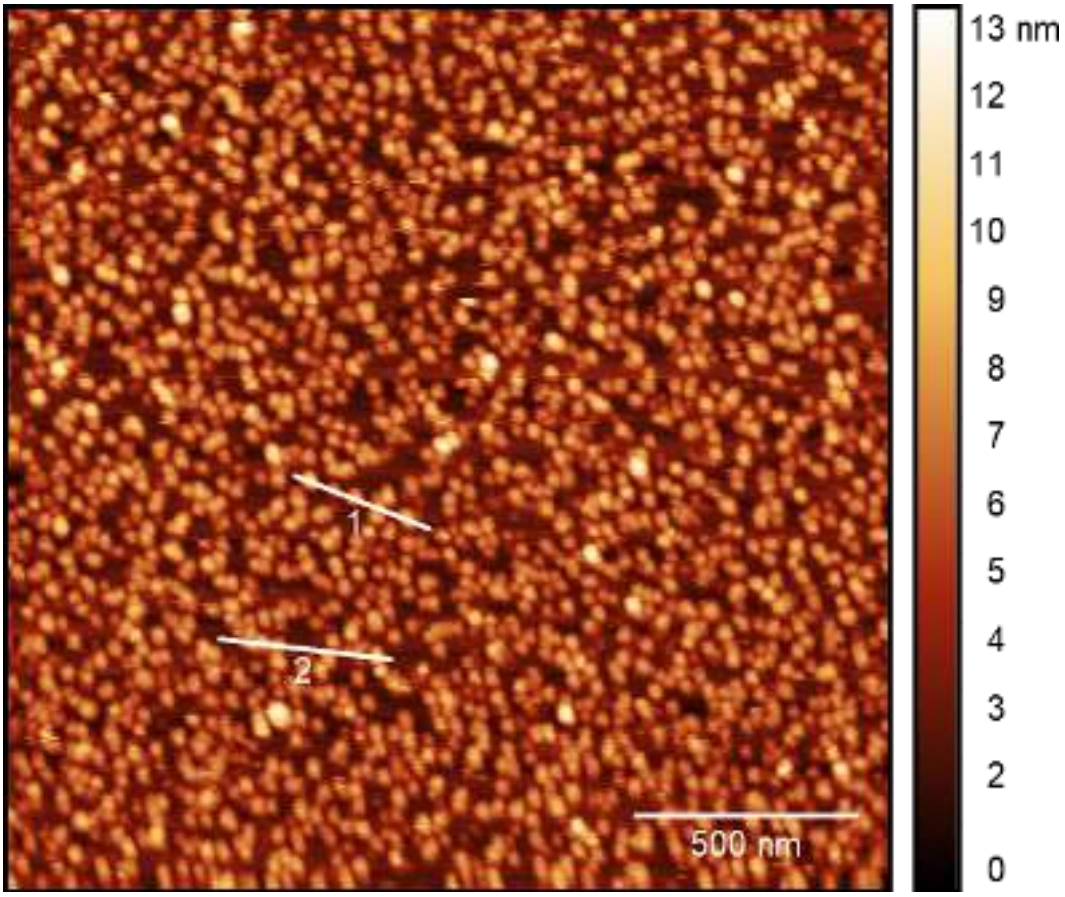

Figure III.2.12 – AFM topography images of a POPC single bilayer with incorporated BR. Image size: 4 μm.

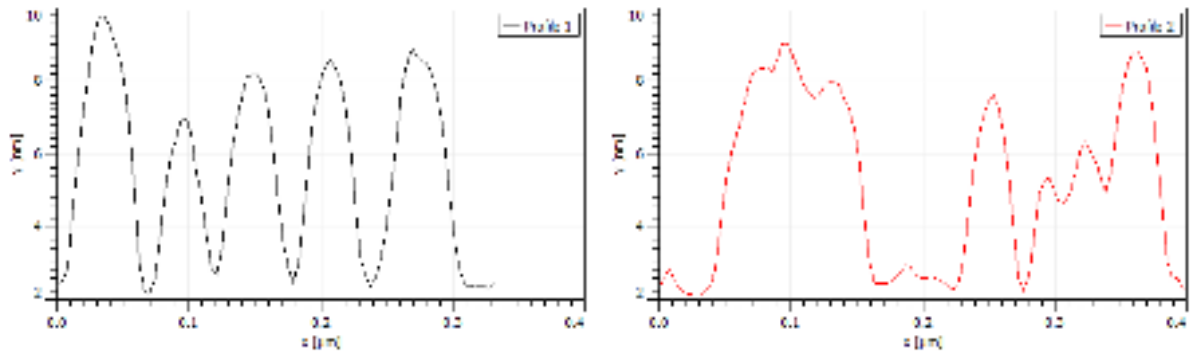

(a) (b)

Figure III.2.13 – (a) Height profile 1; (b) Height profile 2.

2.2.2 BR incorporation into POPC:DPPC single bilayers

Single solid-supported bilayers composed of a mixture of DPPC:POPC lipids (1:1 mol:mol) were formed by vesicle fusion as described in section 1.3.1. The obtained AFM topography images are shown in Fig.III.2.14(a) and III.2.15(a). In Fig. III.2.15(b) the height profile corresponding to the marked region in Fig. III.2.15(a)

is shown. The sample imaging was performed at room temperature, thus the domains formed by the gel-phase DPPC lipids are clearly distinguishable from the fluid phase POPC domains, which makes the interpretation of the outcome of the vesicle fusion and protein incorporation processes much easier.

We have performed protein incorporation by injecting 10 μl of 1 μg/ml BR in 0.05 mM PBS buffer solution with a micro-pipette and leaving the sample at room temperature for 15 minutes of incubation period. The sample was rinsed with PBS buffer and imaged afterwards.

In Fig. III.2.14(b) and III.2.16(a) the obtained topographic images of a bilayer system before and after protein reconstitution are shown. In Fig. III.2.16(b) the height profile corresponding to the marked region in Fig. III.2.16(a) is shown. In Fig. III.2.17 a zoom on selected areas of the lipid bilayer sample with inserted BR is displayed. In the presented figures bright dots of circular shape can be easily distinguished in both regions of the lipid bilayer and on bare mica. These dots are clearly visible in Fig. III.2.17(a), where a patch of the gel phase DPPC lipid bilayer with incorporated BR is shown. These dots have a particular round shape and a lateral size of 35 nm, which may be consistent with the size and shape of BR trimers.

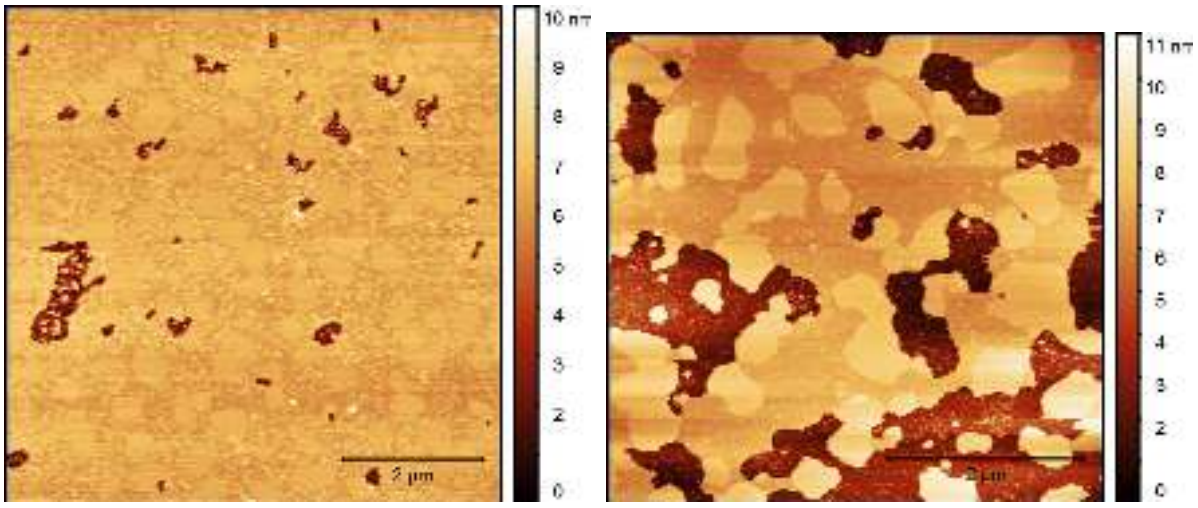

(a) (b)

Figure III.2.14 – AFM topography images of (a) a DPPC:POPC single bilayer on mica. Image size: 7 μm; (b) a DPPC:POPC single bilayer with incorporated BR. Image size: 5 μm.

In Fig. III.2.18 and Fig. III.2.19 topographic images and corresponding height profiles of another DPPC:POPC lipid bilayer sample after BR reconstitution are shown. Protein incorporation was performed following the same procedure as for

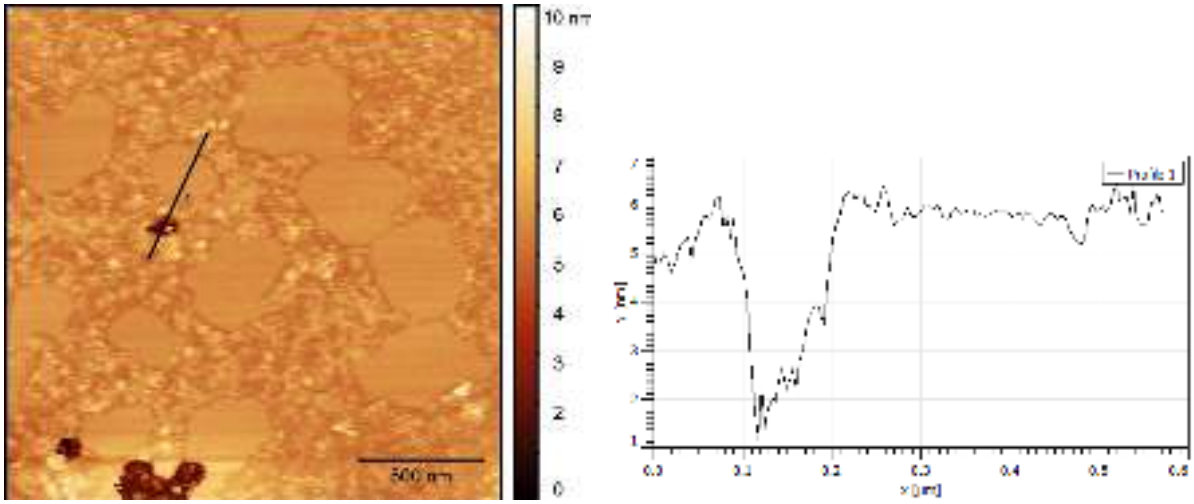

(a) (b)

Figure III.2.15 – AFM topography images of (a) a DPPC:POPC single bilayer on mica. Image size: 2 μm; (b) Height profile corresponding to the marked region in Fig. III.2.15(a).

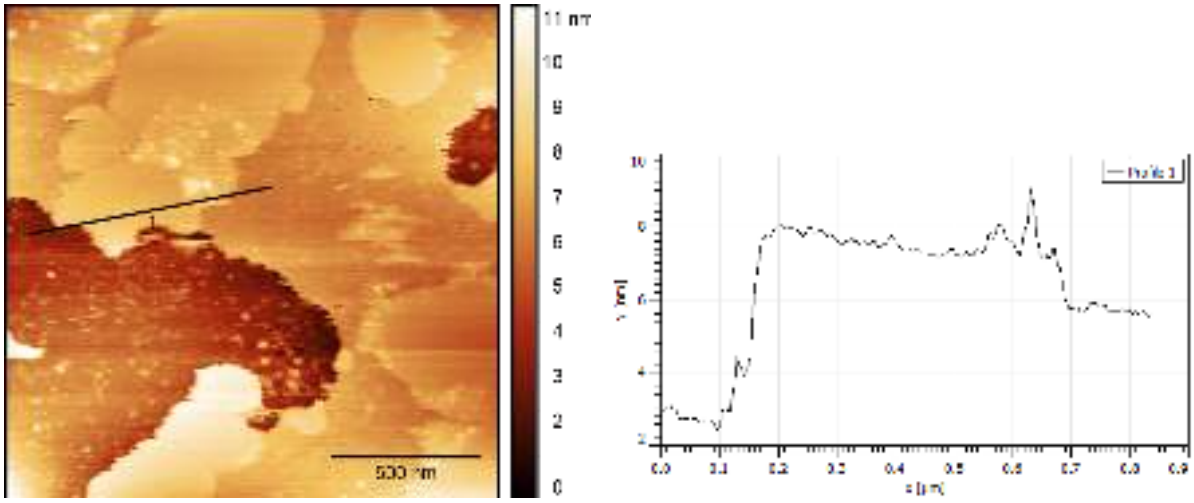

(a) (b)

Figure III.2.16 – (a) AFM topography images of a DPPC:POPC single bilayer with incorporated BR on mica. Image size: 1.7 μm; (b) Height profile corresponding to the marked region in Fig. III.2.16(a).

the previous sample, with an increased concentration of BR (2.5 μg/ml). At the end of the process, a large loss of POPC lipids from the surface was observed, although the domains of DPPC lipid bilayer with and without incorporated BR remained adsorbed on the surface. These measurements have confirmed the previously obtained with AFM result that protein concentration plays one of the decisive roles in the outcome of the reconstitution process. Evidence of the difference in BR interaction with gel and fluid lipid bilayer systems was obtained as well, suggesting

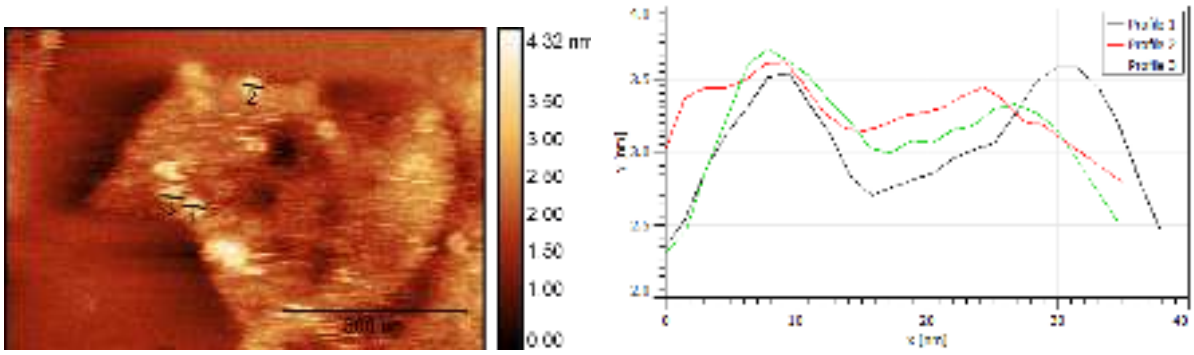

(a) (b)

Figure III.2.17 – (a) AFM topography images of a DPPC:POPC single bilayer with incorporated BR on mica. Image size: 0.8 μm; (b) Height profile corresponding to the marked regions in Fig. III.2.17(a).

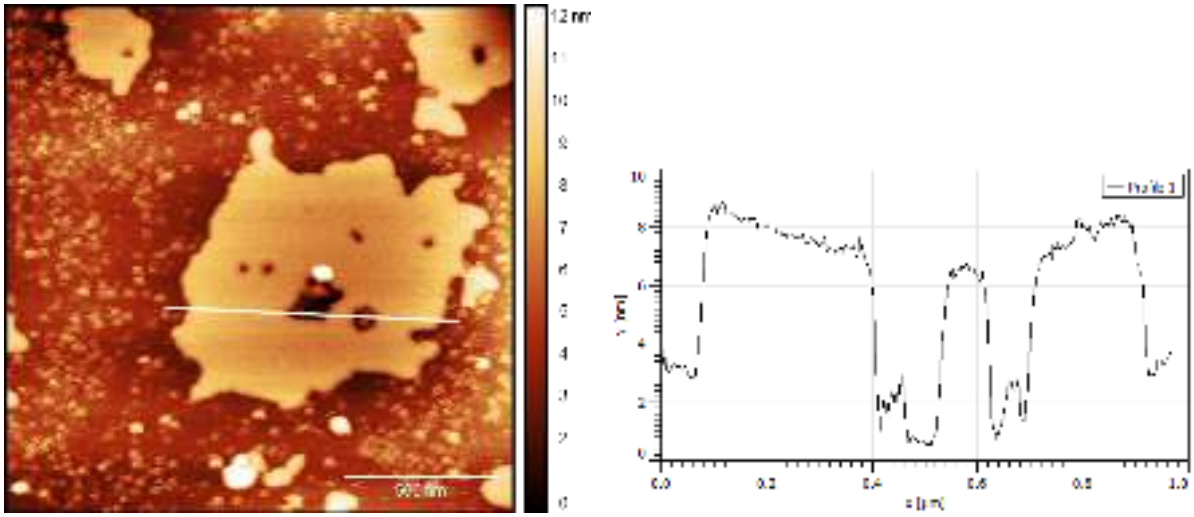

(a) (b)

Figure III.2.18 – (a) AFM topography images of a DPPC:POPC single bilayer with incorporated BR. Image size: 1.7μm; (b) Height profile corresponding to the marked regions in Fig. III.2.18(a).

that the gel-phase lipid bilayer is a more robust system suitable for the detergent mediated protein reconstitution.

Thanks to the performed AFM experiments we were able to demonstrate that BR does not aggregate or unfold in the proximity to the substrate and strongly interacts with the bare mica and lipid bilayer. Also, we have shown that BR incorporates into gel and fluid phase planar lipid bilayer systems in its functional form of a trimer. These results are very promising for the protein activation and membrane fluctuation studies. AFM measurements have demonstrated that protein concentration plays an important role in the reconstitution procedure and lipid bilayer phase plays a

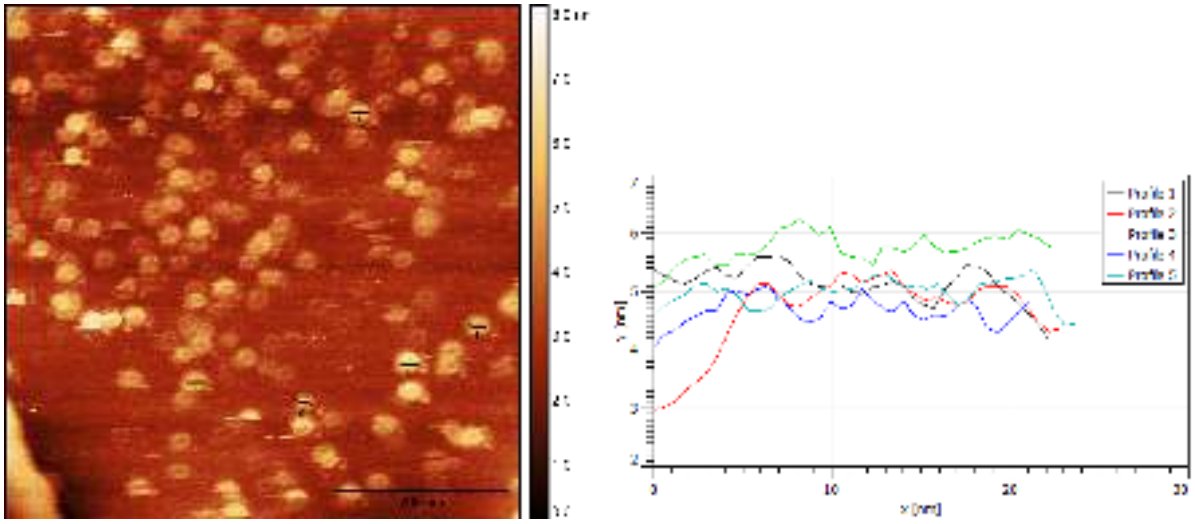

(a) (b)

Figure III.2.19 – AFM topography images of a DPPC:POPC single bilayer with incorporated BR. (a) Image size: 1.5μm; (b) Height profile corresponding to the marked regions in Fig. III.2.19(a).

significant role in the bilayer-protein interaction. Therefore, in order to succeed in the BR reconstitution into lipid bilayers, these parameters have to be carefully chosen and thoroughly adjusted.

2.2.3 AFM experiments on DSPC single bilayers

AFM experiments on single supported DSPC lipid bilayers were performed in Lyon and Grenoble in collaboration with Jean-Paul Rieu (Institut Lumière Matière, Lyon, France).

DSPC lipid bilayer samples were formed by LB/LS deposition on silicon blocks of 2.5x2.5 cm^2 surface as described in section 1.3.6. AFM experiments at the ILM and at the ILL were performed on a XE-70 Park instrument in contact mode using long SiNi tips. The instrument set-up, tip specification and imaging mode are described in section 2.2.

Recorded topographic images of a single solid supported DSPC lipid bilayer are presented in Fig. III.2.20 and Fig. III.2.21(a), the corresponding height profiles of the marked regions in Fig. III.2.21(a) are shown in Fig. III.2.21(b). We have to note that an old not-repolished silicon block was used for this sample preparation, therefore μm-size scratches are visible on the obtained topographic images. The lateral structure of the single DSPC lipid bilayer appears to be very homogeneous

and almost no defects and holes are present in the bilayer structure, unlike the case of the mixed POPC:DPPC lipid bilayer discussed above. The system appears to be very robust to the imaging with the sharp tip.

A "strength" test on the single DSPC bilayer was performed by applying a high force (20 times higher than imaging force) with the AFM tip in order to induce lipid bilayer modification or sample removal from the substrate. No visible bilayer modification or sample damage caused by this test were possible to detect. We can note that no gel-phase lipid bilayer alteration due to the imaging with sharp AFM tip was ever detected, which is different to the case of fluid-phase POPC lipid bilayers.

The height profiles of the defects present in the bilayer (Fig. III.2.21) indicate that the sample thickness is $\approx$ 6 nm, which is consistent with the height of a single DSPC lipid bilayer.

We have tried to perform BR insertion into the DSPC bilayer sample and to follow the structural changes of the bilayer caused by BR insertion with AFM. BR reconstitution was performed injecting solutions of 1-5 μg/ml of BR in 0.05 mM DDM PBS buffer by micropipette onto the sample, incubating for 15 minutes and thoroughly rinsing the system with PBS buffer using micropipettes. After these manipulations, in some cases we were not able to collect any AFM images of the final sample, as it was not possible to approach the sample surface with the AFM tip and to start sample imaging. It can be explained by the presence of remaining detergent molecules in the bulk, which stick to the AFM tip and disturb or even prohibit the imaging process. Additional sample rinsing led to sample disruption. Therefore, further optimization of the sample environment in order to develop an appropriate setup allowing gentle protein-detergent solution injection and thorough sample rinsing will be very helpful for the development of a reproducible and easy sample preparation routine.

In other cases, when using less concentrated protein solution for the BR reconstitution procedure we were not able to detect BR insertion into the single DSPC lipid bilayer. The overall lateral bilayer structure was not modified in the μm-scale after interaction with protein-detergent solution. The obtained result can be consistent with either no BR insertion or BR was reconstituted into the lipid bilayer in a small quantity, but due to the very large imaged area and low resolution of the used AFM,

we were not able to detect BR insertion.

Further optimization of the sample environment, instrument setup and BR reconstitution protocol is needed in order to succeed in BR reconstitution into a gel-phase lipid bilayer and AFM imaging of the single supported lipid bilayer with inserted BR.

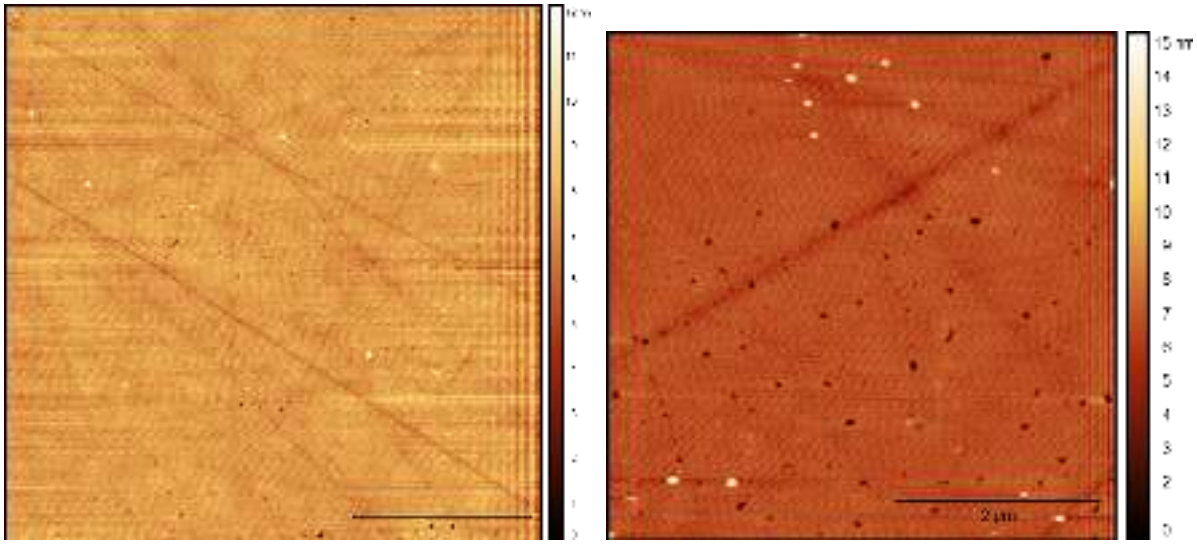

(a) (b)

Figure III.2.20 – AFM topography images of a DSPC single bilayer on silicon. (a) Image size: 15 μm. (b) Image size: 6 μm.

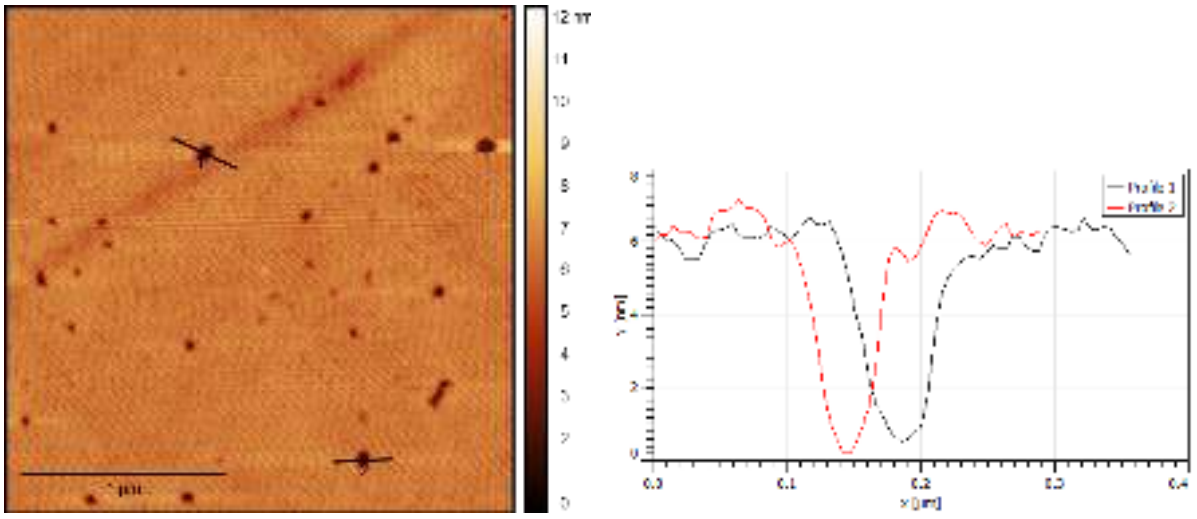

(a) (b)

Figure III.2.21 – (a)AFM topography images of a DSPC single bilayer on silicon substrate. Image size: 2.5 μm. (b) Height profile corresponding to the marked region in Fig. III.2.21(a).

2.2.4 AFM experiment on DSPC trilayer system

We have performed AFM experiments at the ILM (Lyon, France) on lipid trilayer systems in air. A XE-70 Park instrument (section 2.2) in contact mode with a long SiNi tip were used for imaging.

The trilayer sample was composed of three monolayers of DSPC phospholipids and it was deposited on a silicon block of 2.5x2.5 cm^2 surface by LB technique as reported in section 1.3.6.

In Fig. III.2.22 and III.2.23 obtained AFM topography images of a DSPC trilayer system in air are shown. The trilayer appears to be homogeneous with small holes/defects of a depth of 6 nm as can be seen in the height profile in Fig. III.2.22(b). The measured thickness is consistent with the height of the DSPC bilayer. This observation can be explained by the fact that deposition of the first monolayer by LB technique often results in full and homogeneous coverage of the substrate with a DSPC monolayer without any defects. Therefore the measured thickness in the profile in Fig. III.2.22 corresponds to the height between the tails of the first and the third DSPC monolayers.

We have performed trial experiments on DSPC trilayer systems in the attempt to follow the lipid reorganization and lipid bilayer formation from the third DSPC monolayer upon sample hydration. After DSPC trilayer imaging with AFM, several drops of MilliQ water were added by micro-pipette on top of the DSPC trilayer to perform sample hydration and induce lipid reorganization. The outcome of the manipulations was immediately followed by AFM measurements. As a result of these manipulations the third lipid monolayer was completely removed and formation of patches of a double lipid bilayer system upon water addition was not observed. The supported single DSPC bilayer stayed intact and we were able to image this sample in water with AFM.

The loss of the third DSPC monolayer can be explained by the weak interaction between monolayer and bilayer and by the strong water flow which occurs upon water injection. Optimization of the sample hydration method could result in a positive outcome of the experiment - double lipid bilayer formation - avoiding the LS deposition step and proving the possibility to perform AFM imaging in air first, which is more straightforward approach.

Even though this test was not the main goal of our research, this experiment is very interesting and can serve as a good approach to understand lipid self-assembly properties and could provide a new easily formed lipid bilayer model system.

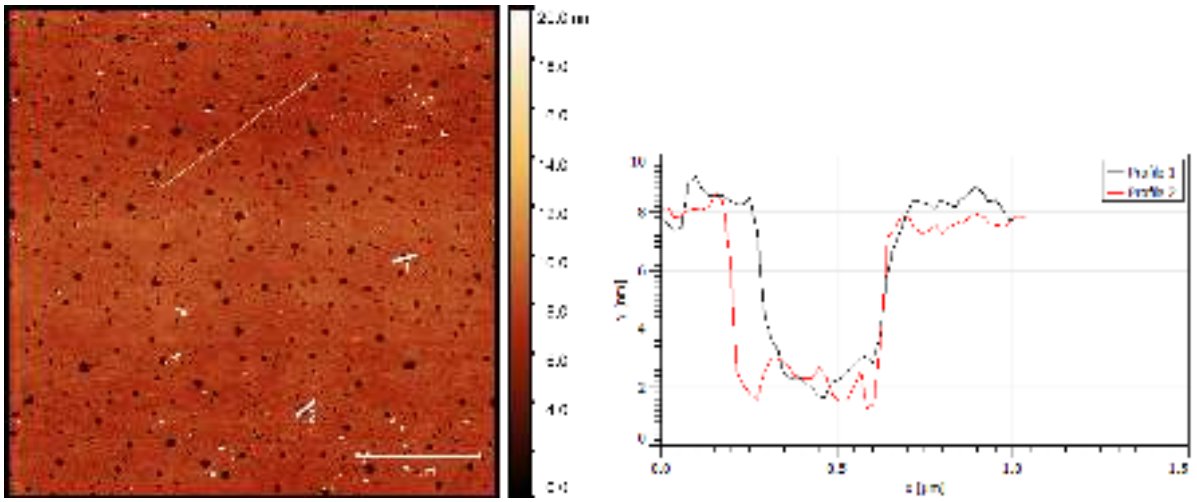

(a) (b)

Figure III.2.22 – (a) AFM topography images of a DSPC trilayer. Image size: 20 μm. (b) Height profile of the noted region in Fig. III.2.22(a).

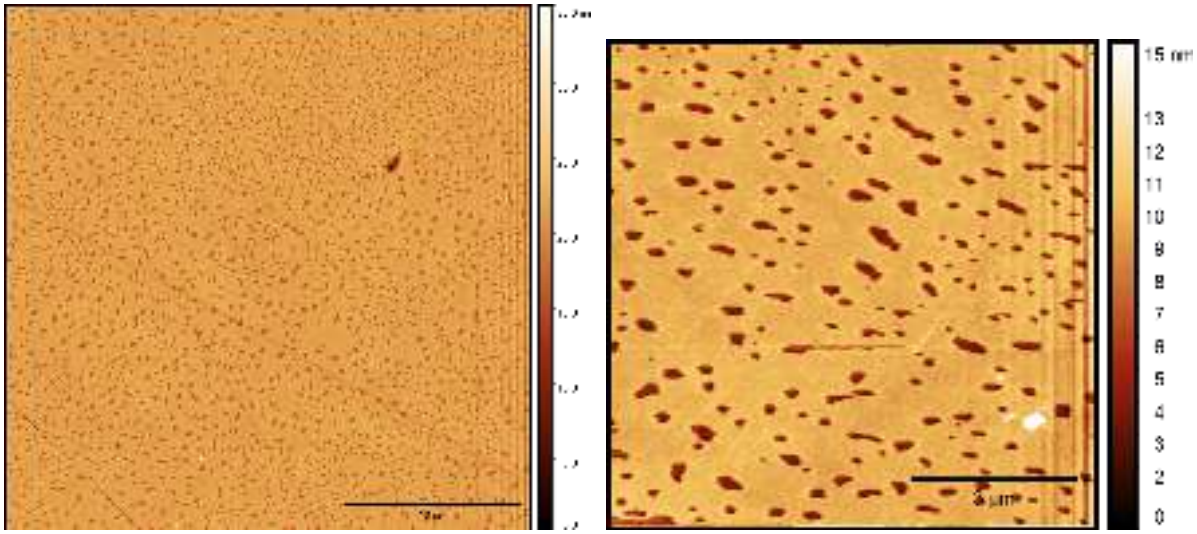

(a) (b)

Figure III.2.23 – AFM topography images of a DSPC trilayer. (a) Image size: 30 μm; (b) Image size: 9 μm.

2.2.5 AFM experiments on DSPC double bilayers

AFM experiments on the double lipid bilayer system were performed in Lyon and Grenoble in collaboration with Jean-Paul Rieu (ILM, Lyon, France). The double

lipid bilayer sample was composed of DSPC lipids and it was formed by LB/LS deposition on a silicon block of 2.5x2.5 cm^2 surface. The detailed sample preparation procedure is discussed in section 1.3.6. AFM experiments at the ILM and at the ILL were performed on a XE-70 Park instrument in contact mode using long SiNi tip. The instruments set-up, tip specification and imaging mode are described in the section 2.2.

As a result of the performed AFM experiments, for the first time AFM topography images of solid supported double lipid bilayer system prepared by LB/LS deposition were collected. The obtained AFM topograpic images and the height profiles corresponding to the marked regions in the topographic images are shown in Fig. III.2.24, III.2.25, III.2.26 and III.2.27.

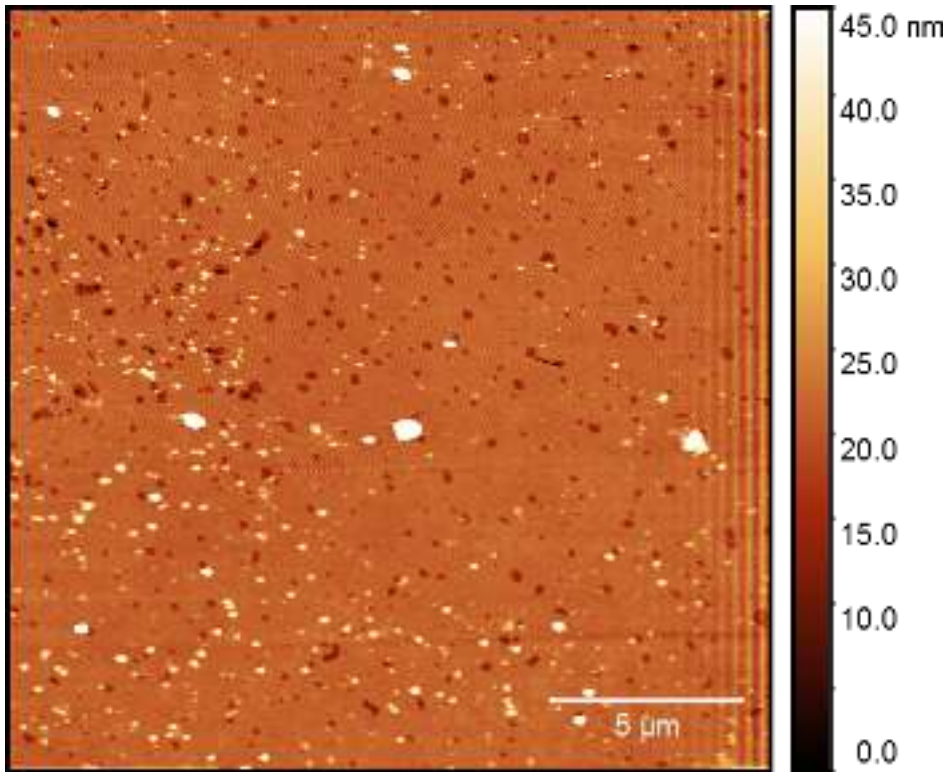

Figure III.2.24 – AFM topography images of a DSPC double bilayer on silicon substrate. Image size: 20 μm.

The height profile lines in the topographic images were drawn through the defective regions in the double bilayer sample. The depth of the bilayer defects can be related to the thickness of the sample on the surface. As can be seen in Fig. III.2.25, III.2.26 and III.2.27 holes of 6 nm and 15 nm are observed in the structure of the bilayer sample. The thicknesses of the single and double DSPC bilayer systems are ≈ 6 nm

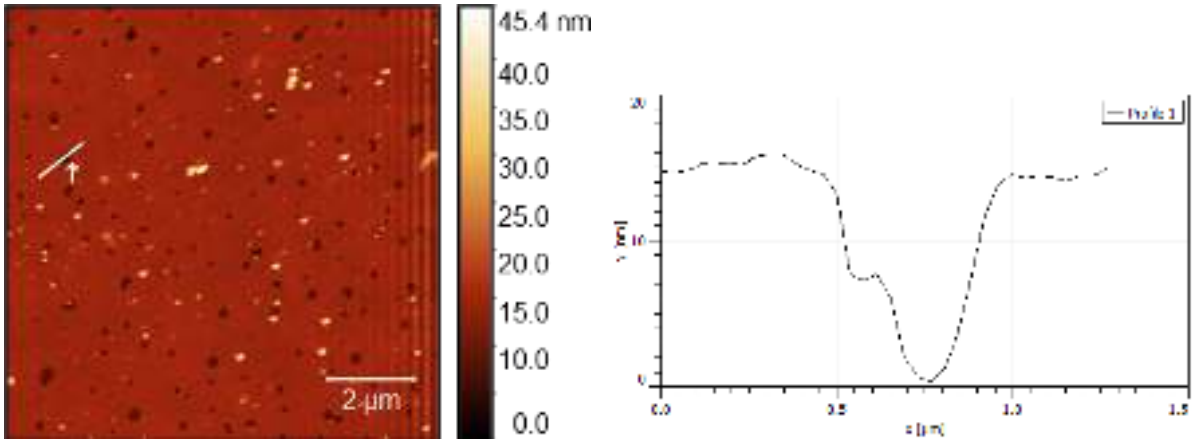

(a) (b)

Figure III.2.25 – (a) AFM topography images of a DSPC double bilayer on silicon substrate. Image size: 10 μm. (b) Height profile corresponding to the marked region in Fig.III.2.25(a).

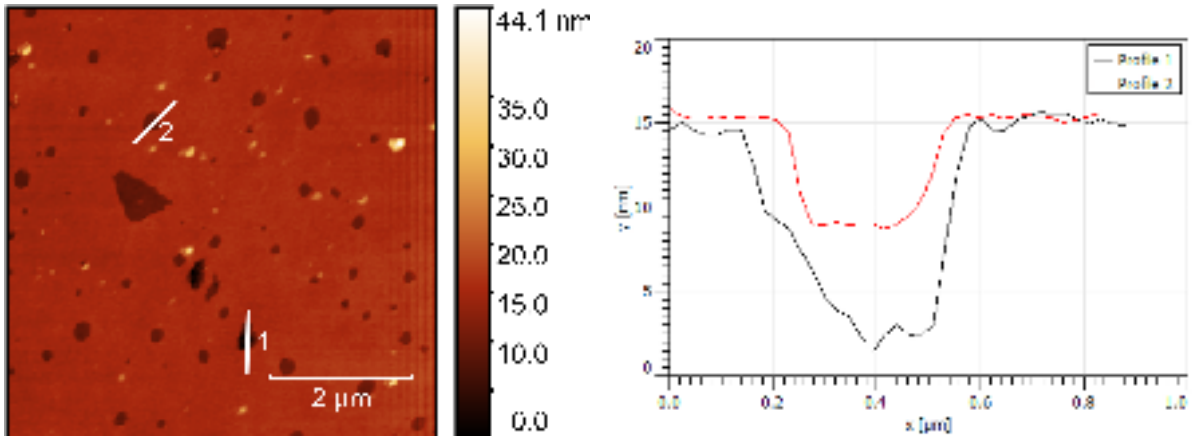

(a) (b)

Figure III.2.26 – (a) AFM topography images of a DSPC double bilayer on silicon substrate. Image size: 6 μm. (b) Height profiles corresponding to the marked regions in Fig. III.2.26(a).

and ≈ 14 nm respectively, which corresponds to the measured thicknesses of the presented defects. The obtained two-step height profiles (Fig. III.2.25 and III.2.27) of sizes ≈ 6-8 nm and 15 nm are consistent with the heights of single (≈ 6 nm) and double (≈ 15 nm) lipid bilayer systems. These observations indicate the presence of a double lipid bilayer sample on the silicon substrate.

To obtain another evidence that the studied system is a double lipid bilayer, we have performed "strength" tests. Applying a high force (10 time higher than the imaging force) we have tried to destroy the sample, removing the second floating lipid bilayer with the AFM tip. In Fig. III.2.28 the AFM topographic image of the

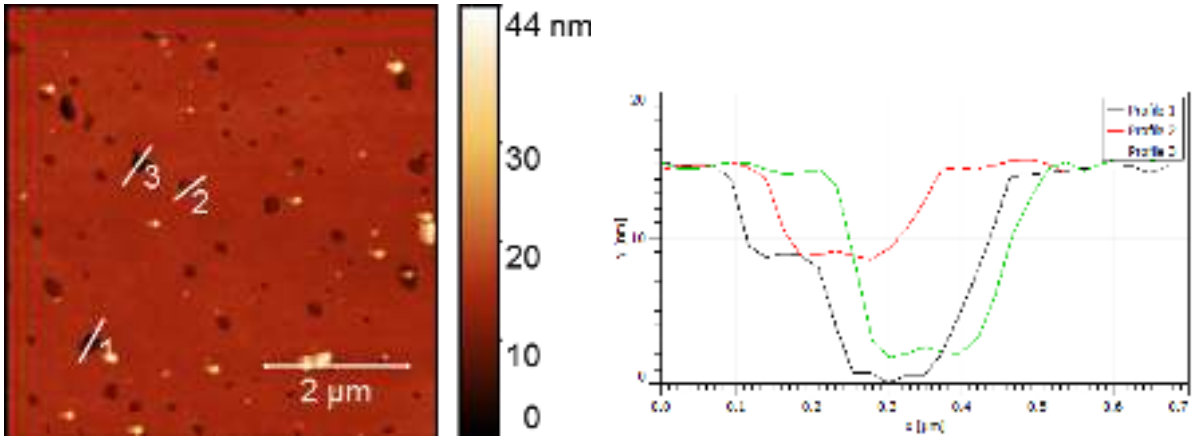

(a) (b)

Figure III.2.27 – (a) AFM topography images of a DSPC double bilayer on silicon substrate. Image size: 6 μm. (b) Height profiles corresponding to the marked regions in Fig. III.2.27(a).

region of a ruined floating bilayer and the corresponding height profiles of the marked regions are shown.

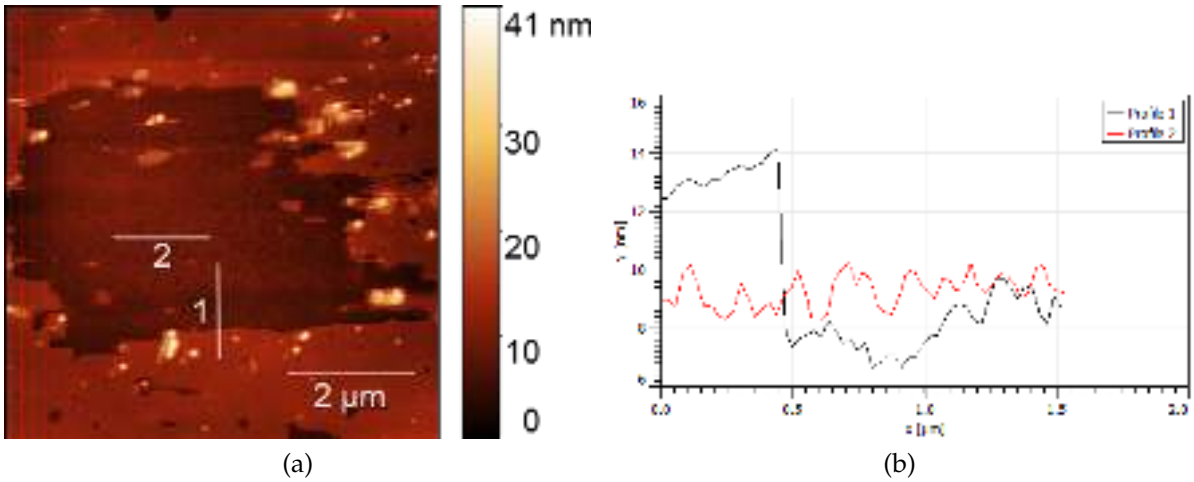

(a) (b)

Figure III.2.28 – (a) AFM topography images of a DSPC double bilayer deposited on silicon substrate. The ruined region of the floating lipid bilayer is shown. Image size: 6 μm. (b) Height profiles corresponding to the marked regions in Fig. III.2.28(a).

As can be seen, applying high force resulted in the destruction and removal of the second floating lipid bilayer. The surface of the first solid supported DSPC bilayer appears to be homogeneous and no structural defects or inhomogeneities were possible to detect. It can be explained either by the low resolution of the used AFM or by the high quality (full coverage) and homogeneous deposition of the first supported DSPC lipid bilayer. The later is often the case, thanks to the chosen sample preparation technique.

We can note that for some double lipid bilayer samples, it was very hard to confirm the presence of the second floating bilayer as no defects in the system structure with thicknesses corresponding to a double lipid bilayer were possible to detect. As an example in Fig. III.2.29 AFM topography images of a DSPC double lipid bilayer system prepared following the same deposition protocol as the previous sample are shown. The depth of all defects presented in this sample is ≈ 6 nm, which corresponds to the thickness of a single lipid bilayer. Therefore, based on the height profile measurements it is not possible to confirm that the studied sample is a double lipid bilayer.

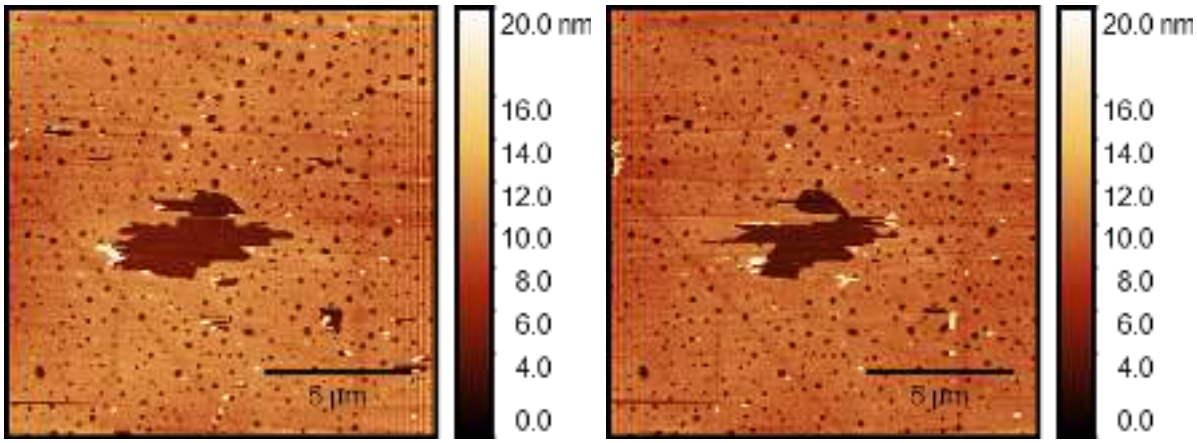

(a) (b)

Figure III.2.29 – AFM topography images of (a) a DSPC double bilayer on silicon substrate. The destroyed region of the floating lipid bilayer due to the imaging is visible. The tip moves over the surface from left to right during the image acquisition. Image size: 15 μm. (b) A DSPC double bilayer on silicon substrate. The destroyed region of the floating lipid bilayer due to the imaging is visible. The tip moves over the surface from right to left during the image acquisition.

The fact that during sample imaging we were able to detect the modification of the lipid bilayer and partial bilayer removal from the surface induced by the AFM tip (Fig. III.2.29) can serve as an indirect evidence of the presence of DSPC double lipid bilayer. In the case of the single supported DSPC bilayers (see section 2.2.3), we were never able to observe DSPC bilayer modification due to the interaction with the AFM tip, as the single solid supported gel-phase lipid bilayer is a very robust system. We can note as well the big difference in the topographic images of the single DSPC and double DSPC bilayers (Fig. III.2.20 and III.2.29), which were obtained in the same experimental conditions: as can be seen a single lipid bilayer possesses

less structural defects than a floating lipid bilayer system and it appears to be more robust and homogeneous.

Taking into account all the discussed arguments and the performed comparisons between single and double lipid bilayers samples, we can conclude that these measurements can serve as a confirmation of the presence of a double lipid bilayer in the discussed case. Double lipid bilayer samples appear to be very fragile and, as it was shown above, application of a very low force with the AFM tip has promoted sample degradation. Therefore the applied force during the image acquisition should be chosen carefully when soft and delicate samples are investigated.

The next step that we aim to achieve is to confirm BR reconstitution into DSPC double lipid bilayers by applying the detergent mediated incorporation approach. Due to lack of time, high complexity of sample preparation for AFM experiments and fragility of the double lipid bilayer system, we did not succeed in the demonstration of BR incorporation into the double lipid bilayer system so far. These experiments are ongoing.

2.2.6 Conclusions

Thanks to the performed AFM experiments we were able to demonstrate that BR strongly interacts with the lipid bilayer and bare support. BR insertion into gel and fluid phase lipid bilayers was observed. It was shown that the lipid bilayer phase plays an important role in the outcome of the reconstitution procedure, as the BR-DDM solution injection had caused removal of a large portion of the fluid lipid bilayer domains. We have shown that BR does not aggregate or unfold in proximity to the substrate and BR organizes into trimers upon reconstitution into the lipid bilayer and upon adsorption onto the bare mica surface. AFM topography images of a double lipid bilayer system were obtained. As a future perspective we aim to confirm BR reconstitution into floating lipid bilayers with AFM experiments. This work is ongoing.

2.3 Fluorescence microscopy

Fluorescence microscopy experiments were performed to study the interaction of the protein BR with single and double lipid bilayers and to investigate the lateral structural modifications of the membrane caused by detergent and protein molecules. Fluorescence microscopy is a lab experimental technique, which is easily accessible (in comparison to NR and XRR experiments), therefore by means of this technique we aimed to develop a robust protocol of BR reconstitution into lipid bilayers, adjusting detergent and protein concentration, as well as incubation/interaction time of detergent-protein solutions with the lipid bilayer systems. We have also performed experiments on both gel and fluid phase bilayers to investigate the influence of the lipid phase on the efficiency of the protein insertion.

Fluorescence microscopy experiments were performed at the ICS, Strasbourg in collaboration with André Schröder using a Nikon TE-2000 (Nikon, Japan) inverted microscope equipped with a mercury light source (Nikon Instruments Inc., Japan) in epifluorescence mode. The instrument description can be found in section 2.3. This microscope is equipped with several microscopy cubes (sets of microscopy filters) which allow to select the wavelength of the emitted light and distinguish the signal of different fluorescent molecules which possess well-separated emission peacks.

We have used two different fluorescent markers to label both lipid bilayer and protein molecules. The fluorescent markers were chosen in such a way that two different microscopy cubes could be used to visualise separately either lipid bilayer or protein molecules (see section 2.3.3). For lipid bilayer labelling 1% (by weight) of NBD-PE lipids were added to the solution of lipids in chloroform. BR molecules were labelled with Cy3 dye following the procedure reported in section 1.4.5.

Lipid bilayer samples were deposited on a very thin microscopy slide (thickness $\approx$ 0.13-0.17 mm) using LB/LS deposition techniques as discussed in section 1.3.6. The great advantage of the LB/LS techniques is the possibility of asymmetric lipid bilayer preparation, as the deposition of each monolayer is performed separately and therefore the composition of each monolayer of the bilayer system can be varied independently.

Thus, forming samples by LB/LS deposition, only the last monolayer of the bilayer system, which is the most distant from the substrate and formed by LS

technique, was labelled fluorescently with NBD-PE lipids. These manipulations were done in order to obtain certainty that the visualised sample was a bilayer (either single or double), as these systems are very fragile and can be easily ruined during the last LS preparation step or during sample transportation. A new solid/liquid cell which was designed and developed within this thesis project (see description in chapter 2.4) and which is compatible with the LB/LS deposition techniques and the inverted fluorescence microscope, was used to host the sample.

Using the fluorescence microscopy technique, membrane surface morphology can be imaged with μm resolution, therefore the detailed structure of both lipids and proteins molecules cannot be resolved.

Due to limited depth-of-field of the available microscope protein incorporation into the lipid membrane could not be confirmed, as it was not possible to distinguish between protein adhesion to the lipid bilayer and its partial or full incorporation. Using this technique, immobile proteins which are attached/incorporated into the lipid bilayer can be discerned from the proteins floating in the bulk.

2.3.1 Incorporation of BR into a solid supported single lipid bilayer

Fluorescence microscopy experiments were carried out to study the lateral morphology of pristine lipid bilayers systems at micron scale. We aimed to visualise the bilayer before and after protein incorporation in order to reveal the effect of detergent and protein molecules on the lateral structural features of the sample and to obtain evidence of BR reconstitution into the bilayer.

We will present the performed experiments on single planar supported bilayer systems composed of DPPC lipids. DPPC lipid bilayers were formed by LB/LS techniques as described in section 1.3.6. In Fig. III.2.30(a), a fluorescence image of a pristine DPPC lipid bilayer is shown. Dark spots in the image indicate the presence of defects in the lipid bilater structure. BR incorporation was performed injecting a solution of 1 μg/ml BR in 0.05 mM DDM PBS buffer into the cell, incubating for 15 minutes and rinsing the system with PBS buffer. All manipulations with the sample were performed at room temperature, so the lipid bilayer was in gel phase. The images in Fig. III.2.31(a) and III.2.32(a) were obtained using a microscopy cube consisting of a set of filters that transmit the emitted light from NBD-PE fluorescent

lipids, but block the signal from the protein dye (cube for lipid visualization) and the image in Fig. III.2.31(b) and III.2.32(b) were taken using another microscopy cube equipped with a set of filters that transmit only the emitted light from the Cy3 dye of the BR molecule, but block the signal from the NBD-PE lipids (cube for BR visualization). We can note that before protein incorporation there was no signal detected when using the cube for the BR visualization as can be seen in Fig. III.2.30(b) (blank experiment), thus all the fluorescence signal detected after BR reconstitution originated only from the protein marker.

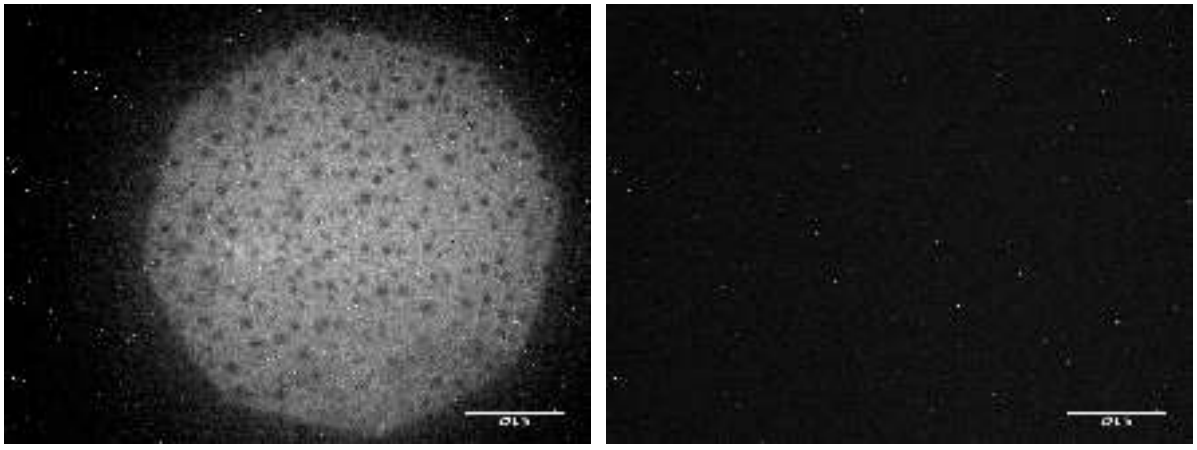

(a) (b)

Figure III.2.30 – Fluorescence microscopy image of a DPPC single bilayer at room temperature: (a) lipids visualised, (b) proteins visualised (blank experiment).

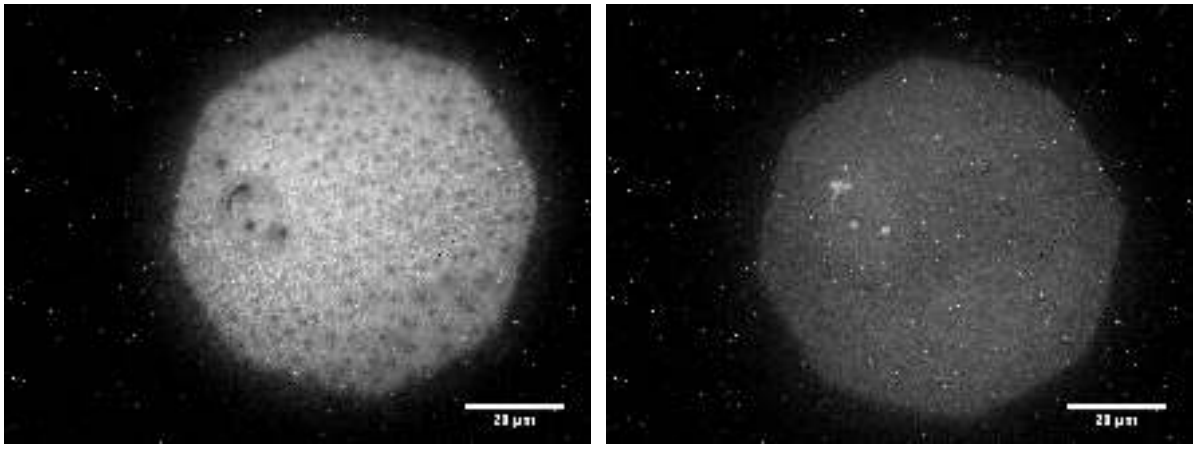

(a) (b)

Figure III.2.31 – Fluorescence microscopy images of a DPPC single bilayer after BR reconstitution at room temperature: (a) lipids visualised, (b) proteins visualised. A 1 μg/ml BR in 0.05 mM DDM PBS buffer solution was used for the BR reconstitution.

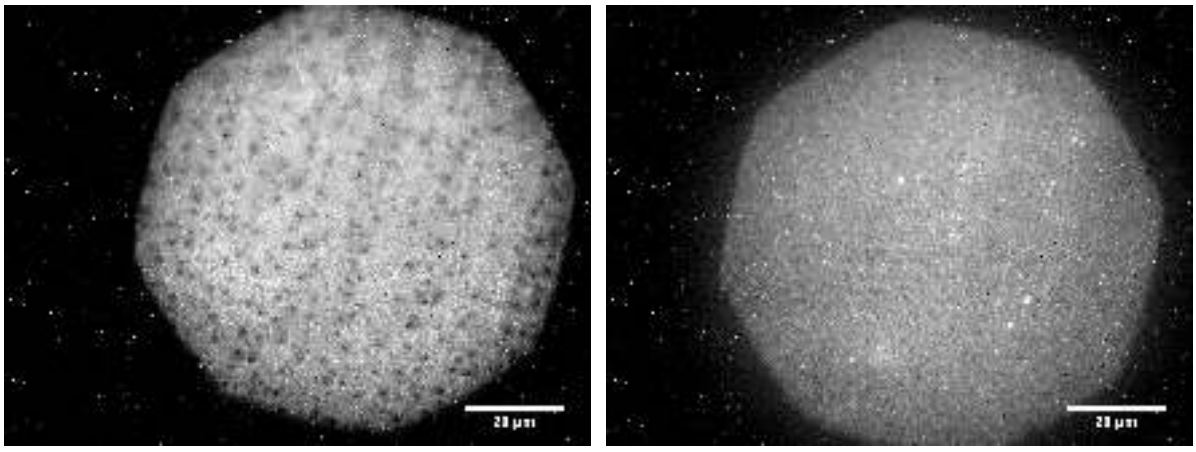

(a) (b)

Figure III.2.32 – Fluorescence microscopy images of a DPPC single bilayer after BR reconstitution at room temperature: (a) lipids visualised, (b) proteins visualised. A 1 μg/ml BR in 0.05 mM DDM PBS buffer solution was used for the BR reconstitution.

We have performed fluorescence microscopy experiments varying the concentration of BR by using 3 μg/ml, 5 μg/ml and 10 μg/ml BR solutions in 0.05 mM DDM PBS buffer. After the BR reconstitution step using these solutions, we were not able to detect any fluorescence signal from the lipid bilayer, thus the samples were solubilized and removed from the substrate.

2.3.2 Incorporation of BR into double lipid bilayer

Fluorescence microscopy experiments on DSPC-DPPC double bilayer systems were performed (section 1.3.6 for the details of sample preparation) to probe the lateral structure of the pristine floating bilayer at the micro-scale and to follow structural changes induced by BR reconstitution into the lipid bilayer.

In Fig. III.2.33(a) and Fig. III.2.34 the fluorescence microscopy images of a pristine DSPC-DPPC double lipid bilayer are shown. Dark areas with the bright boarder in figures indicate the presence of defects in the lipid bilayer structure. BR reconstitution was performed at room temperature (DSPC and DPPC lipid bilayers were in gel phase) applying the detergent incorporation method: a 1 μg/ml BR in 0.05 mM DDM PBS buffer solution was injected into the cell, incubated for 10 minutes and then rinsed out with PBS buffer. In Fig. III.2.35 the DSPC-DPPC double lipid bilayer system after BR incorporation is shown. As for the case of single lipid bilayers, the image in Fig. III.2.35(a) was taken using the cube for the lipid bilayer visualisation

and the image in Fig. III.2.35(b) was taken using the cube for the BR detection. For this sample the "blank" experiment was performed as well and no signal was detected form the sample before BR reconstitution, when using the set of filters for BR imaging (Fig. III.2.33(b)).

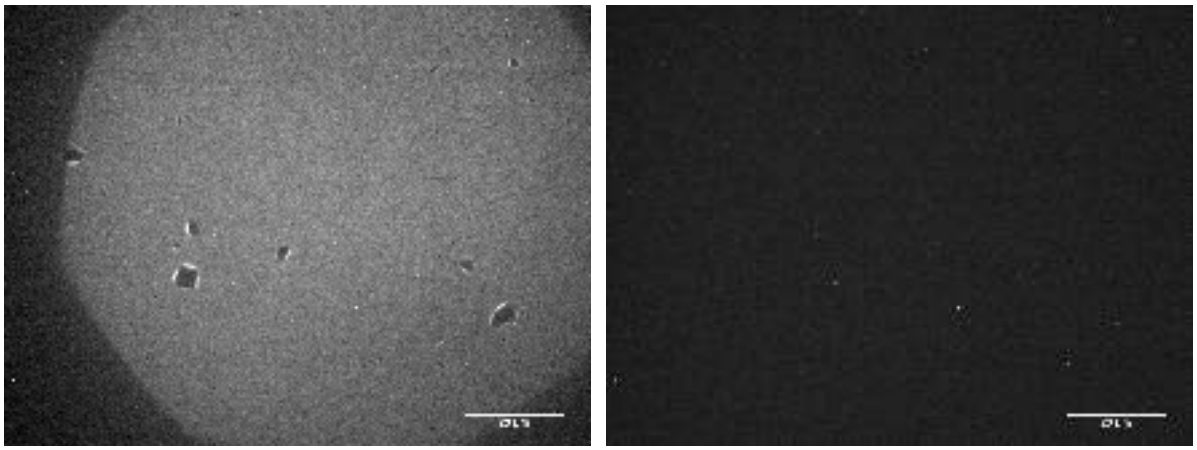

(a) (b)

Figure III.2.33 – Fluorescence microscopy images of a DSPC-DPPC double bilayer at room temperature: (a) lipids are visualised, (b) proteins are visualised (blank experiment).

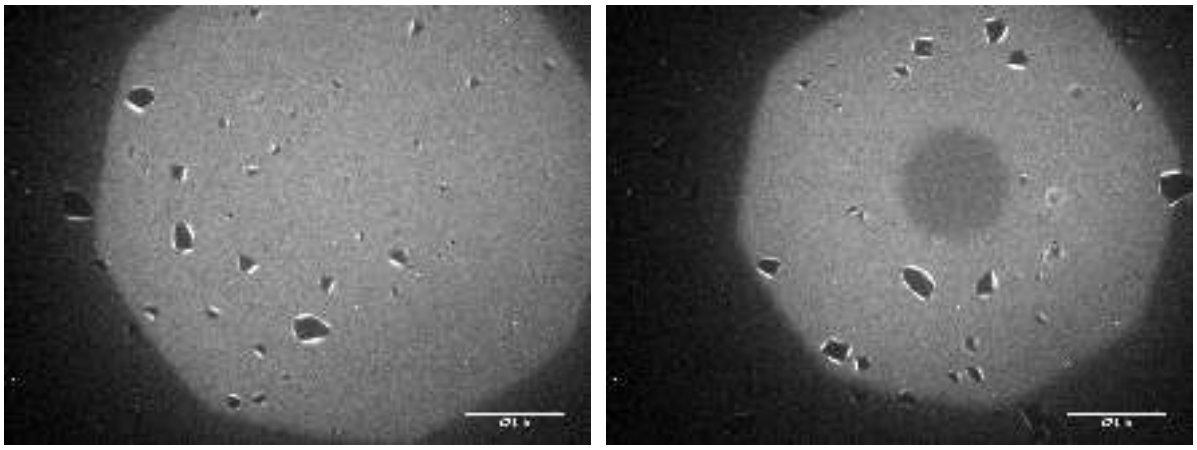

(a) (b)

Figure III.2.34 – Fluorescence microscopy images of a DSPC-DPPC double bilayer at room temperature when lipids are visualised. The dark area in the Fig. III.2.34(b) is an area with bleached fluorescent lipid.

To test membrane stability and to increase the amount of BR inserted, we performed a second injection of the same BR-DMM solution into the cell. After 10 minutes of incubation followed by rinsing with detergent-free buffer, we were able to detect (using the cube for protein visualization) an increase of fluorescence signal

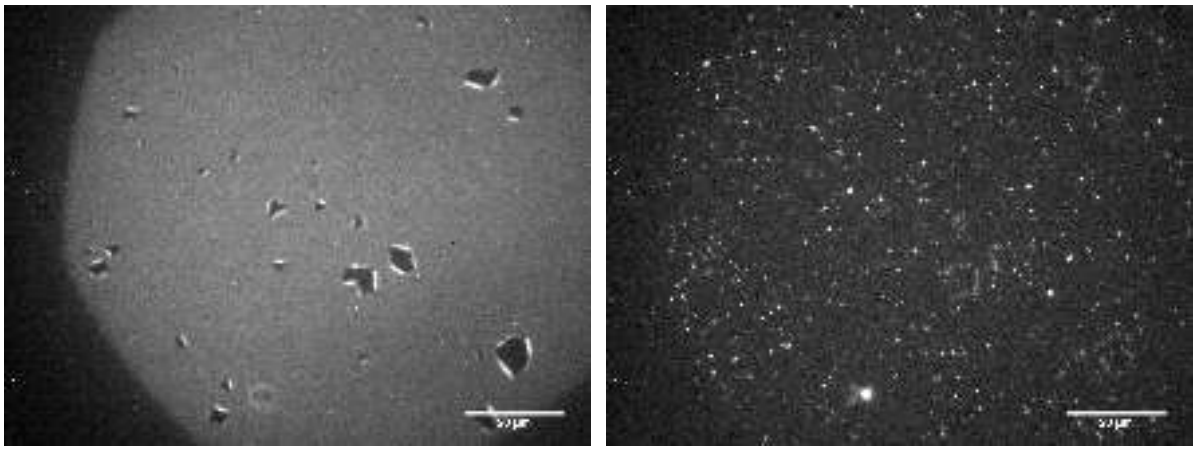

(a) (b)

Figure III.2.35 – Fluorescence microscopy images of a DSPC-DPPC double bilayer after BR reconstitution at room temperature: (a) lipids are visualised, (b) proteins are visualised. A 1 μg/ml BR in 0.05 mM DDM PBS buffer solution was used for the BR reconstitution.

emitted by the fluorescent dye of the BR molecule (Fig. III.2.36). This effect can be explained by the larger amount of proteins reconstituted into the membrane system after the repeated reconstitution step. As we can see the system remained stable and no bilayer loss or destruction occurred upon both injection steps.

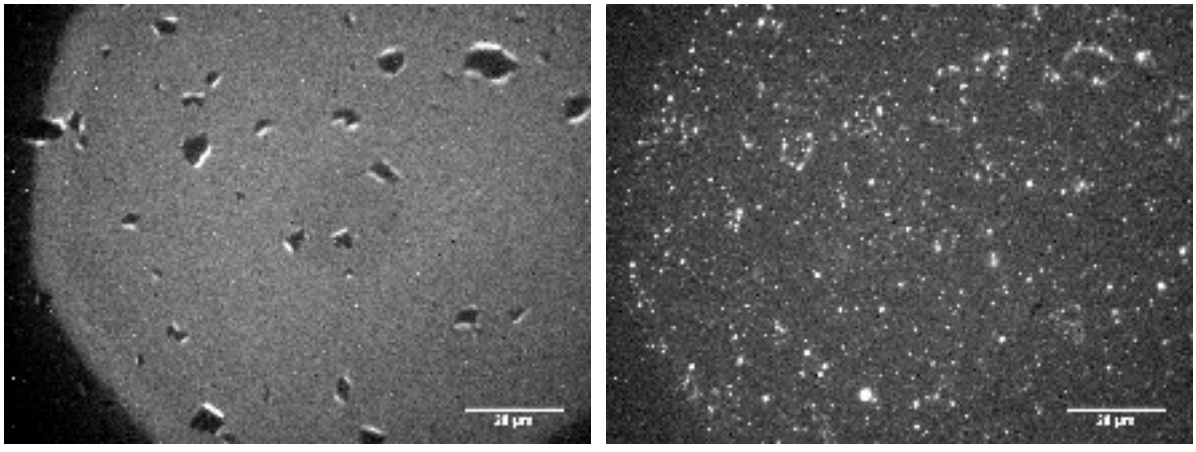

(a) (b)

Figure III.2.36 – Fluorescence microscopy images of a DSPC-DPPC double bilayer after BR reconstitution (second injection) at room temperature: (a) lipids are visualised, (b) proteins are visualised. A 1 μg/ml BR in 0.05 mM DDM PBS buffer solution was used for the BR reconstitution (second injection).

Due to the experimental configuration it was not possible to image the same spot of the sample before and after BR reconstitution: the imaged area is $\approx 10^{-2}$ mm^2, which is substantially smaller than the whole area of the sample (≈ 700 mm^2),

therefore it is not possible to track the position of the studied area. Despite this fact we can note that the overall structure of the sample at micron scale remained mostly unchanged. We have noticed the growth and enlargement of the existing defective regions in the floating lipid bilayer upon each reconstitution step. But no definite conclusion can be made as we were not able to precisely follow the modification of the same spot on the sample.

It is reasonable to assume that BR insertion into planar bilayer systems can be facilitated by performing the insertion into a fluid phase lipid bilayer. In order to test the influence of lipid bilayer phase on the efficiency of protein incorporation, we have carried out experiments testing BR insertion into the following lipid bilayer systems: DPPC single bilayer and DSPC-DPPC double bilayer measured both at 48°C, so that the solid supported DSPC bilayer was kept in the gel phase and the DPPC bilayer was brought to the fluid phase in both samples.

Injection of the BR solution at very low concentrations (0.5 and 1 μg/ml) caused solubilization of the floating bilayer and sample destruction, as we were not able to detect any signal from the sample after the incorporation step. Based on the results of several experiments, we can conclude that the fluid lipid bilayer systems appear to be unstable and too fragile for protein reconstitution using the detergent-mediated incorporation approach.

The influence of the substrate on the membrane stability should be taken into account as well. It is known that the substrate's chemical structure and roughness have a great impact on the bilayer properties and sample stability [56, 58, 196]. Lipid bilayer samples for the microscopy experiments were formed on microscopy glass slides, which have a surface roughness of $\approx$ 2.5 nm. This is substantially larger than the roughness of the silicon substrates (roughness $\approx$ 0.3-0.7 nm) typically used for NR and XRR experiments. This difference in nature and structure of the solid supports can explain the increased sample fragility and unsuccessful outcome of BR incorporation into the fluid floating bilayer.

We have run experiments varying the incubation time (10, 15, 20 minutes) of a 1 μg/ml BR in 0.05 mM DDM solutions with single and double lipid bilayers in the gel phase. 10 minutes incubation time were enough to detect BR in the lipid bilayer, but due to the low microscope resolution it was not possible to distinguish

any difference in the signal upon 10, 15 or 20 minutes of incubation, therefore we were not able to judge whether a larger amount of BR was inserted upon longer incubation periods.

2.3.3 Lipid diffusion in supported lipid bilayers

In order to follow lipid and protein diffusion in the bilayer we have performed bleaching experiments of both lipid and protein molecules in single and double lipid bilayer systems with and without incorporated BR.

To induce bleaching of fluorescent molecules, the aperture diaphragm was closed, leaving a small area of the sample under illumination. The intensity of the light was increased in order to kill the fluorescent dyes in the exposed area. The sample was left under illumination for approximately 30 seconds, afterwards the light intensity was decreased and the aperture diaphragm was opened to perform sample imaging and to follow the recovery of the fluorescence signal due to the lipid or protein molecules diffusion between bleached and not-bleached areas. It should be noted that during imaging the fluorescence signal from the whole sample is gradually eliminated as well, thus light of small intensity should be used for the sample visualisation.

Following the procedure reported above we have performed lipid bleaching experiments on three samples: a gel-phase single bilayer composed of DPPC lipids at room temperature (Fig. III.2.37) (1); a DSPC-DPPC double bilayer system measured at room temperature (Fig. III.2.34 and III.2.38(a)) (2) and at 48°C (Fig. III.2.38(b)) (3), which means that the floating DPPC bilayer was either in gel or fluid phase.

The obtained fluorescence images are shown in Fig. III.2.37, III.2.38 and III.2.39. The dark region in the middle of the bilayer sample is the region where the fluorescent lipids are bleached. We have tried to roughly estimate the diffusion coefficient of lipid molecules, by recording the time needed for the signal to recover in the bleached region. The diffusion coefficient can be estimated using the following formula [197] :

$$D = \frac{x^2}{4\tau} \tag{2.3}$$

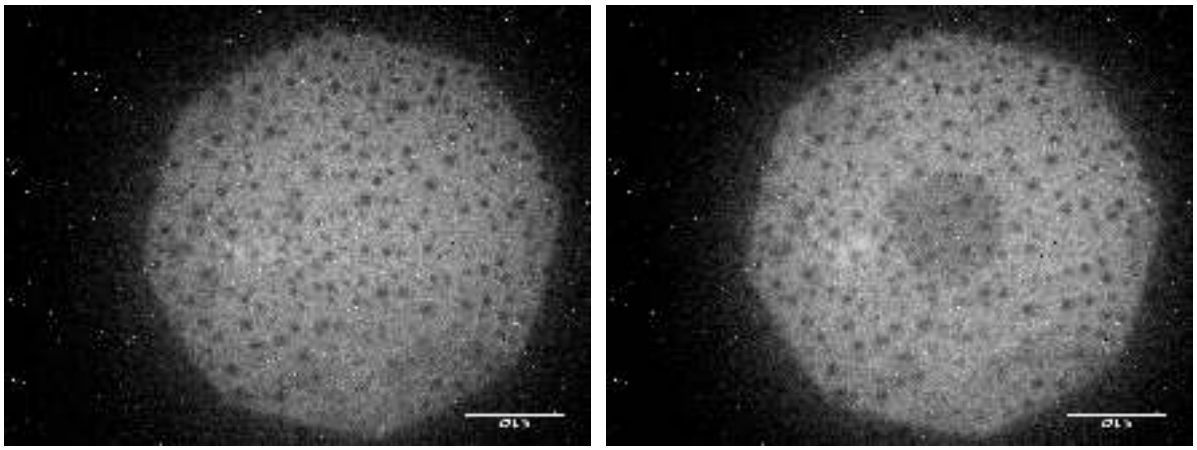

(a) (b)

Figure III.2.37 – Fluorescence microscopy images of a DPPC single bilayer at room temperature. In Fig. III.2.37(b) the area with bleached fluorescent lipids are shown.

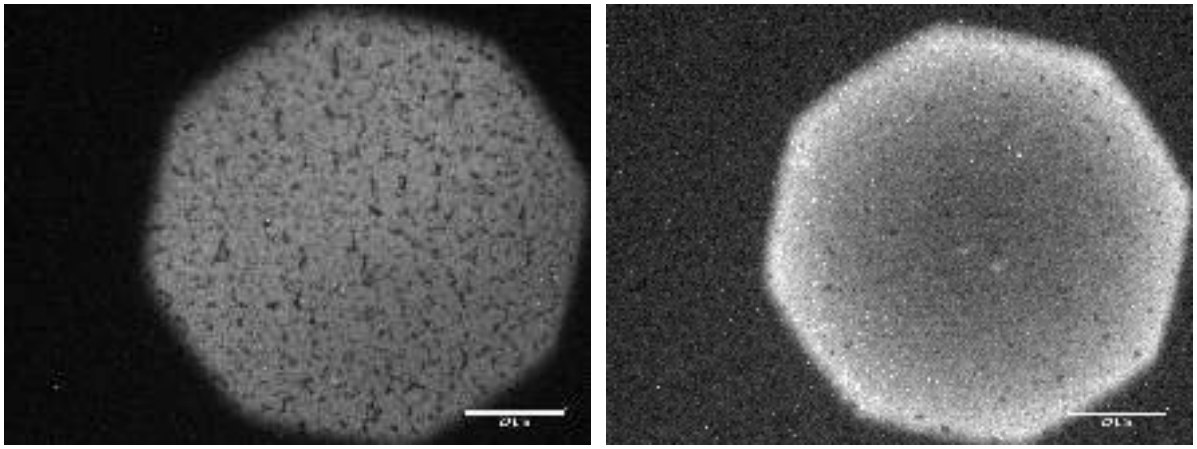

(a) (b)

Figure III.2.38 – Fluorescence microscopy images of a DSPC-DPPC double bilayer (a) at room temperature and (b) at 48°C.

where D is the diffusion coefficient, x is the root mean square displacement during the time τ.

By knowing the size of the bleached area and the time needed for the fluorescence signal recovery τ, we have found that the diffusion coefficients for the single supported gel-phase DPPC lipid bilayer is $\approx 7\ \mu m^2/s$, for the gel-phase floating lipid bilayer is ≈ 0.3 - $1\ \mu m^2/s$ and for the fluid-phase floating lipid bilayer it is $\approx 5\ \mu m^2/s$.

As expected, bleaching and fluorescence recovery was much faster when the lipid bilayer was in the fluid phase, which can be explained by the faster molecular diffusion (larger diffusion coefficient) at high temperature. A slightly smaller value of the diffusion coefficient was estimated for the single solid supported gel-phase

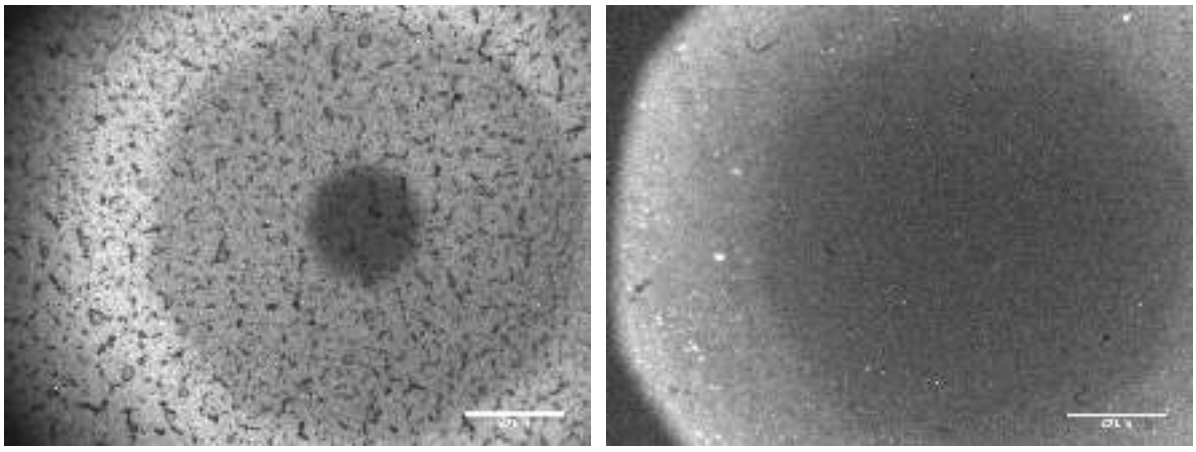

(a) (b)

Figure III.2.39 – Bleaching experiments on a DSPC-DPPC double bilayer (a) at room temperature and (b) at 48°C.

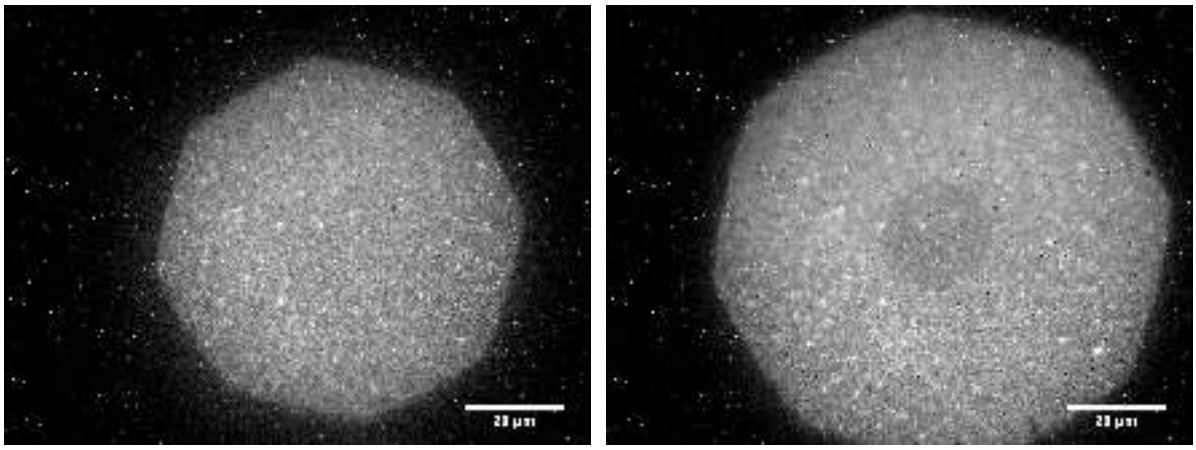

(a) (b)

Figure III.2.40 – Fluorescence microscopy images of a DPPC single bilayer after BR reconstitution at room temperature. Proteins are visualised. A 1 μg/ml BR in 0.05 mM DDM PBS buffer solution was used for the BR reconstitution. In Fig. III.2.40 the region with the bleached BR molecules is shown.

lipid bilayer than for the floating one, which can be explained by the reduced lipid mobility due to the proximity of the substrate. The obtained values of the diffusion coefficients are consistent with the values reported in literature [197–199]. We have to note that the performed estimation is a very rough approach, as the illumination area is very large and it was not measured precisely. The time needed for recording the signal recovery and fluorescent intensity were not controlled precisely as well. To obtain a more accurate estimation of the diffusion coefficient D, FRAPP experiments can be performed on the planar bilayer systems [197, 200, 201].

BR diffusion in supported lipid bilayers.

To probe BR diffusion we have carried out protein bleaching experiments in the single and double lipid bilayer systems at room temperature. In Fig. III.2.40 the fluorescence microscopy images of a single DPPC bilayer with incorporated BR are shown. The images were obtained using the set of filters for BR visualization. A very long exposure time was needed (around 7 minutes) to kill the fluorescence marker of the protein. Such a long bleaching time can be related to the high stability of the Cy3 dye. We did not follow the recovery of the signal in this case as it was very long, supposedly due to the very low mobility of the BR close to the substrate. We have tried to perform protein bleaching experiments in the floating lipid bilayer system with inserted BR. Unfortunately we were not able to detect any signal reduction after 10 minutes of exposure to the high intensity light. This fact can be explained again by the high stability of protein marker.

2.3.4 Conclusions

Thanks to the performed fluorescence microscopy experiments, we were able to obtain an evidence of BR reconstitution into single and double gel-phase lipid bilayer samples. We have shown that the fluid-phase lipid bilayer is a very fragile model system for the protein reconstitution studies using the detergent-mediated approach. The diffusion coefficients of lipids and proteins molecules in the gel-phase lipid bilayer systems were estimated based on the performed bleaching experiments.

Unfortunately, by using fluorescence microscopy techniques we could not distinguish between protein reconstitution, protein partial incorporation or protein adhesion to the lipid bilayer due to the low resolution of the technique. Information about sample structure is known only to the micron scale, therefore we can not obtain a qualitative estimation of the bilayer modification induced by the interaction with protein and detergent molecules and thus cannot quantify the amount of protein inserted. Therefore, NR and XRR experiments should be performed to obtain the information on sample structure and composition at Å-scale.

CHAPTER 3

Protein insertion in floating bilayers

3.1 In-house X-Ray reflectometry

Thanks to the performed AFM and fluorescence microscopy experiments we have obtained evidence that the protocol for BR reconstitution based on detergent-mediated incorporation into single and double lipid bilayer systems works more efficiently when the lipid bilayer is in the gel phase. Numerous attempts to insert BR into fluid lipid bilayers often resulted in the lipid bilayer full or partial removal.

To further develop a robust protocol for the protein reconstitution into planar membranes and to confirm protein insertion into the model bilayer systems, we have performed X-Ray reflectometry experiments using a X-ray bench instrument (see section 2.8 for the instrument description) available at the ILL. Our experiments contributed to the test of the newly acquired sample environment. To be able to carry out these experiments, we have designed and fabricated solid/liquid cells which fulfuill all the requirements imposed by the in-house XRR instrument configuration. A description of this sample environment can be found in section 2.4. Due to the lack of time within this PhD project, no thermalization chamber for the sample temperature control was developed, thus all XRR experiments were carried out at room temperature.

3.1.1 BR reconstitution into a DSPC single bilayer

We have performed in-house XRR experiments on a DSPC single lipid bilayer sample in order to confirm BR reconstitution into gel-phase bilayers. A single DSPC bilayer was formed by LB/LS techniques, following the protocol reported in section 1.3.6. XRR measurements were performed on the pristine DSPC bilayer

and the bilayer after BR insertion. Reflectivity curves, fits and corresponding SLD profiles of the system before and after BR insertion are shown in Fig. III.3.1. The structural parameters obtained from the fit of the reflectivity curve for the pristine DSPC bilayer (Tab. B.12) indicate a good quality (good coverage) sample and are in agreement with the values known from literature [35, 202]. BR reconstitution was performed by injecting solution of 2.5 μg/ml BR in 0.05 mM DDM PBS buffer, incubating for 10 minutes and rinsing the system with buffer afterwards. A very small shift of the reflectivity curves upon protein reconstitution was observed, which leads to the conclusion that no detectable BR incorporation takes place.

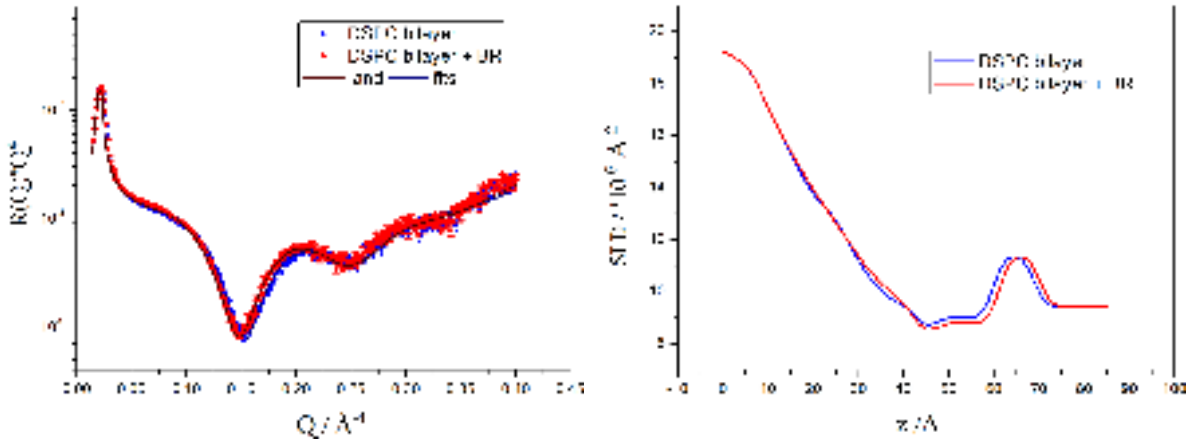

(a) (b)

Figure III.3.1 – (a) XRR curves of a DSPC single bilayer at room temperature before and after BR reconstitution. (b) SLD profiles corresponding to the fits.

3.1.2 BR reconstitution into a DSPC-DPPC double bilayer

As an example of the performed experiments, we would like to present XRR measurements performed on a DSPC-DPPC double bilayer system. The lipid bilayers were deposited on the 2.5x2.5 cm^2 silicon block by LB/LS techniques, following the procedure described in section 1.3.6. The prepared sample was tightly sealed in the specially developed solid/liquid cell. Reflectivities from the pristine double bilayer system and double bilayer after protein reconstitution were measured in order to resolve the sample structure and to distinguish the structural changes caused by protein or detergent molecules. BR insertion was performed applying the detergent-mediated incorporation technique by injecting a solution of 2.5 μg/ml BR in 0.05 mM

DDM PBS buffer, incubating for 15 minutes and rinsing the system with PBS buffer. The obtained reflectivity curves, fits and corresponding SLD profiles are shown in Fig. III.3.2. Reflectivity curves were fitted using the Aurore software and the lipid bilayer sample was modeled using a slab model as described in section 2.9.

The obtained structural parameters for the pristine sample and sample after BR insertion are summarized in Tab. B.11.The values reported in Tab. B.11 are consistent with the parameters obtained from synchrotron XRR experiments performed on similar lipid bilayers samples [172]. For the sample measured after BR reconstitution we have observed an increase of the ED values of the tail and head regions of the second floating bilayer. This variation of ED is consistent with BR insertion into the floating gel-phase lipid bilayer. Other modifications of the floating bilayer such as: 1) increase of the thickness of the water layer between two bilayers (from 1.3 nm to 1.7n m); 2) increase of the thickness of the floating DPPC bilayer (5.1 nm to 5.3 nm) and 3) increase of the bilayer roughness (from 0.2 to $\approx$ 0.1 nm) can be explained by BR insertion as well. The observed structural modifications of the first supported DSPC bilayer cannot be related to protein reconstitution into the solid supported bilayer.

In-house XRR measurements clearly indicate the possibility of BR insertion into gel-phase DPPC floating bilayer. The obtained result is reproducible, as applying the developed protocol repeatedly in order to incorporate BR in DSPC-DPPC or DSPC-DSPC double lipid bilayer systems led to the same positive outcome for these experiments. We can note that no loss of the floating lipid bilayer was observed upon BR-DDM solution injection, when the floating bilayer was in the gel phase. Thus, gel-phase lipid bilayer appears to be a strong and suitable sample for the detergent-mediated protein incorporation technique and thanks to the performed XRR experiments we were able to confirm BR insertion into the floating bilayers.

3.1.3 Arch-3 reconstitution into a DSPC double bilayer

We have performed in-house XRR experiments in order to study Arch-3 reconstitution into a double lipid bilayer system composed of DSPC lipids. X-ray reflectivities were measured for the pristine DSPC double bilayer and the sample after Arch-3 insertion. The SLD profile of the pristine DSPC double bilayer system

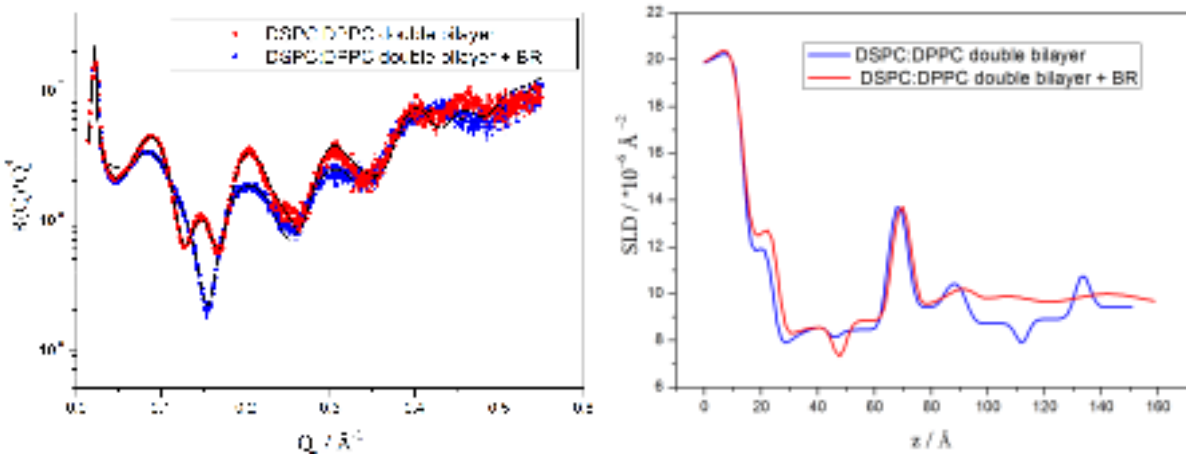

(a) (b)

Figure III.3.2 – (a) XRR curves of a DSPC-DPPC double bilayer at room temperature before and after BR reconstitution. (b) SLD profiles corresponding to the fits.

(Fig. III.3.3) indicates a good quality (full coverage) double lipid bilayer sample. Arch-3 reconstitution into the bilayer was performed by injecting a 3 μg/ml Arch-3 in 0.05 mM DDM PBS buffer solution into the cell, incubating for 10 minutes and rinsing the system with buffer. A very small change of the reflectivity curve was detected after the reconstitution step. The performed procedure was repeated again re-injecting a BR-DMM solution at the same concentration and incubating the system for 20 minutes. A further small modification of the reflectivity curve was detected after the second incubation step as can be seen in Fig. III.3.3. The structural parameters obtained from the fits of the DSPC double lipid bilayer samples before and after Arch-3 insertion are summarized in Tab. B.13. From the structural parameters obtained from the best fits of the data, it was not possible to confirm Arch-3 protein incorporation into the gel-phase DSPC floating lipid bilayer. The positive and important result that we can retrieve from this experiment is that no strong and harmful structural modifications of the double lipid bilayer were observed upon interaction with detergent solution.

3.1.4 Conclusions

XRR in-house experiments serve as an excellent tool to investigate the structure of planar lipid bilayer systems and to reveal structural and compositional changes caused by protein incorporation or detergent molecules. The information obtained

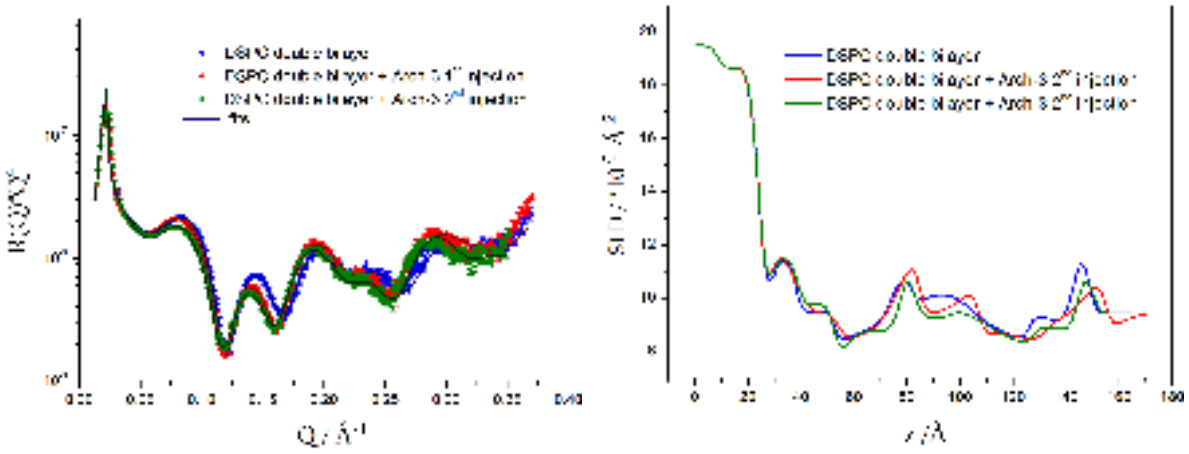

(a) (b)

Figure III.3.3 – (a) XRR curves of a DSPC double bilayer at room temperature before and after Arch-3 reconstitution. (b) SLD profiles corresponding to the fits.

from the XRR experiments can provide a great help in order to develop a robust protocol for the sample preparation as XRR measurements are relatively easy and fast (less than one hour is needed to collect one reflectivity curve of a bilayer sample at solid/liquid interface) and the appropriate sample environment for samples at the solid/liquid interface is now available.

Thanks to the performed experiments we were able to demonstrate BR incorporation into gel-phase floating lipid bilayer and a robust and reproducible protocol bilayers was developed. We have also shown that Arch-3 does not interact strongly with the lipid bilayer sample in the gel phase and no protein insertion was possible to detect. As a future prospective, we plan to perform in-house XRR "control" experiment studying the influence of 0.05 mM DDM solution on the lipid bilayer structure.

3.2 Neutron reflectometry

To resolve the lipid bilayers structure at the molecular scale and to reveal all the induced changes in the bilayer structure and composition caused by protein and detergent insertion, we have performed NR experiments on planar solid-supported bilayers on the MARIA (MLZ, Germany) and D17 (ILL, France) reflectometers.

3.2.1 BR-substrate interaction

We have performed NR experiments studying the interaction/adsorption of BR with/to the bare silicon substrate. This experiment was carried out in the following way: 30 μg/ml BR in 0.05mM DDM in PBS H_2O buffer was injected into the closed and pre-filled with PBS H_2O buffer solid/liquid cell. The system was left for 15 minutes of incubation and was then extensively rinsed with PBS D_2O buffer. Reflectivity of a sample was collected in D_2O PBS buffer. In Fig. III.3.4 the measured reflectivity curves and obtained SLD profile of the system are shown.

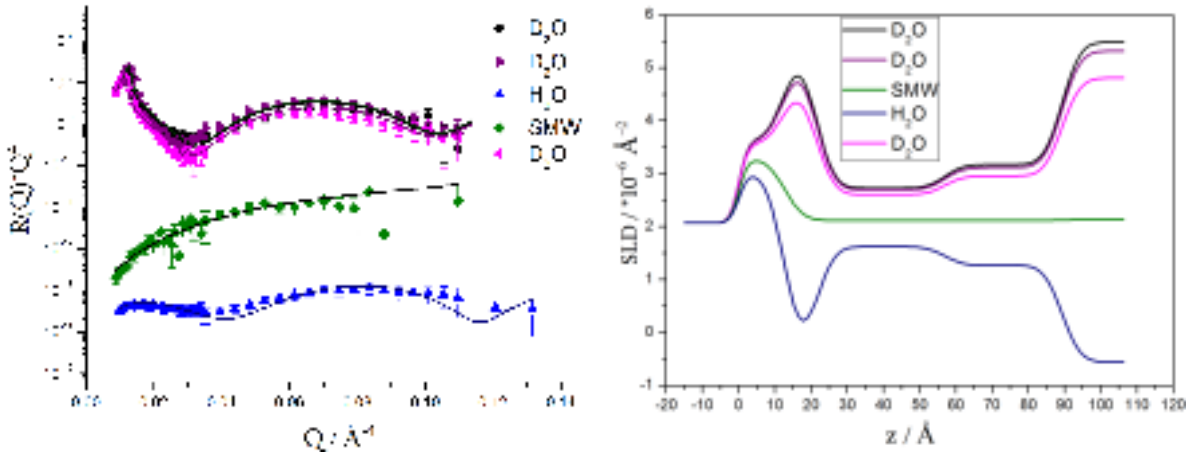

(a) (b)

Figure III.3.4 – (a) Reflectivity curves of a BR protein layer on the bare silicon support. (b) SLD profiles corresponding to the fits. The final system is consistent with two layers of BR on the silicon substrate.

In order to check the stability of the sample and to follow the modification of the system induced by solvent exchange, we have rinsed extensively the system with D_2O PBS buffer and measured reflectivity from this system again. No changes of the reflectivity signal were detected upon additional rinsing with D_2O PBS buffer, as the two collected reflectivity curves overlap. As a next step, we have measured the

reflectivity from the protein layer in two other solvent contrasts (H_2O and SMW) and then in D_2O contrast for a third time. As we can see in Fig. III.3.4, no modification of the reflectivity curves in D_2O contrast was observed upon repeated sample rinsing.

We have performed simultaneous fitting of the reflectivity curves in D_2O, SMW and H_2O contrasts to reveal the structure and composition of the protein layer on the solid support. Based on the obtained SLD profiles and structural parameters (Tab. B.5), we can conclude that the final system is consistent with two layers of BR adsorbed to the silicon support: the first layer has a thickness of 3.6 nm and is composed of 88% by volume of BR, the second layer has a thickness of 3.2 nm and is composed of 69% by volume of BR. The water content in the second protein layer is higher (18% by volume for the first adsorbed layer compared to 31% by volume for the second one).

From the performed NR experiment, we can conclude that BR strongly interacts with the bare silicon support forming a strongly adhesive protein layer. BR does not seem to aggregate or unfold in the proximity of the bare substrate and keeps its structure, as it can be seen from the obtained structural and compositional parameters.

3.2.2 Influence of DDM on the lipid bilayer structure

For a correct interpretation of the collected measurements it is very important to resolve the contribution imposed by detergent molecules separately. To study the effect of 0.05mM DDM detergent solution on the structure of the double lipid bilayer system, we have performed NR experiments similar to those reported above.

Reflectivities were measured from the pristine DSPC-DPPC double lipid bilayer system at 48°C in three solvent contrasts. A 0.05 mM DDM solution was then injected into the cell and the system was left to incubate for 15 minutes, after which it was rinsed with buffer to remove all the detergent molecules from the bulk and supposedly from the lipid bilayer. Reflectivities from the final system were measured in three solvent contrasts (H_2O, SMW, D_2O) and simultaneous fitting of the collected reflectivity curves was performed. Reflectivity curves, fits and corresponding SLD profiles of the system before and after interaction with the detergent solution are shown in Fig. III.3.5. We can observe very small changes of the reflectivity curves

caused by interaction with the detergent solution. From the parameters obtained from the fits, we can notice a small increase of water content in the tail region of the floating lipid bilayer (from 7% to 17%) while the SLD values of the tail or head regions of both bilayers were not modified upon the incubation with detergent solution. The structure and composition of the solid-supported DSPC lipid bilayer was not modified within the errors (Tab. B.7).

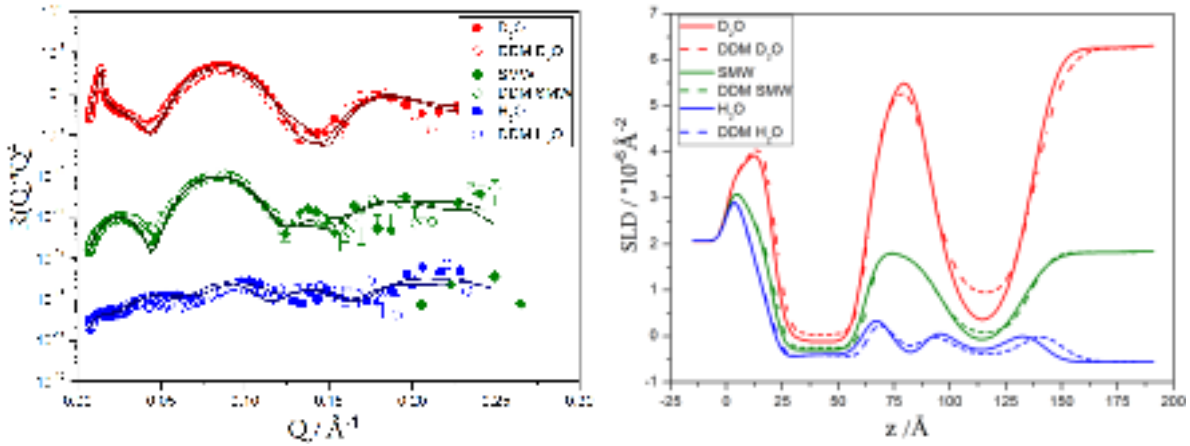

(a) (b)

Figure III.3.5 – (a) Reflectivity curves for a DSPC-DPPC double lipid bilayer measured at 48°C before (closed symbols) and after (open symbols) injection of 0.05 mM DDM detergent solution. (b) SLD profiles corresponding to the fits.

3.2.3 BR incorporation into single solid-supported lipid bilayers.

The experiment at the MARIA reflectometer was carried out on single solid-supported POPC lipid bilayer systems. Samples were prepared on a 5x8 cm^2 silicon crystal surface by vesicle fusion technique as described in section 1.3.6 and were tightly sealed in the solid/liquid cell (section 2.7).

To reveal changes in the bilayer structure and composition induced by BR insertion, reflectivity curves of the sample were measured before and after BR reconstitution. Reflectivity from the pristine POPC bilayer system was measured in 3 different solvent contrasts (D_2O, SMW and H_2O). Protein BR reconstitution was performed applying the detergent-mediated incorporation method by introducing a solution of 10μg/ml BR in 0.05 mM DDM H_2O PBS buffer into the solid/liquid cell with the POPC bilayer. The system was left for 15 minutes and then rinsed with H_2O PBS buffer. The obtained system after all performed manipulations was measured

in 4 different solvent contrasts (D_2O, 4MW, SMW and H_2O). Measured reflectivity curves and obtained fits for this sample are shown in Fig. III.3.6(a).

Data analysis and simultaneous fitting of the reflectivity curves in 3 contrasts for the pristine POPC bilayer and 4 contrasts for the sample after BR insertion were performed following the procedure reported in section 2.9. Obtained SLD profiles of the system before and after BR insertion are plotted in Fig. III.3.6(b). By comparing the SLD profiles, we can deduce that the overall structure of the final system is consistent with a single lipid bilayer system, however the SLD value of the tail region is significantly increased. From the changes of the SLD values of the tail regions ($-0.35 \cdot 10^{-6}$Å^{-2} for the pure POPC bilayer, $0.13 \cdot 10^{-6}$ Å^{-2} for the POPC bilayer with incorporated BR) we were able to quantify the amount of BR inserted into the bilayer and we can conclude that, upon BR insertion, the final system is consistent with BR incorporation and is composed of 22% (by dry volume) of BR molecules and 78% (by dry volume) of POPC lipids. An increase of the water content in the tail regions upon BR reconstitution was also observed (from 8% to 39%). The overall structure of the bilayer with BR is consistent with the structure known for pure POPC bilayers and it was not drastically changed upon BR reconstitution. The structural parameters obtained from the fits are summarized in Tab. B.1.

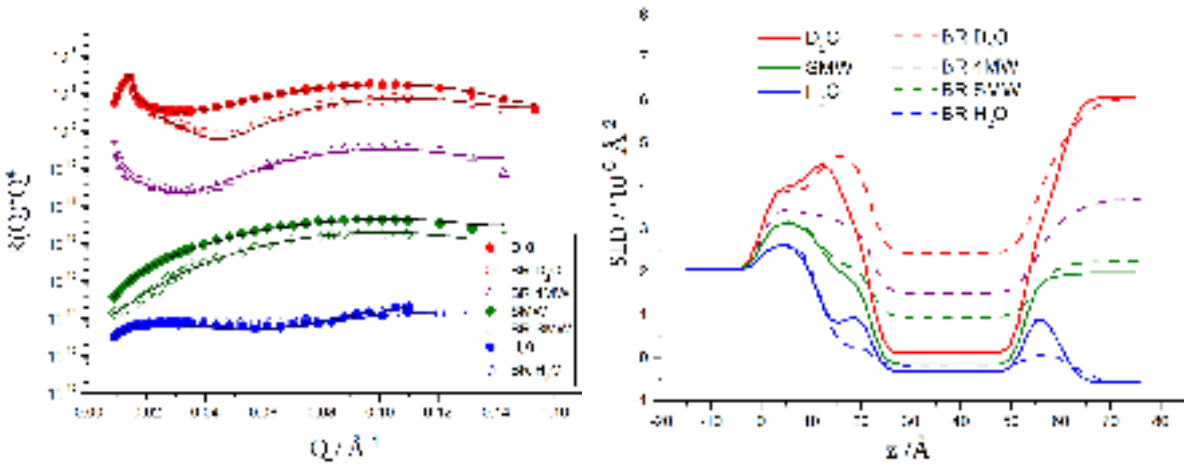

(a) (b)

Figure III.3.6 – (a) Reflectivity curves of a POPC single bilayer at room temperature before (closed symbols) and after (open symbols) BR reconstitution. (b) SLD profiles corresponding to the fits.

3.2.4 Incoherent summation

To exclude the possibility of BR domain formation on the solid support, we have applied another approach of data analysis for this sample. In the analysis of NR experiments the structure and composition of lipid bilayer samples is averaged in the xy plane (parallel to the sample surface) within each slab. Therefore, the two different cases of BR domain formation and homogeneous reconstitution in the bilayer can provide similar SLD profiles.

If lipids and BR form separated domains and if the size of these domains is larger than the coherent length of the beam (~ 300 nm), the measured reflectivity will be composed of the reflectivity signal from the pure POPC bilayer (R_{POPC}) and reflectivity from the pure BR layer (R_{BR}). Therefore, the total reflectivity signal can be calculated as an incoherent sum of two reflectivities R_{POPC} and R_{BR} with only one fitting parameter α, which is the fraction of BR in the sample :

$$R_{cal} = \alpha R_{BR} + (1 - \alpha) R_{POPC} \tag{3.1}$$

where R_{cal} is the total calculated (Eq. 3.1) reflectivity signal from the POPC lipid bilayer with reconstituted BR, R_{BR} is simulated reflectivity signal from the pure protein layer, R_{POPC} is reflectivity measured from the pure POPC lipid bilayer.

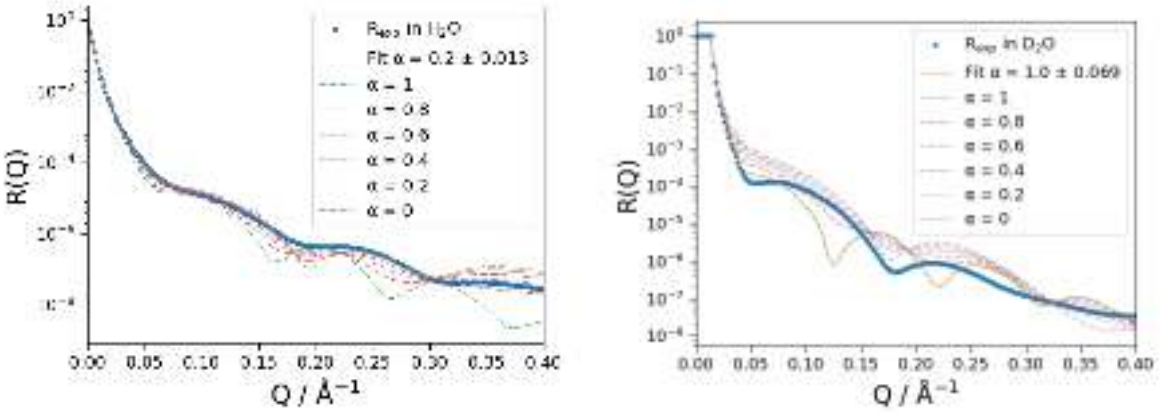

(a) (b)

Figure III.3.7 – Measured reflectivity curve of a POPC single bilayer with BR (R_{exp}) and simulated reflectivity curve (R_{cal}) obtained for different BR fractions (α) in (a) H_2O contrast and (b) D_2O contrasts.

In order to obtain all reflectivity curves (measured R_{exp} and R_{POPC} and simulated

R_{BR}) with identical Q-range, which is needed for the simulations, we have simulated the reflectivity curves R_{exp} and R_{POPC} in different contrasts, taking the parameters obtained from the fits of the measured reflectivities from the pure POPC lipid bilayer (R_{POPC}) and POPC lipid bilayer upon BR reconstitution (R_{exp}) (Sample in Fig. III.3.6). R_{BR} was simulated assuming that BR has a size of ~ 5 nm and an average SLD value of $\sim 2 \cdot 10^{-6}$ Å^{-1}.

We have performed simulations varying the fraction of BR molecules in the sample (parameter α) for all four solvent contrasts (D_2O, 4MW, SMW and H_2O) in order to fit the measured reflectivity curves R_{exp} to the calculated R_{cal}. As can be seen in Fig. III.3.7, it was not possible to obtain the appropriate parameter α in order to match the measured reflectivity curves. Thus, based on this simple, but reasonable approach, we can conclude that the assumption of the separate domain formation of BR and POPC lipid bilayer of size larger that the coherence length can be disregarded.

3.2.5 Influence of BR concentration on the protein reconstitution

To highlight the importance of the protein concentration in the reconstitution process, reflectivity from the pristine POPC lipid bilayer was measured in two solvent contrasts (D_2O and H_2O). Protein reconstitution was performed by injecting a solution of 30 μg/ml BR in 0.05 mM DDM H_2O PBS buffer, incubating the system for 15 minutes and rinsing afterwards with H_2O PBS buffer. Upon BR insertion the final system was measured in three solvent contrasts (D_2O, SMW and H_2O). The collected reflectivity curves and SLD profiles are shown in Fig. III.3.8. Structural parameters obtained from the fits are summarized in Tab. B.2. From the obtained structural parameters of the systems we can judge the modifications in the lipid bilayer structure. The SLD values of the tail regions increase from $-0.35 \cdot 10^{-6}$ Å^{-2} to 1.34 and $1.1 \cdot 10^{-6}$ Å^{-2} (for the two leaflets of the lipid bilayer) upon BR incorporation in the POPC bilayer.

The SLD values of the tail region increase drastically upon BR reconstitution and an additional diffuse (79% of H_2O) layer of material with thickness 3 nm and SLD equal to $2 \cdot 10^{-6}$ Å^{-2} was also necessary to model the data. The parameters describing the adsorbed layer on top of the bilayer are consistent with the SLD and

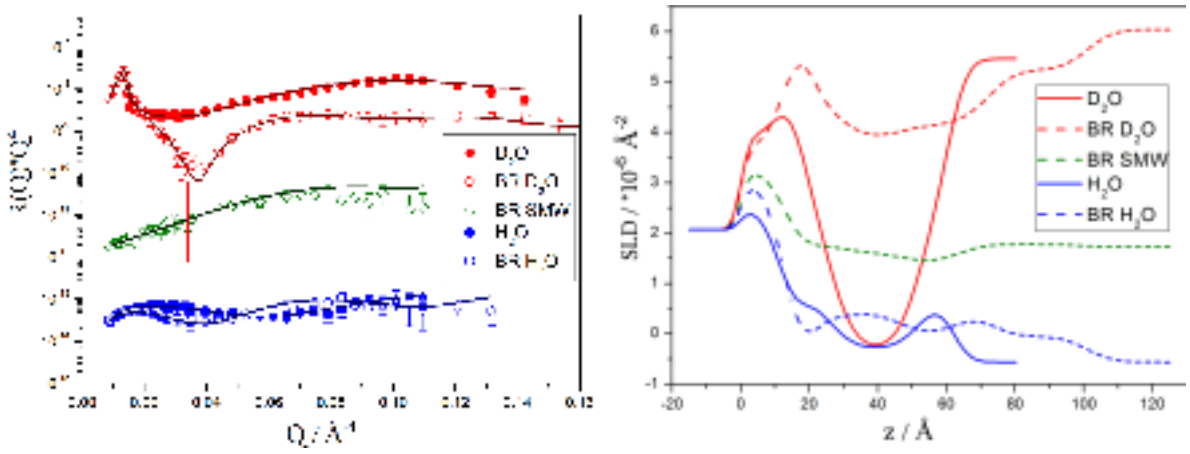

(a) (b)

Figure III.3.8 – (a) Reflectivity curves of a POPC single bilayer at room temperature before (closed symbols) and after (open symbols) BR reconstitution. (b) SLD profiles corresponding to the fits. The final system is consistent with BR incorporation in the POPC bilayer and adsorption of BR on top of the bilayer surface.

size of BR molecules. Therefore, we can conclude that injection of 30 μg/ml BR solution results in protein incorporation in the POPC bilayer and adsorption of BR molecules on top of it. It was not possible to remove the absorbed protein layer by extensively rinsing the system with buffer, thus the final system resulted to be stable and solvent exchange method does not change the sample structure.

To demonstrate the harmful effect of a too high protein concentration, another set of data is presented. In Fig. III.3.9, reflectivity curves in several solvent contrasts from a POPC lipid bilayer before and after BR insertion are shown. BR incorporation was performed by injecting a 50 μg/ml BR in 0.05 mM DDM H_2O PBS buffer solution, incubating the system for 10 minutes and rinsing with H_2O PBS buffer.

Before this injection, another two subsequent injections of 2.5 and 5 μg/ml BR in 0.05 mM DDM H_2O PBS buffer solution were performed, followed by 10 minutes incubation and rinsing, but no modification of the reflectivity curve was observed. In order to reconstitute BR into the lipid bilayer the third injection with an increased amount of BR was carried out. This manipulation resulted in the POPC bilayer destruction and sample removal from the substrate, as we can see from the obtained structural parameters (Tab. B.3) or SLD profiles (Fig. III.3.9(b)). After BR incorporation only 20% (by volume) of the surface was covered with material with an average $SLD = 1.9 \cdot 10^{-6}$ Å^{-2} and thickness of 5.5 nm, which is consistent with

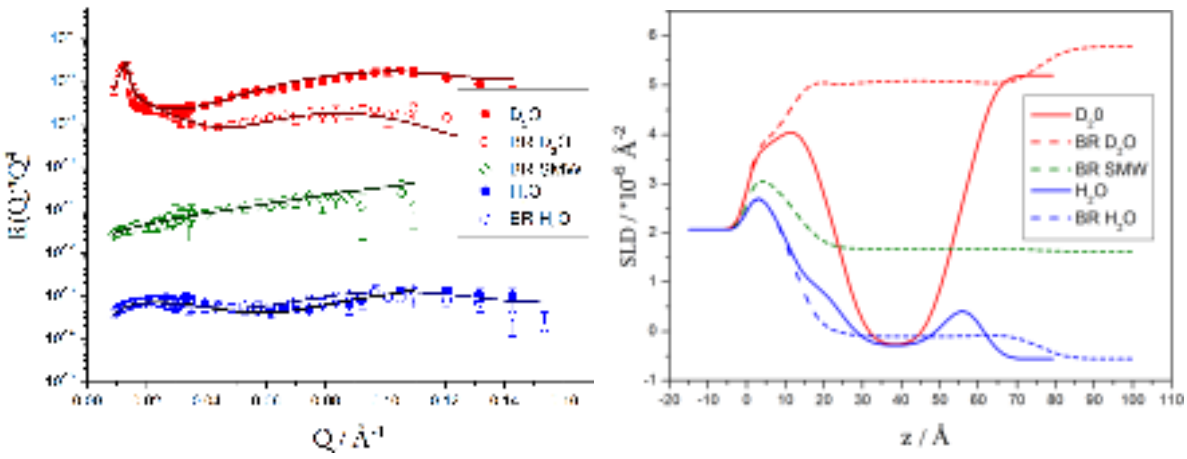

(a) (b)

Figure III.3.9 – (a) Reflectivity curves of a POPC single bilayer at room temperature before (closed symbols) and after (open symbols) BR reconstitution. (b) SLD profiles corresponding to the fits. POPC bilayer removal was caused by protein injection.

patches of BR molecules and lipid bilayer on the substrate.

It is therefore important to optimize the concentration of the protein - detergent solution used for the detergent-mediated incorporation method, as the protein interacts strongly with the lipid bilayer and injection of a too concentrated solution can lead to a strong modification of the sample such as a bilayer destruction or a formation of a protein layer on the sample surface, which is highly undesirable.

3.2.6 Arch-3 - substrate interaction

We have performed NR experiments to investigate the interaction of Arch-3 with the bare silicon support.

A cleaned silicon block was sealed in solid/liquid cell filled with D_2O PBS buffer. The reflectivity from the bare silicon substrate was measured in D_2O PBS buffer contrast. A 10 μg/ml Arch-3 in 0.05mM DDM PBS buffer solution was injected into the cell and left for 15 minutes of incubation period to let proteins absorb on the solid support. Reflectivity from the obtained sample (without a rinsing step) was measured in D_2O contrast. After the performed measurement the system was rinsed with D_2O PBS buffer in order to remove detergent and protein molecules from the bulk and to follow the changes of the sample caused by rinsing step. Reflectivity from the obtained sample was measured in D_2O contrast. As we can see no changes in the reflectivity signal were detected upon the protein injection step (Fig. III.3.10)

and thus no protein adsorption had occurred (Tab. B.10).

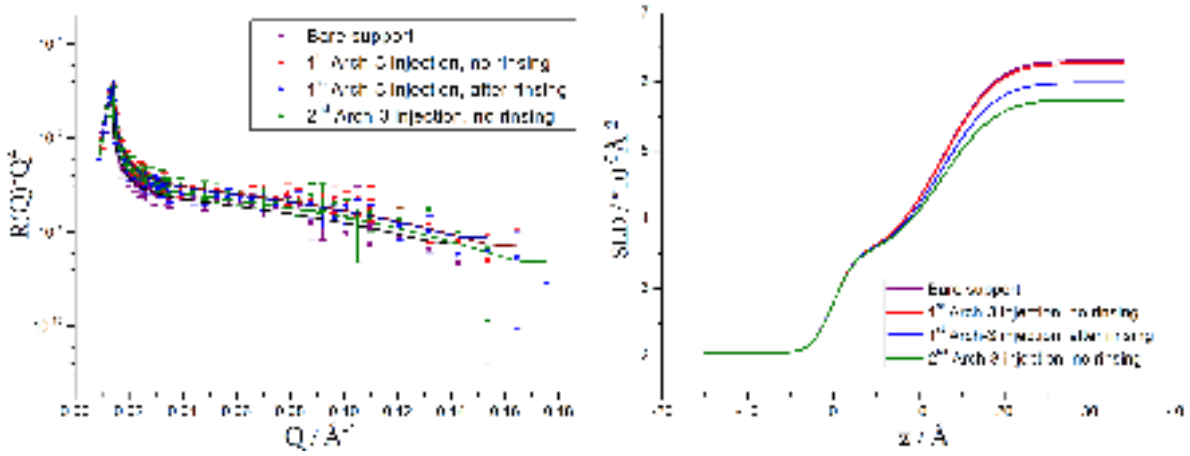

(a) (b)

Figure III.3.10 – (a) Reflectivity curves for the Arch-3 adsorption on the bare support. (b) SLD profiles corresponding to the fits.

A re-injection of an increased concentration of Arch-3 (25μg/ml Arch-3 solution in 0.05mM DDM PBS buffer) into the same solid/liquid cell was performed. A very long incubation time of 1 hour 30 minutes was waited before the system was rinsed with buffer. Reflectivity from the sample upon rinsing with buffer was measured in D_2O contrast. Obtained reflectivity curves and corresponding SLD profiles are shown in Fig. III.3.10. As we can see again no modification of the reflectivity curves was observed, indicating that no detectable protein adsorption on the bare silicon block had occurred. In conclusion, the transmembrane protein Arch-3 does not interact with a bare silicon support.

3.2.7 Arch-3 incorporation into single solid-supported lipid bilayers

We have performed NR experiments on the MARIA reflectometer to investigate the reconstitution of the transmembrane protein Arch-3 into POPC bilayers and to reveal all the structural and compositional changes in the bilayer caused by Arch-3 inclusion.

A POPC lipid bilayer was deposited by vesicle fusion technique (see section 1.3.1 for details on sample preparation) and the reflectivity from the pristine POPC bilayer was measured in D_2O and H_2O PBS buffer solvent contrasts. Arch-3 reconstitution

was performed by injecting a solution of 30 μg/ml of Arch-3 in 0.05mM DDM in PBS Hbuffer, followed by 15 minutes of incubation. Reflectivity from the system after the reconstitution step was measured in three solvent contrasts (H_2O, SMW and D_2O). No modifications of the reflectivity curves caused by the protein-DMM solution injection was observed, thus, no protein Arch-3 incorporation was detected. To increase chances of Arch-3 insertion into POPC lipid bilayer, we have performed a second injection of 30 μg/ml Arch-3 in 0.05mM DDM in PBS Hbuffer solution, increasing the incubation time up to 30 minutes. After system incubation and rinsing with buffer, reflectivity from the final system was measured in three solvent contrasts again. The obtained measurements and resulted SLD profiles of the system are shown in Fig. III.3.11. No modification of the POPC lipid bilayer upon the second insertion step of protein-detergent solution with increased incubation time was observed, thus no Arch-3 protein reconstitution in the POPC bilayer was achieved (Tab. B.8).

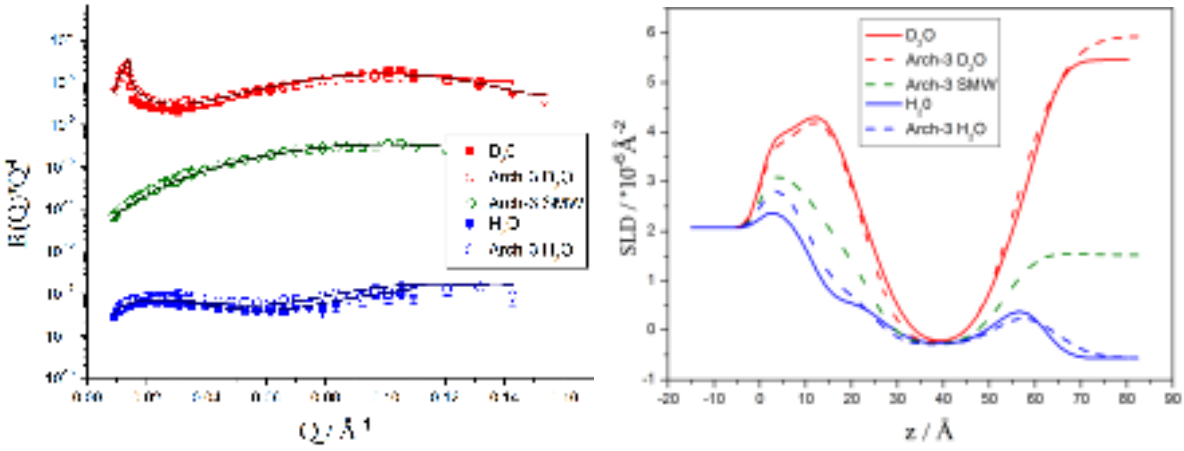

(a) (b)

Figure III.3.11 – (a) Reflectivity curves of a POPC single bilayer at room temperature before (closed symbols) and after (open symbols) second Arch-3 reconstitution. (b) SLD profiles corresponding to the fits. No Arch-3 incorporation was observed.

Based on the obtained measurements, we can highlight other important conclusions on the influence of detergent molecules on the lipid bilayer structure. No modification of the reflectivity signal from the POPC bilayer system upon bilayer incubation with 0.05 mM DDM detergent solution with proteins was observed. This is a very important result, as no bilayer solubilization and modification of the bilayer structure is induced by 0.05 mM DDM detergent solution. Therefore, any possible

modification of the measured reflectivity signal from POPC lipid bilayer is caused by the interaction of protein molecules with the lipid bilayer.

Another couple of experiments were performed in the attempt to reconstitute Arch-3 into POPC lipid bilayers. The reflectivity from the pristine POPC lipid bilayer was measured in two contrasts (D_2O and H_2O). The reflectivity from the system after each Arch-3 reconstitution step was measured in three contrasts (D_2O, SMW and H_2O PBS buffer) in order to reveal the changes in the bilayer structure. After three subsequent injection of 10 μg/ml (15 minutes incubation), 25 μg/ml (15 minutes incubation) and 10 μg/ml (10 minutes incubation) Arch-3 in 0.05 mM DDM in PBS buffer solutions in one sample and 5 μg/ml (7 minutes incubation), 25 μg/ml (15 minutes incubation) and 10 μg/ml (10 minutes incubation) Arch-3 in 0.05 mM DDM PBS buffer solutions into a second sample, no modifications of the reflectivity curves were detected for both samples upon each insertion step, thus no Arch-3 reconstitution was observed for single POPC lipid bilayer samples upon multiple reconstitution steps.

To increase the chances of Arch-3 insertion, we have performed similar experiments after drastically increasing the Arch-3 concentration in the solution. Reflectivity was measured from the pristine POPC bilayer and upon the each reconstitution steps, which were performed injecting subsequently 10 μg/ml (15 minutes incubation) and 20 μg/ml (20 minutes incubation) Arch-3 in 0.05 mM DDM PBS buffer solutions. After performed manipulations, no protein insertion was detected. The third try of Arch-3 reconstitution was performed by introducing a solution of 60 μg/ml Arch-3 in 0.05 mM DDM PBS buffer, incubating the system for 15 minutes and rinsing the cell with buffer afterwards. Measured reflectivity curves from the system before and after the 3rd insertion step are shown in Fig. III.3.12. As we can see the modification of the reflectivity curves were detected. An increase of the SLD value of the tail region from $-0.35 \cdot 10^{-6}$ Å^{-2} to $0.2 \cdot 10^{-6}$ Å^{-2} after Arch-3 reconstitution was observed. We have estimated that the final system is composed of 75% (by dry volume) of POPC lipid bilayer and 25% (by dry volume) of Arch-3 proteins. An increase of the water content in the tail and head regions upon Arch-3 injection was observed, which can be related to the partial lipid bilayer solubilization caused by protein-detergent mixture.

All the obtained structural parameters for this sample before and after Arch-3 insertion are summarized in Tab. B.9.

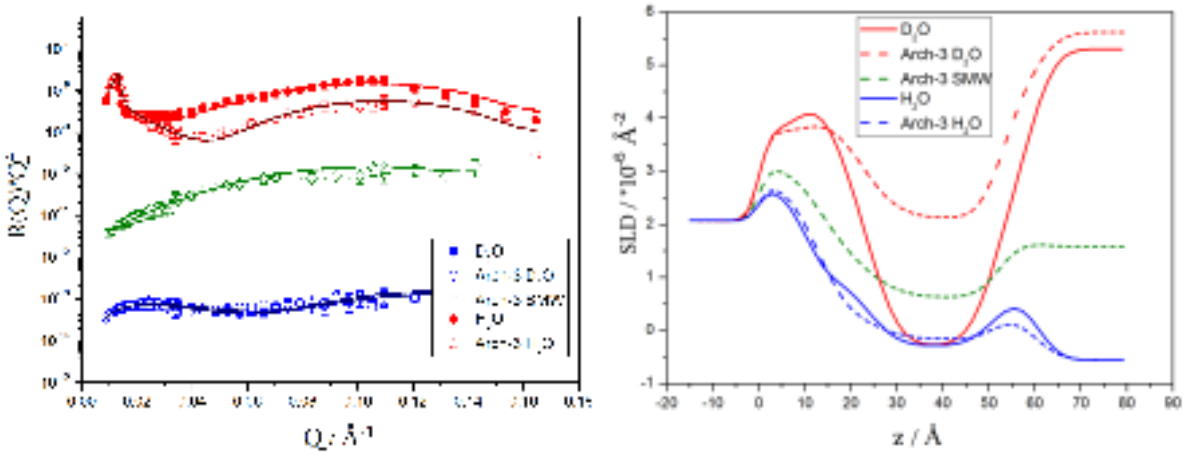

(a) (b)

Figure III.3.12 – (a) Reflectivity curves of a POPC single bilayer at room temperature before (closed symbols) and after (open symbols) third Arch-3 reconstitution.(b) SLD profiles corresponding to the fits.

We can conclude that that transmembrane protein Arch-3 does not interact strongly with fluid POPC lipid bilayers and very high protein concentration is needed in order to observe POPC bilayer modifications, which can be related to the Arch-3 reconstitution in to the bilayer system.

3.2.8 BR incorporation into DSPC-DPPC double bilayers

One of the main aims of this PhD work was to study protein reconstitution into floating phospholipid bilayers and to investigate thermal and active (non-thermal) fluctuations of the membrane-protein system induced by protein pumping activity.

In accordance with the main goal of the work we have performed NR experiments on double lipid bilayer systems on the D17 reflectometer at the ILL in order to characterize the double lipid bilayer structure at Å scale and to reveal all the induced structural and compositional changes caused by BR insertion.

Double lipid bilayer samples were prepared on 5x8 cm^2 surface of the silicon blocks by LB/LS deposition techniques as described in details in section 1.3.6. The sample was then tightly sealed in the solid/liquid cell for NR experiments.

We have performed NR experiments on DSPC-DPPC double lipid bilayer sys-

tems, where the first solid-supported bilayer was composed of DSPC lipids and the second floating lipid bilayer was made of DPPC lipids. The double lipid bilayer system was measured at 48°C, which allows to bring the floating DPPC lipid bilayer into the fluid phase (T_m = 41°C) and at the same time to keep the solid-supported DSPC lipid bilayer in the gel phase (T_m = 55°C). This was done in order to facilitate BR insertion into the floating lipid bilayer, which resides in the biologically more relevant fluid-phase, and prohibit BR insertion into the first solid-supported gel-phase bilayer.

Several NR experiments were performed with the aim to reconstitute BR into the fluid-phase floating lipid bilayer by means of the detergent-mediated incorporation method.

As an example of the performed experiments, reflectivity measured from the pristine DSPC-DPPC double lipid bilayer at 48°C are shown in Fig. III.3.13. The protein reconstitution step was performed by injecting a solution of 0.5 μg/ml BR in 0.05 mM DDM PBS buffer into the cell, incubating for 15 minutes and rinsing with buffer afterwards. Reflectivity from the final system was measured in three solvent contrasts (H_2O, SMW, D_2O). Reflectivity curves, fits and corresponding SLD profiles of the system before and after BR insertion are shown in Fig. III.3.13.

The resulting SLD profiles obtained from data fitting confirmed a good quality pristine double bilayer system (Tab. B.6). After BR incorporation, no change of the first supported bilayer was detected. The SLD of the tail regions of the floating lipid bilayer increased from $-0.35 \cdot 10^{-6}$ Å^{-2} to $-0.19 \cdot 10^{-6}$ Å^{-2} and $0.33 \cdot 10^{-6}$ Å^{-2} for the two leaflets respectively, which can be related to non-uniform BR insertion or asymmetry of the BR SLD profile. We have estimated that the final floating bilayer system is consistent with 93% of DPPC lipid bilayer and 7% of proteins in the lower bilayer leaflet with the final SLD = $-0.19 \cdot 10^{-6}$ Å^{-2} and 68% of DPPC lipid bilayer and 32% of proteins in the upper bilayer leaflet with the final SLD = $0.33 \cdot 10^{-6}$ Å^{-2}. A diffuse layer (90% of H_2O) with a thickness of $\approx$ 5 nm and SLD of $1.8 \cdot 10^{-6}$ Å^{-2} was formed on top of the floating bilayer, consistent with the size and SLD of BR molecules. We can conclude that BR incorporation resulted in the inhomogeneous incorporation of BR into the fluid floating lipid bilayer and formation of a diffuse layer of BR on top of it.

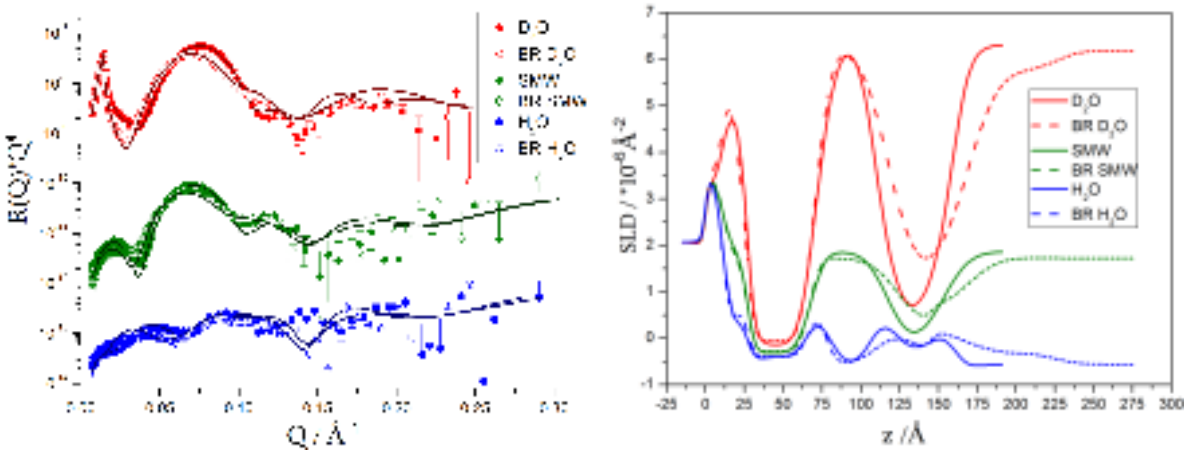

(a) (b)

Figure III.3.13 – (a) Reflectivity curves for the double DSPC-DPPC lipid bilayer measured at 48°C before (closed symbols) and after (open symbols) BR reconstitution. (b) SLD profiles corresponding to the fits.

We would like to note that injection of BR-DDM solution into double lipid bilayer systems often resulted in the loss and solubilization of the floating bilayer. This observation is in total agreement with the results obtained from the performed AFM, XRR and fluorescence microscopy experiments, where it was also demonstrated that fluid lipid bilayers are very fragile and unstable model systems for BR reconstitution studies.

Unfortunately due to the long closure of the ILL during my PhD thesis, we did not have the opportunity to perform more NR experiments. We should note that this kind of experiments - NR experiments on double lipid bilayer systems at the solid/liquid interface - are best performed at the ILL on the D17 or Figaro reflectometers, because of the characteristics of these instruments with the dedicated sample environment for illumination studies (developed in the framework of this thesis) and availability of the appropriate equipment for sample preparation.

3.2.9 Effect of sodium azide on the membrane structure

It is known that oxidation processes in cell membranes can greatly influence lipid-protein interactions and association, but also vastly alter protein function itself. It was reported [203] that hydrogen-bonded networks are essential to facilitate fast proton transfer across BR and properties of these networks are modulated by the presence of weakly acidic anions like azide , cyanate and formate. Azide and other

weakly acidic anions act as catalysts for the formation of hydrogen-bonded networks in proton pathways of proteins, increasing their pumping activity. According to the reference [20], activity of BR incorporated into GUVs leads to an enhancement of the active fluctuations of the membrane. It was pointed out that to observe this effect 1 mM sodium azide (NaN_3) must be present in the solution of proteoliposomes. In the absence of the sodium azide no enhancement of the membrane fluctuation spectrum was observed [170]. This study is in full agreement with reference [203], which claims that sodium azide enhances proton transfer in BR. Therefore, presence of NaN_3 is very important for the BR activity and for the enhancement of the fluctuation of phospholipid bilayers.

In order to facilitate and increase the BR pumping activity, when the protein is reconstituted into the planar lipid bilayer systems, we have introduced a solution of 1 mM NaN_3 in PBS buffer into single and double lipid bilayer samples. Reflectivities were measured in several contrasts from the pristine lipid bilayer samples, from bilayers upon BR insertion and from the same samples after addition of 1 mM NaN_3, thus the induced changes in the sample structure caused by the protein-detergent solution or sodium azide molecules could be extracted independently.

As a result of these experiments, we have noticed large modifications of the reflectivity curves for both the single and double phospholipid bilayers with reconstituted BR caused by the presence of sodium azide in the system. This effect can not be explained by the increased protein pumping activity, because BR is a light driven proton pump and its activity can only be triggered by illumination with light of specific wavelengths. A reversible effect of sodium azide addition on the reflectivity curves for a solid supported DPPC bilayer with incorporated BR was observed. Changing the solution from PBS buffer to PBS buffer + NaN_3 back and forth was altering the reflectivity curves reversibly in the same manner.

We are not presenting this data, as the samples were not of the best quality after the BR insertion step and it was very challenging to fit them in order to extract structural information from the measurements. Qualitative information on the structural changes of the lipid bilayers obtained from these NR measurements provided a strong evidence of the influence of sodium azide on the lipid bilayer structure.

A similar modification of the reflectivity curves upon sodium azide addition

was observed for a pure solid supported bilayer made of fully deuterated d_{75}DPPC lipids (Fig. III.3.14). This sample was investigated during a test NR experiment, when we had time to measure only one contrast for this sample. First, reflectivity from the pure d_{75}DPPC solid supported lipid bilayer was measured in H_2O, afterwards 1 mM NaN_3 solution was added to the sample and reflectivity was measured again. The system was rinsed with H_2O and the final system was measured again in H_2O contrast. The obtained reflectivity curves and resulting SLD profiles are shown in Fig. III.3.14. The effect of azide on the structure of the pure lipid bilayer system is clearly visible (Fig. III.3.14).

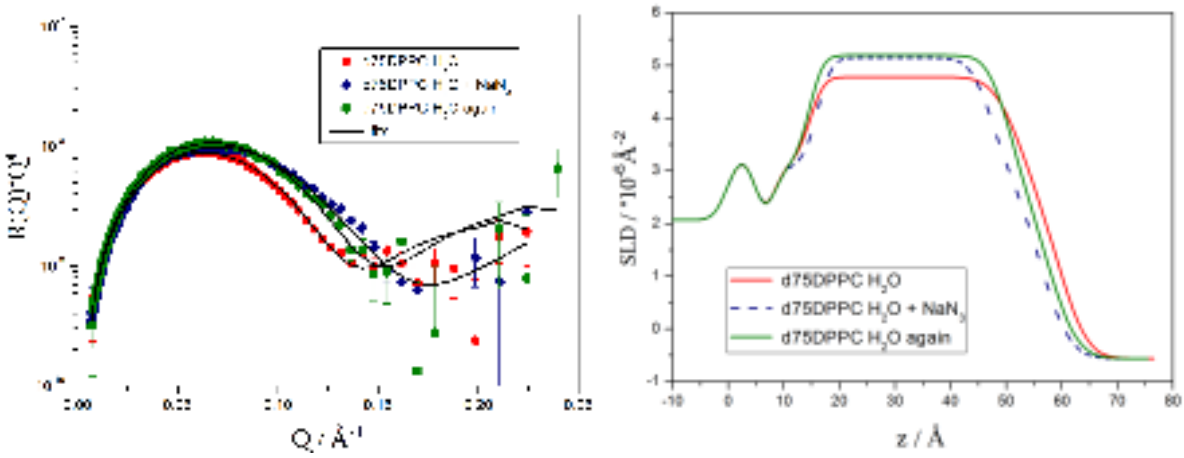

(a) (b)

Figure III.3.14 – (a) Reflectivity curves for the d_{75}DPPC bilayer in H2O contrast; in H2O contrast with 1mM NaN3 and after rinsing with H2O again. A clear change of the structure of the bilayer is observed due to the presence of NaN3. (b) SLD profiles obtained from the fits.

Based on the obtained structural parameters from the performed fits, we can conclude that presence of sodium azide in the system caused the decrease of the thickness of the tail region of the bilayer (from 3.8 nm to 3.1 nm) and an increase of the thicknesses of the head group regions (from $\approx$ 0.8 nm to 0.9 nm) of both leaflets of the bilayer. Structural parameters extracted from the fits for the pristine d_{75}DPPC bilayer, d_{75}DPPC bilayer with azide and d_{75}DPPC bilayer upon rinsing with H_2O can be found in Tab. B.4 in the Appendix. To obtain more precise structural information, this experiment should be performed measuring the sample in several solvent contrasts. We can note that the influence of NaN_3 on the structure of the phospholipid bilayer is not understood yet and to our knowledge no structural

studies are available.

Further experiments devoted to the investigation of the effect of sodium azide on the structure of pure phospholipid bilayers and bilayers with incorporated proteins are foreseen in the near future.

3.2.10 Conclusions

Thanks to the performed NR experiments we were able to confirm BR reconstitution into single solid-supported fluid lipid bilayers and we were able to quantify the amount of protein inserted, revealing structural and compositional sample changes caused by the protein. We have shown that the transmembrane protein Arch-3 does not interact strongly with single lipid bilayers and in order to reconstitute Arch-3 into a planar single bilayer highly concentrated protein solution should be used. This observation is in disagreement with literature where it is reported that Arch-3 more readily incorporates into lipid membranes than its close relative BR [104].

We have shown that BR strongly interacts with the solid support forming a robustly adsorbed protein layer on the bare substrate. BR does not aggregate in the proximity of the substrate and keeps it structural form. Arch-3, on the contrary, does not adsorb to bare silicon blocks and no interaction with the silicon surface was observed.

By means of NR experiments we have shown that the fluid floating lipid bilayer is a very fragile model system and it is not appropriate for protein reconstitution mediated by detergent. This observation also demonstrates that the lipid bilayer phase plays an important role in the outcome of the reconstitution procedure.

No structural and compositional modifications of the fluid single lipid bilayer and only minor structural modifications of the fluid floating lipid bilayer upon interaction with 0.05 mM detergent solution were observed. This is a very important observation as it is crucial to obtain confirmation that detergent solution does not induce harmful effects on the lipid bilayer structure and does not cause lipid bilayer solubilization. Thanks to this result, the effect of detergent and protein molecules on the sample structure can be resolved separately.

We have also studied the effect of NaN_3 on the structure of single and double lipid bilayer samples with and without inserted proteins. Due to lack of time within

this thesis project, consistent studies on the influence of sodium azide molecules on the membrane structure were not performed, thus no strong conclusions based on the observed effect can be made. This effect will be further investigated during scheduled beam-time at the ILL.

CHAPTER 4

BR activation with light

4.1 Neutron reflectometry experiments

We have performed NR experiments using the newly developed set-up for in-situ sample illumination in order to activate BR embedded into a floating lipid bilayer. The experimental program was the following : 1) measurement of reflectivity from the pristine double bilayer system; 2) in-situ BR reconstitution into the floating lipid bilayer and measurement of reflectivity from the system in three different solvent contrasts; 3) shining of light at the appropriate ("activational") wavelength on the sample (adsorption maximum of BR $\approx$ 568 nm) and measurement of reflectivity signal in several contrasts while illuminating the sample; 4) shining of light at a wavelength out of the activational wavelength range to perform a "blank experiment" and collect reflectivity signal while illuminating the sample. The last step is needed to demonstrate that there is no effect of illumination with light at a wavelength out of the "activational" range on the bilayer structure.

Unfortunately during the NR experiment devoted to the investigation of the effect of BR pumping activity on the bilayer structure, we had many problems with sample preparation. We were not able to form good quality (high coverage) double lipid bilayers systems on silicon and quartz blocks. As it was learnt later, a new protocol for the substrate polishing had been implemented by the polishing company on the substrates used during the experiment. This new implementation had a drastic effect on the chemical structure of the surface of the crystals, which had a harmful impact on the substrate-bilayer interaction.

Another beam time devoted to this project is scheduled at the end of September 2019, which coincides with the thesis submission deadline and therefore the

performed measurements and data analysis will not be included in the thesis.

4.2 Synchrotron radiation measurements

4.2.1 General discussion

The most challenging step of this work was the investigation by means of synchrotron radiation (SR) specular and off-specular reflectometry of the structural changes, thermal (equilibrium) and active (non-equilibrium) fluctuations of the membrane-protein system caused by transmembrane protein activity.

For such purpose we have performed combined specular and off-specular SR reflectometry experiments at the SOLEIL synchrotron (France) on the SixS beamline (see section 2.7.3). Specular reflectometry experiments were performed to study structural changes of the double lipid bilayer caused by BR incorporation and activation. The lateral features and out-of-equilibrium fluctuations induced by the protein activation were probed by off-specular measurements. Newly developed sample environment and setup for in-situ sample illumination during reflectometry measurements (see section 2.4) were used during this experiment. BR pumping activity was triggered by sample illumination with visible light. A long-pass filter with a 530 ± 5 nm cut-on wavelength [204] was used to select appropriate activational wavelength.

DSPC double bilayers were formed on the 5x8 cm^2 surface of silicon crystal by LB/LS deposition techniques following the procedure described in section 1.3.6. The Langmuir trough NIMA 1212D (section 1.3.7) was brought from the ILL and reinstalled in the chemistry lab of the SOLEIL synchrotron for the period of experiment.

First, specular reflectivity was measured from the pristine DSPC double lipid bilayer sample (black curve in Fig. III.4.1 and III.4.2). In order to reconstitute BR into the floating lipid bilayer 1 μg/ml of BR in 0.05mM DDM PBS buffer solution was injected into the cell. The BR-DDM solution was left for 10 minutes incubation period and then the system was thoroughly rinsed with PBS buffer to remove all the proteins and detergent molecules from the bulk. Specular and off-specular reflectivities were measured from the obtained system (red curve in Fig. III.4.3 and III.4.4, open red symbols in Fig. III.4.5). In Fig. III.4.4, the SLD profiles obtained from the fit of

the specular reflectivity curves are shown. To trigger BR activity the sample was illuminated with visible light and specular and off-specular reflectivity curves were collected during sample illumination (orange curve in Fig. III.4.3 and III.4.4, closed red symbols in Fig. III.4.5). Large changes of the specular and off-specular signal were observed.

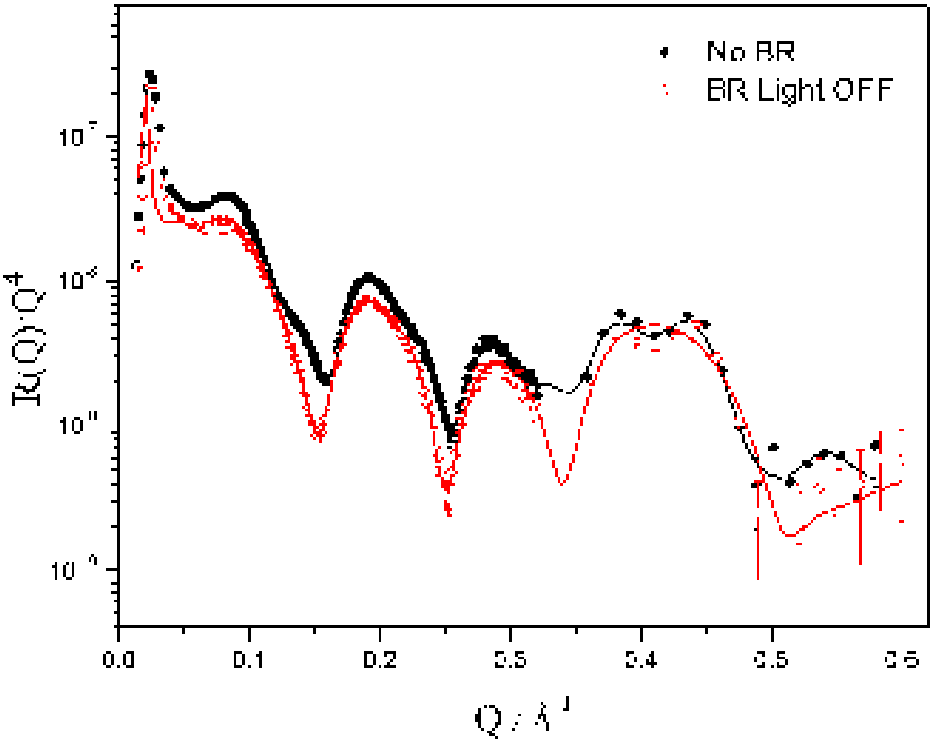

Figure III.4.1 – Specular SR reflectometry measurements for a DSPC double bilayer at 25°C before and after BR protein incorporation.

A blank experiment on a pure DSPC double lipid bilayer system was performed in order to test the effect of light on its structure and dynamics. Measurements were performed with and without illumination with light of a wavelength suitable for BR activation. No changes in the reflectivity curves, and therefore no structural bilayer modifications, were observed. Based on this result, we make the assumption that all modifications on the sample containing the protein upon illumination were induced by protein conformational changes and its pumping activity.

We have performed again specular and off-specular reflectometry measurements (blue curve in Fig. III.4.3 and III.4.4, open blue symbols in Fig. III.4.5) to check the reversibility of the effects of illumination on the sample. To do so, an exposure to light was stopped and the sample was measured again after a resting period of approximately 1-2 hours, which allows BR to go back to the dark-adapted state. As

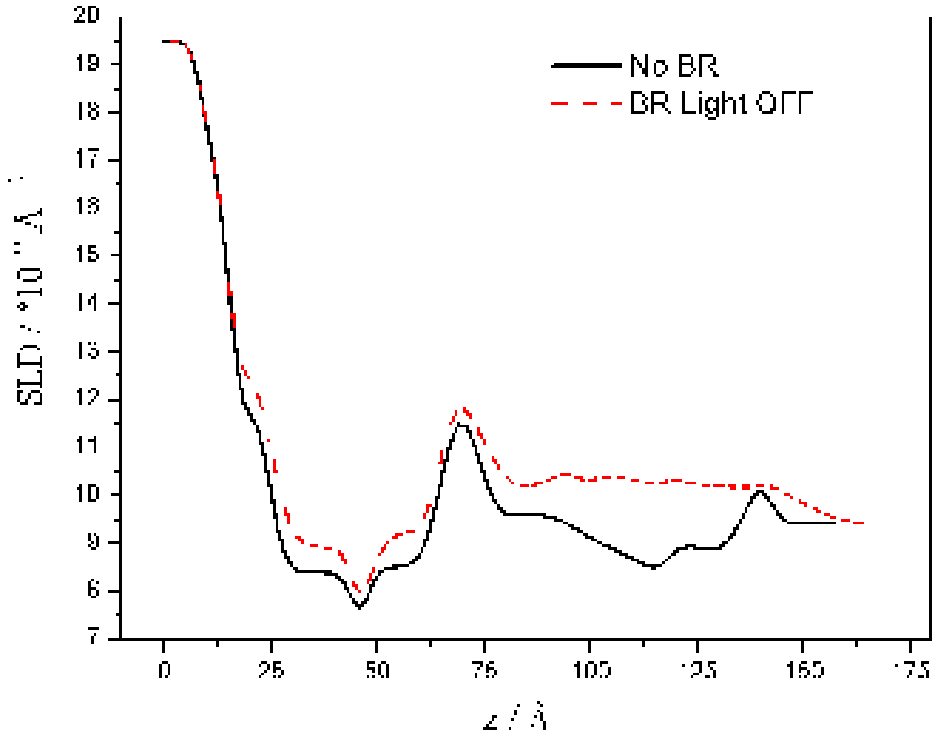

Figure III.4.2 – SLD profile obtained from the fit of the specular SR reflectometry measurements for a DSPC double bilayer at 25°C before and after BR protein incorporation.

can be seen from the specular reflectivity curve (blue curve in Fig. III.4.3 and III.4.4), the effect on the lipid bilayer structure is reversible. In the case of off-specular measurements, reversibility was observed only for the active state when light was switched on (see closed red and blue symbols in Fig. III.4.5), but when the light was switched off after the first illumination the system did not go back to the initial state (see open red and blue symbols in Fig. III.4.5). This may be due to an irreversible reorganization of the lipid and protein molecules within the bilayer caused by the protein pumping activity.

We have repeated measurements of the specular and off-specular signal during the sample exposure to light at an "activational" wavelength. Full reversibility in the specular and off-specular signals was observed, as can be seen in Fig. III.4.3 and III.4.4 from the green curves and blue curve (closed symbols) in Fig. III.4.5, which completely coincide with the orange and red curves collected during the first illumination.

A slab model and the AURORA fitting software were used for the reflectometry data analysis. The slab model is not the best suitable model to analyse high spatial

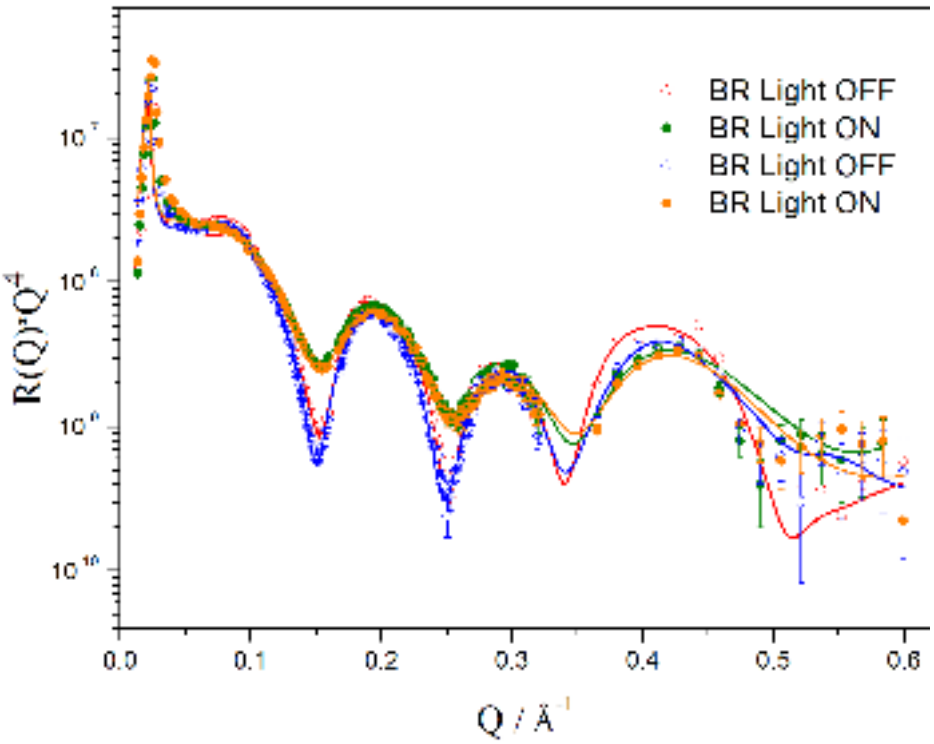

Figure III.4.3 – Specular SR reflectometry measurements for a DSPC double bilayer at 25°C after BR protein incorporation with and without illumination.

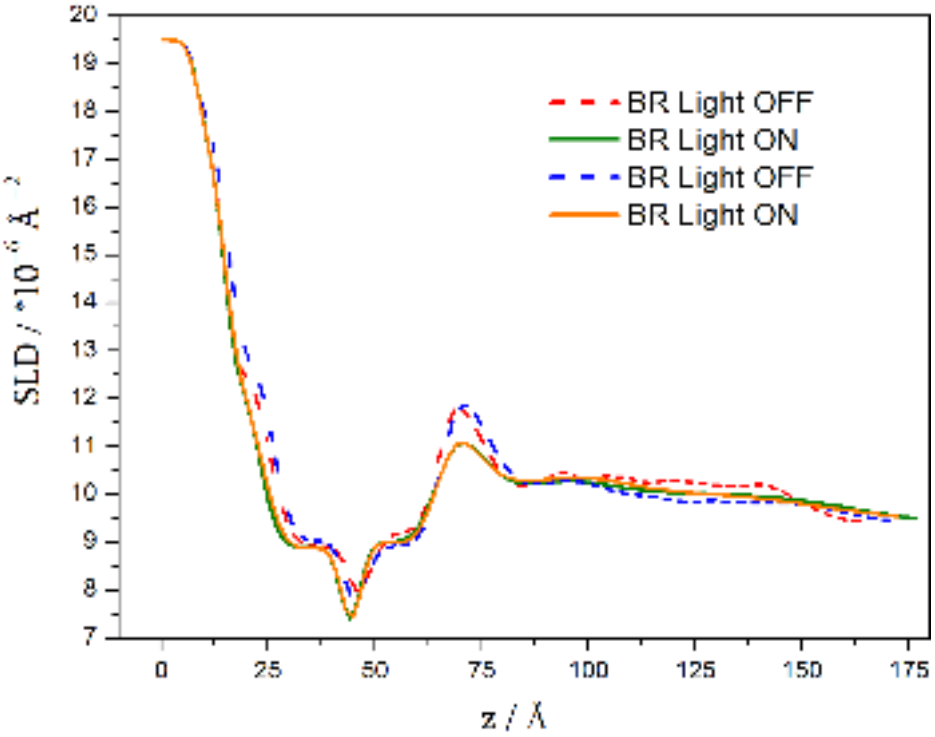

Figure III.4.4 – SLD profile obtained from the fit of the specular SR reflectometry measurements for a DSPC double bilayer at 25°C after BR protein incorporation with and without illumination.

resolution measurements as from the synchrotron reflectometry. Modeling based on the 1G-hybrid model is more appropriate in this case as it allows to describe better the methyl groups of the lipid chains. Results based on the analysis using slab model should be considered as preliminary. In order to obtain the full structural description of the system, we aim to perform combined simultaneous fitting of specular and off-specular reflectivity data. This simultaneous fitting procedure based on the 1G-hybrid model is implemented into a home-made program developped by Charitat and Daillant [166] and dedicated to the analysis of the specular and off-specular reflectometry measurements from double lipid bilayer samples. The fitting procedure is very time-demanding and therefore data are still being analysed.

No effect of 0.05 mM DDM detergent solution on the lipid bilayer structure was observed.

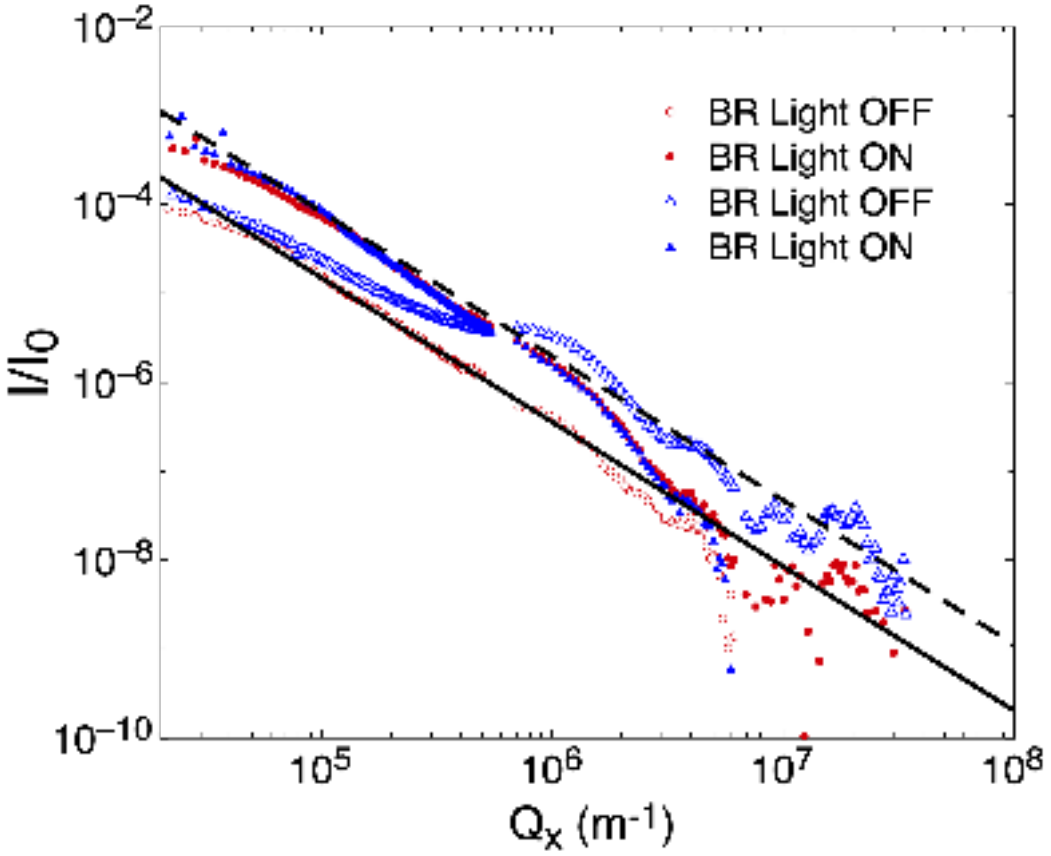

Figure III.4.5 – Off-specular SR reflectometry measurements for a DSPC double bilayer at 25°C with incorporated BR, with and without illumination. The dashed and dotted lines are performed fits in order to estimate the intensity at low Q_x.

4.2.2 Preliminary analysis of specular experiments

The structural parameters of the system before and after BR reconstitution and with and without illumination are summarized in Tab. B.14. Upon BR reconstitution we have observed an increase of the SLD value of the tail region of the floating lipid bilayer (SLD_{ch21}, SLD_{ch32} and SLD_{ch21} in Tab. B.14) and an increase of the floating lipid bilayer thickness (from 5.4 ± 0.3 to 6.1 ± 0.3 nm), the thickness of the water layer between the two bilayers was almost unchanged ($d_{w,2}$ = 1.5± 0.2 vs $d_{w,2}$ = 1.3 ± 0.2 nm). The roughness of the floating lipid bilayer increased from 0.2 ± 0.1 to 0.8 ± 0.2 nm upon BR insertion.

BR activity caused the increase of the thickness of the water layer between the two bilayers (from 1.3 ± 0.2 to 1.8 ± 0.2 nm) and a huge increase of the lipid bilayer roughness from $\sigma_{OFF,spec}$ = 0.8 ± 0.2 nm to $\sigma_{ON,spec}$ = 1.5 ± 0.2 nm. This observation is in qualitative agreement with a magnification of the fluctuation of the membrane-protein system caused by the protein pumping activity. The lipid bilayer thickness also largely increase, when the sample was under illumination (from 6.2 ± 0.5 to 7.2 ± 0.5 nm).

The analysis of the measurements of the reversible effect of the protein pumping activity on the lipid bilayer structure (i.e. measurements after switching off the light) indicated a reduction of bilayer thickness and a value of the roughness back to the initial state. The second BR activation with light caused again an increase of bilayer roughness and thickness (see Tab. B.14 for the details) with values similar to those obtained during the first illumination. All these results are preliminary and have to be confirmed by a more systematic analysis.

4.2.3 Preliminary analysis of off-specular experiments

Analysis of off-specular experiments requires first a careful refinement of the background subtraction. In addition, the height-height correlation functions in real space have to be implemented in the calculation of scattered intensity [166]. Both are complex tasks, that we were not able to achieve within this thesis project due to lack of time. Nevertheless, a discussion of the preliminary analysis will be presented in the following paragraph.

We have observed a significant increase of the scattered intensity under illumination at small Q_x. This is a direct indication of an overall increase in the average roughness of the sample (see Fig. III.4.5). The ratio of the scattered intensities between illuminated and non-illuminated sample at $Q_x \to 0$ gives a rough estimation of the sample roughness increase :

$$\frac{\sigma^2_{\mathrm{ON,off-spec}}}{\sigma^2_{\mathrm{OFF,off-spec}}} = 4.1 \pm 0.8. \tag{4.1}$$

At large Q_x, without illumination, we observe well structured oscillations that are characteristic for a double bilayer system. Under illumination, these oscillations are less pronounced, which is in agreement with an increase of sample roughness. The collected intensity at large Q_x is very sensitive to background subtraction, which needs to be improved before any quantitative analysis.

4.2.4 Discussion

By solving the Stokes equation to describe membrane motion together with the Darcy equation for the permeation of water trough the membrane, J.-B. Manneville *et al.*[16] have calculated the height-height correlation function of a membrane system in reciprocal space. By integrating over all modes, they have predicted that the active fluctuations of a bilayer can be described by an effective temperature T_{eff}. Specular and off-specular reflectivity measurements allow us to estimate this effective temperature independently :

$$\left(\frac{T_{\mathrm{eff}}}{T}\right)_{\mathrm{spec}} = \left(\frac{\sigma_{\mathrm{ON,spec}}}{\sigma_{\mathrm{OFF,spec}}}\right)^2 = 3.5 \pm 2.5, \tag{4.2}$$

$$\left(\frac{T_{\mathrm{eff}}}{T}\right)_{\mathrm{off-spec}} = \frac{\sigma^2_{\mathrm{ON,off-spec}}}{\sigma^2_{\mathrm{OFF,off-spec}}} = 4.1 \pm 0.8. \tag{4.3}$$

Both results are in a very good agreement. These values are of the same order of magnitude as the value obtained by micropipette aspiration experiments ($1.7 < T_{\mathrm{eff}}/T < 2.7$) [16, 19].

4.2.5 Conclusion

By means of specular and off-specular SR reflectometry experiments we were able to confirm BR incorporation into the gel-phase floating lipid bilayer and the preservation of the protein activity. We have demonstrated a reversible effect of BR pumping activity triggered with visible light of appropriate wavelength on the bilayer structure and dynamics. First preliminary analysis of both specular and off-specular experiments are very promising. Based on the specular data analysis, an increase of the bilayer roughness upon sample illumination was observed. This observation agrees well with the preliminary analysis of off-specular XRR measurements. The estimated effective temperatures for the sample with and without illumination are in a very good qualitative agreement with the values known from literature. Ongoing work to analyze simultaneously the SR specular and off-specular scattering experiments will provide a direct access to the fluctuation spectrum of the pure lipid bilayer and the lipid bilayer with inserted BR when the protein is active or not in a wide range of Q, below the micron scale. This combined analysis will allow us to characterize membrane properties such as bending rigidity, membrane tension and interaction potential between membranes (see section 2.6). It will provide a unique opportunity to compare directly experimental data to theoretical results and to achieve a better understanding of active fluctuation mechanisms at play.

CHAPTER 5

Summary and future work

Several different sample environment adapted to the various techniques used for bilayer preparation and characterization were developed within this thesis project. A solid/liquid cell for fluorescence microscopy experiments compatible with the LB/LS deposition techniques and inverted fluorescence microscope were developed at the ICS, Strasbourg, France in collaboration with Patrick Allgayer and André Schroder. Solid/liquid cells with the possibility of in-situ sample illumination during synchrotron and in-house reflectometry measurements were developed at the ILL (Grenoble, France) in collaboration with Kalvin Buckley. Heating/cooling chamber and setup for sample illumination compatible with the solid/liquid cells for synchrotron experiments were developed as well. The setup for NR measurements allowing in-situ sample exposure to light and update of the existing solid/liquid cells to include windows for sample illumination were performed at the ILL in collaboration with Grant Wallace. The performed developments were crucial for the success of this thesis project. These new sample environments and setups are easily available at the ILL within the LSS and SMSS groups. These developments serve for the benefits of all interested users, providing the possibilities to perform a large variety of new lab and large scale structure experiments.

Surface-sensitive techniques such as QCM-D, AFM, fluorescence microscopy, neutron reflectometry and X-ray reflectometry (in-house and synchrotron measurements), have allowed the development of a robust and reproducible protocol for BR reconstitution into membrane-model systems. Successful BR reconstitution into fluid and gel solid-supported single and floating lipid bilayer systems has induced changes of the bilayer structure, which were characterised down to the Å scale. Influence of incubation time, protein concentration and lipid bilayer phase on the

protein insertion efficiency were studied as well. It was shown that incubation time of the protein-detergent solution with the planar lipid bilayer does not play a major role in the outcome of the reconstitution process and that the BR-DDM solution instantly interacts with the lipid bilayer and BR insertion is an immediate process.

The study of the influence of protein concentration on the protein reconstitution process showed that depending on the type of membrane-protein system the concentration of the protein-detergent solution should be adjusted accordingly.

We have demonstrated that gel-phase lipid bilayers are more robust than fluid lipid systems for BR reconstitution. The gel phase floating lipid bilayer appears to be very stable upon multiple reconstitution steps. The concentration of the protein solution should be kept low (1 μg/ml of BR in 0.05 mM DDM solution) to prevent destruction of the floating bilayer. A 0.05 mM DDM solution does not cause structural and composition modifications of single and double lipid bilayers in gel and fluid phases, except for a small increase (10%) of water content in the fluid floating lipid bilayer observed upon the interaction with this solution. Another important observation that we have obtained is that BR keeps its structural integrity in 0.05 mM DDM solution. We have also observed that BR organizes into trimer structure upon insertion into the lipid bilayer or adsorption to the bare support.

Despite reports in literature of Arch-3 incorporation into lipid bilayers, no incorporation of Arch-3 into the fluid-phase single and gel-phase floating lipid bilayer was possible to achieve in this work by using the same experimental conditions as for the successful BR reconstitution. QCM-D measurements confirmed the adsorption of Arch-3 to the bare silicon surface. In contrast, we did not observe Arch-3 adsorption or protein interaction to the bare substrate with NR experiments. We have found that in order to reconstitute Arch-3 into single fluid lipid bilayers a very concentrated protein solution (60 μg/ml of Arch-3 in 0.05 mM DDM PBS buffer) is needed.

Thanks to specular and off-specular synchrotron radiation experiments we have demonstrated BR reconstitution into gel-phase floating lipid bilayers. We have shown the reversible effect of light illumination on the protein pumping activity through the reversible changes in the specular and off-specular reflectivity curves. By turning on and off (alternately) light with appropriate wavelength for activation,

we were able to tune the activity of the protein reconstituted into a gel-phase floating lipid bilayer.

The observed increase of the floating lipid bilayer roughness and thickness upon sample illumination is consistent with the increased lipid bilayer fluctuations caused by the protein conformational changes and its pumping activity. The obtained result from specular SR reflectometry measurements agrees well with the preliminary analysis of the off-specular experiments performed on the same sample, which have shown an increase of the bilayer roughness upon the sample illumination as well. The values of an effective temperature, which is used to characterize the active membrane fluctuations, were obtained from the specular and off-specular measurements independently. The estimated values agree well with the results known form literature.

A further combined analysis of the specular and off-specular SR reflectometry experiments will allow to characterize the membrane active and non-active (thermal) fluctuation spectrum and to evaluate physical properties of the system such as bending modulus, surface tension and interaction potential between membranes and their surroundings.

Using a 1 mM sodium azide solution in order to increase protein pumping activity, we have noticed that sodium azide causes modifications in the structure of the membrane-protein systems. The effect of NaN_3 on the structure of pure solid-supported lipid bilayers was observed as well, resulting in shrinking of the tail region of the lipid bilayer and extension of the lipid heads. Complete structural studies on the effect of sodium azide on the bilayer structure were not performed and no explanation is available yet.

As another perspective of this work, we aim to perform AFM experiments on double lipid bilayer systems to demonstrate BR insertion by means of AFM topography imaging. Preliminary measurements were successfully performed but, because of the complexity of the sample preparation and environment, improvement are still necessary to obtain quantitative description of these systems. All the necessary improvements are being developed but will be completed after the end of this thesis project.

NR reflectometry experiment to monitor BR reconstitution into the floating lipid

bilayer will be performed as well. We aim to obtain good quality gel phase floating membranes with incorporated BR. Composition of the final system can be resolved at molecular level, providing detailed qualitative information on the amount of BR inserted and modifications of the lipid bilayer. This kind of information is not accessible with any other technique. NR experiments in order to study the influence of protein activity triggered with light on the lipid bilayer structure will be performed as well. The specially developed sample environment and setup for the in-situ sample illumination during NR measurements will be used for this purpose.

Part IV

Interaction between charged bilayers

CHAPTER 1

Interaction between flat charged surfaces: state of the art

1.1 Theoretical approaches

Understanding electrostatic interactions between charged confined surfaces in the aqueous electrolytes solutions is important in many fundamental and applied research areas. For example, in industrial applications these interactions are crucial to control properties of colloidal suspensions [205, 206]. In biology, many specific functions of cell membranes strongly depend on electrostatic interactions, such as interactions with biomolecules, membrane adhesion and cell-cell interactions [34]. Electrostatic interactions between charged surfaces have been widely investigated both theoretically and experimentally. In the existing theoretical description a model of two infinitely large planar walls with uniform surface charge density σ_s and positively charged counterions of charge qe at a given temperature T are often implemented. Within this approach, planar lipid bilayers serve as an excellent model for the experimental and theoretical studies.

Within this thesis project we aim to study the interaction between highly negatively charged lipid bilayers composed of DPPS lipids. To position the considered problem within existing theoretical descriptions and experimental investigations, in the following section an overview of the approaches implemented to study the interaction between planar charged surfaces in electrolyte solutions will be present. First, the physical model for the planar lipid bilayers systems and the definitions of all relevant length scales will be given in section 1.1. Further, a short introduction to the theoretical description of WC and SC theories for the one-plate and two-plate case are developed and their limits will be discussed in section 1.1. In section 1.2 the

multiple experimental evidences of charge-like attractions between bilayers systems and the effect of a strong confinement on the water structural and dielectric properties will be considered. Structural and physical properties of the DPPS lipid bilayers will be discussed within this section as well.

1.1.1 Hamiltonian and relevant length scales

First, it is important to introduce the different characteristic length scales by considering the simpler case of infinitely large planar charged surfaces (charge density σ_s) with counterions only of charge qe (q is the counter ion valency) at a given temperature T. The neutralizing positively charged counterions exactly balance the negative surface charge. Thus, the overall system is electroneutral. The case of no salt is added to the system is considered. Such a model of a planar geometry is a physically relevant model for the description of charged planar membranes [207]. In the discussion a model, where particles interact only via Coulombic interaction, no dielectric jump at the charged boundaries is present and the medium is modeled with dielectric constant ε_w will be considered.

The Hamiltonian of this system of N counterions at the charged plate can be expressed as a sum of two terms :

$$\mathcal{H} = k_{\mathrm{B}}T\left(\sum_{i=1}^{N-1}\sum_{j>i}\frac{q^2\ell_{\mathrm{B}}}{|\mathbf{r}_i-\mathbf{r}_j|}+2\pi q\ell_{\mathrm{B}}\sigma_s\sum_i z_i\right), \tag{1.1}$$

where the first term of Eq.1.1 describes the direct interaction between counterions in solution and the second term of Eq.1.1 takes into account the interactions between counterions and surface charges.

The **Bjerrum length** $\ell_{\mathbf{B}}$ is defined as the distance at which two elementary charges interact with thermal energy k_BT, leading to :

$$\ell_{\mathrm{B}} = e^2/\left(4\pi\epsilon_w k_{\mathrm{B}}T\right). \tag{1.2}$$

In water at room temperature the Bjerrum length ℓ_{B} is 0.7 nm [208].

The **Gouy-Chapman length** ℓ_{GC} is defined as the distance from the wall at

which the thermal energy of a counterion $k_B T$ equals the counterion-wall interaction energy, leading to :

$$\ell_{\mathrm{GC}} = 1/\left(2\pi q \sigma_s \ell_{\mathrm{B}}\right). \tag{1.3}$$

The Gouy-Chapman length characterizes the thickness of the diffusive counterions layer close to the surface and it depends on surface charge density σ_s (in e^-/nm^{-2}).

To take into account screening effects, which start to play an important role in the electrostatic interactions, when coions (salt solution of a molar concentration c) are added to the solution, another relevant length Debye-Hückel length ℓ_{D} must be introduced. The **Debye-Hückel length** $\ell_{\mathbf{D}}$ is a length scale over which mobile charge carriers (coions, counterions) screen out an electric field in solution. The electric potential of the system exponentially decreases each Debye length :

$$\ell_{\mathrm{D}} = \sqrt{\left(\epsilon_w k_{\mathrm{B}} T\right) / \left(c N_a q^2 e^2\right)} = 0.3/\sqrt{c}\ \ \mathrm{nm}. \tag{1.4}$$

The **Netz-Moreira electrostatic coupling constant** Ξ is defined as the dimensionless ratio between Gouy-Chapman length ℓ_{GC} and Bjerrum length ℓ_{B} and it quantifies the competition between the counterion-counterion, counterion-wall interactions and thermal agitation $k_{\mathrm{B}} T$. Thus Ξ describes the strength of the electrostatic interaction in the system [208]:

$$\Xi = \frac{\ell_{\mathrm{B}} q^2}{\ell_{\mathrm{GC}}} = 2\pi q^3 \ell_{\mathrm{B}}^2 \sigma_s. \tag{1.5}$$

According to this definition, Ξ can be tuned by changing surface charge density σ_s, counterions valency q or temperature T.

We can re-scale all discussed lengths in units of the Gouy-Chapman length according to $\tilde{r} = r/\ell_{CG}$, which lead to the Hamiltonian $\mathcal{H}$, which only depends on the coupling constant Ξ :

$$\mathcal{H} \;=\; k_{\mathrm{B}} T \left(\sum_{i=1}^{N-1} \sum_{j>i} \frac{\Xi}{|\widetilde{\mathbf{r}}_i - \widetilde{\mathbf{r}}_j|} + \sum_i \widetilde{z}_i \right), \tag{1.6}$$

where $\widetilde{z}_i$ is the distance of the counterion i from the wall.

Depending on the values of ℓ_{B} and ℓ_{GC} and thus on the ratio Ξ, the different

physical regimes where either attractive or repulsive interaction dominates between ions, ions and a charged wall, can be discussed.

For a **small coupling parameter** $\Xi \ll 1$ (low valency counterions, weakly charged surfaces, high temperature), referred as a weak-coupling (WC) regime, the counterion-wall system possesses a relatively large Gouy-Chapman length ℓ_{GC}. The Hamiltonian of the system (Eq. 1.6) is dominated by interactions between counterions and surface charges. In this WC regime the counterion layer behaves like a three-dimensional gas and the correlations between counterions can be neglected. For low coupling constant values, i.e. $\Xi \ll 1$, the counterion distribution can be evaluated by the Poisson-Boltzmann (PB) theory in the mean-field approximation [34].

For a **large coupling parameter** $\Xi \gg 1$ (high valency counterions, highly charged surfaces, low temperature), referred as the strong-coupling regime (SC) [36], the Gouy-Chapman length ℓ_{GC} is relatively small, indicating that counterions are strongly attracted toward the charged wall and form a highly correlated quasi two dimensional layer at the surface. The Hamiltonian of the system (Eq. 1.6) is dominated by interactions between counterions and therefore counterion-counterion correlations can not be neglected. In the limit of $\Xi \gg 1$ the WC approach breaks down and thus the PB theory is not valid anymore [207, 209]. Strong-coupling (SC) theory and extensive numerical simulations were developed to describe electrostatic interactions in the regime of $\Xi \gg 1$ [36, 40, 42, 43, 48, 207, 210]. It was shown that identically charged plates can attract each other at small separations and at sufficiently large coupling parameters $\Xi \geq 20$.

As introduced above, WC and SC theories are theoretical descriptions of electrostatic interactions between charged objects, which provide the ion distribution function near the charged wall, depending on the regime considered. The SC and WC approaches for the description of electrostatic interactions in the one-plate and two plates geometry, when two walls are equally negatively charged, will be shortly discussed below. The geometry of two equally charged plates is relevant for the description of the interaction between two charged membranes. A description of the WC and SC electrostatic interactions between asymmetrically charged planar surfaces can be found in reference [208].

1.1.2 Interaction between flat surfaces: PB theory

Mean-field PB theory and corrections to it (loop expansion in the limit of small coupling parameter $\Xi \ll 1$) were extensively developed and applied to obtain the counterion density distribution near a charged wall and between two equally charged walls by Andelman [34] and Boroudjerdi [211] and by Netz and Moreira [36, 41–43, 207]. The PB approach gives an accurate description of the charge distribution of monovalent ions near the surfaces of small potentials in physiological conditions.

The interaction between two flat charged surfaces as a solution of the PB theory in the weak coupling limit can be described within four different regimes: the linear Debye-Hückel regime, the ideal gas regime, the Gouy-Chapman regime and the intermediate regime, depending on the values of the plate-plate separation d, Gouy-Chapman length ℓ_{GC} and Debye-Hückel screening length ℓ_D.

The diagram in Fig. IV.1.1 is plotted in terms of two dimensionless ratios: ℓ_{GC}/d and ℓ_D/d and defines the limits of validity of these four regimes in the WC limit [34].

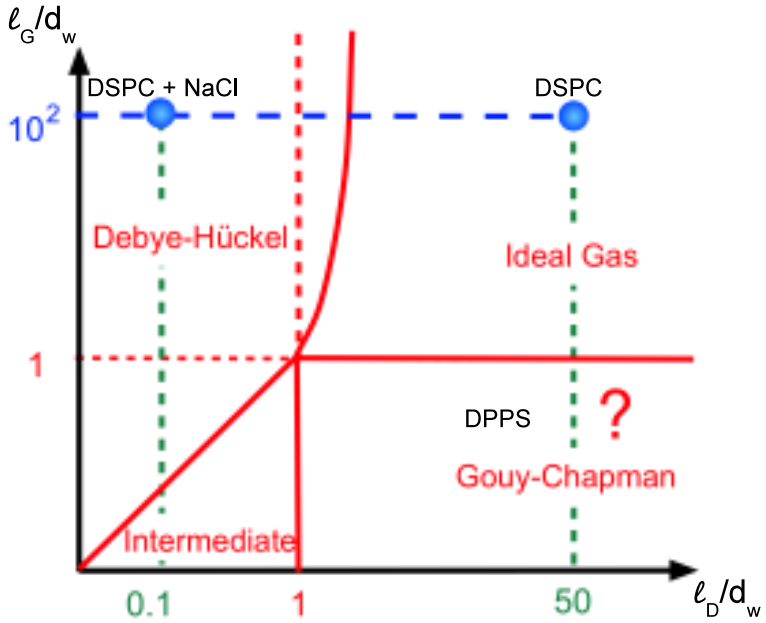

Figure IV.1.1 – Schematic representation of various limits of the Poisson-Boltzmann equation for two flat charged surfaces [34].

In **the ideal-gas region** ($\ell_{GC}/d \gg 1$ and $(\ell_D/d)^2 \gg \ell_{GC}/d$) the surface charge density and the concentration of the counterions between the two walls are small and the ion density distribution is almost constant between the two walls. Therefore

the main contribution to the electrostatic interaction between two counterions and counterions and the charged wall comes from the counterions' entropy. As an example, the electrostatic interaction between two zwitterionic lipid membranes composed of DSPC lipids without added salt can be well described within the ideal gas limit of PB theory, as the Debye-Huckel length $\ell_D \approx 200$ nm is large and the surface charge is very low ($\sigma_s \approx 0.001\ e^-/\text{nm}^2$), which defines a weak electrostatic repulsion between membranes.

The **Debye-Hückel region** extends from small to large separation d between two plates and from low to high screening length ℓ_D , thus two Debye-Hückel regions can be defined: the large-spacing ($\ell_D \ll \ell_{GC}$ and $\ell_D/d \ll 1$) and small-spacing ($(\ell_D/d))^2 \ll \ell_{GC}/d$ and $\ell_D/d \ll 1$) regions. The surface charge of the walls is small in both cases. The electrostatic interaction between two membranes composed of zwitterionic lipids can be describe within the ideal gas region of PB theory, as it was discussed before. It was shown by Hemmerle [35] that addition of NaCl salt to the system allows to access the Debye-Hückel regime, where the electrostatic interaction is screened ($\ell_D \approx 0.3$ nm) (Fig. IV.1.1). Therefore, by adding salt to the system, this way tuning the electrostatic interaction between membranes, the different regions of the solutions of PB equation can be probed.

In the **Gouy-Chapman region** ($\ell_{GC}/d \ll 1$ and $\ell_D/d \gg 1$) the surface charge density is large and and the counterions concentration is very low, thus the electrostatic interaction is very strong and not screened. These conditions bring the Gouy-Chapman regime close to the limit of validity of PB theory.

1.1.3 Interaction between flat surfaces: SC theory

As it was discussed above the PB theory predicts that the electrostatic interaction between similarly charged surfaces is always repulsive. In order to explain the phenomenon of like-charge attraction, we have to go beyond the scope of PB theory and take the correlations between ions into account, which are neglected within the PB description and which are important in the description of the interaction between macroscopic similarly charged objects [207].

SC theory was fully developed by Netz and co-workers [36, 41–43, 207] for the cases of one charged plane and two equally charged planes when only counterions

are present in the solution. This SC theory naturally predicts electrostatic attraction between similarly charged plates and confirms that identically charged plates can attract each other in the presence of monovalent counterions and when the surface charge density is extremely high [36]. Moreira has shown that by applying the SC theory to describe data from Monte Carlo simulation, a good agreement between theory and simulation can be achieved [41–43, 207].

It was shown that the SC theory is valid for the case of multivalent counterions, high surface-charge density and low temperatures, therefore it is easily experimentally accessible. The validity of the strong-coupling theory depends not only on the value of the coupling constant, but also on the distance between the charged plates. It was shown by Moreira and Netz [43] that even for systems with small coupling parameters there is a range of inter-plate distances below which SC theory is valid. In general the SC approach should be valid as long as the distance d from the wall is smaller than the average lateral distance between counterions $a_\perp$. The limits of the validity of SC theory in dependance of the values of d, $a_\perp$ and Ξ will be discussed below for the one plate and two plates cases.

To get an intuitive insight into the attraction phenomena between two like-charged plates, we can consider the case of the interaction between one counterion sandwiched between two like-charged plates and we can demonstrate the existence of attraction between charged plates for this one-particle case.

Denoting the distance between the plates as d, the area of each plate as A, the distances between counterion and the plates as x and $d-x$, we can calculate the electrostatic interaction between the ion and the plates, assuming the distance between the plates d is much smaller than $\sqrt{A}$: $U_1 = 2\pi k_B T \ell_B q \sigma_s x$ and $U_2 = 2\pi k_B T \ell_B q \sigma_s (d-x)$, respectively. The sum of the two interaction potentials is $U_{1+2} = U_1 + U_2 = 2\pi k_B T \ell_B q \sigma_s d$. This result demonstrates that no force is acting on the counterion and that the counterion mediates an effective attraction between the two plates.

The interaction between the two charged plates for $d \ll \sqrt{A}$ is given by $U_{12} = -2\pi k_B T A \ell_B q \sigma_s^2 d$. The system is **electroneutral** and the total energy in the system is $U = U_{1+2} + U_{12} = U_{12} + U_1 + U_2 = 2\pi k_B T A \ell_B \sigma_s^2 d$, taking into account that $q = 2A\sigma_s$. The electrostatic pressure (per unit area A) can be estimated as $P_{el} = -\delta(U/A)/\delta d = -2\pi k_B T \ell_B \sigma_s^2 < 0$, showing that the two plates attract each other [36, 42].

The entropic pressure due to counterion confinement between two plates can be expressed as $P_{en} = k_B T/Ad = 2k_B T\sigma_s/qd$. The total pressure $P_{\text{tot}} = P_{en} + P_{el}$ is given by:

$$P_{\text{tot}} = 2\pi\ell_B k_B T\sigma_s^2(2\frac{\ell_{GC}}{d} - 1). \tag{1.7}$$

The equilibrium plate separation can be found when the total pressure is zero ($P_{\text{tot}} = 0$), leading to $d_{eq} = 1/\pi\ell_B q\sigma_s$.

Thus, considering the interaction between charged plates for the one-particle case, we have shown that the attraction between similarly charged plates arises from the electroneutrality condition of the whole system and that this attraction between charged plates and counterion is stronger than the entropic repulsion at not too small distances between the plates.

It was shown [36, 42] that the results obtained above for the equilibrium distance between the plates d_{eq} and the interaction potential in the limit of SC agree well with the precise description and results of the SC theory, the main results of which will be shortly discussed below.

SC theory. The case of one flat surface

It was shown by Netz [36] that for the one charged wall case, when the coupling parameter $\Xi \gg 1$ and the lateral distance between ions is larger than their separation from the wall (proportional to ℓ_{GC}), the counterions layer is flat and two-dimensional. The structure of the counterion layer near the wall is dominated by mutual repulsion between ions and ion crystallization near the wall takes place .

When the coupling parameter $\Xi \ll 1$, the lateral ion separation is smaller than the layer height ℓ_{GC}, thus the counterion layer is a three-dimensional liquid-like structure and the repulsion between ions is rather unimportant, therefore the PB approach ($\Xi \ll 1$) is valid.

When $\Xi \gg 1$ ion condensation starts to occur and ion correlations start to play an important role. The SC theory, which takes into account the correlated ion-density fluctuations, describes the system at this limit (Fig. IV.1.2).

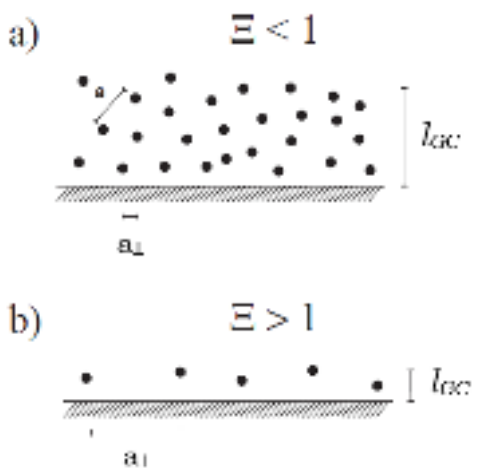

Figure IV.1.2 – Schematic representation of the counterion distribution near a charged wall depending on the value of the coupling parameter Ξ [36].

SC theory. The case of two flat surfaces

Netz [36] has derived PB and SC theories and the explicit results of the density distributions of counterions as a function of the distance from the plate for the cases of a single charged plate and two charged plates in the presence of counterions only. Depending on the values of the coupling constant Ξ, the distance between the plate d and the Gouy-Chapman length ℓ_{GC}, several possible scenarios for the ion distribution and resulting electrostatic interaction between two charged plates can be discussed. All possible cases are schematically represented in Fig. IV.1.3:

When the distance between the plates d is smaller than the lateral distance between ions $a_\perp$, $d < a_\perp$ or $\tilde{d}^2 \ll \Xi$, SC theory correctly predicts the counterion density profile and the inter-plate pressure (Fig. IV.1.3(a)).

When the distance between the plates d is larger than the lateral distance between ions $a_\perp$, $d > a_\perp$, the SC theory for two plates does not systematically describe the interaction between two charged plates.

If the Gouy-Chapman length ℓ_{GC} is the smallest length, (Fig. IV.1.3(b)), the two counterion layers decouple and are quasi-two-dimensional ($\ell_{GC} < a_\perp$ and $\Xi > 1$). The density profiles of each layer are well described separately by the SC theory for a single charged plate.

If the Gouy-Chapman length is intermediate length, $a_\perp < \ell_{GC} < d$ or $\Xi < 1 < d$ (Fig. IV.1.3(c)), two plates attract two separate layers of counterions. The lateral

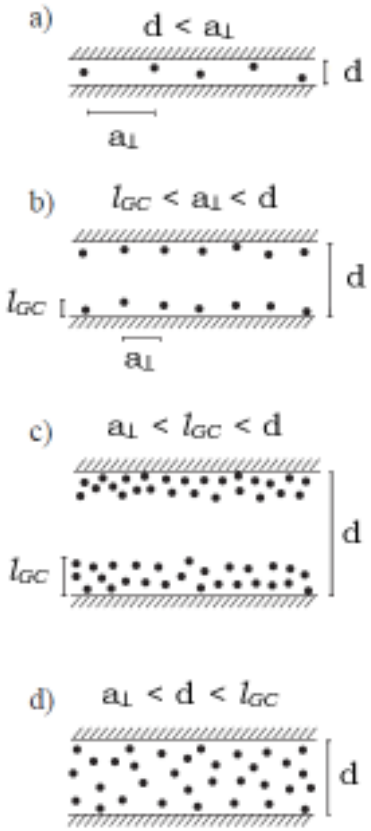

Figure IV.1.3 – Schematic representation of the counterions distribution between two charged walls depending on the values of the coupling constant Ξ, Gouy-Chapman length ℓ_{GC}, inter-plate distance d and lateral distance between counterions $a_\perp$ [36].

distance between ions $a_\perp$ is smaller than the Gouy-Chapman length ℓ_{GC}. The PB approach is valid and correctly describes density profiles and inter-plate pressures.

If the Gouy-Chapman length ℓ_{GC} is the largest length scale, $a_\perp < d < \ell_{\mathrm{GC}}$ or $\Xi < \tilde{d}^2 < 1$ (Fig. IV.1.3(c)), the space between the two plates is filled with a gas of counterions and thus confined three-dimensional gas is formed. Both SC and PB theories predicts the same leading term of the density distribution, but the next correction are different.

Thus, we can conclude that the SC solution becomes more accurate at short distances between the plates (or close to the plate), while the PB approach becomes valid when the distance between the plates is large (or far away from the wall). At intermediate-distances neither the PB nor the SC theory is able to describe accurately the overall system.

Wigner-crystal formulation of the strong-coupling theory (WSC)

An analytical approach for the description of the electrostatic interaction between similarly and highly charged planar interfaces in the presence of counterions only was developed further by Samaj and Trizac [45–48, 210, 212]. This approach to the electrostatic double layer problem is based on the fact that in the asymptotic limit $\Xi \to \infty$ the counterions collapse on the charged surface, creating a 2D hexagonal Wigner crystal. To properly describe the system an expansion of the counterion density profile around the ground state formed by the two-dimensional Wigner crystal in the low temperature limit (in the limit $\Xi \to \infty$) was performed. An excellent agreement for the leading term and next correction terms with Monte Carlo simulations for the cases of strong and intermediate couplings was achieved. Samaj has shown that the original strong couple theory developed by Moreira and Netz [36, 41, 43] is in a good agreement for the leading term, but the first correction within the virial expansion does not describe the MC data correctly.

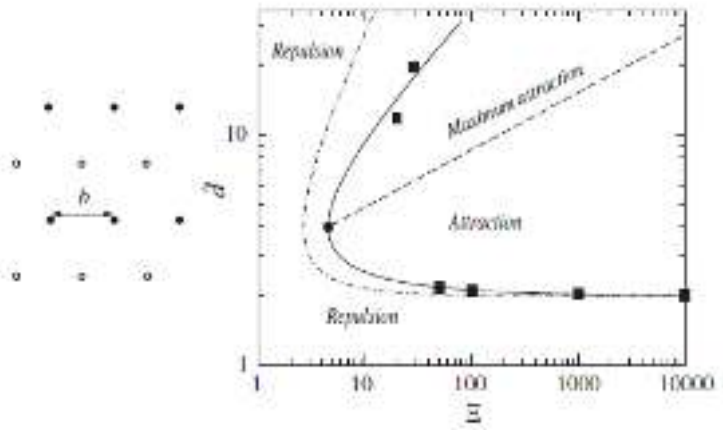

Figure IV.1.4 – Left: Structure of counterions on two parallel charged plates. Right: Phase diagram of the attraction/repulsion between two identically charged plated [46].

Samaj [45] has estimated the pressure between two plates separated by the distance d in the regions where the like-charge attraction phenomenon takes place. The attractive ($P \ll 0$) and repulsive ($P \gg 0$) regions can be defined, depending on the dimensionless distance between the surfaces $\tilde{d} = d/\ell_{GC}$ and the coupling constant Ξ. A phase diagram of the attraction/repulsion regimes between two identically charged plates is shown in Fig. IV.1.4. It should be noted that the upper branch in

Fig. IV.1.4 of the attraction/repulsion boundary is such that $\tilde{d}/\sqrt{\Xi}$ is of the order of unity and hence lies at the limit of validity of the expansion. The filled squares are MC results from Moreira and Netz [36, 41, 43] with $\Xi \gg 20$. The solid curve shows the points, where the pressure is zero. The dash-dotted line is for the corresponding virial SC prediction by Moreira and Netz [36, 41–43, 207]. The continuous line is the SC theory developed by Samaj [45–48, 210, 212]. The straight dashed line represents the values of d_{max}, where $\delta\tilde{P}/\delta\tilde{d} = 0$ and the maximum attraction is taking place.

1.2 Experimental approaches

1.2.1 Structure of charged membranes

In order to study the interaction between charged planar membranes, double lipid bilayers composed of negatively charged DPPS phospholipids were chosen as a model system. Within this thesis project we aim to resolve the structure of DPPS double lipid bilayers in pure water and to follow the structural modifications of the system caused by temperature changes and addition of salt. The structure of the charged system to its non-charged counterparts will be compared as well.

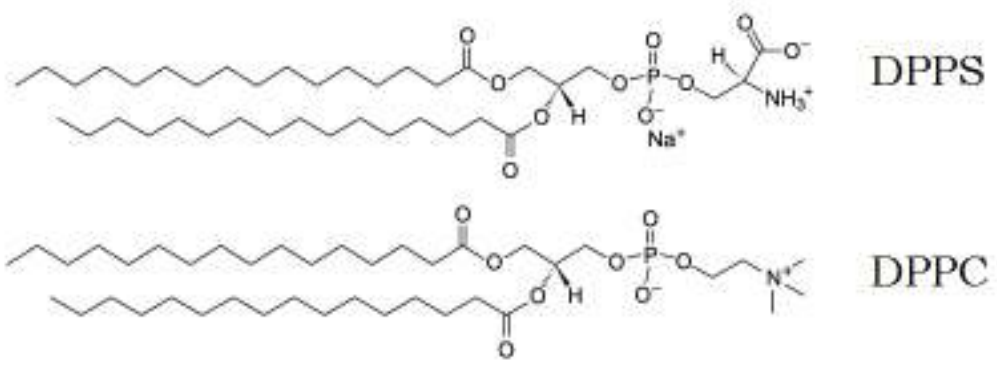

Figure IV.1.5 – Chemical structure of DPPS and DPPC phospholipids used in this work.

The structure of DPPS phospolipids is shown in Fig. IV.1.5. The head group of DPPS holds a carboxylate group which bears one negative charge at natural pH. The monovalent Na^+ counterions, which are present in solution, balance the

negative charge of the head group and make the overall system electroneutral. The chain region of DPPS lipids is identical to the chain region of the zwitterionic DPPC lipids. As it was shown experimentally [213–218] and by means of MD simulations [44, 219–221], the negative charge of lipid molecules has a great influence on the lipid bilayer structure and its physical properties. In order to resolve the difference it is important to investigate and compare the structure and physical properties of charged and zwitterionic systems.

Table 1.1 – Area per lipid molecule for the different lipid type from X-ray diffraction and NMR spectroscopy studies [213] and molecular dynamic simulations [220].

Name	DOPS fluid	DOPC fluid	DMPS gel	DMPC gel	DPPS gel	DPPC gel
A, Å^2	65.3	72.5	40.8	48.1	54	62

It was shown by Petrache *et al.* [213] that the area per headgroup of phosphatidylserine (PS) lipid is considerably smaller in both the gel and the fluid phase than the one of phosphatidylcholine (PC) lipids, but PS bilayers are thicker. It was found that DOPS lipids in the fluid state have an area per headgroup of 65.3 Å^2, compare to DOPC lipids with 72.5 Å^2, which is quite a counter-intuitive result considering the existence of the increased electrostatic repulsion between the negatively charged PS headgroups. For DMPS and DMPC lipids in the gel phase it has been observed that the headgroup area of DMPS lipids in the gel phase is equal to 40.8 Å^2 and for DMPC 48.1 Å^2. This observation was explained by the ion condensation effect, Na^+ counterions interaction with the head groups and formation of extensive hydrogen bonding between neighboring lipids, which is as well consistent with the literature [219, 220]. By means of molecular dynamic simulations Pandit [220] has obtained an area per lipid molecule equal to 54 Å^2 for DPPS lipid bilayers and 62 Å^2 for DPPC lipid bilayers with Na^+ counterions only. The obtained values are summarised in the Tab. 1.1.

Despite the electrostatic repulsion it was observed that the area per lipid molecule for charged lipids is 10% lower than that of zwitterionic ones. This fact clearly demonstrates that electrostatic repulsion does not play an important role in the interaction between lipid head groups.

1.2.2 Electron density profiles of charged bilayers

The available studies on the structure of charged lipid bilayer systems give contradicting findings concerning the ED values of charged lipids.

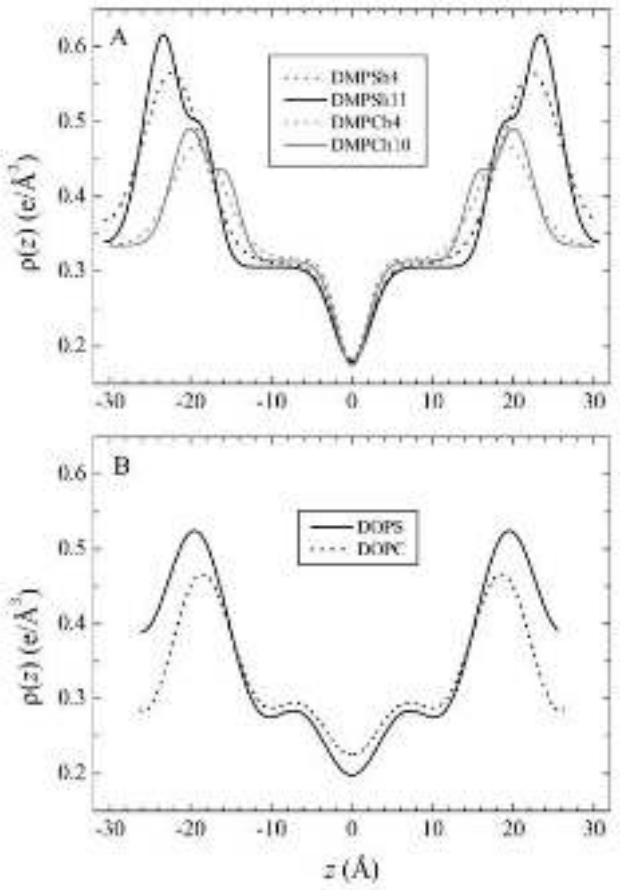

Figure IV.1.6 – Electron density profiles versus normal to the bilayer z for a: (A) Gel phase DMPS bilayer at 20°C (black) and DMPC bilayer at 10°C (gray). (B) Fluid phase DOPS bilayer (solid) and DOPC bilayer (dashed) at 30°C [213].

In the X-ray diffraction studies conducted by Petrache *et al.* [213] the electron density profiles for DMPC (gel phase) and DOPC (fluid phase) lipid bilayers were compared to DMPC and DOPS ones. The obtained ED profiles for these systems are shown in Fig. IV.1.6, where we can clearly see that the ED values of the PS head groups are approximately 12% larger then the ED of PC head groups. The obtained ED values are in contradiction to the values reported by Jing *et al.* [222], where they have observed that the DPPS lipids have a lower headgroups ED ($\approx 17\%$) than DPPC, as shown in Fig. IV.1.7. The reported results clearly indicate that complementary studies on the structure of highly controlled model systems composed of charged

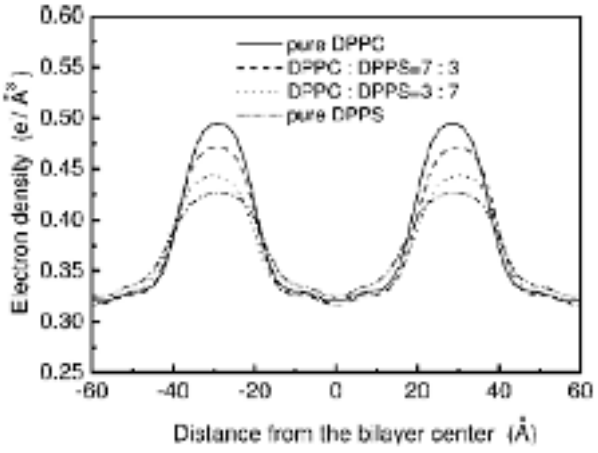

Figure IV.1.7 – Electron density profiles derived from the X-ray reflectivity spectra of the mixed multilayers composed of varied fraction of DPPS and DPPC lipids [222].

PS lipids are necessary in order to resolve the existing contradictions.

1.2.3 Effect of charges on the bending rigidity of the membrane

Experiments carried out on charged membranes have demonstrated the pronounced effect of charge on the bilayer's physical properties, membranes fluctuations and interactions, indicating that charged systems are more rigid than zwitterionic lipid bilayers. It was shown that charged DOPS multilayers have smaller interbilayer fluctuations than multibilayers composed of zwitterionic DOPC lipids at the same interbilayer separation d. This demonstrates that the compressibility and/or the bending modulus of the charged bilayers are larger indicating that DOPS multilamellar systems have a more rigid structure than DOPC ones.

The elastic compressibility modulus of a stack of charged membranes composed of SDS-octanol bilayers with monovalent Na^+ counterions was measured with a surface force apparatus by Herrmann *et al.* [50]. It was shown that electrostatics alone (beyond PB theory) can fully describe the obtained data for the interaction betweeen charged surfaces at distances larger than a few nanometers (above 2-3 nm), where steric repulsion is negligible and the nonelectrostatic contribution plays a minor role. The compressibility values obtained from the SFA of 16.6 ± 2.8 kPa perfectly match the prediction of pure electrostatic interactions in the WC limit (17.7 kPa, $\Xi \sim 3$).

Delorme *et al.* [223] have performed AFM studies on catanionic membranes in

order to directly follow the electrostatic effects on the bending rigidity of charged membranes. It was shown that without added salt, the bending rigidity of the catanionic membrane was very high (450 ± 38 k_BT). When salt was introduced to the solution, a decrease of the bending rigidity was observed and it reached a plateau value of 230 k_BT. The decrease of bending rigidity with increasing salt concentration was detected and the observed phenomenon was explained by a salt-screening effect of the electrostatic contribution to the bending rigidity.

The high rigidity of charged membranes causes a decrease in thermal membrane fluctuations, which makes it difficult to study and independently measure the bending rigidity and compressibility modulus of the charged multubilayer systems by means of X-ray diffraction. Therefore, other experimental approaches should be involved in order to resolve both contributions to the membrane shape fluctuations.

1.2.4 Interactions between highly charged membranes

A large variety of experiments were performed in order to define the electrostatic contribution to the membrane bending rigidity, membrane fluctuations and swelling.

Demé *et al.* [224] have performed small-angle X-ray and neutron scattering and freeze-fracture electron microscopy experiments to study charged DOPS phospholipid membranes in the absence of salt over a wide range of osmotic pressures, which allows to probe the interbilayer d spacing between 1 and 70 nm. Depending on the applied pressure, different structures of the system were observed. At high pressure (high volume fraction of lipid vesicles) a lamellar phase with linear swelling was found. Lowering the osmotic pressure in the system has induced the onset of the formation of the lamellar oyster shell state characterized by giant uncorrelated collective fluctuations. At lower pressure these fluctuations become strongly correlated (Fig. IV.1.8). Further dilution of the system destabilizes membrane and dispersion of stable single or multilamellar vesicles formed spontaneously. It was shown that maximum lamellar periodicity of 70 nm can be reached at low osmotic pressure.

By means of X-ray diffraction Petrache *et al.* [213] have studied the electrostatic interaction between charged membranes composed of DOPS lipids by measuring the interlamellar spacing d as a function of applied osmotic pressure P_{osm}. The obtained pressure-d-spacing curves for zwitterionic DOPC and negatively charged

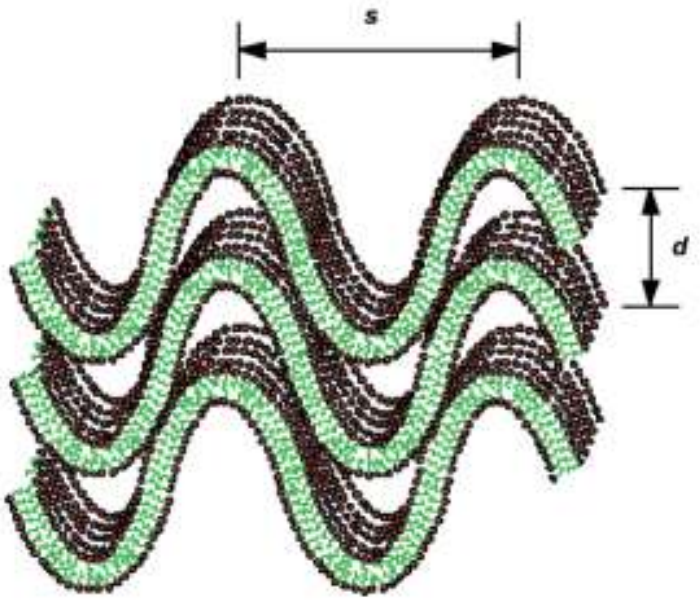

Figure IV.1.8 – Intermediate oyster shell state structure of the membrane occurring before destabilization and vesicle formation. Membrane fluctuations are highly correlated and large [224].

DOPS lipids are shown in Fig. IV.1.9. It was demonstrated that charged DOPS multilayers can swell indefinitely upon system hydration which is contrary to the case of zwitterionic DOPC lipids, where the interlamellar spacing reaches a constant value and does not change upon further pressure increase [213]. It was shown that for DOPS multilayers *d*-spacings of up to 10 nm at 1 atm were observable. The modeled interaction between adjacent DOPS bilayers appears to be in the good agreement with the PB theory in the Gouy-Chapman regime (high surface charge). It was shown that the electrostatic large range interactions completely dominate the fluctuation pressure in the case of charged bilayers and the calculated osmotic pressure in this case properly describes the measured data as can be seen in Fig. IV.1.9.

Komorowski *et al.* [225] have studied by means of small-angle X-ray scattering the structure and adhesion behavior of vesicles composed of pure DOPS and a mixture of DOPC:DOPS (1:1) lipids with the addition of $CaCl^{2+}$ and $MgCl^{2+}$ ions of varied concentrations. It was shown that $CaCl^{2+}$ or $MgCl^{2+}$ divalent ions have induced a strong adhesion state in DOPC:DOPS vesicles, demonstrating the like-charge attraction caused by ion condensation and ion correlations. The water layer thickness between two adhered vesicles was found to be equal to $d_w = 1.5 - 1.7$ nm. It was shown as well that the bilayer thickness increases upon ion addition. The

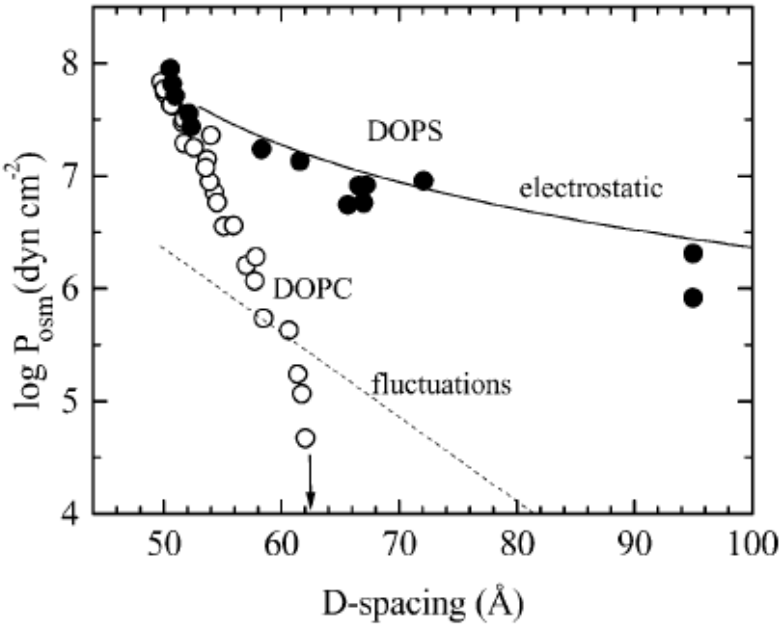

Figure IV.1.9 – The interlamellar repeat spacings versus osmotic pressures for zwitterionic DOPC and negatively charged DOPS lipids in the fluid phase. Dotted line - estimated contribution from thermal agitations; solid line - calculated contribution from the electrostatic interaction [213].

obtained value of water spacing between membranes quantitatively agrees with the predictions of the SC theory of Netz and Moreira ($\Xi \simeq 20$), which interprets the observed induced attractive interaction between membranes by modeling the interaction potential as a superposition of hydration repulsion and electrostatic forces in the SC regime.

Sonneville-Aubrun *et al.* [226] have studied hexadecane-in-water biliquid foams stabilized with sodium dodecyl sulfate (SDS). They have shown that the obtained oil-in-water emulsions can be compressed to produce biliquid foams, which undergo a transition between two states of the common black film (CBF) and the Newton black film (NBF) under the compression. The CBF is characterised by a water thickness between oil droplets of above 2.5 nm and exists at low pressure (1-50 atm). The NBF is characterised by a water thickness of around 1.3 nm and exists at high pressure (20-200 atm). They have shown that the transition between the repulsive state (CBF) and an attractive state (NBF) of the films is induced solely by the application of an osmotic pressure, which causes a modification of the electrostatic interactions in the limit of high charge densities and very short separations.

The CBF state was accurately described by mean-field PB theory, which reproduces the measured pressure and suggests that counterions are excluded from the vicinity of the polar/apolar interface. However, PB theory failed to describe the attraction which occurs upon CBF to NBF transition. It was shown [49] that at short separations the dielectric constant of water in the films is lower than that of the bulk water due to the layered organization of water molecules close to the surface in the confined geometry and differences in the correlations that water molecules possess in the ion hydration shells and in bulk water. This finding will be discussed in more detailed below. Thus, assuming a lower value of the dielectric constant of water ($\epsilon \approx 65$), the pressure between two membranes in the NBF state calculated using Monte Carlo simulation allows to estimate the thickness between membranes of around 0.8 nm, which is in good agreement with the measured value. Therefore, for sufficiently high charge densities, the entropic component of the pressure decreases and the attractive ion-ion correlation becomes more important, which turns the repulsive interaction into attractive.

The dielectric constant ϵ of interfacial water has been predicted to be smaller than that of bulk water ($\epsilon \sim 80$) because the rotational freedom of water dipoles is expected to decrease near surfaces [49]. Using the scanning dielectric microscopy method of AFM, Fumagalli *et al.* [49] have performed capacitance measurements of dielectric constant of water confined between two atomically flat walls separated by various distances down to 1 nm (Fig. IV.1.10). The measurements have shown the existence of a 2-3 molecules thick interfacial layer with vanishingly small out-of-plane polarization $\epsilon \approx 2$ caused by the surface-induced alignment of the water molecular dipoles. The extensive measurements varying the thickness of the confined water layer from 1 to 300 nm were performed. The bulk behavior of water ($\epsilon \approx 80$) was observed only for water layers as thick as ~ 100 nm, which shows that confinement could affect the dielectric properties of even relatively thick water layers. Extremely low values of $\epsilon \approx 15.5$, 4.4, and 2.3 were obtained for thicknesses of the confined water of approximately 10 nm, 3.8 nm, and 1.4 nm, respectively. At separations lower then 2 nm (only a few layers of water could fit inside the channels), ϵ has approached a limiting value of 2.1 ± 0.2, which is very close to the limit of water at optical frequencies $\epsilon_{\perp} \approx 1.8$. The observed ϵ remains anomalously small (< 20) over

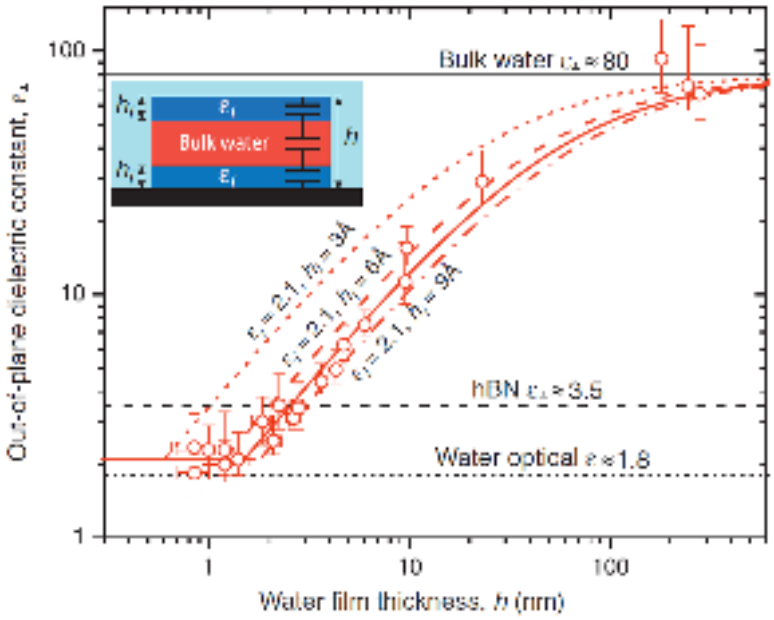

Figure IV.1.10 – Dielectric constant of water under strong confinement. Symbols denote experimental values of $\epsilon_\perp$ for water inside channels with different thickness h. Red curves: calculated $\epsilon_\perp(h)$ for the model sketched in the inset: a near-surface layer with $\epsilon_i = 2.1$ and thickness h_i is present and the rest of the channel contains the ordinary bulk water. Solid curve: best fit giving $h_i = 7.4$ Å. The dotted, dashed, and dashed-dotted curves are for $h_i = 3$ Å, 6 Å and 9 Å, respectively. Horizontal black lines: Dielectric constants of bulk water (solid) and material of the channel (hBN) (dashed). The dielectric constant of water at optical frequencies is shown by the dotted black line. The inset represent the capacitance model with different ϵ values for the bulk and interfacial water.

a wide range of water layer thicknesses up to 20 nm (Fig. IV.1.10). These low values of the measured dielectric constant in a confined geometry were explained by the fact that water exhibits a distinct layered structure near all surfaces, independently of their hydrophilicity.

CHAPTER 2

Highly charged bilayers in a strongly-confined geometry

Investigation of the interaction between highly charged membrane is interesting and challenging from fundamental point of view as the behavior of the system cannot be described within the mean-field approach of the PB theory, which predicts only repulsion between equally charged walls. Another theoretical description - the SC theory - was developed by Netz and Moreira, Samaj and Trizac. It was showed that a like-charge attraction phenomenon naturally arises within the SC theory at sufficiently large coupling constants. It was shown that at small plates separations the water molecules' structure, ion correlation, ion binding phenomenon and ion condensation on the plane surface start to play a dominant role, defining the interaction between charged plates.

As previously discussed a lot of experimental works was performed in order to understand the interaction between charged planar surfaces probing the WC and SC regimes. Interaction between zwitterionic lipid bilayers [175] and between charged membranes composed of SDS-octanol bilayers [50], when only Na^+ counterions were present in the system could be well described within the WC regime as the surface charge is low and the Bjerrum length is large.

Most of the experimental investigations of the interaction between charged plates in the SC regime were performed in the presence of divalent counterions in the solution in order to increase the coupling constant Ξ and screen the electrostatic repulsion. In such conditions, the observed attraction between like-charged plates was in good qualitative agreement with the SC limit. The interaction between mica surfaces [227], lamellar systems [224, 228] with the divalent counterions present

in the solution, between two charged vesicles [225] with $CaCl_2$ or $MgCl_2$ divalent counterions ($\Xi \simeq 20$, d_w = 1.5 - 1.7 nm) were well described by SC theory of Moreira and Netz.

In this thesis we present strong evidence of the like-charge attraction between highly negatively charged planar lipid bilayers composed of DPPS lipids with only counterions are present in solution (no salt added). The DPPS double bilayer system possesses a highly control structure and composition (thanks to the chosen sample preparation technique (see section 1.3.6)) and it represents an excellent model to study the interaction between like-charged plates in the strong confinement.

We aim to investigate the interaction between highly negatively charged lipid bilayers in the presence of monovalent ions combining both neutron reflectivity (NR) and X-ray reflectivity (XRR) experiments in order to characterize with a high resolution ($\approx$ 0.1 nm) the structure of DPPS double bilayer systems and to compare our experimentally obtained results with existing theoretical descriptions of WC and SC limits. We have investigated the electrostatic interactions between highly charged double bilayers by measuring the equilibrium distance between like-charged bilayers and by exploring the poorly understood limit of strong confinement, where continuous theories reach their limits, as it was highlighted numerically [44] and evidenced by pioneering works on black films [226].

In the next section 2.2, we will present the performed NR and XRR experiments on double lipid bilayer systems composed of negatively charged lipids, zwitterionic lipids and a mixture of the two. We have to note that some of the NR and XRR experiments on the DPPS double bilayer were performed before this thesis by Malaquin and Hemmerle, while the analysis of the measured data was accomplished within this thesis work. The influence of monovalent ions and temperature on the bilayer structure and on water layer thicknesses between lipid bilayers and between bilayer and planar support will be discussed in sections 2.3.1 and 2.3.2. In section 2.3.3 the interaction between charged membranes will be considered within the SC theory.

2.1 Sample preparation: double and triple bilayers

Lipid bilayer systems were deposited on ultra-flat and highly polished silicon substrates by means of LB/LS deposition techniques following the well-developed protocol for planar lipid bilayer preparation (see section 1.3.6 for the details) [164, 172, 175].

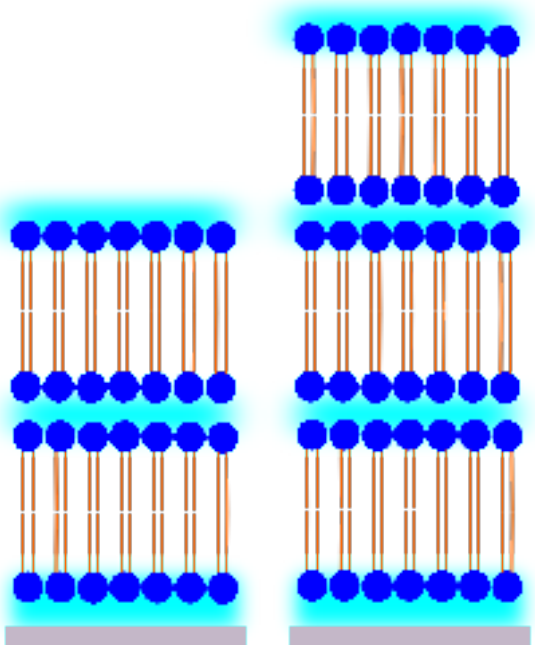

Figure IV.2.1 – Schematic illustration of the double (a) and triple (b) lipid bilayer systems investigated within this project.

By means of LB/LS deposition we have formed symmetric and asymmetric double and triple bilayer systems composed of zwitterionic DPPC and DSPC phospholipids and negatively charged DPPS lipids. The following samples were investigated by NR and XRR experiments during this project:

1. Highly charged double bilayers composed of DPPS lipids (denoted as $DPPS_2$-$DPPS_2$).

2. Neutral double bilayers composed of DSPC lipids (denoted as $DSPC_2$-$DSPC_2$).

3. Asymmetric double bilayers composed of DPPC and DPPS lipids (denoted as DPPC/DPPS-DPPS/DPPC).

4. Asymmetric double bilayers composed of fully deuterated d_{75}DPPC lipids and hydrogenated DPPS lipids (denoted as d_{75}DPPC/DPPS-DPPS/d_{75}DPPC).

5. Triple bilayers systems composed of DPPS lipids (denoted as $DPPS_2$-$DPPS_2$-$DPPS_2$).

Within this project the influence of temperature on the structure of fully charged DPPS double bilayers and on the water thickness between bilayer and support $d_{w,1}$ as well as on the inter-bilayer water thickness $d_{w,2}$ was investigated. A wide temperature range was tested (from 25°C to 60°C), allowing to probe the lipid bilayer structure in gel and fluid phases. The modifications in $d_{w,1}$, $d_{w,2}$ and the bilayer structure as a function of the Debye screening length, which was tuned by addition of NaCl in a concentration range from 0.01-0.3M, were also monitored by means of NR and XRR experiments.

2.2 Samples characterization

2.2.1 Neutron and X-Ray Reflectometry experiments

In order to characterize with a high resolution (≈ 0.1 nm) the structure of highly charged lipid bilayers samples, we have performed NR and XRR experiments. NR measurements were carried out on the D17 reflectometer [157] at the Institut Laue-Langevin (ILL, Grenoble, France) (see section 2.7.1 for details). XRR measurements were performed at the CRG-IF beamline of the European Synchrotron Radiation Facility (ESRF) using a 27 keV X-ray beam (wavelength $\lambda = 0.0459$ nm) (see section 2.7.3 for the details). As the example of the performed measurements, X-ray and neutrons reflectivity curves and the best fits obtained upon data analysis for a highly charged DPPS double lipid bilayer are shown in Fig. IV.2.2(a). Both samples were prepared following the same protocol and were further measured under the same experimental conditions. The corresponding SLD and ED profiles are plotted in Fig. IV.2.2(b). The structural parameters separately obtained from the fits of NR and XRR data are in good quantitative agreement, highlighting the great complementarity of both techniques.

The NR curves together with the best fit of the data and corresponding SLD profiles for an asymmetric double bilayer system composed of DPPC and DPPS lipids (DPPC/DPPS-DPPS/DPPC) are shown in Fig. IV.2.2. These measurements and

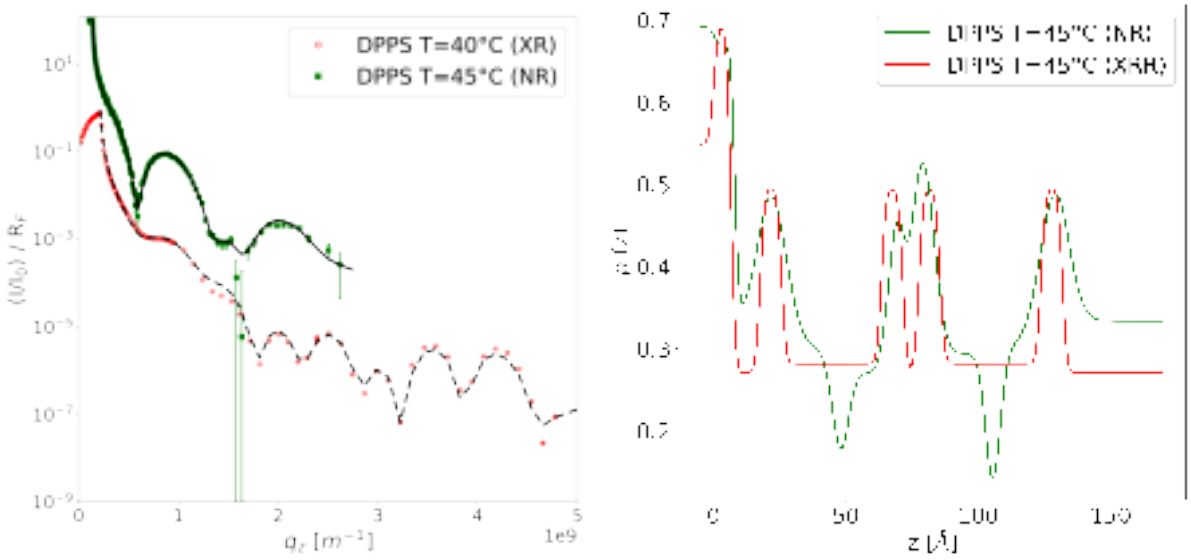

(a) (b)

Figure IV.2.2 – (a) NR and XRR for a DPPS double bilayer at T = 45 °C and at T = 40 °C (in the gel phase), respectively. Dashed and solid lines are the best fits corresponding to the SLD profiles shown in Fig. IV.2.2(b).

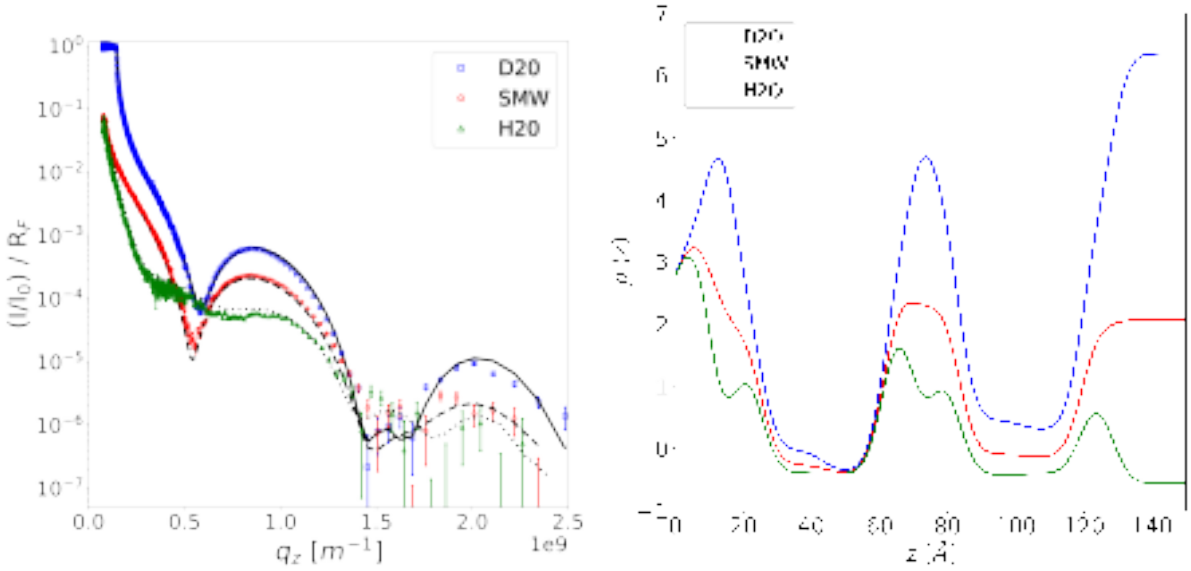

(a) (b)

Figure IV.2.3 – (a) Neutron reflectivity (NR) for a DPPC/DPPS-DPPS/DPPC double bilayer at T = 25°C (in the gel phase). Dashed and solid lines are the best fits corresponding to the SLD profiles shown in Fig. IV.2.3 (b). NR data was measured in 3 different contrasts: (○) D_2O; (○)SiMW and (○) H_2O.

performed analysis have demonstrated the good quality (full coverage) of both the supported and the floating bilayers and no lipid mixing between the two leaflets of both bilayers was detected for this sample. This observation was confirmed with

an additional experiment on a sample possessing similar structure (d_{75}DPPC/DPPS-DPPS/d_{75}DPPC), where fully deuterated d_{75}DPPC lipids were used instead of fully hydrogenated ones. The measured reflectivity curves and corresponding SLD profiles for this sample are shown in Fig. IV.2.3, the structural parameters are summarized in Tab. D.4 and D.5 in the Appendix.

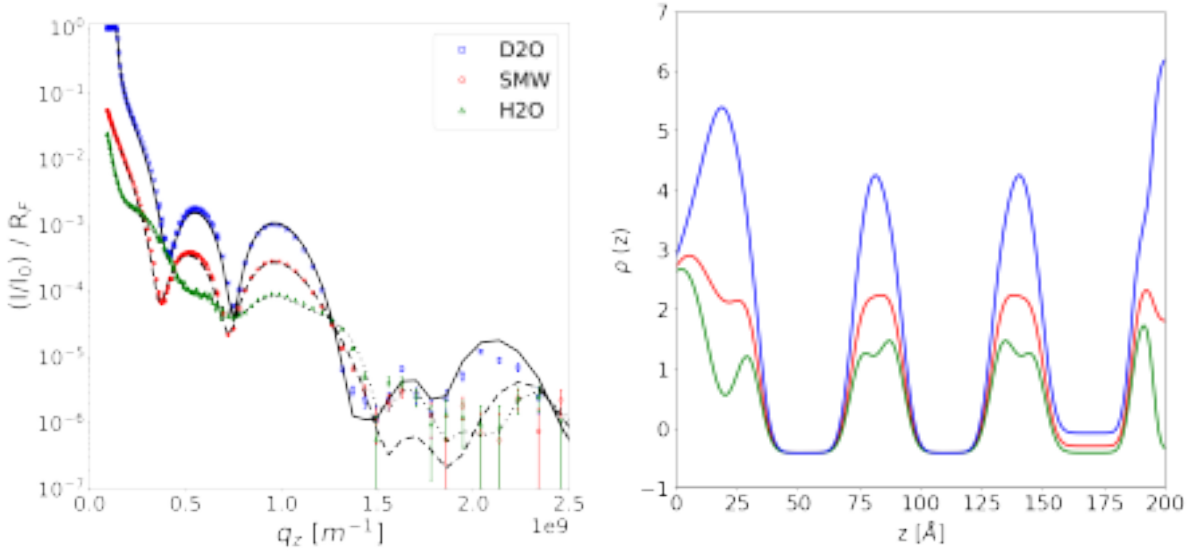

(a) (b)

Figure IV.2.4 – (a) NR for a DPPS triple lipid bilayer at T = 25°C (in the gel phase). Dashed and solid lines are the best fits corresponding to the SLD profiles shown in Fig. IV.2.4(b). NR data was measured in 3 different contrasts: (○) D_2O; (○) SiMW and (○) H_2O.

In order to demonstrate the possibility to form mutli-bilayers with negatively charged lipids and to resolve their structure, we have performed NR experiment on $DPPS_2$-$DPPS_2$-$DPPS_2$ triple lipid bilayer system in pure water with no added salt (only counterions are present in the solution). The reflectivity curves measured in three solvent contrasts (H_2O, SMW, D_2O) and the SLD profiles obtained from the performed fits are presented in Fig. IV.2.4. Each DPPS bilayer of the triple bilayer system appears to be of a very high quality (full coverage), as the water content in the tails regions was 0, 0 and 10% for the first, second and third lipid bilayer, respectively (see Tab. D.3 for the obtained structural parameters).

The extracted structural parameters from NR and XRR experiments cannot be compared directly, as different models were implemented for the lipid bilayer modeling. We have re-defined the parameters in the way reported below in order to

compare the information obtained from the two techniques.

2.2.2 Data analysis

In order to perform analysis and fits of collected NR data, planar lipid bilayer systems were modeled using a slab (box) model (see section 2.9 for details), which imposes that the thicknesses of the water layers between the substrate and the first bilayer ($d_{w,1}$) and between the two bilayers ($d_{w,2}$) or the thicknesses of the head or tail group regions correspond to the thicknesses of the corresponding slabs in the model (Fig. IV.2.5(a)). XRR data was fitted using a hybrid Gaussian continuous profile for the bilayer system (see section 2.9.2 for details), therefore in this case the thickness of the interbilayer water layer was defined as a peak-to-peak distance between the peaks of the Gaussian functions representing the headgroups of the adjacent bilayers. The thicknesses of the head-groups ($d_{h,1}$ and $d_{h,2}$) in this model were defined as the full width at half maximum of the Gaussian peak (Fig. IV.2.5(b)).

Due to the discrepancies in the definitions of the structural parameters, the values of $d_{w,1}$ and $d_{w,2}$ obtained from NR and XRR experiments cannot be directly compared. In order to be able to do that, we have re-defined the values of $d_{w,1}$ and $d_{w,2}$ from the hybrid Gaussian continuous profile by subtracting $(\sigma_{1h})/2$ from $d_{w,1}$ and $(\sigma_{2h} + \sigma_{3h})/2$ from $d_{w,2}$, where σ_{1h}, σ_{2h} and σ_{3h} are the roughnesses of the corresponding head groups (see Fig. IV.2.5(b)). After these corrections the values $d_{w,1}$ and $d_{w,2}$ extracted from NR and the re-defined values from XRR experiments can be directly compared. As an example, the interlayer water thicknesses $d_{w,2}$ before and after correction is shown in Fig. IV.2.6. After these performed corrections, as excellent agreement between the results from NR and XRR was achieved, which demonstrates again the great complementarity between the two techniques. Within this work symmetric lipid bilayers (DPPS), asymmetric lipid bilayers (DPPC/DPPS-DPPS/DPPC), zwitterionic (non-charged) lipid bilayers ($DSPC_2$-$DSPC_2$) and triple lipid bilayer systems composed of DPPS lipids were studied by means of NR and XRR reflectometry. A comparison between $d_{w,1}$ and $d_{w,2}$ for all the presented charged, non-charged or mixed systems was performed and the obtained results will be discussed in the next sections. We would like to start our discussion presenting the results obtained studying the influence of salt and temperature on $d_{w,1}$ and $d_{w,2}$.

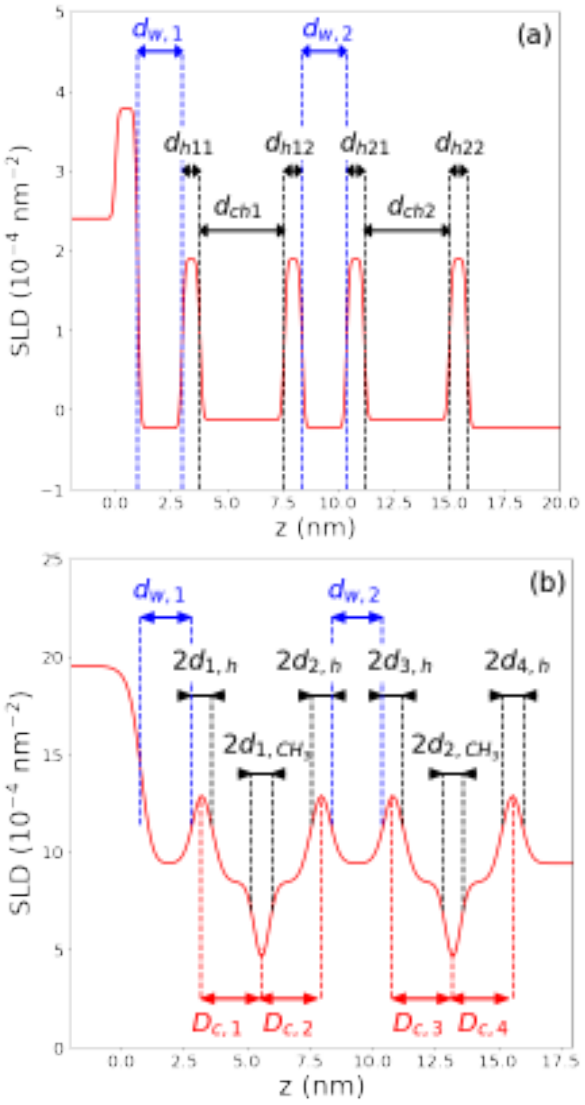

Figure IV.2.5 – (a) Definition of the parameters used for the SLD profiles for NR data. (b) Definition of the parameters used for the SLD profiles for XRR data (1G-hybrid model). For the sake of clarity we used artificial values for $\sigma_{i,j}$, $d_{w,1}$ and $d_{w,2}$ ($\sigma_{i,j}$ = 0.1 nm, $d_{w,1}$ = 2 nm, $d_{w,2}$ = 2 nm)

2.3 Discussion

2.3.1 First water layer $d_{w,1}$

We have investigated the variation of $d_{w,1}$ and $d_{w,2}$ as a function of the temperature (Fig. IV.2.7 and IV.2.8) and as a function of the Debye length, which was tuned by changing the NaCl concentration (0.01-0.3M) (Fig. IV.2.9(a) and (b)) for $DSPC_2$-$DSPC_2$ double lipid bilayer, data from [175, 229] (in Fig. IV.2.9 ■, □), $DSPC_2$-$DSPC_2$ double lipid bilayer in presence of NaCl (0.5 M), data from [175] (in Fig. IV.2.9 ■),

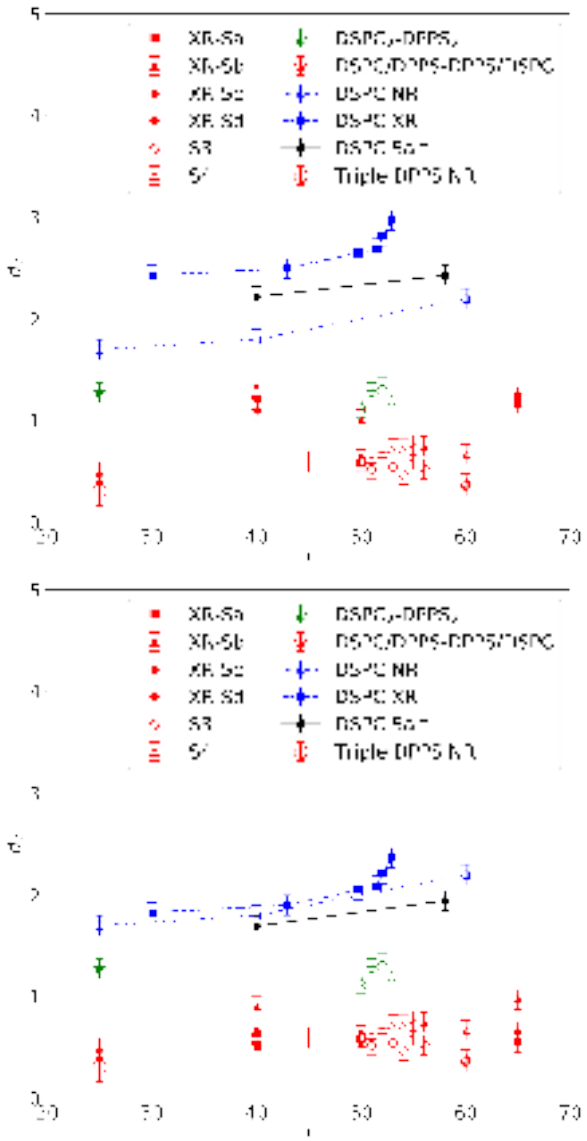

Figure IV.2.6 – (a)$d_{w,2}$ vs T obtained from NR (open symbols) and XRR (closed symbols) before (a) and after corrections (b) for different sample systems : $DSPC_2$-$DSPC_2$ double bilayer with (●) and without salt (■, □); $DPPS_2$-$DPPS_2$ double bilayer (XRR, ■, ▲, ●, ♦ and NR, △, ◊); $DPPS_2$-$DPPS_2$-$DPPS_2$ triple bilayer (◯); DSPC/DPPS-DPPS/DSPC double asymmetric bilayer (☆).

DPPC/DPPS-DPPS/DPPC double bilayer (in Fig. IV.2.9 ☆) and $DPPS_2$-$DPPS_2$-$DPPS_2$ triple bilayer (in Fig. IV.2.9 ◯).

As expected, the first water layer thickness $d_{w,1}$ between the silicon oxide and the bilayer is significantly larger when the first bilayer is charged ($d_{w,1} \approx 1 \pm 0.1$ nm for $DPPS_2$-$DPPS_2$ and $d_{w,1} \approx 1.32 \pm 0.2$ nm for $DPPS_2$-$DPPS_2$-$DPPS_2$ triple lipid bilayer systems) than when it is zwitterionic ($d_{w,1} \approx 0.6 \pm 0.1$ nm for $DSPC_2$-$DSPC_2$). This water layer thickness $d_{w,1}$ is mainly controlled by the weak electrostatic repulsive

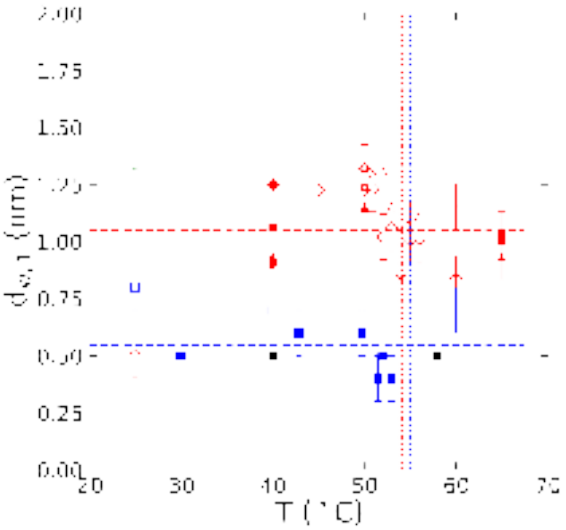

Figure IV.2.7 – $d_{w,1}$ derived from NR (open symbols) and XRR (closed symbols) measurements: $DSPC_2$-$DSPC_2$ double bilayer with (●) and without salt (■, □); $DPPS_2$-$DPPS_2$ double bilayer (XRR, ■, ▲, ●, ♦ and NR, △, ◊); $DPPS_2$-$DPPS_2$-$DPPS_2$ triple bilayer (◯); DSPC/DPPS-DPPS/DSPC asymmetric double bilayer (☆). Dotted lines correspond to the gel to fluid transition temperature for DSPC (·····) and DPPS (·····) bilayers. Horizontal dotted lines (- - -) and (- - -) correspond to the average values of $d_{w,1}$ for zwitterionic and charged lipids.

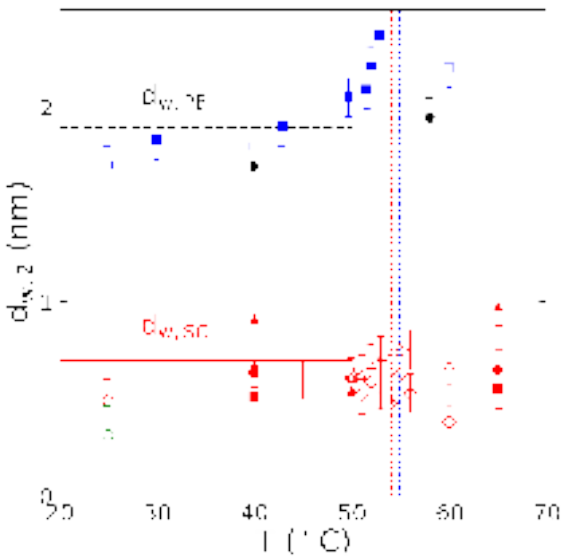

Figure IV.2.8 – $d_{w,2}$ derived from NR (open symbols) and XRR (closed symbols) measurements: $DSPC_2$-$DSPC_2$ double bilayer with (●) and without salt (■, □); $DPPS_2$-$DPPS_2$ double bilayer (XRR, ■, ▲, ●, ♦ and NR, △, ◊); $DPPS_2$-$DPPS_2$-$DPPS_2$ triple bilayer (◯); DSPC/DPPS-DPPS/DSPC asymmetric double bilayer (☆). Dashed black line (- - -) corresponds to $d_{w,vdW}$ = 1.9 nm obtained by minimizing Eq.2.8 and solid red line (—) corresponds to $d_{w,SC}$ = 0.7 nm obtained by minimizing Eq.2.10. Dotted lines correspond to the gel to fluid transition temperature for DSPC (·····) and DPPS (·····) bilayers.

interactions between the first monolayer and the substrate. It has to be noted that because of the experimental conditions and the surface treatment prior to the deposition (see section A), the surface of the silicon block is covered with a silicon oxide layer, which is negatively charged. Therefore, we can attribute these effects to the repulsive electrostatic interaction between the weakly negatively charged silicon oxide surface and the highly negatively charged DPPS monolayer. This observation is confirmed by the results obtained on the asymmetric sample DPPC/DPPS-DPPS/DPPC (and d_{75}DPPC/DPPS-DPPS/d_{75}DPPC) (Fig. IV.2.7(a)) for which the first water layer thickness is $d_{w,1} \approx 0.6 \pm 0.1$ nm in agreement with the case of the symmetric zwitterionic sample $DSPC_2$-$DSPC_2$.

We did not observe any significant variation of $d_{w,1}$ with temperature even when charged DPPS lipid bilayers went through the gel to fluid phase transition. This demonstrates the negligible effect of entropic contributions in the interaction potential between charged surfaces. The measured $d_{w,1}$ values are in quantitative agreement with PB theory in the WC limit [34, 208].

Finally, we have observed that $d_{w,1}$ was decreasing with increasing salt concentration and reaching a value close to the zwitterionic case ($d_{w,1} \approx 0.5$ nm for a DSPC lipid bilayer (blue dashed line in Fig. IV.2.7(a)). This observation is in a good agreement with an osmotic pressure effect [230], which will be discussed below.

We can note that it is difficult to compare our obtained results for $d_{w,1}$ with the existing theory, as this situation is complex from a theoretical point of view. The considered case of a water layer between silicon oxide surface and lipid bilayer ($d_{w,1}$) is an asymmetric case with a different surface charge on each side: the highly charged lipid bilayer on one and the slightly charge silicon oxide surface, charge of which is not possible to control, on the other. Our obtained results are in good agreement with the results reported by Anderson [231].

Osmotic pressure effect

Within this work we have investigated the effect of salt on the double bilayer system by exposing it to NaCl salt solutions of different concentration (0.01-0.3M). 0.3 M NaCl solution corresponds to a Debye length of $\ell_D \approx 0.8$ nm, which is substantially larger than the observed water spacings $d_{\mathrm{w},1}$ and $d_{\mathrm{w},2}$. Therefore no screening effect

can be observed. Due to the strongly confined geometry as previously described by Hishida [230], the coions are expelled from the interbilayer spacing, resulting in an osmotic pressure effect P_{osmo}. As $d_{\text{w},1} > d_{\text{w},2}$, the interaction potential between the two bilayers is stiffer than the interaction potential between the supported bilayer and the substrate and this osmotic pressure will have a greater effect on $d_{\text{w},1}$ spacing. The osmotic pressure can be described as:

$$P_{\text{osmo}} = ck_{\text{B}}T, \tag{2.1}$$

where c is the coion concentration, which can directly related to the Debye length by $c = \epsilon_w k_{\text{B}}T/(2e^2\ell_D^2)$.

The total potential for the first bilayer may thus be written as :

$$U_{1,\text{salt}}(z) = U_{1,\text{no salt}}(z) + P_{\text{osmo}}z, \tag{2.2}$$

where $U_{1,\text{no salt}}(z)$ is the interaction potential without salt.

To avoid describing this potential in detail and to keep only the effects of osmotic pressure, we can make a quadratic approximation of the potential :

$$U_{1,\text{salt}}(z) = \frac{1}{2}U''_{1,\text{nosalt}}\left[z - d_{w,1}\left(P_{\text{osmo}} = 0\right)\right]^2 + P_{\text{osmo}}z, \tag{2.3}$$

where $d_{\text{w},1}\left(P_{\text{osmo}} = 0\right)$ is the equilibrium position without added salt.

By minimizing the potential in Eq. 2.3 we obtain an approximate expression for the water layer thickness in the presence of salt :

$$d_{\text{w},1} = d_{\text{w},1}\left(P = 0\right) - \frac{P}{U''} = d_{\text{w},1}\left(P = 0\right) - \frac{k_{\text{B}}T}{8\pi U''_{1,\text{no salt}}}\frac{1}{\ell_D^2}. \tag{2.4}$$

The expression 2.4 was used to fit the data presented in Fig. IV.2.9 with only one fitting parameter $U''_{1,\text{nosalt}}$. We found $U''_{1,\text{nosalt}} \simeq 10^{11}$ J.m^{-4}, which is in good qualitative agreement with the values reported by Hemmerle [175].

2.3.2 Interbilayer water layer $d_{w,2}$

Now we would like to discuss the case of the influence of salt and temperature on the interbilayer water thickness $d_{w,2}$. In the case of charged $DPPS_2$-$DPPS_2$ lipid bilayer

samples (red symbols in Fig. IV.2.8(b)), we have observed that $d_{w,2} \approx 0.5 - 0.7$ nm is significantly smaller than for the case of zwitterionic $DSPC_2$-$DSPC_2$ bilayer samples, where $d_{w,2} \approx 1.8 - 2.5$ nm (blue and black symbols). The decrease of $d_{w,2}$ in the fully charged systems clearly indicates that there is an attractive interaction between two highly like-charged membranes, which is a very counterintuitive observation. We have also noticed an enhanced stability of the system, which was confirmed by the successful deposition of more than three DPPS monolayers (up to 8 DPPS monolayers were transferred on the silicon support (see Fig. VI.C.2)) by means of the Langmuir-Blodgett technique onto highly polished (roughness ≈ 0.5 nm) silicon substrates. This achievement highlights once again the strong attractive interactions between the like-charged leaflets of the adjacent DPPS bilayers and the high stability of the overall system.

We can note that in the case of zwitterionic lipids such as phosphocholines, where a small electrostatic repulsion between the opposing headgroups of lipid leaflets [175] exists, it is not possible to perform more than three successive LB depositions in water, as an attempt to deposit a fourth monolayer by LB technique usually leads to the partial removal of the third one or zero deposition (no fourth monolayer adsorption) (see Fig. VI.C.1). Therefore, the Langmuir-Schaefer deposition technique is usually used to form the fourth monolayer of double bilayer systems composed of zwitterionic phosphiolipids. A detailed discussion of sample quality evaluation via the transfer ratio estimation is given in section C of the Appendix. Interestingly, the interbilayer water thickness ($d_{w,2} = 0.6 \pm 0.2$ nm) as shown in Fig. IV.2.8(b) and IV.2.9(b) appears to be constant for all measured charged samples, which demonstrates that the silicon substrate has only a minor influence on the deposition after the first monolayer.

The major role of electrostatic interactions is confirmed by complementary experiments on asymmetric DSPC/DPPS-DPPS/DSPC double bilayer systems (☆ in Fig. IV.2.8(b)). For this sample we have obtained $d_{w,2} \simeq 0.5 \pm 0.1$ nm, which is in agreement with the values obtained for symmetric $DPPS_2$-$DPPS_2$ double lipid bilayer. For the case of $DPPS_2$-$DPPS_2$-$DPPS_2$ triple bilayer system, the measured values of the water thicknesses between first and second bilayer ($d_{w,2} \simeq 0.32 \pm 0.2$ nm) and the second and third bilayers ($d_{w,3} \simeq 0.31 \pm 0.2$ nm) are in agreement with

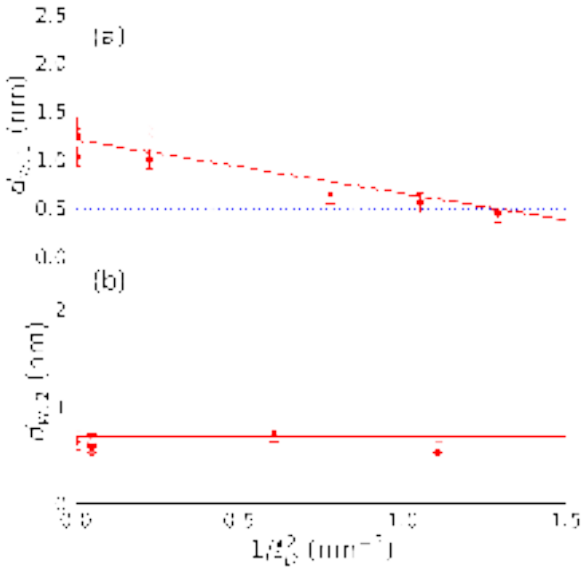

Figure IV.2.9 – (a) $d_{w,1}$ and (b) $d_{w,2}$ vs $1/\ell_D^2$ (same notations as in Fig. IV.2.7 and IV.2.7). (a) Blue dotted line (·····) corresponds to $d_{w,1} = 0.5$ nm (average value for DSPC) and (- - -) to osmotic pressure effect; (b) Red solid line (—) corresponds to the prediction of SC theory $d_{w,SC} = 0.7$ nm.

the values of fully negatively charged $DPPS_2$-$DPPS_2$ double bilayers ($d_{w,2} \simeq 0.5 - 0.7$ nm) as shown in Fig. IV.2.8(b).

We did not observe a variation of $d_{w,2}$ with temperature for $DPPS_2$-$DPPS_2$ double lipid bilayer samples, unlike for the zwitterionic lipid bilayers (see Fig. IV.2.8(b)), indicating again that entropic contributions in the interactions between charged membranes are negligible. Finally, the increase of NaCl concentration in the solution also has a negligible effect on the value of $d_{w,2}$ as clearly shown in Fig. IV.2.9(b).

2.3.3 Interaction between charged membranes

In order to compare our experimental results with theoretical models in different regimes of WC or SC, we have to take different contributions to the interaction potential between the bilayers into account, as it was described for the case of DSPC double bilayers in [175]. Interaction between two lipid bilayer is governed by the superposition of attractive van der Waals interactions, repulsion hydration, electrostatic interactions and entropic repulsion due to the membranes thermal fluctuations.

First, the short range hydration repulsion can be described by a potential :

$$U_{\mathrm{hyd}} = P_h \lambda_h \exp\left(-d_w/\lambda_h\right) \tag{2.5}$$

where $P_h = 4 \cdot 10^9$ Pa is the hydration pressure and $\lambda_h = 0.1 - 0.2$ nm is the decay length.

The attractive van der Waals contribution to the total interaction potential is modeled as :

$$U_{\mathrm{vdW}} = -\frac{H}{12\pi\left(d_w + 2d_{\mathrm{head}}\right)} \tag{2.6}$$

where $H = 5.3 \cdot 10^{-21}$ Jm^2 is the Hamaker constant and $d_{\mathrm{head}} \approx 0.5$ nm is the head group thickness [175].

As it was described by Hemmerle [175] the lipid bilayers posseses a small surface charge $\sigma \sim 0.001\ e^-/\mathrm{nm}^2$ due to the amphoteric character of the phosphatidylcholine group, which leads to a weak electrostatic repulsion between membranes. This repulsion can be described within the ideal gas limit of the mean-field Poisson-Boltzmann theory. Thus, the electrostatic interaction between plates within PB approach has the form [34]:

$$U_{\mathrm{PB}}(z) = -2k_{\mathrm{B}}Tq\sigma_s \log z. \tag{2.7}$$

For gel phase lipid bilayers, neglecting entropic contribution, when only the hydration repulsion, van der Waals interactions and electrostatic interaction (desctibed within PB theory) contributes to the total interaction potential, this potential can be modeled as:

$$U_0(z) = U_{\mathrm{vdW}}(z) + U_{\mathrm{hyd}}(z) + U_{\mathrm{PB}}(z)\,. \tag{2.8}$$

This leads to an equilibrium value for the water thickness $d_{w,\mathrm{vdW}} \simeq 1.9$ nm (black dashed line in Fig. IV.2.8(b)). This estimated value is in good agreement with those measured values for a $DSPC_2$-$DSPC_2$ system in the presence of salt or in the gel phase. As demonstrated in the work of Hemmerle [175], the small increase of $d_{w,2}$ for the case of zwitterionic lipids in absence of salt and close to the gel-fluid transition (shown in Fig. IV.2.8(b)) is well described by the model which takes into account the entropic contribution in the framework of PB theory.

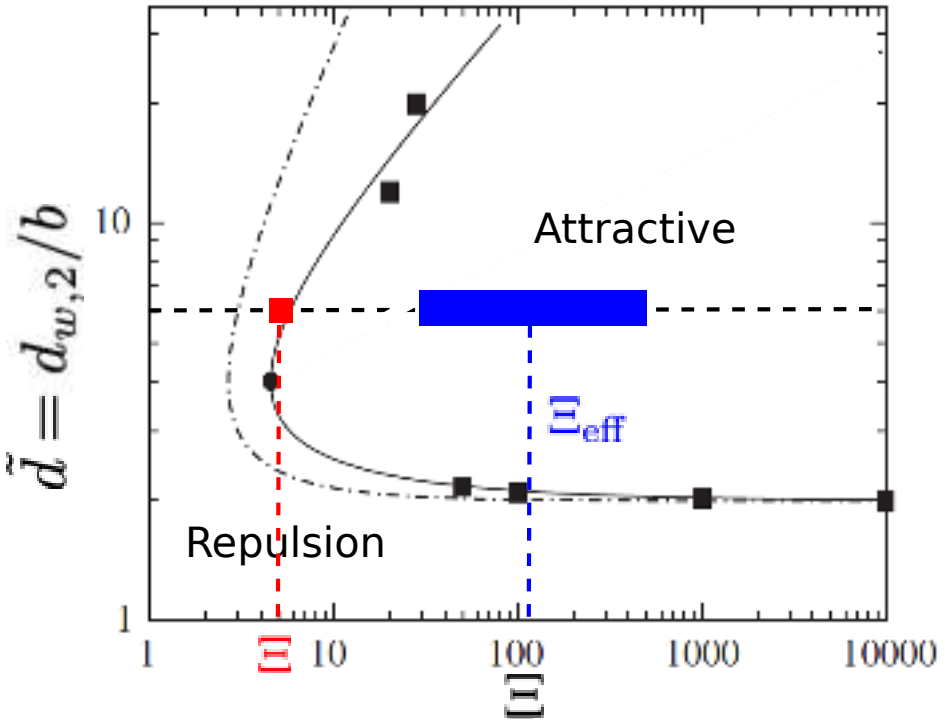

Figure IV.2.10 – Phase diagram showing attraction and repulsion regimes. The rescaled water thickness $\tilde{d} = d_{w,2}/b$ as a function of the coupling constant Ξ (figure adapted from [210] is shown. The dashed-dotted line is the prediction obtained within the original Virial Strong Coupling theory from [36] and black squares are the Monte Carlo simulation data from [42]. The solid line corresponds to the prediction of the Wigner Strong Coupling theory from [210]. Our experiments are represented by the red area using $\epsilon_{\mathrm{w}} = 80\epsilon_0$ ($\Xi \sim 5, \tilde{d} \sim 5-7$) and by the blue area, when renormalization induced by water structuring ($10 \leq \epsilon_{\mathrm{w}} \leq 30 \Leftrightarrow 30 \leq \Xi \leq 300$) has been taken into account.

For DPPS double and triple bilayers the entropic contribution is clearly negligible, as we did not observe a significant variation of $d_{w,2}$ with temperature. To model the interaction between charged membranes, the electrostatic interaction between charged surfaces has to be taken into account. The area per molecule of DPPS lipids can be estimated to be 0.55 nm^2 [232], which leads to a charge density of $\sigma_s \sim 1.82$

e^-/nm^2. Taking the water dielectric constant $\epsilon_w \simeq 80\epsilon_0$ at T = 20°C we have obtained values for the coupling constant of $\Xi \simeq 5$, which is outside the attractive region described by the SC theory [36, 210] (see red area in Fig. IV.2.10). In this limit, using realistic values of P_h, λ_h and H, it is not possible to access equilibrium values of $d_{w,2}$ smaller than 1.5 nm. In such a strongly confined geometry, the rotational degrees of freedom of water dipoles are expected to be frozen near surfaces, inducing a strong decrease of the dielectric permittivity. Fumagalli [49] has experimentally demonstrated the presence of an interfacial two to three molecules thick layer with $\epsilon_\text{w} \sim 2\epsilon_0$, close to the limit for water at optical frequencies ($\epsilon_\text{w} \sim 1.8\epsilon_0$). Since Ξ is scaling with $\sim 1/\epsilon^2$, this leads to a strong increase of the coupling constant.

In a configuration which is close to our experiments, Schlaich *et al.* [44] have recently demonstrated that attractive behavior can occur between two surfaces even at a moderate surface charge density ($\sigma_s \sim 0.77\ e^-/\text{nm}^2$, $\Xi \sim 3$) by performing water-explicit simulations of decanol bilayers with variable surface charge density. This effect was explained within a modified PB theory taking into account the counterion correlations and the surface charge induced reorientation of hydration water. It is known that the surface induced water structure in a strong confinement causes a change of the dielectric constant ϵ [49, 226] as well as the hydration repulsion, which significantly increases the coupling parameter. For moderate surface charge density $\sigma_s \sim 0.77\ e^-/\text{nm}^2$, Schlaich *et al.* [44] have shown that the obtained numerical results are in good agreement with an effective coupling constant $\Xi_{eff} \sim 20$ which corresponds to a decrease of ϵ_w down to 30. Taking into the account the observed decrease of the relative dielectric constant induced by water organization due to the strong confinement, we can estimate the coupling constant to $\Xi_\text{eff} \sim 30$ for our case, which clearly falls into the attractive regime described by the SC theory. Therefore it is appropriate to use the analytical expression for the electrostatic pressure in the SC regime [36, 207]:

$$P_\text{SC} = 2\pi\ell_\text{B}\sigma_s^2\left(\frac{2\ell_\text{GC}}{z} - 1\right)k_\text{B}T. \tag{2.9}$$

The decrease of ϵ_w also induces a decrease of the Hamaker constant [233] and van der Waals interactions are negligible compare to the SC term. Therefore, the interaction potential between two planar bilayers in the SC regime can be expressed

as:

$$U(z) = U_0(z) - 2\pi k_B T \ell_B \ell_{GC} \sigma_s^2 \left(2\log\left(\frac{z}{\ell_{GC}}\right) - \frac{z}{\ell_{GC}}\right). \tag{2.10}$$

By minimizing this potential $U(z)$, we have obtained an equilibrium value of $d_{w,SC} = 0.7$ nm, which is in very good agreement with our experimental data as shown in Fig. IV.2.8(b) and Fig. IV.2.9(b).

CHAPTER 3

Conclusions and Perspectives

With a combination of NR and XRR experiments, the structure of highly charged lipid bilayers, composed of DPPS lipids in the presence of monovalent counterions only, without added salt (coions). Electrostatic interactions between highly charged double bilayers (planar geometry, negligible fluctuations, strong confinement) were investigated by measuring the equilibrium distance between the two like-charged bilayers. A theoretical interpretation of the measured data within WC and SC theories was performed, taking into account the decrease of water dielectric constant induced by the strongly confined geometry.

We have shown that the water layer between charged bilayers is significantly thinner than that between bilayers consisting of zwitterionic lipids, demonstrating the existence of a counter-intuitive electrostatic attractive interaction between two negatively charged bilayers. This like-charge attraction phenomenon cannot be explained within the classical Poisson-Boltzmann theory of electrostatics. As only monovalent ions were present in the solution, the coupling constant is $\Xi \sim 5$, which is too low to fall in the attractive regime (Fig. IV.2.10) predicted by the SC theory. Recent water-explicit numerical simulations [44] have shown that ion correlation effects can tremendously influence the interaction between charged surfaces even at moderate surface charge densities and in the presence of monovalent counterions only. It was demonstrated that the relative dielectric constant of water in planar strong confinement could decrease drastically, which in turn causes the increase of the coupling constant value Ξ. Taking this finding into account, the attraction between two negatively charged DPPS bilayers clearly falls in the attractive regime described by the SC theory and thus our experimental results are in strong agreement with predictions from numerical simulations [44]. These findings are important to

gain a deeper understanding of electrostatic interactions in strong confinement, where continuous models are not applicable anymore and the discrete nature of ions must be taken into account explicitly. Future work will involve the study of the effect of ions on the bilayers structure and interactions by introducing different salts (monovalent, divalent) to the system. In order to expand the theoretical description of the electrostatic interactions between highly negatively charged membranes the comparison with the numerical simulations performed on similar systems will be carried out.

Part V

Conclusions and Perspectives

Two different projects were carried out during this PhD thesis work involving double lipid bilayer systems as useful platforms for biological and physical studies. The structure, function and physical properties of phospholipid systems were investigated by combining a large number of experimental techniques.

The first project focused on the investigation of out-of-equilibrium membrane fluctuations caused by protein activity. A robust protocol for detergent-mediated BR protein reconstitution in the gel and fluid phase single and floating lipid bilayers systems on the planar substrates was developed. The protein insertion was confirmed and quantified by combined laboratory (QCM-D, AFM, fluorescence microscopy, in-house XRR), NR and SR reflectometry experiments. The protein pumping activity was triggered by sample illumination with visible light and the reversible effect of illumination (light on/light off) on the structure and fluctuations of the membrane-protein system was demonstrated by means of specular and off-specular SR reflectometry experiments. The preliminary analysis of the specular and off-specular reflectometry measurements is consistent with the magnification of membrane shape fluctuations induced by BR activity.

As a perspective, we aim to perform the analysis of NR and specular SR reflectivity measurements by implementing the SLD and ED profiles of BR modeled using the existing protein structure form the Protein Data Bank. The combined analysis of specular and off-specular SR reflectivity measurements will be performed as well, improving the background subtraction and including the protein as an active center in the calculations of membrane height-height correlation functions. NR experiments allowing to resolve the structural changes of membrane-protein system caused by BR activation will be performed as well. We aim to expand further the developed approach in order to investigate other transmembrane proteins and membrane-mimic systems.

Within the second project the interaction between highly negatively charged lipid bilayers, with monovalent couterions and in a strongly confined geometry was investigated. The structure of DPPS double bilayers was fully characterized by means of neutron and SR reflectometry experiments focusing on the equilibrium distance between like-charged bilayers. The influence of added salt and temperature on the lipid bilayer structure and interlayer water thicknesses was monitored as

well. The existence of an attractive interaction between highly charged bilayers was demonstrated, in good agreement with the theoretical description of like-charge attraction within the SC limit, taking into account the decrease of water dielectric constant induced by the strong confinement.

As a perspective, we aim to perform combined analysis of the specular and off-specular SR reflectometry measurements in order to quantify the physical properties of the charged DPPS lipid bilayer (bending modulus, surface tension, interaction potential) and to characterize and compare thermal fluctuation spectrum of charged and zwitterionic membranes. We aim to expand the theoretical description of the electrostatic interactions between highly negatively charged membranes by performing the comparison with the numerical simulations of similar systems.

Part VI

Appendix

APPENDIX A

Sample environment preparation. Cleaning procedure

All the **substrates** used for formation of solid supported lipid bilayers were cleaned very thoroughly to remove any possible contaminant.

Two alternative methods were used depending on the availability of the necessary tools in the different labs where experiments were performed. The most common procedure involved the subsequent sonication of the substrates for 20 minutes in a series of different solvents: 2% detergent solution (Decon Neutracon), MilliQ water, Chloroform, Acetone, Ethanol and MilliQ. These steps were followed by the exposure of the substrate to UV-ozone (20 minutes exposure) (UV/ozone ProCleaner Plus instrument) or to air plasma (3 min exposure) (Harrick plasma cleaner instrument). This step was performed just before the sample deposition to remove any remaining organic contaminant, and to enhance the hydrophilicity of the substrate surface [234, 235].

The alternative method, often used for practical reasons, was based on the use of **piranha solution**. A mild pirahna solution (5:4:1 of H_2O : concentrated H_2SO_4 : 30% H_2O_2 by volume) was prepared adding the concentrated sylfuric acid to H_2O. Hydrogen peroxide was then slowly poured into the diluted acid solution while temperature was continuously monitored and was not allowed to exceed 85 °C. The piranha solution was stirred and kept at 80°C using a stirring heating plate. Dry solid substrates were slowly immersed into piranha and kept in solution for 20 minutes. They were then thoroughly rinsed with MilliQ and kept in water till their use for sample preparation. It is important to note that the use of the piranha solution removes organic molecules from the substrate and etches the surface at the

same time. Therefore, the exposure to ozone or plasma is not necessary after this cleaning procedure.

Solid/liquid cells were cleaned following the same sonication procedure as for substrate cleaning.

Tubes (PTFE), valves (PTFE) and O-rings (viton) were sonicated in a 2 % detergent solution (Decon Neutracon), followed by extensive rinsing and sonication in MilliQ water. O-rings were then rinsed in pure ethanol followed by sonication in MilliQ water. Sonication time was 20 minutes for each solvent. The interior of the tubes used for sample and water injection was cleaned by rinsing it using a syringe with detergent solution, MilliQ water, ethanol and MilliQ water again.

APPENDIX B

Structural parameters

Because of the general phase problem typical for scattering experiments [236], $R(Q_z)$ curves needed to be modeled to find the appropriate scattering length density (SLD) profiles. In order to reduce the number of free parameters during the analysis of double bilayer systems, the bare silicon substrates were characterized prior to the deposition by means of NR and XRR. The errors for the parameters were determined by evaluating the variation of the χ^2 upon changes in parameter values.

B.1 SLD profile for NR

NR data was fitted with the AURORE software [185], where the specular reflectivity is calculated by the Parratt's recursive formalism for stratified interfaces [160]. NR curves originating from the same bilayer systems and collected in different contrasts were analysed simultaneously by applying the same structural model as described in [185]. Only the subphase SLD was changed for different contrasts. Single lipid bilayers were fitted using a 5 or 6 slab model. Double bilayers were fitted using a 9 or 11 slab model (see Fig. VI.B.1(a)). Slab i is described by a scattering length density SLD_i, a fraction of solvent (H_2O or D_2O) $f_{w,i}$ and a thickness d_i:

1. i =SiO_2, silicon oxide layer;
2. $i = w, 1$, first water layer;
3. $i = h11$, lipid head of the first monolayer;
4. $i = ch1$, lipid chain of the first bilayer;

5. $i = h12$, lipid head of the second monolayer;

6. $i = w, 2$, second water layer;

7. $i = h21$, lipid head of the third monolayer;

8. $i = ch2$, lipid chain of the second bilayer;

9. $i = h22$, lipid head of the fourth monolayer.

Each interface between two slabs i and j is also characterized by a width $\sigma_{i,j}$.

B.2 SLD profile for XRR

XRR data was fitted using a 1G-hybrid gaussian continuous profile (see [164, 166] and Fig. VI.B.1(b)).

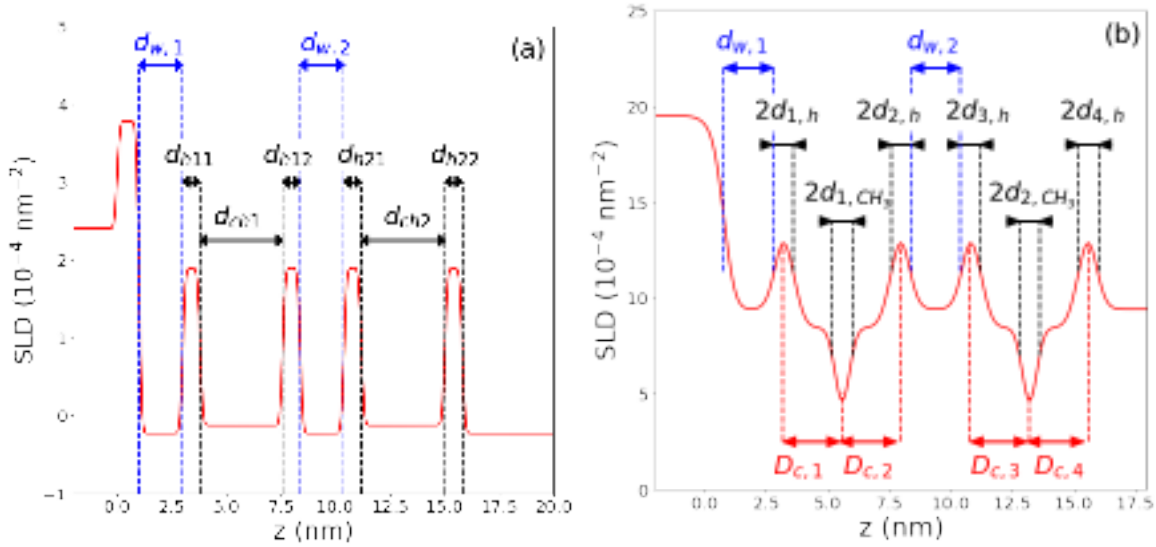

Figure VI.B.1 – (a) Definition of the parameter used for SLD profile in case of NR. For sake of clarity we used articial values for $\sigma_{i,j}$, $d_{w,1}$ and $d_{w,2}$ ($\sigma_{i,j}$ = 0.1 nm, $d_{w,1}$ = 2 nm, $d_{w,2}$ = 2 nm). (b). Definition of the parameter used for SLD profile in case of XR (1G-hybrid model). For sake of clarity we used articial values for $d_{w,1}$ and $d_{w,2}$ ($\sigma_{i,j}$ = 0.1 nm, $d_{w,1}$ = 2 nm, $d_{w,2}$ = 2 nm)

Table B.1 – Values of structural parameters obtained from the fit of the NR data for a POPC single bilayer before and after BR reconstitution. 10 μg/ml BR in 0.05 mM DDM solution was used for BR reconstitution. Values without error bars were fixed during the fitting procedure. For a definition of the parameters see section 2.10.

Parameter	POPC single bilayer	POPC single bilayer + BR
d_{SiO_2} [nm]	1.2 ± 0.2	1.2 ± 0.1
SLD_{SiO_2} [10^{-4}/nm^2]	3.47	3.47
f_{w,SiO_2} [%]	0	0
σ_{SiO_2} [nm]	0.3 ± 0.1	0.3 ± 0.1
$d_{w,1}$ [nm]	0.3±0.1	0.3±0.1
$SLD_{w,1}$ [10^{-4}/nm^2]	$SLD_{solvent}$	$SLD_{solvent}$
$\sigma_{w,1}$ [nm]	0.3 ± 0.1	0.6 ± 0.1
d_{h11}[nm]	0.7 ± 0.3	0.8 ± 0.2
SLD_{h11} [10^{-4}/nm^2]	1.8	1.8
$f_{w,\ h11}$ [%]	30± 2	52± 2
$\sigma_{h11/ch1}$ [nm]	0.3 ± 0.1	0.2 ± 0.1
d_{ch1} [nm]	3.2 ± 0.2	3.3±0.2
SLD_{ch1} [10^{-4}/nm^2]	-0.35	0.13 ± 0.05
$f_{w,\ ch1}$ [%]	8 ±1	39 ±1
$\sigma_{ch1/h12}$ [nm]	0.3 ± 0.2	0.3 ± 0.1
d_{h12} [nm]	0.7 ± 0.2	0.6 ± 0.2
SLD_{h12} [10^{-4}/nm^2]	1.8	1.8
$f_{w,\ h12}$ [%]	30 ± 2	56 ± 2
$\sigma_{h12/w}$ [nm]	0.5 ± 0.2	0.5 ± 0.2

Table B.2 – Values of structural parameters obtained from the fit of the NR data for a POPC single bilayer before and after BR reconstitution. 30 μg/ml BR in 0.05 mM DDM solution was used for BR reconstitution. Values without error bars were fixed during the fitting procedure. For a definition of the parameters see section 2.10.

Parameter	POPC single bilayer	POPC single bilayer + BR
d_{SiO_2} [nm]	1.2 ± 0.2	1.2 ± 0.1
SLD_{SiO_2} [10^{-4}/nm^2]	3.47	3.47
f_{w,SiO_2} [%]	0	0
σ_{SiO_2} [nm]	0.3 ± 0.1	0.5 ± 0.1
$d_{w,1}$ [nm]	0.3±0.1	0.7±0.1
$SLD_{w,1}$ [10^{-4}/nm^2]	$SLD_{solvent}$	$SLD_{solvent}$
$\sigma_{w,1}$ [nm]	0.3 ± 0.1	0.4 ± 0.1
d_{h11}[nm]	0.7 ± 0.3	0.9 ± 0.2
SLD_{h11} [10^{-4}/nm^2]	1.88	1.88 ± 0.05
$f_{w,\ h11}$ [%]	30± 2	58± 2
$\sigma_{h11/ch1}$ [nm]	0.3 ± 0.1	0.6 ± 0.1
d_{ch1} [nm]	3.2 ± 0.2	1.7±0.2
SLD_{ch1} [10^{-4}/nm^2]	-0.35	1.34 ± 0.05
$f_{w,\ ch1}$ [%]	7 ±1	55 ±1
$\sigma_{ch1/h12}$ [nm]	0.3 ± 0.2	0.6 ± 0.1
d_{ch12} [nm]	-	1.7±0.2
SLD_{ch12} [10^{-4}/nm^2]	-	1.1 ± 0.05
$f_{w,\ ch12}$ [%]	-	60 ±1
$\sigma_{ch12/h12}$ [nm]	-	0.6 ± 0.1
d_{h12} [nm]	0.6 ± 0.2	0.9 ± 0.2
SLD_{h12} [10^{-4}/nm^2]	1.88	1.88 ± 0.05
$f_{w,\ h12}$ [%]	30 ± 2	60 ± 2
$\sigma_{h12/w}$ [nm]	0.5 ± 0.2	0.6 ± 0.2
d_{h22} [nm]	-	3.0±0.2
SLD_{h22} [10^{-4}/nm^2]	-	2.0 ± 0.05
$f_{w,\ h22}$ [%]	-	80±1
$\sigma_{h22/w}$ [nm]	-	0.6 ± 0.1

Table B.3 – Values of structural parameters obtained from the fit of the NR data for a POPC single bilayer before and after BR reconstitution. 50 μg/ml BR in 0.05 mM DDM solution was used for BR reconstitution. Values without error bars were fixed during the fitting procedure. For a definition of the parameters see section 2.10.

Parameter	POPC single bilayer	POPC single bilayer + BR
d_{SiO_2} [nm]	1.3 ± 0.2	1.3 ± 0.1
SLD_{SiO_2} [10^{-4}/nm^2]	3.41	3.41
f_{w,SiO_2} [%]	0	0
σ_{SiO_2} [nm]	0.5 ± 0.1	0.6 ± 0.1
$d_{w,1}$ [nm]	0.6±0.1	0.6±0.1
$SLD_{w,1}$ [10^{-4}/nm^2]	$SLD_{solvent}$	$SLD_{solvent}$
$\sigma_{w,1}$ [nm]	0.3 ± 0.1	0.4 ± 0.1
d_{h11}[nm]	0.8 ± 0.3	0.9 ± 0.2
SLD_{h11} [10^{-4}/nm^2]	1.88	1.9 ± 0.05
$f_{w,\ h11}$ [%]	10± 2	80± 2
$\sigma_{h11/ch1}$ [nm]	0.1 ± 0.1	0.5 ± 0.1
d_{ch1} [nm]	2.7 ± 0.2	3.7±0.2
SLD_{ch1} [10^{-4}/nm^2]	-0.35	1.95 ± 0.05
$f_{w,\ ch1}$ [%]	5 ±1	82 ±1
$\sigma_{ch1/h12}$ [nm]	0.5 ± 0.2	0.7 ± 0.1
d_{h12} [nm]	0.6 ± 0.2	1± 0.2
SLD_{h12} [10^{-4}/nm^2]	1.88	1.9 ± 0.05
$f_{w,\ h12}$ [%]	23 ± 2	78 ± 2
$\sigma_{h12/w}$ [nm]	0.4 ± 0.2	0.6 ± 0.2

Table B.4 – Values of structural parameters obtained from the fit of the NR data for a d_{75}DPPC single lipid bilayer with and without NaN_3. Values without error bars were fixed during the fitting procedure. For a definition of the parameters see section 2.10.

Parameter	d_{75}DPPC in H_2O	d_{75}DPPC + 1 mM NaN_3	d_{75}DPPC in H_2O again
d_{SiO_2} [nm]	0.6 ± 0.2	0.6 ± 0.2	0.6 ± 0.2
SLD_{SiO_2} [10^{-4}/nm^2]	3.41	3.41	3.41
f_{w,SiO_2} [%]	0	0	0
σ_{SiO_2} [nm]	0.2 ± 0.1	0.2 ± 0.1	0.2 ± 0.1
$d_{w,1}$ [nm]	0.1±0.1	0.1±0.1	0.1±0.1
$SLD_{w,1}$ [10^{-4}/nm^2]	$SLD_{solvent}$	$SLD_{solvent}$	$SLD_{solvent}$
$\sigma_{w,1}$ [nm]	0.2 ± 0.2	0.2 ± 0.2	0.2 ± 0.2
d_{h11}[nm]	0.8 ± 0.2	0.9 ± 0.2	0.8 ± 0.2
SLD_{h11} [10^{-4}/nm^2]	5.87	5.87	5.87
$f_{w,\ h11}$ [%]	43± 5	43± 5	43± 5
$\sigma_{h11/ch1}$ [nm]	0.2 ± 0.1	0.2 ± 0.1	0.2 ± 0.1
d_{ch12} [nm]	3.7 ±0.2	3.1 ±0.2	3.5 ±0.2
SLD_{ch1} [10^{-4}/nm^2]	6.79	6.79	6.79
$f_{w,\ ch1}$ [%]	27±2	22±2	22±2
$\sigma_{ch1/h12}$ [nm]	0.3 ± 0.2	0.3 ± 0.2	0.4 ± 0.2
d_{h12} [nm]	0.8 ± 0.2	0.9 ± 0.2	0.8 ± 0.2
SLD_{h12} [10^{-4}/nm^2]	5.87	5.87	5.87
$f_{w,\ h12}$ [%]	52 ± 2	43 ± 2	43 ± 2
$\sigma_{h12/w}$ [nm]	0.4 ± 0.2	0.4 ± 0.2	0.4 ± 0.2

Table B.5 – Values of structural parameters obtained from the fit of the NR data for the adsorbed BR layer on the silicon support. 30 μg/ml BR in 0.05 mM DDM solution was used. Values without error bars were fixed during the fitting procedure. For a definition of the parameters see section 2.10.

Parameter	BR on bare substrate
d_{SiO_2} [nm]	1.2 ± 0.2
SLD_{SiO_2} [10^{-4}/nm^2]	3.41
f_{w,SiO_2} [%]	0
σ_{SiO_2} [nm]	0.4 ± 0.2
$d_{w,1}$ [nm]	0.9±0.2
$SLD_{w,1}$ [10^{-4}/nm^2]	$SLD_{solvent}$
$\sigma_{w,1}$ [nm]	0.4 ± 0.2
d_{h1}[nm]	3.6 ± 0.2
SLD_{h1} [10^{-4}/nm^2]	2.11
$f_{w,\ h1}$ [%]	18± 1
$\sigma_{h1/h2}$ [nm]	0.4 ± 0.1
d_{ch1} [nm]	3.2 ±0.2
SLD_{ch1} [10^{-4}/nm^2]	2.11
$f_{w,\ ch1}$ [%]	31± 1
$\sigma_{ch1/h12}$ [nm]	0.4 ± 0.1

Table B.6 – Values of structural parameters obtained from the fit of the NR data for a DSPC-DPPC double bilayer at 48°C before and after BR reconstitution. 0.5 μg/ml BR in 0.05 mM DDM solution was used for BR reconstitution. Values without error bars were fixed during the fitting procedure. For a definition of the parameters see section 2.10.

Parameter	DSPC-DPPC double bilayer	DSPC-DPPC double bilayer + BR
d_{SiO_2} [nm]	1.2 ± 0.1	1.2 ± 0.1
SLD_{SiO_2} [10^{-4}/nm^2]	3.47	3.47
f_{w,SiO_2} [%]	0	0
σ_{SiO_2} [nm]	0.4 ± 0.2	0.4 ± 0.2
$d_{w,1}$ [nm]	0.6±0.1	0.6±0.1
$SLD_{w,1}$ [10^{-4}/nm^2]	$SLD_{solvent}$	$SLD_{solvent}$
$\sigma_{w,1}$ [nm]	0.9 ± 0.2	0.4 ± 0.1
d_{h11}[nm]	0.9 ± 0.2	0.9 ± 0.2
SLD_{h11} [10^{-4}/nm^2]	1.8	1.8
$f_{w,\ h11}$ [%]	43± 2	44± 2
$\sigma_{h11/ch1}$ [nm]	0.4 ± 0.1	0.4 ± 0.1
d_{ch1} [nm]	4.1 ±0.2	4.1 ±0.2
SLD_{ch1} [10^{-4}/nm^2]	-0.39	-0.39
$f_{w,\ ch1}$ [%]	4 ±1	5 ±1
$\sigma_{ch1/h12}$ [nm]	0.7 ± 0.1	0.6 ± 0.1
d_{h12} [nm]	1 ± 0.2	1 ± 0.2
SLD_{h12} [10^{-4}/nm^2]	1.88	1.88
$f_{w,\ h12}$ [%]	35 ± 2	41 ± 2
$\sigma_{h12/w}$ [nm]	0.8 ± 0.2	0.6 ± 0.2
$d_{w,2}$ [nm]	3 ±0.2	3.7 ±0.2
$SLD_{w,2}$ [10^{-4}/nm^2]	$SLD_{solvent}$	$SLD_{solvent}$
$\sigma_{w,2}$ [nm]	1 ± 0.2	1.2 ± 0.2
d_{h21} [nm]	0.9 ± 0.2	0.9 ± 0.2
SLD_{h21} [10^{-4}/nm^2]	1.88	1.88 ± 0.05
$f_{w,\ h21}$ [%]	32±3	35±3
$\sigma_{h21/w}$ [nm]	0.9 ± 0.1	1.3 ± 0.2
d_{ch21} [nm]	3.4 ±0.2	2.5 ±0.2
SLD_{ch21} [10^{-4}/nm^2]	-0.36	-0.19 ± 0.05
$f_{w,\ ch21}$ [%]	4±1	23±2
$\sigma_{ch21/ch22}$ [nm]	1.6 ± 0.1	0.4 ± 0.1
d_{ch22} [nm]	-	2.3 ±0.2
SLD_{ch22} [10^{-4}/nm^2]	-	0.33 ± 0.05
$f_{w,\ ch22}$ [%]	-	19±2
$\sigma_{ch22/h22}$ [nm]	-	1.6±0.1
d_{h22} [nm]	0.9 ± 0.2	5.7 ± 0.2
SLD_{h22} [10^{-4}/nm^2]	1.8	1.8 ± 0.05
$f_{w,\ h22}$ [%]	44±3	90 ±3
$\sigma_{h22/w}$ [nm]	0.9 ± 0.1	1.2 ± 0.1

Table B.7 – Values of structural parameters obtained from the fit of the NR data for a DSPC-DPPC double bilayer at 48°C before and after interaction with DMM solution. Values without error bars were fixed during the fitting procedure. For a definition of the parameters see section 2.10.

Parameter	DSPC-DPPC bilayer	DSPC-DPPC bilayer + DDM
d_{SiO_2} [nm]	1.1 ± 0.2	1 ± 0.1
SLD_{SiO_2} [10^{-4}/nm^2]	3.47	3.47
f_{w,SiO_2} [%]	0	0
σ_{SiO_2} [nm]	0.7 ± 0.2	0.4 ± 0.2
$d_{w,1}$ [nm]	3.1±0.2	3.7±0.2
$SLD_{w,1}$ [10^{-4}/nm^2]	$SLD_{solvent}$	$SLD_{solvent}$
$\sigma_{w,1}$ [nm]	0.9 ± 0.2	0.7 ± 0.1
d_{h11}[nm]	0.7 ± 0.2	0.8 ± 0.2
SLD_{h11} [10^{-4}/nm^2]	1.8	1.8
$f_{w,\,h11}$ [%]	42± 2	25± 2
$\sigma_{h11/ch1}$ [nm]	0.4 ± 0.1	0.4 ± 0.1
d_{ch1} [nm]	4.1 ±0.2	4.0 ±0.2
SLD_{ch1} [10^{-4}/nm^2]	-0.39	-0.39
$f_{w,\,ch1}$ [%]	4 ±1	6 ±1
$\sigma_{ch1/h12}$ [nm]	0.4 ± 0.2	0.6 ± 0.1
d_{h12} [nm]	1.0 ± 0.2	0.7 ± 0.2
SLD_{h12} [10^{-4}/nm^2]	1.88	1.88
$f_{w,\,h12}$ [%]	37 ± 2	33 ± 2
$\sigma_{h12/w}$ [nm]	0.8 ± 0.2	0.4 ± 0.2
$d_{w,2}$ [nm]	1.7 ±0.2	1.7 ±0.2
$SLD_{w,2}$ [10^{-4}/nm^2]	$SLD_{solvent}$	$SLD_{solvent}$
$\sigma_{w,2}$ [nm]	0.6 ± 0.2	0.4 ± 0.2
d_{h21} [nm]	0.7 ± 0.2	0.8 ± 0.2
SLD_{h21} [10^{-4}/nm^2]	1.88	1.88
$f_{w,\,h21}$ [%]	45±3	35±3
$\sigma_{h21/w}$ [nm]	0.9 ± 0.1	0.8 ± 0.2
d_{ch21} [nm]	3.7 ±0.2	4 ±0.2
SLD_{ch21} [10^{-4}/nm^2]	-0.36	-0.36
$f_{w,\,ch21}$ [%]	7±1	17±2
$\sigma_{ch21/h22}$ [nm]	1 ± 0.2	0.8 ± 0.1
d_{h22} [nm]	0.6 ± 0.2	0.7 ± 0.2
SLD_{h22} [10^{-4}/nm^2]	1.8	1.8
$f_{w,\,h22}$ [%]	37±3	35 ±3
$\sigma_{h22/w}$ [nm]	0.8 ± 0.1	0.4 ± 0.1

Table B.8 – Values of structural parameters obtained from the fit of the NR data for a POPC single bilayer before and after Arch-3 reconstitution (no effect). 30 μg/ml Arch-3 in 0.05 mM DDM solution was used for Arch-3 reconstitution. Values without error bars were fixed during the fitting procedure. For a definition of the parameters see section 2.10.

Parameter	POPC single bilayer	POPC single bilayer + Arch-3
d_{SiO_2} [nm]	1.3 ± 0.2	1.3 ± 0.1
SLD_{SiO_2} [10^{-4}/nm^2]	3.47	3.47
f_{w,SiO_2} [%]	13.6 ±0.2	10 ±0.2
σ_{SiO_2} [nm]	0.6 ± 0.1	0.6 ± 0.1
$d_{w,1}$ [nm]	0.6±0.1	0.6±0.1
$SLD_{w,1}$ [10^{-4}/nm^2]	$SLD_{solvent}$	$SLD_{solvent}$
$\sigma_{w,1}$ [nm]	0.3 ± 0.1	0.5 ± 0.1
d_{h11}[nm]	0.9 ± 0.3	0.7 ± 0.2
SLD_{h11} [10^{-4}/nm^2]	1.8	1.9 ± 0.05
$f_{w,\ h11}$ [%]	10± 2	10± 2
$\sigma_{h11/ch1}$ [nm]	0.5 ± 0.1	0.5 ± 0.1
d_{ch1} [nm]	2.8 ± 0.2	3.7±0.2
SLD_{ch1} [10^{-4}/nm^2]	-0.35	0.11 ± 0.05
$f_{w,\ ch1}$ [%]	4.2 ±1	4.2 ±1
$\sigma_{ch1/h12}$ [nm]	0.5 ± 0.2	0.5 ± 0.1
d_{h12} [nm]	0.7 ± 0.2	0.7± 0.2
SLD_{h12} [10^{-4}/nm^2]	1.88	1.9 ± 0.05
$f_{w,\ h12}$ [%]	19 ± 2	30 ± 2
$\sigma_{h12/w}$ [nm]	0.5 ± 0.2	0.4 ± 0.2

Table B.9 – Values of structural parameters obtained from the fit of the NR data for a POPC single bilayer before and after Arch-3 reconstitution. 60 μg/ml Arch-3 in 0.05 mM DDM solution was used for Arch-3 reconstitution. Values without error bars were fixed during the fitting procedure. For a definition of the parameters see section 2.10.

Parameter	POPC single bilayer	POPC single bilayer + Arch-3
d_{SiO_2} [nm]	1.3 ± 0.2	1.3 ± 0.1
SLD_{SiO_2} [10^{-4}/nm^2]	3.47	3.47
f_{w,SiO_2} [%]	10.8 ±0.2	16 ±0.2
σ_{SiO_2} [nm]	0.6 ± 0.1	0.6 ± 0.1
$d_{w,1}$ [nm]	0.6±0.1	0.6±0.1
$SLD_{w,1}$ [10^{-4}/nm^2]	$SLD_{solvent}$	$SLD_{solvent}$
$\sigma_{w,1}$ [nm]	0.3 ± 0.1	0.7 ± 0.1
d_{h11}[nm]	0.8 ± 0.3	0.7 ± 0.2
SLD_{h11} [10^{-4}/nm^2]	1.88	1.9 ± 0.05
$f_{w,\ h11}$ [%]	10± 2	49± 2
$\sigma_{h11/ch1}$ [nm]	0.5 ± 0.1	0.5 ± 0.1
d_{ch1} [nm]	2.8 ± 0.2	3.1±0.2
SLD_{ch1} [10^{-4}/nm^2]	-0.35	0.2 ± 0.05
$f_{w,\ ch1}$ [%]	5±1	3.6 ±1
$\sigma_{ch1/h12}$ [nm]	0.5 ± 0.2	0.4 ± 0.1
d_{h12} [nm]	0.6 ± 0.2	0.67± 0.2
SLD_{h12} [10^{-4}/nm^2]	1.88	1.9 ± 0.05
$f_{w,\ h12}$ [%]	23 ± 2	60 ± 2
$\sigma_{h12/w}$ [nm]	0.4 ± 0.2	0.5 ± 0.2

Table B.10 – Values of structural parameters obtained from the fit of the NR data for Arch-3 adsprption on the bare silicon substrate. 25 μg/ml Arch-3 in 0.05 mM DDM solution was used for Arch-3 reconstitution. Values without error bars were fixed during the fitting procedure. For a definition of the parameters see section 2.10.

Parameter	Arch-3 on bare substrate
d_{SiO_2} [nm]	1.3 ± 0.2
SLD_{SiO_2} [10^{-4}/nm^2]	3.47
f_{w,SiO_2} [%]	0
σ_{SiO_2} [nm]	0.5 ± 0.1

Table B.11 – Values of structural parameters obtained from the fit of the XRR measurements (in-house experiments) for a DSPC-DPPC bilayer at T = 25 °C before and after BR reconstitution. 2.5 μg/ml BR in 0.05 mM DDM solution was used. Values without error bars were fixed during the fitting procedure. For a definition of the parameters see section 2.10.

Parameter	DSPC-DPPC bilayer	DSPC-DPPC bilayer + BR
d_{SiO_2} [nm]	0.5 ± 0.1	0.5 ± 0.1
SLD_{SiO_2} [10^{-4}/nm^2]	19.0 ± 0.05	19.0 ± 0.05
f_{w,SiO_2} [%]	0	0
σ_{SiO_2} [nm]	0.2 ± 0.1	0.2 ± 0.1
$d_{w,1}$ [nm]	0.5±0.1	0.2 ± 0.1
$SLD_{w,1}$ [10^{-4}/nm^2]	9.41	9.41
$\sigma_{w,1}$ [nm]	1.2 ± 0.2	1.1 ± 0.2
d_{h11}[nm]	0.6 ± 0.2	1.1 ± 0.2
SLD_{h11} [10^{-4}/nm^2]	14.1 ± 0.1	14.1 ± 0.1
$f_{w,\ h11}$ [%]	0	0
$\sigma_{h11/ch1}$ [nm]	0.2 ± 0.1	0.2 ± 0.1
d_{ch11} [nm]	2.1 ±0.2	2 ±0.2
SLD_{ch11} [10^{-4}/nm^2]	8.6 ± 0.05	8.6 ± 0.05
$f_{w,\ ch11}$ [%]	0	0
$\sigma_{ch11/h12}$ [nm]	0.2 ± 0.1	0.2 ± 0.1
d_{ch31} [nm]	0.2 ±0.1	0.4 ± 0.1
SLD_{ch31} [10^{-4}/nm^2]	7.2 ± 0.05	6.67 ± 0.05
$f_{w,\ ch31}$ [%]	0	0
$\sigma_{ch31/ch12}$ [nm]	0.2 ± 0.1	0.2 ± 0.1
d_{ch12} [nm]	1.8 ±0.2	1.6 ± 0.2
SLD_{ch12} [10^{-4}/nm^2]	8.4 6± 0.05	8.84 ± 0.05
$f_{w,\ ch12}$ [%]	0	0
$\sigma_{ch12/h12}$ [nm]	0.2 ± 0.1	0.2 ± 0.1
d_{h12} [nm]	0.73 ± 0.2	0.7 ± 0.2
SLD_{h12} [10^{-4}/nm^2]	14.1 ± 0.05	14.1 ± 0.05
$f_{w,\ h12}$ [%]	0	0
$\sigma_{h12/w}$ [nm]	0.2 ± 0.1	0.2 ± 0.1
$d_{w,2}$ [nm]	1.3±0.2	1.7 ± 0.2
$SLD_{w,2}$ [10^{-4}/nm^2]	9.41	9.41
$\sigma_{w,2}$ [nm]	0.2 ± 0.1	0.8 ± 0.1
d_{h21} [nm]	0.8 ± 0.2	0.5 ± 0.2
SLD_{h21} [10^{-4}/nm^2]	10.5 ± 0.05	11.1 ± 0.05
$f_{w,\ h21}$ [%]	0	0
$\sigma_{h21/w}$ [nm]	0.2 ± 0.1	0.4 ± 0.2
d_{ch21} [nm]	1.8 ±0.2	1.6 ±0.2
SLD_{ch21} [10^{-4}/nm^2]	8.7	9.7
$f_{w,\ ch21}$ [%]	0	0
$\sigma_{ch21/ch32}$ [nm]	0.2 ± 0.1	1.2 ± 0.1
d_{ch32} [nm]	0.2 ±0.2	0.3 ±0.2
SLD_{ch32} [10^{-4}/nm^2]	6.7± 0.1	11.1 ± 0.1
$f_{w,\ ch32}$ [%]	0	0
$\sigma_{ch32/ch22}$ [nm]	0.2 ± 0.1	0.9 ± 0.1
d_{ch22} [nm]	1.8 ±0.2	2.1 ±0.2
SLD_{ch22} [10^{-4}/nm^2]	8.9 ± 0.05	11.9 ± 0.05
$f_{w,\ ch22}$ [%]	0	0
$\sigma_{ch22/h22}$ [nm]	0.2 ± 0.1	1.2 ± 0.1
d_{h22} [nm]	0.5 ± 0.1	0.9 ± 0.1
SLD_{h22} [10^{-4}/nm^2]	11.3 ± 0.1	11.4 ± 0.1
$f_{w,\ h22}$ [%]	0	0
$\sigma_{h22/w}$ [nm]	0.2 ± 0.1	1.5 ± 0.2

Table B.12 – Values of structural parameters obtained from the fit of the XRR measurements (in-house experiments) for a DSPC single bilayer at T = 25 °C before and after BR reconstitution. 1 μg/ml BR in 0.05 mM DDM solution was used. Values without error bars were fixed during the fitting procedure. For a definition of the parameters see section 2.10.

Parameter	DSPC-DPPC double bilayer	DSPC-DPPC double bilayer + BR
d_{SiO_2} [nm]	0.9 ± 0.2	0.9 ± 0.2
SLD_{SiO_2} [10^{-4}/nm^2]	18.6± 0.1	18.6 ± 0.1
f_{w,SiO_2} [%]	0	0
σ_{SiO_2} [nm]	0.9 ± 0.2	0.9 ± 0.1
$d_{w,1}$ [nm]	0.4±0.1	0.4 ±0.1
$SLD_{w,1}$ [10^{-4}/nm^2]	9.41	9.41
$\sigma_{w,1}$ [nm]	0.5 ± 0.1	0.5 ± 0.2
d_{h11}[nm]	0.9 ± 0.2	0.8 ± 0.2
SLD_{h11} [10^{-4}/nm^2]	11.2 ± 0.05	11.4 ± 0.05
$f_{w,\ h11}$ [%]	0	0
$\sigma_{h11/ch1}$ [nm]	0.4 ± 0.1	0.8 ± 0.1
d_{ch11} [nm]	1.4 ±0.2	1.2 ±0.2
SLD_{ch11} [10^{-4}/nm^2]	9.4 ± 0.05	9.4 ± 0.05
$f_{w,\ ch11}$ [%]	0	0
$\sigma_{ch11/h12}$ [nm]	0.2 ± 0.1	0.2 ± 0.1
d_{ch31} [nm]	0.2 ±0.1	0.5 ±0.1
SLD_{ch31} [10^{-4}/nm^2]	7.5 ± 0.05	8.4 ± 0.05
$f_{w,\ ch31}$ [%]	0	0
$\sigma_{ch31/ch12}$ [nm]	0.3 ± 0.1	0.2 ± 0.1
d_{ch12} [nm]	1.4 ±0.2	1.4 ±0.2
SLD_{ch12} [10^{-4}/nm^2]	9.0 ± 0.05	8.8 ± 0.05
$f_{w,\ ch12}$ [%]	0	0
$\sigma_{ch12/h12}$ [nm]	0.2 ± 0.1	0.2 ± 0.1
d_{h12} [nm]	0.9 ± 0.2	0.9 ± 0.2
SLD_{h12} [10^{-4}/nm^2]	11.4 ± 0.05	11.4 ± 0.05
$f_{w,\ h12}$ [%]	0	0
$\sigma_{h12/w}$ [nm]	0.2 ± 0.1	0.2 ± 0.1

Table B.13 – Values of structural parameters obtained from the fit of the XRR data (in-house measurements) for a DSPC double bilayer at T = 25 °C before and after the first and second Arch-3 reconstitution attempt. 1 μg/ml Arch-3 in 0.05 mM DDM solutions were used for the first and second Arch-3 reconstitution attempts. Values without error bars were fixed during the fitting procedure. For a definition of the parameters see section 2.10.

Parameter	DSPC double bilayer	+ Arch-3 (1st inj.)	+ Arch-3 (2nd inj.)
d_{SiO_2} [nm]	1.5 ±0.1	1.5 ±0.1	1.5 ±0.1
SLD_{SiO_2} [10^{-4}/nm^2]	18.7	18.7	18.7
f_{w,SiO_2} [%]	0	0	0
σ_{SiO_2} [nm]	0.3 ± 0.1	0.3 ± 0.1	0.3 ± 0.1
$d_{w,1}$ [nm]	0.5±0.1	0.5 ±0.1	0.5 ± 0.1
$SLD_{w,1}$ [10^{-4}/nm^2]	9.41	9.41	9.41
$\sigma_{w,1}$ [nm]	0.2 ± 0.1	0.3 ± 0.1	0.3 ± 0.1
d_{h11}[nm]	0.9± 0.2	0.9 ± 0.2	1.0 ± 0.2
SLD_{h11} [10^{-4}/nm^2]	11.5 ± 0.08	11.8 ± 0.08	11.5 ± 0.08
$f_{w,\,h11}$ [%]	0	0	0
$\sigma_{h11/ch1}$ [nm]	0.2 ± 0.1	0.5 ± 0.1	0.2 ± 0.1
d_{ch11} [nm]	1.5 ±0.2	1.6 ±0.2	1.1 ±0.2
SLD_{ch11} [10^{-4}/nm^2]	9.4 ± 0.05	9.3 ± 0.05	9.8 ± 0.05
$f_{w,\,ch11}$ [%]	0	0	0
$\sigma_{ch11/h12}$ [nm]	0.2 ± 0.1	0.3 ± 0.1	0.2 ± 0.1
d_{ch31} [nm]	0.3 ±0.1	0.4 ±0.1	0.4 ±0.1
SLD_{ch31} [10^{-4}/nm^2]	7.9 ± 0.05	7.9 ± 0.05	7.5 ± 0.05
$f_{w,\,ch31}$ [%]	0	0	0
$\sigma_{ch31/ch12}$ [nm]	0.2 ± 0.1	0.9 ± 0.1	0.4 ± 0.1
d_{ch12} [nm]	1.8 ±0.2	1.9 ±0.2	2.2 ±0.2
SLD_{ch12} [10^{-4}/nm^2]	8.8 ± 0.05	8.9 ± 0.05	8.8± 0.05
$f_{w,\,ch12}$ [%]	0	0	0
$\sigma_{ch12/h12}$ [nm]	0.4 ± 0.1	0.6 ± 0.1	0.3 ± 0.1
d_{h12} [nm]	0.8 ± 0.2	0.8 ± 0.2	0.5 ± 0.2
SLD_{h12} [10^{-4}/nm^2]	10.7 ± 0.05	11.7 ± 0.05	11.3 ± 0.05
$f_{w,\,h12}$ [%]	0	0	0
$\sigma_{h12/w}$ [nm]	0.2 ± 0.1	0.2 ± 0.1	0.2 ± 0.1
$d_{w,2}$ [nm]	1.5± 0.2	1.7 ± 0.2	1.4 ± 0.2
$SLD_{w,2}$ [10^{-4}/nm^2]	9.41	9.41	9.41
$\sigma_{w,2}$ [nm]	1.5 ± 0.1	0.7 ± 0.1	0.4 ± 0.1
d_{h21} [nm]	0.7 ± 0.2	0.6 ± 0.2	0.5 ± 0.2
SLD_{h21} [10^{-4}/nm^2]	11.75 ± 0.05	10.7 ± 0.05	10.3 ± 0.05
$f_{w,\,h21}$ [%]	0	0	0
$\sigma_{h21/w}$ [nm]	1.0 ± 0.1	0.2 ± 0.2	0.8 ± 0.2
d_{ch21} [nm]	2.1 ±0.2	2.1 ± 0.2	2.1 ± 0.2
SLD_{ch21} [10^{-4}/nm^2]	8.9 ± 0.05	8.8 ± 0.05	8.8 ± 0.05
$f_{w,\,ch21}$ [%]	0	0	0
$\sigma_{ch21/ch32}$ [nm]	0.8 ± 0.1	0.9 ± 0.1	1.0 ± 0.1
d_{ch32} [nm]	0.2 ± 0.2	0.4 ± 0.2	0.5 ± 0.2
SLD_{ch32} [10^{-4}/nm^2]	7.9 ± 0.05	7.9 ± 0.05	7.9 ± 0.05
$f_{w,\,ch32}$ [%]	0	0	0
$\sigma_{ch32/ch22}$ [nm]	0.2 ± 0.1	0.3 ± 0.1	0.2 ± 0.1
d_{ch22} [nm]	1.7±0.2	1.7 ±0.2	1.7 ±0.2
SLD_{ch22} [10^{-4}/nm^2]	9.11 ± 0.05	8.8 ± 0.05	8.8 ± 0.05
$f_{w,\,ch22}$ [%]	0	0	0
$\sigma_{ch22/h22}$ [nm]	0.3 ± 0.1	1.0 ± 0.2	0.2 ± 0.2
d_{h22} [nm]	0.6 ± 0.1	0.6 ± 0.1	0.6 ± 0.1
SLD_{h22} [10^{-4}/nm^2]	11.8 ± 0.05	11.6 ± 0.05	11.0 ± 0.05
$f_{w,\,h22}$ [%]	0	0	0
$\sigma_{h22/w}$ [nm]	0.2 ± 0.1	0.2 ± 0.2	0.2 ± 0.2

Table B.14 – Values of structural parameters obtained from the fit of synchrotron radiation specular reflectivity measurements for a DSPC double bilayer. Values without error bars were fixed during the fitting procedure. For a definition of the parameters see section 2.10.

Parameter	DSPC	BR light off	Light on	light off	light on
d_{SiO_2} [nm]	0.7 ± 0.1	0.7 ± 0.1	0.7 ± 0.1	0.7 ± 0.1	0.7 ± 0.1
SLD_{SiO_2} [10^{-4}/nm^2]	17.5	17.5	17.5	17.5	17.5
f_{w,SiO_2} [%]	0	0	0	0	0
σ_{SiO_2} [nm]	0.3 ± 0.2	0.3 ± 0.2	0.3 ± 0.2	0.3 ± 0.2	0.3 ± 0.2
$d_{w,1}$ [nm]	0.3 ±0.1	0.3 ±0.1	0.2 ±0.1	0.1 ± 0.1	1.5 ± 0.2
$SLD_{w,1}$ [10^{-4}/nm^2]	9.41	9.41	9.41	9.41	9.41
$\sigma_{w,1}$ [nm]	0.3 ± 0.2	0.2 ± 0.1	0.2 ± 0.1	0.4 ± 0.1	0.2 ± 0.1
d_{h11}[nm]	0.6 ± 0.2	0.6 ± 0.2	0.6 ± 0.2	0.9 ± 0.2	0.7 ± 0.2
SLD_{h11} [10^{-4}/nm^2]	12.2 ± 0.05	13.4 ± 0.05	12.0± 0.05	13.5± 0.05	12.2 ± 0.05
$f_{w,\,h11}$ [%]	0	0	0	0	0
$\sigma_{h11/ch1}$ [nm]	0.3 ± 0.1	0.4 ± 0.2	0.3 ± 0.2	0.4 ± 0.2	0.4± 0.2
d_{ch11} [nm]	2 ±0.2	2 ±0.2	1.9 ±0.2	1.7 ± 0.2	1.9 ± 0.2
SLD_{ch11} [10^{-4}/nm^2]	8.4 ± 0.05	8.9 ± 0.05	8.9 ± 0.05	9 ± 0.05	8.8 ± 0.05
$f_{w,\,ch11}$ [%]	0	0	0	0	0
$\sigma_{ch11/h12}$ [nm]	0.3 ± 0.1	0.2 ± 0.1	0.2 ±0.1	0.2 ± 0.1	0.2 ±0.1
d_{ch31} [nm]	0.3 ±0.2	0.4 ±0.1	0.4 ±0.2	0.4 ±0.2	0.4 ±0.1
SLD_{ch31} [10^{-4}/nm^2]	6.74 ± 0.05	7.12 ± 0.05	6.67± 0.05	6.67± 0.05	6.67± 0.05
$f_{w,\,ch31}$ [%]	0	0	0	0	0
$\sigma_{ch31/ch12}$ [nm]	0.2 ± 0.1	0.4 ± 0.1	0.2 ±0.1	0.3 ±0.2	0.2 ±0.1
d_{ch12} [nm]	1.7 ±0.2	1.7 ±0.2	1.9 ±0.2	2 ±0.2	1.8 ±0.1
SLD_{ch12} [10^{-4}/nm^2]	8.5± 0.05	9.22± 0.05	9 ± 0.05	8.94 ± 0.05	9± 0.05
$f_{w,\,ch12}$ [%]	0	0	0	0	0
$\sigma_{ch12/h12}$ [nm]	0.3 ± 0.1	0.3 ± 0.1	0.4 ±0.2	0.4 ±0.2	0.4 ±0.2
d_{h12} [nm]	0.8 ± 0.2	0.8 ±0.2	0.7±0.2	1 ±0.2	0.6 ±0.2
SLD_{h12} [10^{-4}/nm^2]	12.53 ± 0.05	13 ± 0.05	12.53 ± 0.05	12.92± 0.05	12.53 ± 0.05
$f_{w,\,h12}$ [%]	0	0	0	0	0
$\sigma_{h12/w}$ [nm]	0.4 ± 0.2	0.6 ± 0.2	0.8±0.2	0.7 ±0.2	0.8 ±0.2
$d_{w,2}$ [nm]	1.5±0.2	1.3 ±0.2	1.8 ±0.2	1.7 ±0.2	1.6 ±0.2
$SLD_{w,2}$ [10^{-4}/nm^2]	9.41	9.41	9.41	9.41	9.41
$\sigma_{w,2}$ [nm]	0.7 ± 0.1	1 ± 0.2	1.5 ±0.2	1.2±0.2	1.5 ±0.2
d_{h21} [nm]	0.6 ± 0.2	0.9 ± 0.2	1 ±0.2	0.7±0.1	1 ±0.2
SLD_{h21} [10^{-4}/nm^2]	10.5 ± 0.05	10.9 ± 0.05	11.55 ± 0.05	11.6 ± 0.05	12 ± 0.05
$f_{w,\,h21}$ [%]	0	0	0	0	0
$\sigma_{h21/w}$ [nm]	0.7 ± 0.1	0.2 ± 0.1	1.6 ±0.2	0.7±0.2	1.5 ±0.2
d_{ch21} [nm]	2.2 ±0.2	1.9 ±0.3	2.5 ±0.3	2.3±0.2	2.5 ±0.2
SLD_{ch21} [10^{-4}/nm^2]	8.82 ± 0.05	10.5 ± 0.05	10 ± 0.05	10 ± 0.05	10 ± 0.05
$f_{w,\,ch21}$ [%]	0	0	0	0	0
$\sigma_{ch21/h22}$ [nm]	0.6 ± 0.1	0.7 ± 0.1	1.2 ±0.2	1.2±0.2	1 ±0.2
d_{ch32} [nm]	0.2 ±0.1	0.2 ±0.1	0.4±0.1	0.4±0.2	0.4 ±0.2
SLD_{ch32} [10^{-4}/nm^2]	7.75 ± 0.05	9 ± 0.05	10 ± 0.05	9.54 ± 0.05	10 ± 0.05
$f_{w,\,ch32}$ [%]	0	0	0	0	0
$\sigma_{ch32/ch22}$ [nm]	0.3 ± 0.1	0.2 ± 0.1	1.5±0.3	0.2±0.1	1 ±0.2
d_{ch22} [nm]	1.8 ±0.2	2.2 ± 0.2	2.3 ±0.2	2.3±0.2	2.2 ±0.2
SLD_{ch22} [10^{-4}/nm^2]	8.82 ± 0.05	10.2 ± 0.05	10 ± 0.05	9.7 ± 0.05	10 ± 0.05
$f_{w,\,ch22}$ [%]	0	0	0	0	0
$\sigma_{ch22/h22}$ [nm]	0.4 ± 0.1	0.2 ± 0.2	1.1±0.2	1±0.2	1 ±0.2
d_{h22} [nm]	0.6 ± 0.2	1 ± 0.2	1±0.2	0.6±0.2	1±0.2
SLD_{h22} [10^{-4}/nm^2]	10.5 ± 0.05	10.4 ± 0.05	10 ± 0.05	10.5 ± 0.05	10 ± 0.05
$f_{w,\,h22}$ [%]	0	0	0	0	0
$\sigma_{h22/w}$ [nm]	0.2 ± 0.2	0.8 ± 0.2	1.5±0.3	1±0.2	2 ±0.2

APPENDIX C

LB transfer efficiency

During LB deposition the quality of the monolayer transfer can be evaluated by monitoring the transfer ratio, t.r.. This ratio is defined as :

$$t.r. = w \times \frac{\Delta Y_{block}}{\Delta A_{mono}} \tag{C.1}$$

where ΔY_{block} is the part of the substrate covered by the monolayer, w is the perimeter of the substrate section facing the water phase and ΔA_{mono} is the reduction of the area in the trough occupied by the Langmuir monolayer. Fig. VI.C.1 shows the variation of Y_{block} vs. A_{mono} during the deposition of DSPC and DPPS monolayers.

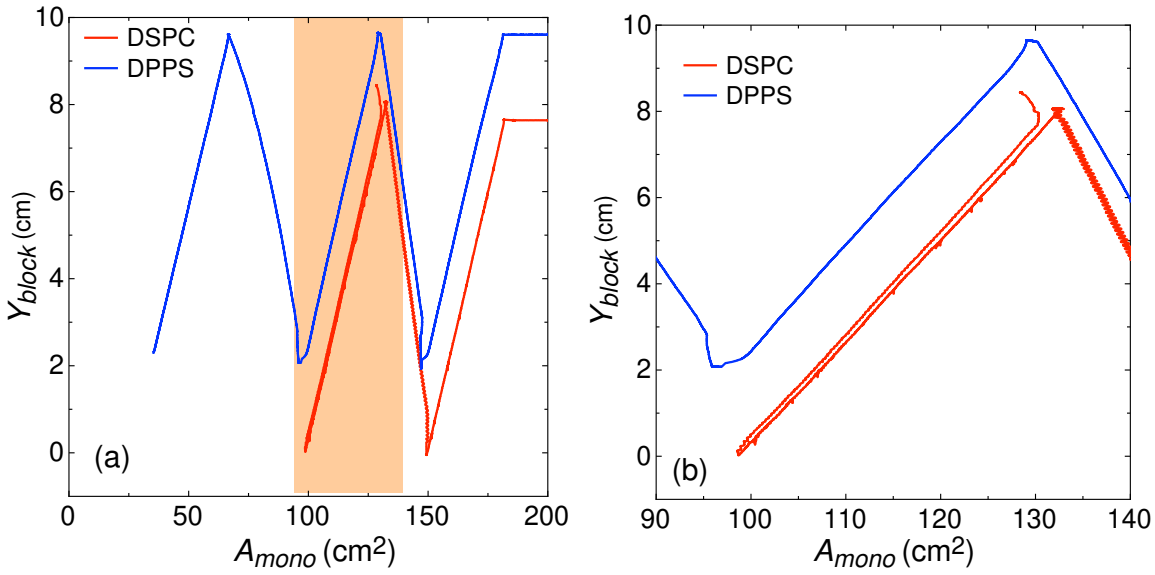

Figure VI.C.1 – (a) Successive deposition of lipid monolayers on a silicon block at Π = 40 mN/m. For DSPC (red) the fourth deposition attempt removes the third layer and for DPPS (blue) successful five layer deposition was achieved. (b) Zoom on the highlighted zone of (a) (third and fourth monolayer deposition).

We can observe that, contrarily to the case of DPPS, it was not possible to

deposit more than 3 successive DSPC monolayers; the attempt of depositing a fourth monolayer on top of the third one failed systematically. More importantly, the trend shown in Figure VI.C.1(b) indicates that the deposition did not simply fail, but it has promoted the removal of the lipids composing the third monolayer, as indicated by the increase of A_{mono}. For a successful deposition the monolayer area should decrease upon transfer or stay constant in the case of null transfer. For this reason, the last monolayer for zwitterionic systems was routinely deposited using the LS technique, which proved to be more efficient. This problem was not present in the case of charged monolayers (DPPS), as can be seen in Fig. VI.C.1(a), but we have decided to apply the same preparation protocol to all the samples for better comparability. Therefore, the last DPPS monolayer was deposited using LS technique as well.

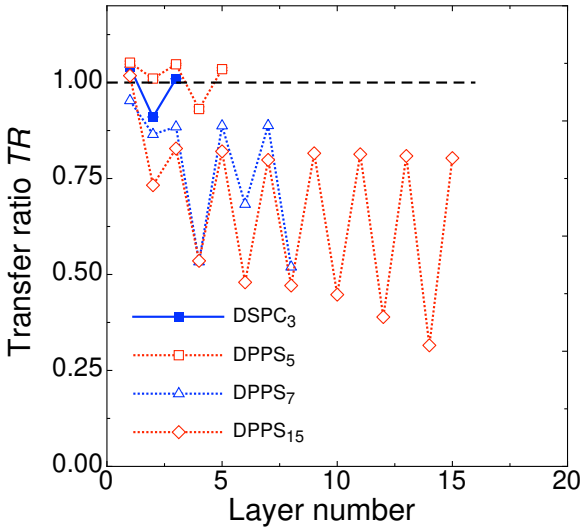

Figure VI.C.2 – Transfer ratios for the successively deposited layers at Π = 40 mN/m: DSPC (■), DPPS (◯) and DSPC/DPPS-DPPS (☆).

The t.r. values obtained from the analysis of $Y_{block} - A_{mono}$ curves for different samples are shown in Fig VI.C.2. The values of t.r. are all close to 1, demonstrating the good quality of the samples. Since all surfaces of the blocks - polished (39% of the total surface of the substrate) and non-polished (61% of the total surface of the substrate)- were treated following the same preparation protocol, the t.r. can reach values larger than 1 if non-polished faces of the blocks get covered with lipids. On the other hand, t.r. lower than 1 clearly indicates that the deposition quality is poor. Another interesting effect of the alternating behaviour of the transfer ratio between odd layers (deposited by moving the block upwards, out of the water subphase) and

even ones (deposited by lowering the block from air into the water) was noticed. The t.r. values reported in Fig. VI.C.2 indicate that the transfer efficiency on all the surfaces of the substrate is higher when depositing odd layers than it is for the even ones. However, from the analysis of NR and XRR data it was not possible to detect any difference in the coverage of the different leaflets of the lipid bilayer, despite the alternating t.r. behaviour. This might be an indication that this behaviour is caused by the deposition of material on the non-polished faces (which sum up to 61 % of the total surface).

APPENDIX D

Structural parameters for highly charged double bilayers

Table D.1 – Values of structural parameters obtained from the fit of the synchrotron radiation specular XRR data for the highly charged DPPS double bilayer at T = 40°C.

Parameter	Value
ρ_{SiO_2} [10^{-4}/nm^2]	0.67 ± 0.02
d_{SiO_2} [nm]	0.8 ± 1
σ_{SiO_2} [Å]	1.80 ± 0.1
$d_{w,1}$ [nm]	0.97 ± 2
$\rho_{1,head}$ [10^{-4}/nm^2]	0.50 ± 0.02
$\rho_{2,head}$ [10^{-4}/nm^2]	0.47 ± 0.02
$\rho_{1,tail}$ [10^{-4}/nm^2]	0.30 ± 0.01
$\rho_{2,tail}$ [10^{-4}/nm^2]	0.27 ± 0.01
ρ_{1,CH_3} [10^{-4}/nm^2]	0.23 ± 0.02
$d_{1,head}$ [nm]	0.55 ± 0.2
$d_{2,head}$ [nm]	0.3 ± 0.2
$D_{1,tail}$ [nm]	2.5 ± 0.5
$D_{2,tail}$ [nm]	2.1 ± 0.5
d_{1,CH_3}[nm]	0.4 ± 0.2
$d_{w,2}$ [nm]	0.51 ± 1
$\rho_{3,head}$ [10^{-4}/nm^2]	0.54 ± 0.02
$\rho_{4,head}$ [10^{-4}/nm^2]	0.50 ± 0.02
$\rho_{3,tail}$ [10^{-4}/nm^2]	0.29 ± 0.01
$\rho_{4,tail}$ [10^{-4}/nm^2]	0.30 ± 0.01
ρ_{2,CH_3} [10^{-4}/nm^2]	0.18 ± 0.02
$d_{3,head}$ [nm]	0.4 ± 0.2
$d_{4,head}$ [nm]	0.55 ± 0.2
$D_{3,tail}$ [nm]	2.6 ± 0.5
$D_{4,tail}$ [nm]	2.3 ± 0.5
d_{2,CH_3} [nm]	0.3 ± 0.2

Table D.2 – Values of structural parameters obtained from the fit of the NR data for a highly charged DPPS double bilayer at T = 45°C. Values without error bars were fixed during the fitting procedure. For a definition of the parameters see section 2.10.

Parameter	Value
d_{SiO_2} [nm]	1.0 ± 0.1
SLD_{SiO_2} [10^{-4}/nm^2]	3.47
f_{w,SiO_2} [%]	0
σ_{SiO_2} [nm]	0.4 ± 0.2
$d_{w,1}$ [nm]	1.1±0.2
$SLD_{w,1}$ [10^{-4}/nm^2]	$SLD_{solvent}$
$\sigma_{w,1}$ [nm]	0.7 ± 0.2
d_{h11}[nm]	0.7 ± 0.2
SLD_{h11} [10^{-4}/nm^2]	2.63
$f_{w,\ h11}$ [%]	10± 2
$\sigma_{h11/ch1}$ [nm]	0.2 ± 0.1
d_{ch1} [nm]	3.8 ±0.2
SLD_{ch1} [10^{-4}/nm^2]	-0.41
$f_{w,\ ch1}$ [%]	0
$\sigma_{ch1/h12}$ [nm]	0.2 ± 0.1
d_{h12} [nm]	0.8 ± 0.2
SLD_{h12} [10^{-4}/nm^2]	2.63
$f_{w,\ h12}$ [%]	10 ± 2
$\sigma_{h12/w}$ [nm]	0.4 ± 0.2
$d_{w,2}$ [nm]	0.6 ±0.2
$SLD_{w,2}$ [10^{-4}/nm^2]	$SLD_{solvent}$
$\sigma_{w,2}$ [nm]	0.2 ± 0.1
d_{h21} [nm]	0.8 ± 0.2
SLD_{h21} [10^{-4}/nm^2]	2.63
$f_{w,\ h21}$ [%]	10±3
$\sigma_{h21/w}$ [nm]	0.2 ± 0.1
d_{ch2} [nm]	3.8 ±0.2
SLD_{ch2} [10^{-4}/nm^2]	-0.41
$f_{w,\ ch2}$ [%]	0
$\sigma_{ch2/h22}$ [nm]	0.2 ± 0.1
d_{h22} [nm]	0.8 ± 0.2
SLD_{h22} [10^{-4}/nm^2]	2.63
$f_{w,\ h22}$ [%]	10±3
$\sigma_{h22/w}$ [nm]	0.4 ± 0.2

Table D.3 – Values of structural parameters obtained from the fit of the NR data for a highly charged DPPS triple bilayer at T = 25°C. Values without error bars were fixed during the fitting procedure. For a definition of the parameters see section 2.10.

Parameter	Value
d_{SiO_2} [nm]	1.5 ± 0.05
SLD_{SiO_2} [10^{-4}/nm^2]	3.47
f_{w,SiO_2} [%]	0
σ_{SiO_2} [nm]	0.7 ±0.1
$d_{w,1}$ [nm]	1.3±0.2
$SLD_{w,1}$ [10^{-4}/nm^2]	$SLD_{solvent}$
$\sigma_{w/h11}$ [nm]	0.7 ± 0.2
d_{h11}[nm]	0.9 ± 0.2
SLD_{h11} [10^{-4}/nm^2]	2.63
$f_{w,h11}$ [%]	25± 3
$\sigma_{h11/ch1}$ [nm]	0.3 ± 0.1
d_{ch1} [nm]	3.5 ±0.2
SLD_{ch1} [10^{-4}/nm^2]	-0.41
$f_{w,\ ch1}$ [%]	0
$\sigma_{ch1/h12}$ [nm]	0.4 ± 0.2
d_{h12} [nm]	0.9 ± 0.2
SLD_{h12} [10^{-4}/nm^2]	2.63
$f_{w,\ h12}$ [%]	29 ± 3
$\sigma_{h12/w}$ [nm]	0.4 ± 0.2
$d_{w,2}$ [nm]	0.3 ±0.2
$SLD_{w,2}$ [10^{-4}/nm^2]	$SLD_{solvent}$
$\sigma_{w/h21}$ [nm]	0.2 ± 0.1
d_{h21} [nm]	0.9 ± 0.2
SLD_{h21} [10^{-4}/nm^2]	2.63
$f_{w,\ h21}$ [%]	23±3
$\sigma_{h21/ch2}$ [nm]	0.4 ± 0.1
d_{ch2} [nm]	3.8 ±0.2
SLD_{ch2} [10^{-4}/nm^2]	-0.41
$f_{w,\ ch2}$ [%]	0
$\sigma_{ch2/h22}$ [nm]	0.4 ± 0.2
d_{h22} [nm]	0.9 ± 0.2
SLD_{h22} [10^{-4}/nm^2]	2.63
$f_{w,\ h22}$ [%]	24±3
$\sigma_{h22/w}$ [nm]	0.4 ± 0.2
$d_{w,3}$ [nm]	0.3 ±0.2
$\sigma_{w/h31}$ [nm]	0.3 ± 0.1
d_{h31} [nm]	0.9 ± 0.2
SLD_{h31} [10^{-4}/nm^2]	2.63
$f_{w,h31}$ [%]	0.1 ± 0.02
$\sigma_{h31/ch3}$ [Å]	0.3 ± 0.1
d_{ch3} [nm]	3.8 ±0.2
SLD_{ch3} [10^{-4}/nm^2]	-0.41
$f_{w,\ ch3}$ [%]	0
$\sigma_{ch3/h32}$ [nm]	0.2 ± 0.1
d_{h32} [nm]	0.9 ±0.2
SLD_{h32} [10^{-4}/nm^2]	2.63
$f_{w,h32}$ [%]	10±2
$\sigma_{h32/w}$ [nm]	0.3 ± 0.1

Table D.4 – Values of structural parameters obtained from the fit of the NR data for a highly charged DPPC/DPPS-DPPS/DPPC double bilayer at T = 25°C. Values without error bars were fixed during the fitting procedure. For a definition of the parameters see section 2.10.

Parameter	Value
d_{SiO_2} [nm]	1.1 ± 0.05
SLD_{SiO_2} [10^{-4}/nm^2]	3.47
f_{w,SiO_2} [%]	0
σ_{SiO_2} [nm]	0.4 ± 0.2
$d_{w,1}$ [nm]	0.5±0.1
$SLD_{w,1}$ [10^{-4}/nm^2]	$SLD_{solvent}$
$\sigma_{w,1}$ [nm]	0.4 ± 0.2
d_{h11}[nm]	0.9 ± 0.2
SLD_{h11} [10^{-4}/nm^2]	1.88
$f_{w,\ h11}$ [%]	14± 2
$\sigma_{h11/ch1}$ [nm]	0.5 ± 0.1
d_{ch11} [nm]	1.8 ±0.2
SLD_{ch11} [10^{-4}/nm^2]	-0.39
$f_{w,\ ch11}$ [%]	0
$\sigma_{ch11/h12}$ [nm]	0.5 ± 0.1
d_{ch12} [nm]	1.8 ±0.2
SLD_{ch12} [10^{-4}/nm^2]	-0.41
$f_{w,\ ch12}$ [%]	0
$\sigma_{ch12/h12}$ [nm]	0.4 ± 0.1
d_{h12} [nm]	0.9 ± 0.2
SLD_{h12} [10^{-4}/nm^2]	2.63
$f_{w,\ h12}$ [%]	10 ± 2
$\sigma_{h12/w}$ [nm]	0.4 ± 0.2
$d_{w,2}$ [nm]	0.4±0.2
$SLD_{w,2}$ [10^{-4}/nm^2]	$SLD_{solvent}$
$\sigma_{w,2}$ [nm]	0.4 ± 0.1
d_{h21} [nm]	0.9 ± 0.2
SLD_{h21} [10^{-4}/nm^2]	2.63
$f_{w,\ h21}$ [%]	39±3
$\sigma_{h21/w}$ [nm]	0.4 ± 0.1
d_{ch21} [nm]	1.8 ±0.2
SLD_{ch21} [10^{-4}/nm^2]	-0.41
$f_{w,\ ch21}$ [%]	12
$\sigma_{ch21/h22}$ [nm]	0.4 ± 0.1
d_{ch22} [nm]	1.8 ±0.2
SLD_{ch22} [10^{-4}/nm^2]	-0.39
$f_{w,\ ch22}$ [%]	10
$\sigma_{ch22/h22}$ [nm]	0.4 ± 0.2
d_{h22} [nm]	0.9 ± 0.2
SLD_{h22} [10^{-4}/nm^2]	1.88
$f_{w,\ h22}$ [%]	39±3
$\sigma_{h22/w}$ [nm]	0.4 ± 0.2

Table D.5 – Values of structural parameters obtained from the fit of the NR data for a highly charged d_{75}DPPC/DPPS-DPPS/d_{75}DPPC double bilayer at T = 25°C. Values without error bars were fixed during the fitting procedure. For a definition of the parameters see section 2.10.

Parameter	Value
d_{SiO_2} [nm]	1.1 ± 0.05
SLD_{SiO_2} [10^{-4}/nm^2]	3.47
f_{w,SiO_2} [%]	0
σ_{SiO_2} [nm]	0.3 ± 0.2
$d_{w,1}$ [nm]	0.5±0.1
$SLD_{w,1}$ [10^{-4}/nm^2]	$SLD_{solvent}$
$\sigma_{w,1}$ [nm]	0.3 ± 0.2
d_{h11}[nm]	0.7 ± 0.2
SLD_{h11} [10^{-4}/nm^2]	5.32
$f_{w,\ h11}$ [%]	11± 2
$\sigma_{h11/ch1}$ [nm]	0.5 ± 0.1
d_{ch11} [nm]	1.8 ±0.2
SLD_{ch11} [10^{-4}/nm^2]	6.53
$f_{w,\ ch11}$ [%]	0
$\sigma_{ch11/h12}$ [nm]	0.3 ± 0.1
d_{ch12} [nm]	1.9 ±0.2
SLD_{ch12} [10^{-4}/nm^2]	-0.32
$f_{w,\ ch12}$ [%]	0
$\sigma_{ch12/h12}$ [nm]	0.3 ± 0.1
d_{h12} [nm]	0.9 ± 0.2
SLD_{h12} [10^{-4}/nm^2]	3.13
$f_{w,\ h12}$ [%]	10 ± 2
$\sigma_{h12/w}$ [nm]	0.5 ± 0.2
$d_{w,2}$ [nm]	0.5±0.1
$SLD_{w,2}$ [10^{-4}/nm^2]	$SLD_{solvent}$
$\sigma_{w,2}$ [nm]	0.3 ± 0.1
d_{h21} [nm]	0.9 ± 0.2
SLD_{h21} [10^{-4}/nm^2]	3.49
$f_{w,\ h21}$ [%]	10±3
$\sigma_{h21/w}$ [nm]	0.5 ± 0.1
d_{ch21} [nm]	1.6 ±0.2
SLD_{ch21} [10^{-4}/nm^2]	-0.06
$f_{w,\ ch21}$ [%]	0
$\sigma_{ch21/h22}$ [nm]	0.3 ± 0.1
d_{ch22} [nm]	1.9 ±0.2
SLD_{ch22} [10^{-4}/nm^2]	6.59
$f_{w,\ ch22}$ [%]	0
$\sigma_{ch22/h22}$ [nm]	0.3 ± 0.1
d_{h22} [nm]	0.9 ± 0.2
SLD_{h22} [10^{-4}/nm^2]	4.53
$f_{w,\ h22}$ [%]	10±3
$\sigma_{h22/w}$ [nm]	0.5 ± 0.2

Bibliography

[1] Berta Gumí-Audenis, Luca Costa, Francesco Carlá, Fabio Comin, Fausto Sanz, and Marina I. Giannotti. Structure and Nanomechanics of Model Membranes by Atomic Force Microscopy and Spectroscopy: Insights into the Role of Cholesterol and Sphingolipids. *Membranes*, 6(4), December 2016.

[2] S. J. Singer and G. L. Nicolson. The fluid mosaic model of the structure of cell membranes. *Science (New York, N.Y.)*, 175(4023):720–731, February 1972.

[3] William Stillwell. Introduction to Biological Membranes. In *An Introduction to Biological Membranes*, pages 1–12. Elsevier, 2013.

[4] Fuild Mosaic Model. https://en.wikipedia.org. Accessed: 2019-09-01.

[5] Kai Simons and Elina Ikonen. Functional rafts in cell membranes. *Nature*, 387(6633):569–572, June 1997.

[6] L. Rajendran. Lipid rafts and membrane dynamics. *Journal of Cell Science*, 118(6):1099–1102, February 2005.

[7] Michael Edidin. The State of Lipid Rafts: From Model Membranes to Cells. *Annual Review of Biophysics and Biomolecular Structure*, 32(1):257–283, June 2003.

[8] Linda J. Pike. Lipid rafts: bringing order to chaos. *Journal of Lipid Research*, 44(4):655–667, April 2003.

[9] M. J. Karnovsky, A. M. Kleinfeld, R. L. Hoover, and R. D. Klausner. The concept of lipid domains in membranes. *The Journal of Cell Biology*, 94(1):1–6, July 1982.

[10] Erdinc Sezgin, Ilya Levental, Satyajit Mayor, and Christian Eggeling. The mystery of membrane organization: composition, regulation and roles of lipid rafts. *Nature Reviews Molecular Cell Biology*, 18(6):361–374, 2017.

[11] Kai Simons and Mathias J. Gerl. Revitalizing membrane rafts: new tools and insights. *Nature Reviews Molecular Cell Biology*, 11(10):688–699, 2010.

[12] Daniel Lingwood and Kai Simons. Lipid rafts as a membrane-organizing principle. *Science*, 327(5961):46–50, 2010.

[13] J. Prost, J.-B. Manneville, and R. Bruinsma. Fluctuation-magnification of non-equilibrium membranes near a wall. *The European Physical Journal B*, 1(4):465–480, March 1998.

[14] J. Prost and R. Bruinsma. Shape fluctuations of active membranes. *Europhysics Letters*, 33(4):321–326, February 1996.

[15] Sriram Ramaswamy, John Toner, and Jacques Prost. Nonequilibrium Fluctuations, Traveling Waves, and Instabilities in Active Membranes. *Physical Review Letters*, 84(15):3494–3497, April 2000.

[16] J.-B. Manneville, P. Bassereau, S. Ramaswamy, and J. Prost. Active membrane fluctuations studied by micropipet aspiration. *Physical Review E*, 64(2):021908, July 2001.

[17] N. Gov. Membrane Undulations Driven by Force Fluctuations of Active Proteins. *Physical Review Letters*, 93(26):268104, December 2004.

[18] Jean-Baptiste Manneville, Patricia Bassereau, Daniel Lévy, and Jacques Prost. Magnification of Shape Fluctuations of Active Giant Unilamellar Vesicles. In Pier Luigi Luisi and Peter Walde, editors, *Perspectives in Supramolecular Chemistry*, pages 351–359. John Wiley & Sons, Ltd., Chichester, UK, March 2007.

[19] J.-B. Manneville, P. Bassereau, D. Lévy, and J. Prost. Activity of Transmembrane Proteins Induces Magnification of Shape Fluctuations of Lipid Membranes. *Physical Review Letters*, 82(21):4356–4359, May 1999.

[20] M. D. El Alaoui Faris, D. Lacoste, J. Pécréaux, J.-F. Joanny, J. Prost, and P. Bassereau. Membrane Tension Lowering Induced by Protein Activity. *Physical Review Letters*, 102(3), January 2009.

[21] Philippe Girard, Jacques Pécréaux, Guillaume Lenoir, Pierre Falson, Jean-Louis Rigaud, and Patricia Bassereau. A New Method for the Reconstitution of Membrane Proteins into Giant Unilamellar Vesicles. *Biophysical Journal*, 87(1):419–429, July 2004.

[22] J.-L. Rigaud. Membrane proteins: functional and structural studies using reconstituted proteoliposomes and 2-D crystals. *Brazilian Journal of Medical and Biological Research*, 35(7):753–766, July 2002.

[23] Ida Louise Jørgensen, Gerdi Christine Kemmer, and Thomas Günther Pomorski. Membrane protein reconstitution into giant unilamellar vesicles: a review on current techniques. *European Biophysics Journal*, 46(2):103–119, March 2017.

[24] Jean-Louis Rigaud, Mohammed Chami, Olivier Lambert, Daniel Levy, and Jean-Luc Ranck. Use of detergents in two-dimensional crystallization of membrane proteins. *Biochimica et Biophysica Acta (BBA) - Biomembranes*, 1508(1–2):112–128, November 2000.

[25] Annela M. Seddon, Paul Curnow, and Paula J. Booth. Membrane proteins, lipids and detergents: not just a soap opera. *Biochimica Et Biophysica Acta*, 1666(1-2):105–117, November 2004.

[26] Marc le Maire, Philippe Champeil, and Jesper V Møller. Interaction of membrane proteins and lipids with solubilizing detergents. *Biochimica et Biophysica Acta (BBA) - Biomembranes*, 1508(1–2):86–111, November 2000.

[27] R. Michael Garavito and Shelagh Ferguson-Miller. Detergents as Tools in Membrane Biochemistry. *Journal of Biological Chemistry*, 276(35):32403–32406, August 2001.

[28] Gregory J. Hardy, Rahul Nayak, and Stefan Zauscher. Model cell membranes:

Techniques to form complex biomimetic supported lipid bilayers via vesicle fusion. *Current opinion in colloid & interface science*, 18(5):448–458, October 2013.

[29] Jean-Louis Rigaud, Bruno Pitard, and Daniel Levy. Reconstitution of membrane proteins into liposomes: application to energy-transducing membrane proteins. *Biochimica et Biophysica Acta (BBA) - Bioenergetics*, 1231(3):223–246, October 1995.

[30] Motonari Shibakami, Hisayoshi Tsuihiji, Shin Miyoshi, Makoto Nakamura, Rie Goto, Shigeki Mitaku, and Masashi Sonoyama. Reconstitution of bacteriorhodopsin into cyclic lipid vesicles. *Bioscience, Biotechnology, and Biochemistry*, 72(6):1623–1625, June 2008.

[31] Pierre-Emmanuel Milhiet, Francesca Gubellini, Alexandre Berquand, Patrice Dosset, Jean-Louis Rigaud, Christian Le Grimellec, and Daniel Lévy. High-Resolution AFM of Membrane Proteins Directly Incorporated at High Density in Planar Lipid Bilayer. *Biophysical Journal*, 91(9):3268–3275, November 2006.

[32] Alexandre Berquand, Daniel Lévy, Francesca Gubellini, Christian Le Grimellec, and Pierre-Emmanuel Milhiet. Influence of calcium on direct incorporation of membrane proteins into in-plane lipid bilayer. *Ultramicroscopy*, 107(10–11):928–933, October 2007.

[33] M. Dezi, A. Di Cicco, P. Bassereau, and D. Levy. Detergent-mediated incorporation of transmembrane proteins in giant unilamellar vesicles with controlled physiological contents. *Proceedings of the National Academy of Sciences*, 110(18):7276–7281, April 2013.

[34] David Andelman. Electrostatic Properties of Membranes: The Poisson-Boltzmann Theory. *Structure and Dynamics of Membranes*, 1, January 1995.

[35] Arnaud Hemmerle. *X-ray scattering on a floating membrane: interaction potential and effects of an electric field*. Theses, Université de Strasbourg, September 2013.

[36] R.R. Netz. Electrostatistics of counter-ions at and between planar charged walls: From Poisson-Boltzmann to the strong-coupling theory. *The European Physical Journal E*, 5(1):557–574, August 2001.

[37] Per Linse and Vladimir Lobaskin. Electrostatic Attraction and Phase Separation in Solutions of Like-Charged Colloidal Particles. *Physical Review Letters*, 83(20):4208–4211, November 1999.

[38] Dautzenberg H. Polyelectrolytes: formation, characterization and application. H. Dautzenberg, W. Jaeger, J. Kötz, B. Philipp, Ch. Seidel and D. Stscherbina. Carl Hanser Verlag, Munich, 1994. pp. xiv + 343, price DM168.00. ISBN 1-56990-127-9. ISBN 3-446-17127-4 - Cameron - 1995 - Polymer International - Wiley Online Library.

[39] Victor A Bloomfield. DNA condensation. *Current Opinion in Structural Biology*, 6(3):334–341, June 1996.

[40] Ioulia Rouzina and Victor A. Bloomfield. Macroion Attraction Due to Electrostatic Correlation between Screening Counterions. 1. Mobile Surface-Adsorbed Ions and Diffuse Ion Cloud. *The Journal of Physical Chemistry*, 100(23):9977–9989, January 1996.

[41] A. G. Moreira and R. R. Netz. Strong-coupling theory for counter-ion distributions. *EPL (Europhysics Letters)*, 52(6):705, December 2000.

[42] André G. Moreira and Roland R. Netz. Binding of Similarly Charged Plates with Counterions Only. *Physical Review Letters*, 87(7):078301, July 2001.

[43] A.G. Moreira and R.R. Netz. Simulations of counterions at charged plates. *The European Physical Journal E*, 8(1):33–58, May 2002.

[44] Alexander Schlaich, Alexandre P. dos Santos, and Roland R. Netz. Simulations of Nanoseparated Charged Surfaces Reveal Charge-Induced Water Reorientation and Nonadditivity of Hydration and Mean-Field Electrostatic Repulsion. *Langmuir*, 35(2):551–560, January 2019.

[45] L. Samaj and E. Trizac. Strong-Coupling Theory of Counter-ions at Charged Plates. *arXiv:1009.4640 [cond-mat]*, September 2010. arXiv: 1009.4640.

[46] Ladislav Šamaj and Emmanuel Trizac. Wigner-crystal formulation of strong-coupling theory for counterions near planar charged interfaces. *Physical Review E*, 84(4), October 2011.

[47] Ladislav Šamaj and Emmanuel Trizac. Ground state of classical bilayer Wigner crystals. *EPL (Europhysics Letters)*, 98(3):36004, 2012.

[48] Ladislav Šamaj, Martin Trulsson, and Emmanuel Trizac. Strong-coupling theory of counterions between symmetrically charged walls: from crystal to fluid phases. *Soft Matter*, 14(20):4040–4052, 2018.

[49] L. Fumagalli, A. Esfandiar, R. Fabregas, S. Hu, P. Ares, A. Janardanan, Q. Yang, B. Radha, T. Taniguchi, K. Watanabe, G. Gomila, K. S. Novoselov, and A. K. Geim. Anomalously low dielectric constant of confined water. *Science*, 360(6395):1339–1342, June 2018.

[50] Laure Herrmann, Albert Johner, and Patrick Kékicheff. Interactions between Charged Lamellae in Aqueous Solution. *Physical Review Letters*, 113(26), December 2014.

[51] A chemical structure of the phospholipid molecules. https://avantilipids.com. Accessed: 2019-09-16.

[52] Phase transition temperatures for glycerophospholipids. https://avantilipids.com/. Accessed: 2019-09-01.

[53] Yuri Gerelli. Phase Transitions in a Single Supported Phospholipid Bilayer: Real-Time Determination by Neutron Reflectometry. *Physical Review Letters*, 122(24):248101, June 2019.

[54] Gary Bryant, Matthew B. Taylor, Tamim A. Darwish, Anwen M. Krause-Heuer, Ben Kent, and Christopher J. Garvey. Effect of deuteration on the phase behaviour and structure of lamellar phases of phosphatidylcholines - Deuterated lipids as proxies for the physical properties of native bilayers. *Colloids and Surfaces. B, Biointerfaces*, 177:196–203, May 2019.

[55] Tania K. Lind and Marité Cárdenas. Understanding the formation of supported lipid bilayers via vesicle fusion—A case that exemplifies the need for the complementary method approach (Review). *Biointerphases*, 11(2):020801, March 2016.

[56] Florence Blachon, Frédéric Harb, Bogdan Munteanu, Agnès Piednoir, Rémy Fulcrand, Thierry Charitat, Giovanna Fragneto, Olivier Pierre-Louis, Bernard Tinland, and Jean-Paul Rieu. Nanoroughness Strongly Impacts Lipid Mobility in Supported Membranes. *Langmuir*, 33(9):2444–2453, March 2017.

[57] Hanna P. Wacklin. Composition and Asymmetry in Supported Membranes Formed by Vesicle Fusion. *Langmuir*, 27(12):7698–7707, June 2011.

[58] Ryugo Tero. Substrate Effects on the Formation Process, Structure and Physicochemical Properties of Supported Lipid Bilayers. *Materials*, 5(12):2658–2680, December 2012.

[59] Frank Heinrich and Mathias Lösche. Zooming in on disordered systems: Neutron reflection studies of proteins associated with fluid membranes. *Biochimica et Biophysica Acta (BBA) - Biomembranes*, 1838(9):2341–2349, September 2014.

[60] Giovanna Fragneto, Thierry Charitat, and Jean Daillant. Floating lipid bilayers: models for physics and biology. *European Biophysics Journal*, 41(10):863–874, October 2012.

[61] James Kurniawan, Joao Francisco Ventrici de Souza, Amanda T. Dang, Gangyu Liu, and Tonya L. Kuhl. Preparation and Characterization of Solid Supported Lipid Bilayers Formed by Langmuir-Blodgett Deposition – a Tutorial. *Langmuir*, November 2018.

[62] Samira Hertrich, Frank Stetter, Adrian Rühm, Thorsten Hugel, and Bert Nickel. Highly Hydrated Deformable Polyethylene Glycol-Tethered Lipid Bilayers. *Langmuir*, 30(31):9442–9447, August 2014.

[63] M L Wagner and L K Tamm. Tethered polymer-supported planar lipid bilayers for reconstitution of integral membrane proteins: silane-polyethyleneglycol-lipid as a cushion and covalent linker. *Biophysical Journal*, 79(3):1400–1414, September 2000.

[64] J Y Wong, J Majewski, M Seitz, C K Park, J N Israelachvili, and G S Smith. Polymer-cushioned bilayers. I. A structural study of various preparation meth-

ods using neutron reflectometry. *Biophysical Journal*, 77(3):1445–1457, September 1999.

[65] J. Y. Wong, C. K. Park, M. Seitz, and J. Israelachvili. Polymer-cushioned bilayers. II. An investigation of interaction forces and fusion using the surface forces apparatus. *Biophysical Journal*, 77(3):1458–1468, September 1999.

[66] Hanna P. Vacklin, F. Tiberg, and R. K. Thomas. Formation of supported phospholipid bilayers via co-adsorption with β-d-dodecyl maltoside. *Biochimica et Biophysica Acta (BBA) - Biomembranes*, 1668(1):17–24, February 2005.

[67] Ryugo Tero, Morio Takizawa, Yan-Jun Li, Masahito Yamazaki, and Tsuneo Urisu. Lipid Membrane Formation by Vesicle Fusion on Silicon Dioxide Surfaces Modified with Alkyl Self-Assembled Monolayer Islands. *Langmuir*, 20(18):7526–7531, August 2004.

[68] Ralf Richter, Anneke Mukhopadhyay, and Alain Brisson. Pathways of Lipid Vesicle Deposition on Solid Surfaces: A Combined QCM-D and AFM Study. *Biophysical Journal*, 85(5):3035–3047, November 2003.

[69] Ralf P. Richter, Rémi Bérat, and Alain R. Brisson. Formation of Solid-Supported Lipid Bilayers: An Integrated View. *Langmuir*, 22(8):3497–3505, April 2006.

[70] James A. Svetlovics, Sterling A. Wheaten, and Paulo F. Almeida. Phase separation and fluctuations in mixtures of a saturated and an unsaturated phospholipid. *Biophysical journal*, 102(11):2526–2535, June 2012.

[71] Wilhelmy plate. https://www.biolinscientific.com. Accessed: 2019-09-01.

[72] Rhoderick E. Brown and Howard L. Brockman. Using Monomolecular Films to Characterize Lipid Lateral Interactions. *Methods in molecular biology (Clifton, N.J.)*, 398:41–58, 2007.

[73] Régine Maget-Dana. The monolayer technique: a potent tool for studying the interfacial properties of antimicrobial and membrane-lytic peptides and their interactions with lipid membranes. *Biochimica et Biophysica Acta (BBA) - Biomembranes*, 1462(1):109–140, December 1999.

[74] KyuHan Kim, Siyoung Q. Choi, Joseph A. Zasadzinski, and Todd M. Squires. Interfacial microrheology of dppc monolayers at the air–water interface. *Soft Matter*, 7:7782–7789, 2011.

[75] Paula Toimil, Gerardo Prieto, José Miñones, José M. Trillo, and Félix Sarmiento. Monolayer and brewster angle microscopy study of human serum albumin—dipalmitoyl phosphatidyl choline mixtures at the air–water interface. *Colloids and Surfaces B: Biointerfaces*, 92:64 – 73, 2012.

[76] Nagayuki Hasegawa, Hideyuki Jonotsuka, Kunio Miki, and Kazuki Takeda. X-ray structure analysis of bacteriorhodopsin at 1.3 Å resolution. *Scientific Reports*, 8(1):13123, September 2018.

[77] U. Haupts, J. Tittor, and D. Oesterhelt. Closing in on bacteriorhodopsin: progress in understanding the molecule. *Annual Review of Biophysics and Biomolecular Structure*, 28:367–399, 1999.

[78] Magnus Andersson, Erik Malmerberg, Sebastian Westenhoff, Gergely Katona, Marco Cammarata, Annemarie B. Wöhri, Linda C. Johansson, Friederike Ewald, Mattias Eklund, Michael Wulff, Jan Davidsson, and Richard Neutze. Structural dynamics of light-driven proton pumps. *Structure (London, England: 1993)*, 17(9):1265–1275, September 2009.

[79] Dmitry Bratanov, Taras Balandin, Ekaterina Round, Vitaly Shevchenko, Ivan Gushchin, Vitaly Polovinkin, Valentin Borshchevskiy, and Valentin Gordeliy. An Approach to Heterologous Expression of Membrane Proteins. The Case of Bacteriorhodopsin. *PLOS ONE*, 10(6):e0128390, June 2015.

[80] S. L. Reichow and T. Gonen. Lipid-protein interactions probed by electron crystallography. *Current opinion in structural biology*, 19(5):560–565, October 2009.

[81] H. Belrhali, P. Nollert, A. Royant, C. Menzel, J. P. Rosenbusch, E. M. Landau, and E. Pebay-Peyroula. Protein, lipid and water organization in bacteriorhodopsin crystals: a molecular view of the purple membrane at 1.9 A resolution. *Structure (London, England: 1993)*, 7(8):909–917, August 1999.

[82] J. K. Lanyi and H. Luecke. Bacteriorhodopsin. *Current Opinion in Structural Biology*, 11(4):415–419, August 2001.

[83] Eva Pebay-Peyroula, Richard Neutze, and Ehud M. Landau. Lipidic cubic phase crystallization of bacteriorhodopsin and cryotrapping of intermediates: towards resolving a revolving photocycle. *Biochimica et Biophysica Acta (BBA) - Bioenergetics*, 1460(1):119–132, August 2000.

[84] Richard Neutze, Eva Pebay-Peyroula, Karl Edman, Antoine Royant, Javier Navarro, and Ehud M. Landau. Bacteriorhodopsin: a high-resolution structural view of vectorial proton transport. *Biochimica Et Biophysica Acta*, 1565(2):144–167, October 2002.

[85] Yoshiaki Kimura, Dmitry G. Vassylyev, Atsuo Miyazawa, Akinori Kidera, Masaaki Matsushima, Kaoru Mitsuoka, Kazuyoshi Murata, Teruhisa Hirai, and Yoshinori Fujiyoshi. Surface of bacteriorhodopsin revealed by high-resolution electron crystallography. *Nature*, 389(6647):38323, September 1997.

[86] H. Luecke, B. Schobert, H. T. Richter, J. P. Cartailler, and J. K. Lanyi. Structure of bacteriorhodopsin at 1.55 A resolution. *Journal of Molecular Biology*, 291(4):899–911, August 1999.

[87] Colin D. Heyes and Mostafa A. El-Sayed. Thermal Properties of Bacteriorhodopsin. *The Journal of Physical Chemistry B*, 107(44):12045–12053, November 2003.

[88] Mary Luckey. *Membrane structural biology: with biochemical and biophysical foundations*. Cambridge University Press, Cambridge ; New York, second edition edition, 2014.

[89] E. London and H. G. Khorana. Denaturation and renaturation of bacteriorhodopsin in detergents and lipid-detergent mixtures. *The Journal of Biological Chemistry*, 257(12):7003–7011, June 1982.

[90] Three-dimensional view of ultrafast dynamics in photoexcited bacteriorhodopsin. *Nature Communications*, 10(1):1–17, 2019.

[91] Hartmut Luecke. Atomic resolution structures of bacteriorhodopsin photocycle intermediates: the role of discrete water molecules in the function of this light-driven ion pump. *Biochimica et Biophysica Acta (BBA) - Bioenergetics*, 1460(1):133–156, August 2000.

[92] Daniel J. Muller and Andreas Engel. Strategies to prepare and characterize native membrane proteins and protein membranes by AFM. *Current Opinion in Colloid & Interface Science*, 13(5):338–350, October 2008.

[93] P.N.T. Unwin and R. Henderson. Molecular structure determination by electron microscopy of unstained crystalline specimens. *Journal of Molecular Biology*, 94(3):425–440, May 1975.

[94] V. Pomerleau, E. Harvey-Girard, and F. Boucher. Lipid-protein interactions in the purple membrane: structural specificity within the hydrophobic domain. *Biochimica Et Biophysica Acta*, 1234(2):221–224, March 1995.

[95] Teruhisa Hirai, Sriram Subramaniam, and Janos K. Lanyi. Structural snapshots of conformational changes in a seven-helix membrane protein: lessons from bacteriorhodopsin. *Current Opinion in Structural Biology*, 19(4):433–439, August 2009.

[96] Yann Gohon, Tassadite Dahmane, Rob W. H. Ruigrok, Peter Schuck, Delphine Charvolin, Fabrice Rappaport, Peter Timmins, Donald M. Engelman, Christophe Tribet, Jean-Luc Popot, and Christine Ebel. Bacteriorhodopsin/Amphipol Complexes: Structural and Functional Properties. *Biophysical Journal*, 94(9):3523–3537, May 2008.

[97] T. Kouyama, R. A. Bogomolni, and W. Stoeckenius. Photoconversion from the light-adapted to the dark-adapted state of bacteriorhodopsin. *Biophysical journal*, 48(2):201–208, August 1985.

[98] Franz-Xaver Schmid. Biological Macromolecules: UV-visible Spectrophotometry. In John Wiley & Sons, Ltd, editor, *Encyclopedia of Life Sciences*. John Wiley & Sons, Ltd, Chichester, UK, April 2001.

[99] Dieter Oesterhelt and Walther Stoeckenius. [69] Isolation of the cell membrane of Halobacterium halobium and its fractionation into red and purple membrane. In *Methods in Enzymology*, volume 31 of *Biomembranes Part A*, pages 667–678. Academic Press, January 1974.

[100] Valentin I. Gordeliy, Ramona Schlesinger, Rouslan Efremov, Georg Büldt, and Joachim Heberle. Crystallization in lipidic cubic phases: a case study with bacteriorhodopsin. *Methods in Molecular Biology (Clifton, N.J.)*, 228:305–316, 2003.

[101] Valentin I. Borshchevskiy, Ekaterina S. Round, Alexandr N. Popov, Georg Büldt, and Valentin I. Gordeliy. X-ray-Radiation-Induced Changes in Bacteriorhodopsin Structure. *Journal of Molecular Biology*, 409(5):813–825, June 2011.

[102] Vadim Cherezov, Jeffrey Liu, Mark Griffith, Michael A. Hanson, and Raymond C. Stevens. LCP-FRAP Assay for Pre-Screening Membrane Proteins for In Meso Crystallization †. *Crystal Growth & Design*, 8(12):4307–4315, December 2008.

[103] Brian Y. Chow, Xue Han, Allison S. Dobry, Xiaofeng Qian, Amy S. Chuong, Mingjie Li, Michael A. Henninger, Gabriel M. Belfort, Yingxi Lin, Patrick E. Monahan, and Edward S. Boyden. High-performance genetically targetable optical neural silencing by light-driven proton pumps. *Nature*, 463(7277):98–102, January 2010.

[104] Erica C. Saint Clair, John I. Ogren, Sergey Mamaev, Daniel Russano, Joel M. Kralj, and Kenneth J. Rothschild. Near-IR Resonance Raman Spectroscopy of Archaerhodopsin 3: Effects of Transmembrane Potential. *The journal of physical chemistry. B*, 116(50):14592–14601, December 2012.

[105] Jie Feng, Hong-Can Liu, Jin-Fang Chu, Pei-Jin Zhou, Ji-An Tang, and Shuang-Jiang Liu. Genetic cloning and functional expression in Escherichia coli of an archaerhodopsin gene from Halorubrum xinjiangense. *Extremophiles*, 10(1):29–33, February 2006.

[106] E. V. Borisova, E. A. Epifanova, S. A. Tutukova, V. A. Salina, and A. A. Babaev.

Optogenetic approaches in neurobiology. *Molecular Genetics, Microbiology and Virology*, 31(4):203–207, October 2016.

[107] Nicholas C. Flytzanis, Claire N. Bedbrook, Hui Chiu, Martin K. M. Engqvist, Cheng Xiao, Ken Y. Chan, Paul W. Sternberg, Frances H. Arnold, and Viviana Gradinaru. Archaerhodopsin variants with enhanced voltage-sensitive fluorescence in mammalian and *Caenorhabditis elegans* neurons. *Nature Communications*, 5:4894, September 2014.

[108] Bastien Seantier, Manuela Dezi, Francesca Gubellini, Alexandre Berquand, Cédric Godefroy, Patrice Dosset, Daniel Lévy, and Pierre-Emmanuel Milhiet. Transfer on hydrophobic substrates and AFM imaging of membrane proteins reconstituted in planar lipid bilayers. *Journal of Molecular Recognition*, 24(3):461–466, May 2011.

[109] Lars Rose and A.T.A. Jenkins. The effect of the ionophore valinomycin on biomimetic solid supported lipid DPPTE/EPC membranes. *Bioelectrochemistry*, 70(2):387–393, May 2007.

[110] J. L. Rigaud, M. T. Paternostre, and A. Bluzat. Mechanisms of membrane protein insertion into liposomes during reconstitution procedures involving the use of detergents. 2. Incorporation of the light-driven proton pump bacteriorhodopsin. *Biochemistry*, 27(8):2677–2688, April 1988.

[111] A. W. Scotto and D. Zakim. Reconstitution of membrane proteins. Spontaneous incorporation of integral membrane proteins into preformed bilayers of pure phospholipid. *Journal of Biological Chemistry*, 263(34):18500–18506, December 1988.

[112] Anthony W. Scotto and Matthew E. Gompper. Spontaneous incorporation of bacteriorhodopsin into large preformed vesicles. *Biochemistry*, 29(31):7244–7251, August 1990.

[113] Jean-Louis Rigaud and Daniel Lévy. Reconstitution of Membrane Proteins into Liposomes. volume 372 of *Liposomes, Part B*, pages 65–86. Academic Press, 2003.

[114] Nicoletta Kahya, Eve-Isabelle Pécheur, Wim P. de Boeij, Douwe A. Wiersma, and Dick Hoekstra. Reconstitution of Membrane Proteins into Giant Unilamellar Vesicles via Peptide-Induced Fusion. *Biophysical Journal*, 81(3):1464–1474, September 2001.

[115] Michel Seigneuret and Jean Louis Rigaud. Analysis of passive and light-driven ion movements in large bacteriorhodopsin liposomes reconstituted by reverse-phase evaporation. 1. Factors governing the passive proton permeability of the membrane. *Biochemistry*, 25(21):6716–6722, October 1986.

[116] Michel Seigneuret and Jean Louis Rigaud. Analysis of passive and light-driven ion movements in large bacteriorhodopsin liposomes reconstituted by reverse-phase evaporation. 2. Influence of passive permeability and back-pressure effects upon light-induced proton uptake. *Biochemistry*, 25(21):6723–6730, October 1986.

[117] Matthias Garten, Sophie Aimon, Patricia Bassereau, and Gilman E. S. Toombes. Reconstitution of a transmembrane protein, the voltage-gated ion channel, KvAP, into giant unilamellar vesicles for microscopy and patch clamp studies. *Journal of Visualized Experiments: JoVE*, (95):52281, January 2015.

[118] Daniel Lévy, Annette Gulik, Aline Bluzat, and Jean-Louis Rigaud. Reconstitution of the sarcoplasmic reticulum Ca2+-ATPase: mechanisms of membrane protein insertion into liposomes during reconstitution procedures involving the use of detergents. *Biochimica et Biophysica Acta (BBA) - Biomembranes*, 1107(2):283–298, June 1992.

[119] Marie Therese Paternostre, Michel Roux, and Jean Louis Rigaud. Mechanisms of membrane protein insertion into liposomes during reconstitution procedures involving the use of detergents. 1. Solubilization of large unilamellar liposomes (prepared by reverse-phase evaporation) by Triton X-100, octyl glucoside, and sodium cholate. *Biochemistry*, 27(8):2668–2677, April 1988.

[120] F. Höök, M. Rodahl, P. Brzezinski, and B. Kasemo. Energy Dissipation Kinetics for Protein and Antibody-Antigen Adsorption under Shear Oscillation on a Quartz Crystal Microbalance. *Langmuir*, 14(4):729–734, February 1998.

[121] M V Voinova, M Rodahl, M Jonson, and B Kasemo. Viscoelastic Acoustic Response of Layered Polymer Films at Fluid-Solid Interfaces: Continuum Mechanics Approach. *Physica Scripta*, 59(5):391–396, May 1999.

[122] Adam Mechler, Slavica Praporski, Kiran Atmuri, Martin Boland, Frances Separovic, and Lisandra L. Martin. Specific and Selective Peptide-Membrane Interactions Revealed Using Quartz Crystal Microbalance. *Biophysical Journal*, 93(11):3907–3916, December 2007.

[123] Kathleen F. Wang, Ramanathan Nagarajan, and Terri A. Camesano. Differentiating antimicrobial peptides interacting with lipid bilayer: Molecular signatures derived from quartz crystal microbalance with dissipation monitoring. *Biophysical Chemistry*, 196:53–67, January 2015.

[124] Qian Chen, Shengming Xu, Qingxia Liu, Jacob Masliyah, and Zhenghe Xu. QCM-D study of nanoparticle interactions. *Advances in Colloid and Interface Science*, 233:94–114, July 2016.

[125] Matthew C. Dixon. Quartz Crystal Microbalance with Dissipation Monitoring: Enabling Real-Time Characterization of Biological Materials and Their Interactions. *Journal of Biomolecular Techniques : JBT*, 19(3):151–158, July 2008.

[126] Edurne Tellechea, Diethelm Johannsmann, Nicole F. Steinmetz, Ralf P. Richter, and Ilya Reviakine. Model-Independent Analysis of QCM Data on Colloidal Particle Adsorption. *Langmuir*, 25(9):5177–5184, May 2009.

[127] Nam-Joon Cho, Curtis W Frank, Bengt Kasemo, and Fredrik Höök. Quartz crystal microbalance with dissipation monitoring of supported lipid bilayers on various substrates. *Nature Protocols*, 5(6):1096–1106, June 2010.

[128] Tania Kjellerup Lind, Marité Cárdenas, and Hanna Pauliina Wacklin. Formation of Supported Lipid Bilayers by Vesicle Fusion: Effect of Deposition Temperature. *Langmuir*, 30(25):7259–7263, July 2014.

[129] Günter Sauerbrey. Verwendung von Schwingquarzen zur Wägung dünner Schichten und zur Mikrowägung. *Zeitschrift für Physik*, 155(2):206–222, April 1959.

[130] Søren B. Nielsen and Daniel E. Otzen. Quartz Crystal Microbalances as Tools for Probing Protein–Membrane Interactions. In Jörg H. Kleinschmidt, editor, *Lipid-Protein Interactions*, volume 974, pages 1–21. Humana Press, Totowa, NJ, 2013.

[131] QCM-D measurements for the soft and rigid films. http://www.biolinscientific.com. Accessed: 2019-09-04.

[132] Marie-Paule Mingeot-Leclercq, Magali Deleu, Robert Brasseur, and Yves F Dufrêne. Atomic force microscopy of supported lipid bilayers. *Nature Protocols*, 3(10):1654–1659, October 2008.

[133] Shu-wen W. Chen, Jean-Marie Teulon, Christian Godon, and Jean-Luc Pellequer. Atomic force microscope, molecular imaging, and analysis. *Journal of Molecular Recognition*, 29(1):51–55, 2016.

[134] G. Binnig, C. F. Quate, and Ch. Gerber. Atomic Force Microscope. *Physical Review Letters*, 56(9):930–933, March 1986.

[135] Luca Costa. *The Force Feedback Microscope : an AFM for soft condensed matter*. Theses, Université de Grenoble, January 2014.

[136] Patrick L.T.M. Frederix, Patrick D. Bosshart, and Andreas Engel. Atomic Force Microscopy of Biological Membranes. *Biophysical Journal*, 96(2):329–338, January 2009.

[137] Nader Jalili and Karthik Laxminarayana. A review of atomic force microscopy imaging systems: application to molecular metrology and biological sciences. *Mechatronics*, 14(8):907–945, October 2004.

[138] PeakForce Tapping mode of imaging. https://www.bruker.com/. Accessed: 2019-09-01.

[139] The Multimode 8, Nanoscope V AFM instrument from Bruker. http://www.ibs.fr. Accessed: 2019-09-04.

[140] Scanfluid probe for the PeakForce Tapping mode of imaging. https://www.brukerafmprobes.com. Accessed: 2019-09-01.

[141] SiNi probe for the contact mode imaging. https://www.budgetsensors.com. Accessed: 2019-09-01.

[142] Fred Rost. Fluorescence Microscopy, Applications. In John C. Lindon, editor, *Encyclopedia of Spectroscopy and Spectrometry*, pages 565–570. Elsevier, Oxford, January 1999.

[143] André Pierre Schroder, Jérôme Joseph Crassous, Carlos Manuel Marques, and Ulf Olsson. Rapid confocal imaging of vesicle-to-sponge phase droplet transition in dilute dispersions of the C10e3 surfactant. *Scientific Reports*, 9(1), December 2019.

[144] Georges Weber, Thierry Charitat, Maurício S. Baptista, Adjaci F. Uchoa, Christiane Pavani, Helena C. Junqueira, Yachong Guo, Vladimir A. Baulin, Rosangela Itri, Carlos M. Marques, and André P. Schroder. Lipid oxidation induces structural changes in biomimetic membranes. *Soft Matter*, 10(24):4241, 2014.

[145] Mattia I. Morandi, Fabrice J. Thalmann, Monika Kluzek, Andre P. Schroder, and Carlos M. Marques. DPPC Lipid Melting Transition in Concentrated Sucrose Solutions. *Biophysical Journal*, 116(3):79a, February 2019.

[146] Yasmine Miguel Serafini Micheletto, Carlos M. Marques, Nádya Pesce da Silveira, and André P. Schroder. Electroformation of Giant Unilamellar Vesicles: Investigating Vesicle Fusion versus Bulge Merging. *Langmuir*, 32(32):8123–8130, August 2016.

[147] Guohua Lei and Robert C. MacDonald. Lipid Bilayer Vesicle Fusion: Intermediates Captured by High-Speed Microfluorescence Spectroscopy. *Biophysical Journal*, 85(3):1585–1599, September 2003.

[148] Michael J. Sanderson, Ian Smith, Ian Parker, and Martin D. Bootman. Fluorescence Microscopy. *Cold Spring Harbor protocols*, 2014(10):pdb.top071795, October 2014.

[149] Nikon. Lateral resolution of a microscope. https://www.microscopyu.com/. Accessed: 2019-07-10.

[150] Nikon. Depth of field of a microscope. https://www.microscopyu.com/. Accessed: 2019-07-10.

[151] Thermofisher. Epifluorescence microscope. https://www.thermofisher.com/. Accessed: 2019-09-01.

[152] Fluorescence SpectraViewer.thermofisher. https://www.thermofisher.com. Accessed: 2019-09-04.

[153] ImageJ. https://imagej.nih.gov/ij/. Accessed: 2019-09-04.

[154] Giovanna Fragneto-Cusani. Neutron reflectivity at the solid/liquid interface: examples of applications in biophysics. *Journal of Physics: Condensed Matter*, 13(21):4973–4989, May 2001.

[155] Roger Pynn. Neutron Scattering—A Non-destructive Microscope for Seeing Inside Matter. In Ian S. Anderson, Alan J. Hurd, Robert L. McGreevy, Liyuan Liang, Romano Rinaldi, and Helmut Schober, editors, *Neutron Applications in Earth, Energy and Environmental Sciences*, pages 15–36. Springer US, Boston, MA, 2009.

[156] Schober Helmut. An introduction to the theory of nuclear neutron scattering in condensed matter. *Journal of Neutron Research*, (3-4):109–357, 2014.

[157] Robert Cubitt and Giovanna Fragneto. Neutron Reflection:. In *Scattering*, pages 1198–1208. Elsevier, 2002.

[158] Thomas Brueckel, Gernot Heger, Dieter Richter, Georg Roth, and Reiner Zorn. Neutron scattering. Lectures.

[159] Fabrice Cousin and Alexis Chennevière. Neutron reflectivity for soft matter. *EPJ Web of Conferences*, 188:04001, 2018.

[160] L. G. Parratt. Surface studies of solids by total reflection of x-rays. *Phys. Rev.*, 95:359–369, Jul 1954.

[161] Max Born, Emil Wolf, A. B. Bhatia, P. C. Clemmow, D. Gabor, A. R. Stokes, A. M. Taylor, P. A. Wayman, and W. L. Wilcock. Principles of Optics by Max Born, October 1999.

[162] J. Daillant, K. Quinn, C. Gourier, and F. Rieutord. Grazing incidence surface scattering of X-rays. *Journal of the Chemical Society, Faraday Transactions*, 92(4):505–513, January 1996.

[163] Jean Daillant and Alain Gibaud. *X-Ray and Neutron Reflectivity: Principles and Applications*. Lecture Notes in Physics Monographs. Springer-Verlag, Berlin Heidelberg, 1999.

[164] J. Daillant, E. Bellet-Amalric, A. Braslau, T. Charitat, G. Fragneto, F. Graner, S. Mora, F. Rieutord, and B. Stidder. Structure and fluctuations of a single floating lipid bilayer. *Proceedings of the National Academy of Sciences*, 102(33):11639–11644, August 2005.

[165] Linda Malaquin. *Interactions et déstabilisation de membranes lipidiques supportées*. PhD thesis, 2009. Thèse de doctorat dirigée par Charitat, Thierry et Daillant, Jean Physique Strasbourg 2009.

[166] L. Malaquin, T. Charitat, and J. Daillant. Supported bilayers: Combined specular and diffuse X-ray scattering. *The European Physical Journal E*, 31(3):285–301, March 2010.

[167] Serge Mora. *Structure d'interface de fluides complexes*. Theses, Université Paris Sud - Paris XI, September 2003.

[168] Sriram Ramaswamy, John Toner, and Jacques Prost. Nonequilibrium noise and instabilities in membranes with active pumps. *Pramana*, 53(1):237–242, July 1999.

[169] P. Girard, J. Prost, and P. Bassereau. Passive or Active Fluctuations in Membranes Containing Proteins. *Physical Review Letters*, 94(8):088102, March 2005.

[170] A. Giahi, M. El Alaoui Faris, P. Bassereau, and T. Salditt. Active membranes studied by X-ray scattering. *The European Physical Journal E*, 23(4):431–437, August 2007.

[171] W. Helfrich. Elastic properties of lipid bilayers: theory and possible experiments. *Zeitschrift Fur Naturforschung. Teil C: Biochemie, Biophysik, Biologie, Virologie*, 28(11):693–703, December 1973.

[172] T. Charitat, E. Bellet-Amalric, G. Fragneto, and F. Graner. Adsorbed and free lipid bilayers at the solid-liquid interface. *The European Physical Journal B*, 8(4):583–593, April 1999.

[173] Arnaud Hemmerle, Giovanna Fragneto, Jean Daillant, and Thierry Charitat. Reduction in Tension and Stiffening of Lipid Membranes in an Electric Field Revealed by X-Ray Scattering. *Physical Review Letters*, 116(22):228101, June 2016.

[174] Martin Bauer, Max Bernhardt, Thierry Charitat, Patrick Kékicheff, Christophe Fajolles, Giovanna Fragneto, Carlos M. Marques, and Jean Daillant. Membrane insertion of sliding anchored polymers. *Soft Matter*, 9(5):1700–1710, 2013.

[175] A. Hemmerle, L. Malaquin, T. Charitat, S. Lecuyer, G. Fragneto, and J. Daillant. Controlling interactions in supported bilayers from weak electrostatic repulsion to high osmotic pressure. *Proceedings of the National Academy of Sciences*, 109(49):19938–19942, December 2012.

[176] R. A. Campbell, H. P. Wacklin, I. Sutton, R. Cubitt, and G. Fragneto. FIGARO: The new horizontal neutron reflectometer at the ILL. *The European Physical Journal Plus*, 126(11), November 2011.

[177] R. Cubitt and G. Fragneto. D17: the new reflectometer at the ILL. *Applied Physics A: Materials Science & Processing*, 74(0):s329–s331, December 2002.

[178] Stefan Mattauch, Alexandros Koutsioubas, Ulrich Rücker, Denis Korolkov, Vicenzo Fracassi, Jos Daemen, Ralf Schmitz, Klaus Bussmann, Frank Suxdorf, Michael Wagener, Peter Kämmerling, Harald Kleines, Lydia Fleischhauer-Fuß, Manfred Bednareck, Vladimir Ossoviy, Andreas Nebel, Peter Stronciwilk, Simon Staringer, Marko Gödel, Alfred Richter, Harald Kusche, Thomas Kohnke, Alexander Ioffe, Earl Babcock, Zahir Salhi, and Thomas Bruckel. The high-intensity reflectometer of the Jülich Centre for Neutron Science: MARIA. *Journal of Applied Crystallography*, 51(3):646–654, June 2018.

[179] Neutron reflectometers at the ILL, Grenoble, France. https://www.ill.eu. Accessed: 2019-09-04.

[180] Neutron reflectometers at the MLZ, Garching, Germany. https://www.mlz-garching.de/maria. Accessed: 2019-09-04.

[181] LAMP. https://www.ill.eu/users/support-labs-infrastructure/software-scientific-tools/lamp/. Accessed: 2019-09-04.

[182] SixS beamline. https://www.synchrotron-soleil.fr/en/beamlines/sixs. Accessed: 2019-09-04.

[183] Sigolène Lecuyer. *Fluctuations et déstabilisation d'une bicouche lipidique supportée*. PhD thesis, 2006. Thèse de doctorat dirigée par Charitat, Thierry Physique Strasbourg 1 2006.

[184] Panalytical X-ray bench. http://www.panalytical.com/Empyrean.htm. Accessed: 2019-09-04.

[185] Y. Gerelli. Aurore: new software for neutron reflectivity data analysis. *Journal of Applied Crystallography*, 49(1):330–339, February 2016.

[186] Andrew Nelson. Co-refinement of multiple-contrast neutron/X-ray reflectivity data using *MOTOFIT*. *Journal of Applied Crystallography*, 39(2):273–276, April 2006.

[187] O. S. Heavens. Optical properties of thin films. *Reports on Progress in Physics*, 23(1):1–65, January 1960.

[188] A. Corana, M. Marchesi, C. Martini, and S. Ridella. Minimizing Multimodal Functions of Continuous Variables with the "Simulated Annealing" algorithmCorrigenda for This Article is Available Here. *ACM Trans. Math. Softw.*, 13(3):262–280, September 1987.

[189] J. F. Nagle and M. C. Wiener. Structure of fully hydrated bilayer dispersions. *Biochimica Et Biophysica Acta*, 942(1):1–10, July 1988.

[190] John F Nagle and Stephanie Tristram-Nagle. Lipid bilayer structure. *Current Opinion in Structural Biology*, 10(4):474–480, August 2000.

[191] John F. Nagle and Stephanie Tristram-Nagle. Structure of lipid bilayers. *Biochimica et Biophysica Acta (BBA) - Reviews on Biomembranes*, 1469(3):159–195, November 2000.

[192] Stephanie Tristram-Nagle and John F. Nagle. Lipid bilayers: thermodynamics, structure, fluctuations, and interactions. *Chemistry and physics of lipids*, 127(1):3–14, January 2004.

[193] Biomolecular Scattering Length Density Calculator. http://psldc.isis.rl.ac.uk/Psldc/. Accessed: 2019-09-06.

[194] DDM detergent. https://www.clinisciences.com. Accessed: 2019-08-21.

[195] JEAN-BAPTISTE MANNEVILLE. *Fluctuations de membranes actives*. PhD thesis, 1999. Thèse de doctorat dirigée par Prost, Jacques Sciences biologiques fondamentales et appliquées Paris 7 1999.

[196] Motomu Tanaka and Erich Sackmann. Polymer-supported membranes as models of the cell surface. *Nature*, 437(7059):656–663, September 2005.

[197] C. Scomparin, S. Lecuyer, M. Ferreira, T. Charitat, and B. Tinland. Diffusion in supported lipid bilayers: influence of substrate and preparation technique on the internal dynamics. *The European Physical Journal. E, Soft Matter*, 28(2):211–220, February 2009.

[198] Paulo F. F. Almeida, Winchil L. C. Vaz, and T. E. Thompson. Lipid Diffusion, Free Area, and Molecular Dynamics Simulations. *Biophysical Journal*, 88(6):4434–4438, June 2005.

[199] Radek Macháň and Martin Hof. Lipid diffusion in planar membranes investigated by fluorescence correlation spectroscopy. *Biochimica et Biophysica Acta (BBA) - Biomembranes*, 1798(7):1377–1391, July 2010.

[200] J Davoust, P F Devaux, and L Leger. Fringe pattern photobleaching, a new method for the measurement of transport coefficients of biological macromolecules. *The EMBO Journal*, 1(10):1233–1238, 1982.

[201] Enshinn Wu, Kenneth Jacobson, and Demetrios Papahadjopoulos. Lateral diffusion in phospholipid multibilayers measured by fluorescence recovery after photobleaching. *Biochemistry*, 16(17):3936–3941, August 1977.

[202] G. Fragneto, T. Charitat, F. Graner, K. Mecke, L. Perino-Gallice, and E. Bellet-Amalric. A fluid floating bilayer. *Europhysics Letters*, 53(1):100–106, January 2001.

[203] H J Steinhoff, M Pfeiffer, T Rink, O Burlon, M Kurz, J Riesle, E Heuberger, K Gerwert, and D Oesterhelt. Azide reduces the hydrophobic barrier of the bacteriorhodopsin proton channel. *Biophysical Journal*, 76(5):2702–2710, May 1999.

[204] The activational 20cga-530 colored-glass alternative long-pass filter with a 530 ± 5 nm cut-on wavelength. https://www.newport.com/p/20CGA-530. Accessed: 2019-08-21.

[205] K. Norrish and J. P. Quirk. Crystalline Swelling of Montmorillonite: Use of Electrolytes to Control Swelling. *Nature*, 173(4397):255–256, February 1954.

[206] Luc Belloni. Colloidal interactions. *Journal of Physics: Condensed Matter*, 12(46):R549–R587, October 2000.

[207] Ali Naji, Swetlana Jungblut, André G. Moreira, and Roland R. Netz. Electrostatic interactions in strongly coupled soft matter. *Physica A: Statistical Mechanics and its Applications*, 352(1):131–170, July 2005.

[208] M. Kanduč, M. Trulsson, A. Naji, Y. Burak, J. Forsman, and R. Podgornik. Weak- and strong-coupling electrostatic interactions between asymmetrically charged planar surfaces. *Physical Review E*, 78(6), December 2008.

[209] Moritz Antlanger, Gerhard Kahl, Martial Mazars, Ladislav Šamaj, and Emmanuel Trizac. Rich polymorphic behavior of wigner bilayers. *Phys. Rev. Lett.*, 117:118002, Sep 2016.

[210] Ladislav Šamaj and Emmanuel Trizac. Counterions at Highly Charged Interfaces: From One Plate to Like-Charge Attraction. *Physical Review Letters*, 106(7):078301, February 2011.

[211] H Boroudjerdi, Y Kim, A Naji, R Netz, X Schlagberger, and A Serr. Statics and dynamics of strongly charged soft matter. *Physics Reports*, 416(3-4):129–199, September 2005.

[212] Ladislav Šamaj and Emmanuel Trizac. Ground-state structure of a bilayer Wigner crystal with repulsive dielectric images. *EPL*, 100(5):56005, December 2012.

[213] Horia I. Petrache, Stephanie Tristram-Nagle, Klaus Gawrisch, Daniel Harries, V. Adrian Parsegian, and John F. Nagle. Structure and fluctuations of charged phosphatidylserine bilayers in the absence of salt. *Biophysical Journal*, 86(3):1574–1586, March 2004.

[214] Eva Nováková, Klaus Giewekemeyer, and Tim Salditt. Structure of two-component lipid membranes on solid support: An x-ray reflectivity study. *Physical Review E*, 74(5), November 2006.

[215] Shuichi Taguchi and Nobuyuki Wakayama. Atomic force microscopy observation of the phase separation in acidic phospholipid/neutral phospholipid supported bilayers. *Japanese Journal of Applied Physics*, 41(Part 1, No. 7B):4987–4989, jul 2002.

[216] Timothy A. Oleson, Nita Sahai, and Joel A. Pedersen. Electrostatic effects on deposition of multiple phospholipid bilayers at oxide surfaces. *Journal of Colloid and Interface Science*, 352(2):327–336, December 2010.

[217] Yi Zhang, Xiong Cheng, Jianxiu Wang, and Feimeng Zhou. Bi- and tetralayered dipalmitoyl phosphatidylserine (dpps) patterns produced by hydration of langmuir–blodgett monolayers and the subsequent enzymatic digestion. *Colloids and Surfaces A: Physicochemical and Engineering AspectsZhang2009*, 337(1):26 – 32, 2009.

[218] Olga B. Florek, Luke A. Clifton, Marleen Wilde, Thomas Arnold, Rebecca J. Green, and Richard A. Frazier. Lipid composition in fungal membrane models: effect of lipid fluidity. *Acta Crystallographica Section D Structural Biology*, 74(12):1233–1244, December 2018.

[219] Parag Mukhopadhyay, Luca Monticelli, and D. Peter Tieleman. Molecular Dynamics Simulation of a Palmitoyl-Oleoyl Phosphatidylserine Bilayer with Na+ Counterions and NaCl. *Biophysical Journal*, 86(3):1601–1609, March 2004.

[220] Sagar A. Pandit and Max L. Berkowitz. Molecular Dynamics Simulation of Dipalmitoylphosphatidylserine Bilayer with Na+ Counterions. *Biophysical Journal*, 82(4):1818–1827, April 2002.

[221] Sagar A. Pandit, David Bostick, and Max L. Berkowitz. Mixed Bilayer Containing Dipalmitoylphosphatidylcholine and Dipalmitoylphosphatidylserine: Lipid Complexation, Ion Binding, and Electrostatics. *Biophysical Journal*, 85(5):3120–3131, November 2003.

[222] H. Y. Jing, D. H. Hong, B. D. Kwak, D. J. Choi, K. Shin, C.-J. Yu, J. W. Kim, D. Y. Noh, and Y. S. Seo. X-ray Reflectivity Study on the Structure and Phase Stability of Mixed Phospholipid Multilayers†, January 2009.

[223] N. Delorme, J.-F. Bardeau, D. Carrière, M. Dubois, A. Gourbil, H. Mohwald, Th. Zemb, and A. Fery. Experimental Evidence of the Electrostatic Contribution to the Bending Rigidity of Charged Membranes. *The Journal of Physical Chemistry B*, 111(10):2503–2505, March 2007.

[224] Bruno Demé, Monique Dubois, Thaddée Gulik-Krzywicki, and Thomas Zemb. Giant Collective Fluctuations of Charged Membranes at the Lamellar-to-Vesicle Unbinding Transition. 1. Characterization of a New Lipid Morphology by SANS, SAXS, and Electron Microscopy. *Langmuir*, 18(4):997–1004, February 2002.

[225] Karlo Komorowski, Annalena Salditt, Yihui Xu, Halenur Yavuz, Martha Brennich, Reinhard Jahn, and Tim Salditt. Vesicle Adhesion and Fusion Studied by Small-Angle X-Ray Scattering. *Biophysical Journal*, 114(8):1908–1920, April 2018.

[226] O. Sonneville-Aubrun, V. Bergeron, T. Gulik-Krzywicki, Bo Jönsson, H. Wennerström, P. Lindner, and B. Cabane. Surfactant Films in Biliquid Foams. *Langmuir*, 16(4):1566–1579, February 2000.

[227] P. Kékicheff, S. Marčelja, T. J. Senden, and V. E. Shubin. Charge reversal seen in electrical double layer interaction of surfaces immersed in 2:1 calcium electrolyte. *The Journal of Chemical Physics*, 99(8):6098–6113, October 1993.

[228] Ali Khan, Bengt Joensson, and Haakan Wennerstroem. Phase equilibria in the mixed sodium and calcium di-2-ethylhexylsulfosuccinate aqueous system. An illustration of repulsive and attractive double-layer forces. *The Journal of Physical Chemistry*, 89(24):5180–5184, November 1985.

[229] Giovanna Fragneto, Thierry Charitat, Edith Bellet-Amalric, Robert Cubitt, and François Graner. Swelling of Phospholipid Floating Bilayers: The Effect of Chain Length. *Langmuir*, 19(19):7695–7702, September 2003.

[230] Mafumi Hishida, Yoko Nomura, Ryo Akiyama, Yasuhisa Yamamura, and Kazuya Saito. Electrostatic double-layer interaction between stacked charged bilayers. *Physical Review E*, 96(4), October 2017.

[231] Travers H. Anderson, Younjin Min, Kim L. Weirich, Hongbo Zeng, Deborah Fygenson, and Jacob N. Israelachvili. Formation of supported bilayers on silica substrates. *Langmuir*, 25(12):6997–7005, 2009. PMID: 19354208.

[232] R. L. Thurmond, S. W. Dodd, and M. F. Brown. Molecular areas of phospholipids as determined by 2h NMR spectroscopy. Comparison of phosphatidylethanolamines and phosphatidylcholines. *Biophysical Journal*, 59(1):108–113, January 1991.

[233] V.A. Parsegian. *Van der Waals Forces: A Handbook for Biologists, Chemists, Engineers, and Physicists*. Cambridge University Press, 2005.

[234] M. Ishii, K. Nakashima, I. Tajima, and M. Yamamoto. Properties of silicon surface cleaned by hydrogen plasma. *Applied Physics Letters*, 58(13):1378–1380, April 1991.

[235] Michiharu Tabe. UV ozone cleaning of silicon substrates in silicon molecular beam epitaxy. *Applied Physics Letters*, 45(10):1073–1075, November 1984.

[236] Simon J. L. Billinge and Igor Levin. The problem with determining atomic structure at the nanoscale. *Science (New York, N.Y.)*, 316(5824):561–565, April 2007.

Université de Strasbourg

ECOLE DOCTORALE pcp

Tetiana MUKHINA

Active Fluctuations and Electrostatic Interactions in Floating Lipid Membranes

Résumé en français

Le projet principal de ce travail a porté sur l'étude des fluctuations hors d'équilibres de membranes lipidiques induites par la bactériorhodopsine (BR), une protéine transmembranaire activée par la lumière. Un protocole robuste pour l'incorporation de BR dans les systèmes mimétiques de membrane a été développé et les changements structurels induits par l'incorporation et l'activation de la BR ont été étudiés en détail par réflectivité spéculaire (neutrons et rayons X) et par réflectivité hors-spéculaire (rayons X). Nous avons pu observer un effet réversible induit par l'activité de la protéine sur la structure de la membrane et sur ses fluctuations. Ces résultats ouvrent la voie à l'étude du spectre des fluctuations hors-équilibres d'un système protéo-membranaire planaire, et à l'accès aux propriétés physiques de la membrane active. Dans un second projet nous avons étudié l'interaction entre deux bicouches lipidiques fortement chargées. Nous avons finement caractérisé la structure du système et clairement démontré que des interactions attractives existaient entre les bicouches chargées, en accord avec la théorie de couplage fort.

Les mots-clés : membrane active, bactériorhodopsine, spectre de fluctuation membranaire, réflectométrie de neutrons, réflectométrie des rayons X, interactions membranaires, théorie de couplage fort.

Résumé en anglais

The main project of this work was focused on the investigation of out-of-equilibrium fluctuation of phospholipid membranes induced by light-activated transmembrane protein bacteriorhodopsin (BR). A robust protocol for the BR incorporation into the membrane-mimic systems was developed and the induced structural changes caused by BR incorporation and activation with light were probed by means of neutron and X-ray specular and off-specular reflectometry. The reversible effect of light illumination on the protein activity (on /off) via its effect on the bilayer structure and fluctuation spectrum was demonstrated. These results open the way to investigate the active fluctuation spectrum of a planar membrane-protein system and to access the physical properties of the active membrane. The aim of the second project was to investigate the interaction between highly negatively charged DPPS lipid bilayers. We fully characterized the structure of the system and clearly demonstrated that attractive interactions existed between charged bilayers, in good agreement with Strong-Coupling theory.

Keywords: active membrane, bacteriorhodopsin, membrane fluctuation spectrum, neutron reflectometry, X-ray reflectometry, membrane interactions, Strong-Coupling theory